Advancing Quantum Chemistry Simulations with Relativistic Electronic Structure and Quantum Computation

Torin F. Stetina

A dissertation
submitted in partial fulfillment of the
requirements for the degree of

Doctor of Philosophy

University of Washington

2021

Reading Committee:

Xiaosong Li, Chair

Cody Schlenker

Stefan Stoll

Program Authorized to Offer Degree:
Chemistry

University of Washington

Abstract

Advancing Quantum Chemistry Simulations with Relativistic Electronic Structure and Quantum Computation

Torin F. Stetina

Chair of the Supervisory Committee:
Harry and Catherine Jaynne Boand Endowed Professor Xiaosong Li
Department of Chemistry

This dissertation covers two main topics: relativistic Hamiltonians for quantum chemistry, and quantum computation. The main theme of the work presented within is the development of higher accuracy *ab initio* quantum chemistry simulations within the context of relativistic theory, and the theoretical analysis of quantum computational algorithms. In the first chapter, approximate density functionals are calibrated with a variational two-component relativistic Hamiltonian for the prediction of excited state X-ray absorption spectra. The second chapter presents a new method for computing four-component Dirac Hartree–Fock ground states of molecules, with an emphasis on its practical efficiency for large heavy element molecular systems in the future. The third and final chapter goes beyond the realm of Dirac Hartree–Fock theory, and analyzes how one could model the fully correlated molecular Hamiltonian including second order effective quantum electrodynamic effects within the digital model of quantum computation.

TABLE OF CONTENTS

LIST OF FIGURES

Figure Number Page

GLOSSARY

AO: Atomic orbital.

LCAO: Linear combination of atomic orbitals

MO: Molecular orbital

SCF: Self-consistent field

FCI: Full configuration interaction

XAS: X-ray absorption spectroscopy

XANES: X-ray absorption near edge structure

NEXAFS: Near edge X-ray absorption fine structure

MCSCF: Multi-configurational self-consistent field

DFT: Density functional theory

TDDFT: Time-dependent density functional theory

CAS: Complete active space

GPLHR: Generalized preconditioned locally harmonic residual

2C: 2-component

4C: 4-component

X2C: Exact 2-component

MAE: Mean absolute error

MPE: Mean percent error

GGA: Generalized gradient approximation

DHF: Dirac Hartree–Fock

DC: Dirac–Coulomb

DCG: Dirac–Coulomb–Gaunt

QED: Quantum electrodynamics

EQED: Effective quantum electrodynamics

FLOP: Floating point operation

RKB: Restricted kinetic balance

UKB: Unrestricted kinetic balance

ERI: Electron repulsion integral

MRCI: Multi-reference configuration interaction

JW: Jordan-Wigner

TS: Trotter-Suzuki

QPE: Quantum phase estimation

BQP: Bounded-error quantum polynomial (complexity class)

QMA: Quantum Merlin-Arthur (complexity class)

ACKNOWLEDGMENTS

Over the past five years at the University of Washington, (nine if I include my time as an undergraduate) I have had the privilege of working with some of the most amazing and intelligent people. I want to express my gratitude to everyone that I have worked with. This would not have been possible without your help, encouragement, and constructive criticism along the way. Additionally, my growth as a scientist wouldn't have been possible without my collaborators outside the university as well, and I thank them tremendously.

First, I would like to sincerely thank my advisor, Prof. Xiaosong Li for everything that he has done to support my growth as a scientist. Thank you for seeing my potential as an undergraduate, and taking me on as a graduate student. You gave me the encouragement and insight I needed to succeed, at a time where I was unsure about my future. From you I have learned perseverance is the key trait of being an excellent scientist, and I admire the way you don't give up easily. Additionally, I appreciate the freedom you gave me to explore my interests and side projects even if it differed from your own.

Next, Prof. Nathan Wiebe, thank you for investing your time to teach me both the details and the big picture of quantum information science. Our impromptu meetings to discuss science and life in general have been some of the most beneficial and intellectually stimulating pieces of my graduate education.

During my summer internship at Microsoft, and afterwards, I had the pleasure of working with Dr. Guang Hao Low. Guang Hao, thank you for teaching me even just a fraction about your knowledge of quantum algorithms. Your contribution to my education has been invaluable, and I have greatly enjoyed our conversations about quantum chemistry.

My graduate school experience would be nothing without the many grad students and

postdocs that I have worked alongside with in the Li research group. They have been an endless source of scientific insight, and humor alike. I would specifically like to thank David Williams–Young, Alessio Petrone, Patrick Lestrange, Josh Goings, and David Lingerfelt for helping me with all of my dumb questions when I was a new graduate student. Your guidance was invaluable to me. To Andrew Wildman and Ryan Beck, it would have been infinitely harder to complete this degree without your camaraderie over the past five years together. I think we pushed each other to become better scientists, and I will never forget the good times at happy hours. Additionally I would like to thank Joe Kasper, Shichao Sun, Hongbin Liu, Andrew Valentine, Chad Hoyer, Lauren Koulias, Hang Hu, and Tianyuan Zhang for being great coworkers and friends. The Li group would not have been the same without you, or the other members that I have forgot to mention here.

I would also like to thank my good friends Navdeep, Enzo, Nick, Kaleb, Dave, Jordan, Aaron, Jason, and many more that I am leaving out here, for all the laughs and helping me keep my sanity through this process. Additionally, to my late friend Daniel, thank you for always reminding me to be my authentic self. You will be missed.

To my parents Marla and Craig, thank you for always nurturing my love for science since I was just a kid. Your encouragement throughout my whole life was vital for me to becoming the person I am today, and I cannot truly express my gratitude in words.

Finally, thank you Emily. Without your love, support, and understanding even when times got hard, this wouldn't have been possible.

DEDICATION

To my parents and Emily

PREFACE

In our day and age, scientific research has become so specialized that the archetype of the "lone scientist" is exceptionally rare. Science is truly a team sport, and the work presented below is the result of a combined effort of myself and my collaborators. A description of my contributions to each chapter is presented below.

Chapter 1 presents a theoretical background to provide context to the methods utilized in my thesis, and only contains well established results and not original work.

In Chapter 2, I present work highlighting the capabilities of specific density functionals of relativistic time-dependent density functional theory to model L-edge X-ray absorption spectra. The iterative diagonalization method was implemented in Gaussian by Joe Kasper, but we both worked to collect the large amount of data required for this calibration study, and analyzed the results in the context of previously developed relativistic methods.

Chapter 3 presents a new method for efficiently computing the Dirac Hartree–Fock ground state is presented. I was in part responsible for the initial idea, and I developed the main software infrastructure for the method in the Chronus Quantum software package. Shichao Sun contributed with Coulomb and exchange matrix derivations, as well as some atomic calculations. Additionally, I contributed to the data collection of the heavy metal dimers, and atoms as well as computational timings. Prof. Xiaosong Li spearheaded the integral contraction algorithm, and was in part responsible for the atom and dimer data collection as well.

In the 4th and final chapter, a novel algorithm and analysis of the asymptotic scaling of an effective quantum electrodynamical Hamiltonian is presented for a quantum computer, with numerical results on a model relativistic jellium system. In this work I was responsible the numerical results of the expected commutator bounds for the model system, and the asymptotic cost analysis for quantum phase estimation. Additionally, I programmed the routine for computing the integrals for the numerical model system. Furthermore, I provided the theoretical analysis for the state preparation step. Anthony Ciavarella provided the lattice Hamiltonian results, and helped developed the diagonalization scheme for the unique Pauli gates requires for this quantum simulation. Prof. Nathan Wiebe provided expertise in deriving asymptotic bounds for the lattice based simulation and qubitization methods.

Chapter 1

THEORETICAL BACKGROUND AND CONCEPTUAL OVERVIEW

1.1 Electronic Structure Theory

Electronic structure theory is based on the idea that electrons surrounding the nucleus of each atomic element, behave according to the laws of quantum mechanics. Therefore, the behavior of electrons in molecules and condensed matter are governed by the Schrödinger equation

$$i\frac{\partial}{\partial t}|\Psi\rangle = \hat{H}|\Psi\rangle \tag{1.1}$$

where $|\Psi\rangle$ is the wavefunction of the physical system, and $\hat{H}$ is the Hamiltonian which is the total energy operator of the system. Unless otherwise noted, the equations presented throughout this thesis are in atomic units, meaning $\hbar = a_0 = e = m_e = 1$, where $\hbar$ is the reduced Planck's constant, a_0 is the Bohr radius, e is the elementary charge, and m_e is the electronic mass. One of the fundamental axioms of quantum mechanics states that the pure wavefunction, or state of the physical system is fully described by the state vector over a complex vector space. This vector space is known as a Hilbert space, $\mathcal{H}$, with infinite dimensionality, when there exists an inner product of vectors defined as $\langle\Psi|\Psi\rangle$, and the space is complete, where the wavefunction $|\Psi\rangle \in \mathcal{H}$. [1] The structure of the $\mathcal{H}$ is defined by the definition of the physical system's Hamiltonian $\hat{H}$. The Dirac bra-ket notation used here means that the bra vector, $\langle\Psi|$ is the complex conjugate transpose of a ket vector $|\Psi\rangle$. For simulating quantum mechanical systems, such as molecules, we can choose a basis, such as a real space lattice, or single particle atomic orbitals as a finite dimensional representation of the of Hamiltonian $\hat{H}$ and the wavefunction $|\Psi\rangle$. The finite basis wavefunction can be described as a complex vector

$$|\Psi\rangle = \begin{bmatrix} \alpha_1 \\ \alpha_2 \\ \vdots \\ \alpha_n \end{bmatrix}, \quad \alpha_i \in \mathbb{C} \tag{1.2}$$

where α_i is a complex number representing the probabilty amplitude of the ith basis vector. In a finite dimensional space, we can then use standard linear algebra methods to perform simulation.

Next, one can simplify the Schrödinger equation to be time-independent when describing standing waves, often called stationary states, of a quantum system. The form of the time-independent Schrödinger equation is

$$\hat{H}|\Psi\rangle = E|\Psi\rangle \tag{1.3}$$

where E is the energy of the wavefunction. This of course can be solved by an eigenvalue decomposition, since the Hamiltonian $\hat{H}$ is represented as a matrix operator of size $n \times n$ for a finite dimensional quantum state $|\Psi\rangle$ vector of size n. The eigenspectrum of $\hat{H}$ then gives all possible ground, and excited stationary states as eigenvectors, where the energies of each state are the corresponding eigenvalues.

In the context of modeling molecules and materials, we typically focus on the Coulomb Hamiltonian, $\hat{H}_C$ which can be thought of as the "standard model" of electronic structure. This Hamiltonian is defined as

$$\hat{H}_C = -\sum_A \frac{1}{2M_A}\nabla^2_{\mathbf{R}_A} - \sum_i \frac{1}{2}\nabla^2_{\mathbf{r}_i} - \sum_A \sum_i \frac{Z_A}{|\mathbf{R}_A - \mathbf{r}_i|} + \sum_i \sum_j \frac{1}{|\mathbf{r}_i - \mathbf{r}_j|} + \sum_A \sum_B \frac{Z_A Z_B}{|\mathbf{R}_A - \mathbf{R}_B|} \tag{1.4}$$

where indices A, B and i, j are over nuclei and electrons respectively, $\mathbf{R}_A$ is the nuclear position vector, $\mathbf{r}_i$ is the electronic position vector, M_A is the nuclear mass, Z_A is the nuclear charge, and ∇^2 is the Laplace operator. The physical meaning of the individual Hamiltonian terms are as follows; The first term is the kinetic energy of the nuclei, the second term is the kinetic energy of the electrons, the third term is the attractive potential energy of electrons and nuclei, the fourth term is the repulsive potential energy of electron-electron interactions, and the last term is the repulsive potential energy of the nuclear-nuclear interactions.

In the case of ground state electronic structure theory, one typically simplifies the problem by taking the Born-Oppenheimer approximation [2], where the nuclear and electronic wavefunctions are deemed separable, since nuclei are thousands of times heavier than an electron. As a consequence, we can take the clamped-nuclei approach, where the nuclei are static in time and frozen in real space. This means that the first term in Eq. 1.4 goes to zero, and the last term just becomes a scalar value. With these approximations we can then focus solely on the electronic structure that is parameterized by the clamped nuclear positions with the following electronic structure Hamiltonian

$$\hat{H}_E = -\sum_i \frac{1}{2}\nabla^2_{\mathbf{r}_i} - \sum_A \sum_i \frac{Z_A}{|\mathbf{R}_A - \mathbf{r}_i|} + \sum_i \sum_j \frac{1}{|\mathbf{r}_i - \mathbf{r}_j|} + \sum_A \sum_B \frac{Z_A Z_B}{|\mathbf{R}_A - \mathbf{R}_B|} \tag{1.5}$$

1.1.1 Hartree-Fock Theory and Basis Sets

While the choice of a finite basis for representing the electronic structure is arbitrary, one of the most natural and compact approaches for chemistry is the atomic orbital (AO) approach, where each atomic center has a set of Gaussian type orbitals, with the form $z^\ell e^{-\alpha z^2}$, representing one-electron hydrogenic wavefunctions, where α is a scalar coefficient, ℓ is the angular momentum quantum number, and z represents a cartesian direction. The choice of using Gaussian functions is convenient for two reasons. First, since the non-relativistic electronic Hamiltonian has a cusps of electronic density at the nuclei, the single electron orbitals are best described by Slater-type orbitals that decay as $e^{-\alpha z}$. These functions can be closely approximated by a linear combination of Gaussian functions whose coefficients, α, can be tuned to best approximate a Slater function. Second, when computing the integrals defined in the Hamiltonian, Gaussian orbitals are a convenient representation, since the integral overlap of two separate Gaussian functions is a Gaussian function itself. This greatly simplifies computing electronic structure integrals. The electronic structure integrals can be defined in the following form

$$h_{pq} = \int d\boldsymbol{r}\, \phi_p^*(\boldsymbol{r}) \left(\frac{1}{2}\nabla_{\boldsymbol{r}}^2 - \sum_A \frac{Z_A}{|\mathbf{R}_A - \boldsymbol{r}|} \right) \phi_q(\boldsymbol{r}) \tag{1.6}$$

$$h_{pqrs} = \int \int d\boldsymbol{r}\, d\boldsymbol{r}'\, \phi_p^*(\boldsymbol{r}) \phi_q^*(\boldsymbol{r}') \left(\frac{1}{|\boldsymbol{r} - \boldsymbol{r}'|} \right) \phi_r(\boldsymbol{r}) \phi_s(\boldsymbol{r}') \tag{1.7}$$

where ϕ represents the orbital basis function and the spin degrees of freedom are omitted.

With a given basis, we then want to construct an appropriate finite basis representation of the N-electron wavefunction. First, we need to ensure that the wavefunction is antisymmetric with respect to exchange of 2 electrons (labeled as x_i), where

$$|\Psi(x_1, x_2, ..., x_N)\rangle = -|\Psi(x_2, x_1, ..., x_N)\rangle \tag{1.8}$$

This is commonly known as the Pauli exclusion principle, where we find that two identical fermions cannot occupy the same quantum state. To enforce this physical constraint on our system, we can use a commonly known ansatz of an N-fermion wavefunction known as a slater determinant, which is defined as

$$|\Phi\rangle = \frac{1}{\sqrt{N!}} \begin{vmatrix} \phi_1(x_1) & \phi_2(x_1) & \cdots & \phi_N(x_1) \\ \phi_1(x_2) & \phi_2(x_2) & \cdots & \phi_N(x_2) \\ \vdots & \vdots & \ddots & \vdots \\ \phi_1(x_N) & \phi_2(x_N) & \cdots & \phi_N(x_N) \end{vmatrix} \tag{1.9}$$

where ϕ_i represents the single electron wavefunction, also known as an orbital.

In Hartree-Fock theory, we assume that the wavefunction of the system can be approximated as a single slater determinant, and the ground state energy is solved by minimizing the energy expectation value which is determined by $E_0 = \langle\Phi|\hat{H}_E|\Phi\rangle$ with the constraint that the orbitals must be orthogonal to one another. Therefore, the Hartree-Fock procedure aims to minimize the following Lagrangian

$$\mathcal{L} = \langle\Phi|\hat{H}_E|\Phi\rangle - \sum_{ij} \lambda_{ij} \left(\langle\phi_i|\phi_j\rangle - \delta_{ij} \right) \tag{1.10}$$

where λ_{ij} is the set of Lagrange multipliers, δ_{ij} is the Dirac delta function, and $\langle\phi_i|\phi_j\rangle$ is the overlap between two orbitals. Upon minimizing this Lagrangian, we end up with a set of one-particle eigenstates that satisfy

$$\hat{f}(x_1)\phi_i(x_1) = \lambda_i\phi_i(x_1) \tag{1.11}$$

where λ_i is then the one-particle eigenenergy, also called the orbital energy. $\hat{f}(x_i)$ is known as the Fock operator, which is the mean-field Hamiltonian which describes a single electron interacting with the fixed nuclei in the molecule, and also the "smeared" average potential of the other electrons. Specifically,

$$\hat{f}(x_1) = \hat{h}(x_1) + \hat{J}(x_1) - \hat{K}(x_1) \tag{1.12}$$

where $\hat{h}(x_1)$ is the core Hamiltonian, consisting of the electronic kinetic energy, and the nuclear-electron attraction potential

$$\hat{h}(x_1) = -\frac{1}{2}\nabla^2_{x_1} - \sum_A \frac{Z_A}{|\mathbf{R}_A - x_1|} \tag{1.13}$$

from the first two terms in Eq. 1.5. The Coulomb and exchange operators in Eq. 1.12, $\hat{J}(x_1)$ and $\hat{K}(x_1)$ respectively are defined as

$$\hat{J}(x_1)\phi_i(x_1) = \sum_j^N \left(\int dx_2\, \phi_j^*(x_2) r_{12}^{-1} \phi_j(x_2)\right) \phi_i(x_1) \tag{1.14}$$

$$\hat{K}(x_1)\phi_i(x_1) = \sum_j^N \left(\int dx_2\, \phi_j^*(x_2) r_{12}^{-1} \phi_i(x_2)\right) \phi_j(x_1) \tag{1.15}$$

where the r_{12}^{-1} is shorthand for the Coulomb kernel, the two electron repulsion interaction, and N is the total number of electrons.

Within a finite basis, such as the atomic orbital basis, we can cast the Hartree-Fock equations into matrix form using a linear combination of atomic orbitals (LCAO)

$$\phi_k(r) = \sum_\mu^M C_{\mu k}\chi_\mu \tag{1.16}$$

where χ_μ is the atomic orbital basis function, $C_{\mu k}$ is the coefficient (or contribution) of the μ^{th} atomic orbital to the k^{th} molecular orbital (MO). Therefore, a molecular orbital is in fact a vector of coefficients representing the weights of the LCAO. In short, the finite basis LCAO approach to Hartree-Fock theory can be casted into matrix form, and solved as a generalized eigenvalue problem

$$\mathbf{FC} = \mathbf{SC}\lambda \tag{1.17}$$

where **F** is the Fock matrix in the AO basis, **C** is the full MO coefficient matrix from Eq. 1.16, **S** is the atomic orbital overlap matrix, required because the atomic orbital basis set is not orthonormal in general, and finally λ represents the vector of eigenenergies for each molecular orbital. While solving Eq. 1.17 by itself is straightforward, theres an additional caveat: **F** depends on the molecular orbitals **C**, so that means this is actually a nonlinear problem, requiring a self-consistent solution, known as an SCF procedure. **F** and **C** are updated each step starting from an initial guess of the MO coefficients, until a variational minimum is reached. More details about finite basis Hartree-Fock theory can be found in Ref. [3].

1.1.2 Full Configuration Interaction

With the above Hartree-Fock approach, one can generate a set of orthogonal molecular orbitals based on the mean-field electronic wavefunction of the system. However, Hartree-Fock wavefunctions are defined as having no electronic correlation at all (except for electronic exchange), whereas the true wavefucntion will have all other correlations included. Intuitively, electronic correlation can be thought of as the interaction each electron has with the other electrons in the system, *dependent* on each of their relative spatial positions. This phenomenon then describes all of the interactions that are not included in the Hartree-Fock wavefunction, since the mean-field approximation assumes electronic interactions are *independent* of the position of the other particles in the system. For the most accurate calculations, one must solve for the fully correlated wavefunction that captures all the relevant physics.

In order to compute the full ground state wavefunction, we can construct the full configuration interaction (FCI) Hamiltonian in second quantization representation. [4] Specifically, second quantization allows us to describe the the FCI Hamiltonian in a basis of occupation number vectors of spin-orbitals. A spin-orbital, ϕ, can be defined as a product of the spatial orbital, and the single fermion spin function $\phi(\mathbf{r},\omega)=\chi(\mathbf{r})\sigma(\omega)$, where $\sigma(\omega)$ typically corresponds to the spin-up or spin-down state, $m_s=\pm\frac{1}{2}$, but can be a linear combination of the two in general with ω as the spin coordinate. For example, a system of 2 electrons and 4 spin-orbitals would have occupation number vectors of the form $|1100\rangle$, $|1010\rangle$, $|0011\rangle$, etc. More formally, this corresponds to a particle number conserving subspace of the full Fock space

$$\mathcal{F}_{\pm}(\mathcal{H}_0)=\bigoplus_{n=0}^{\infty} S_{\pm}\mathcal{H}_0^{\otimes n} \tag{1.18}$$

where $\mathcal{H}_0$ is a single particle Hilbert space, $\oplus$ is the direct sum of the vector spaces, and $S_{\pm}$ denotes the symmetry or anti-symmetry operator for bosonic and fermionic statistics respectively. The exponent $\otimes n$ represents the tensor product of Hilbert spaces $\mathcal{H}_0\otimes\mathcal{H}_0\cdots\otimes\mathcal{H}_0$, n times, where n is the number of particles in the finite basis. Physically, this general form of the Fock space includes an infinite number of basis states for an infinite range of the number of particles in the quantum system of interest. This general form is not useful in the interest of finite basis simulations, so we end up using only a small subspace of the full Fock space

$$\mathcal{F}_{n-}(\mathcal{H}_0)=S_{-}\mathcal{H}_0^{\otimes n} \tag{1.19}$$

For the energy regime of electronic structure, we also assume that the number of electrons is conserved, so the relevant subspace puts a constraint on Eq. 1.19 that $\sum_i^M n_i=N$ where M is the total number of modes in the space, N is the total number of electrons in the system, and $n_i\in\{0,1\}$ can only be one of two values due to the Pauli exclusion principle, in the general occupation number vector $|n_1,n_2,\cdots,n_M\rangle$ format. With this Fock basis for electrons, we can then define creation and annihilation operators, $a^\dagger$ and a, that raise and lower the number of particles in a single particle mode defined as

$$a_k^\dagger|0_1 0_2 \cdots 0_k \cdots 0_M\rangle = |0_1 0_2 \cdots 1_k \cdots 0_M\rangle \tag{1.20}$$

$$a_k|0_1 0_2 \cdots 1_k \cdots 0_M\rangle = |0_1 0_2 \cdots 0_k \cdots 0_M\rangle \tag{1.21}$$

$$a_k^\dagger|0_1 0_2 \cdots 1_k \cdots 0_M\rangle = 0 \tag{1.22}$$

$$a_k|0_1 0_2 \cdots 0_k \cdots 0_M\rangle = 0 \tag{1.23}$$

where the † superscript represents the complex conjugate. Additionally, the operators have the following anticommutation relations

$$\{a_k^\dagger, a_l^\dagger\} = a_k^\dagger a_l^\dagger + a_l^\dagger a_k^\dagger = 0 \tag{1.24}$$

$$\{a_k, a_l\} = a_k a_l + a_l a_k = 0 \tag{1.25}$$

$$\{a_k^\dagger, a_l\} = a_k^\dagger a_l + a_l a_k^\dagger = \delta_{kl} \tag{1.26}$$

where δ_{kl} is the Dirac delta function. More generally, in order to preserve fermion antisymmetry the creation an annihilation operators acting on Fock states can be defined as

$$a_p^\dagger|1_0 1_1 \cdots 0_p \cdots 0_M\rangle = \Gamma_p|1_0 1_1 \cdots 1_p \cdots 0_M\rangle \tag{1.27}$$

$$a_p|1_0 1_1 \cdots 1_p \cdots 0_M\rangle = \Gamma_p|1_0 1_1 \cdots 0_p \cdots 0_M\rangle \tag{1.28}$$

where $\Gamma_p = \prod_{k=1}^{p-1}(-1)^{n_k}$ and $n_k \in \{0, 1\}$ counts the occupied modes. Acting on a single particle state vector, the creation and annihilation operators can be defined as 2-dimensional matrices

$$a^\dagger = \begin{bmatrix} 0 & 0 \\ 1 & 0 \end{bmatrix} \tag{1.29}$$

$$a = \begin{bmatrix} 0 & 1 \\ 0 & 0 \end{bmatrix} \tag{1.30}$$

With these creation and annihilation operators, we can then represent the molecular electronic structure Hamiltonian in a compact form with only the one and two-body integral coefficients,

$$\hat{H} = \sum_{pq} h_{pq} a_p^\dagger a_q + \sum_{pqrs} h_{pqrs} a_p^\dagger a_q^\dagger a_r a_s \tag{1.31}$$

where h_{pq}, and h_{pqrs} are calculated from the integrals in Eq. 1.6 and Eq. 1.7. The indices p, q, r, s are a general index over spin-orbitals in the MO basis for the system. With this second quantized electronic Hamiltonian, and the occupation number vector basis, we then have a way to represent the FCI Hamiltonian, and subsequently the FCI wavefunction. As an example, for the 2 electron, 4 spin-orbital system, the FCI ground state wavefunction may be of the form

$$|\Psi_{\mathrm{FCI}}\rangle = c_0|1100\rangle + c_1|1010\rangle + c_2|1001\rangle + \cdots \tag{1.32}$$

where c_i is the complex probability amplitude for each configuration in the basis. If our occupation number vectors are based on molecular orbitals solved from the Hartree-Fock procedure, then the Hartree-Fock wavefunction amounts to only taking the single mean-field slater determinant by setting $c_0 = 1$ and all other coefficients $c_{i>0} = 0$

$$|\Psi_{\mathrm{HF}}\rangle = |1100\rangle \tag{1.33}$$

The basis states present in $|\Psi_{\mathrm{FCI}}\rangle$ contain the missing electronic correlation from the Hartree-Fock wavefunction as a superposition of different electronic configurations.

Ultimately, to understand the electronic structure of a system we want to be able to compute $|\Psi_{\mathrm{FCI}}\rangle$. Unfortunately, this is typically intractable for all but the smallest molecular systems. This is due to the fact the number of slater determinants, or occupation number basis vectors, in the FCI Hamiltonian scales exponentially as $O(2^M)$ where M is the number of basis states in the single particle basis. The notation, $O(\cdot)$, here is the standard "Big O" notation representing the set of functions that asymptotically upper bound the argument. In general, the field of quantum chemistry has focused on introducing truncations and approximations to the FCI Hamiltonian, such as coupled cluster, truncated CI, complete active space methods, multi-reference methods, Kohn-Sham density functional theory and much more. The ultimate goal is to retain important contributions of the electronic correlation terms in the wavefunction, that have computationally tractable (polynomial scaling in the number of modes, M) algorithms, and have high overlap with the true FCI wavefunctions.

1.2 Quantum Computation

Quantum computing is a rapidly growing new paradigm for computer hardware, first devised in the 1980's with Yuri Manin [5], and Richard Feynman at the forefront [6]. One of the most exciting prospects of quantum computation is the fact that certain algorithms that scale exponentially on classical computers, in fact scale only polynomially on a quantum computer. [7, 8, 9, 10]. For the specific task of simulating quantum systems, Lloyd [11] demonstrated the first explicit quantum algorithm for simulating k-local Hamiltonians (where the Hamiltonian can be represented as a sum smaller terms that only act on k qubits out of the total system) in 1996. Simulating the molecular electronic structure Hamiltonian only scales polynomially with the input size, which is in stark contrast to the exponential scaling we see when implementing a molecular FCI simulation on a classical computer. [12, 13] This prospect of successfully simulating Hamiltonians that would not be possible with even the best classical supercomputers, is obviously exciting for physicists and chemists alike who model systems at the quantum mechanical scale. The following section provides a simple overview of the digital quantum computational model, and a full exposition can be found in Ref. [14]

1.2.1 Quantum Gates and Registers

The standard digital model of quantum computation focuses on a mathematical representation of a system of coupled two-level quantum systems. Specifically two-level quantum systems are referred to as *qubits*. Qubits are the quantum analog of "bits" in classical computers where a single bit can be only in one of two states, 0 or 1.

A single qubit, $|q\rangle$, is described by a two-dimensional complex vector,

$$|q\rangle = \begin{bmatrix} \alpha \\ \beta \end{bmatrix} = \alpha|0\rangle + \beta|1\rangle \in \mathbb{C}^2 \tag{1.34}$$

where α and β are complex numbers that are normalized to one.

$$|\alpha|^2 + |\beta|^2 = 1 \tag{1.35}$$

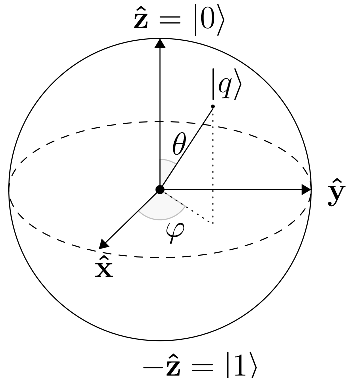

Figure 1.1: A Bloch sphere with a general state vector $|q\rangle$ defining the state of a single qubit.

Since a qubit is a two level quantum system, its possible states can be described geometrically by a Bloch sphere. This compact representation is equivalent to the states of a qubit due to the fact that the two complex numbers needed to describe the probability amplitudes of both the $|0\rangle$ and $|1\rangle$ states contain redundant information due to the normalization constraint in Eq. 1.35 and the fact that global phases can be ignored. Specifically, since a complex number can be defined by two real numbers, naively one could describe a qubit as a vector in a 4-dimensional real valued vector space. However because of the normalization constraint, $|a + ib|^2 + |c + id|^2 = 1$, where α and β are expanded into real numbers a, b, c, d, the qubit can be represented on the surface of a 3-sphere, reducing one degree of freedom since we are restricted to states on the sphere's surface. Next, if we see that the definition α and β on the 3-sphere is $\alpha = e^{i\psi}\cos(\theta/2)$ and $\beta = e^{i(\psi+\varphi)}\sin(\theta/2)$, we actually have another redundant degree of freedom, in the global phase $e^{i\psi}$. This is due to the fact that only the relative phase between α and β matter for physical observables. Therefore we can reduce the dimension again, and represent the qubit on a 2-sphere, which is known as the Bloch sphere where $\alpha = \cos(\theta/2)$ and $\beta = e^{i\varphi}\sin(\theta/2)$. A pictoral representation of the Bloch sphere is shown in Fig. 1.1, where $|q\rangle$ is a general state vector for a single qubit. By convention, the $|0\rangle$ and $|1\rangle$ states are defined in 1.37 corresponding to "up" and "down" states on the Bloch sphere respectively.

$$|0\rangle = \begin{bmatrix} 1 \\ 0 \end{bmatrix} \tag{1.36}$$

$$|1\rangle = \begin{bmatrix} 0 \\ 1 \end{bmatrix} \tag{1.37}$$

Adding more than one qubit results in the size of the complex Hilbert space representing the full quantum state increasing in dimension by 2^n where n is the number of qubits. Therefore, a quantum state with two qubits is represented by a 4-dimensional complex vector. For example, the two qubit state $|00\rangle$ is represented as the Kronecker product:

$$|00\rangle = |0\rangle \otimes |0\rangle = \begin{bmatrix} 1 \\ 0 \\ 0 \\ 0 \end{bmatrix} \tag{1.38}$$

In general, a quantum register which contains the current state of the quantum computer, is a quantum state vector that spans a Hilbert space which is a product of the Hilbert space of each of the n qubits $\mathcal{H} = \mathcal{H}_0 \otimes \mathcal{H}_1 \otimes \cdots \otimes \mathcal{H}_{n-1}$. Ultimately, the state of the register used in quantum computation is a complex vector of length 2^n. Therefore you only need n qubits to span 2^n basis states.

Within a given computational model, the obvious next requirement is a set of gates that can manipulate the data on a given register. Quantum gates are defined as unitary operations that manipulate a subset of qubits in the quantum register. Typically these are in the form of one and two-qubit operations that allow for local Bloch sphere rotations, and entanglement between qubits respectively. The Pauli matrices comprise of a subset of single qubit rotations possible.

$$\sigma_x = \begin{bmatrix} 0 & 1 \\ 1 & 0 \end{bmatrix}, \ \sigma_y = \begin{bmatrix} 0 & -i \\ i & 0 \end{bmatrix}, \ \sigma_z = \begin{bmatrix} 1 & 0 \\ 0 & -1 \end{bmatrix} \tag{1.39}$$

As a simple example, the Pauli X gate, σ_x, operating on the first qubit in a 2-qubit register acts as a single bit-flip operation, $|00\rangle \rightarrow |10\rangle$

$$(\sigma_x \otimes 1_2)\ |0\rangle \otimes |0\rangle = |1\rangle \otimes |0\rangle \tag{1.40}$$

where 1_2 is the 2-dimensional identity matrix. In order to introduce superpositions and entanglement capabilities, one then needs the single qubit Hadamard gate, and the two qubit controlled-σ_x gate (commonly known as the CNOT gate) respectively. The Hadamard gate is defined as

$$H = \frac{1}{\sqrt{2}} \begin{bmatrix} 1 & 1 \\ 1 & -1 \end{bmatrix} \tag{1.41}$$

where application onto a single qubit, rotates the state into a superposition with a phases depending on the starting state in the computational basis.

$$H|0\rangle = \frac{1}{\sqrt{2}}|0\rangle + \frac{1}{\sqrt{2}}|1\rangle \tag{1.42}$$

$$H|1\rangle = \frac{1}{\sqrt{2}}|0\rangle - \frac{1}{\sqrt{2}}|1\rangle \tag{1.43}$$

Next, we can entangle 2 qubits with the CNOT gate

$$CNOT = |0\rangle\langle 0| \otimes 1_2 + |1\rangle\langle 1| \otimes \sigma_x = \begin{bmatrix} 1 & 0 & 0 & 0 \\ 0 & 1 & 0 & 0 \\ 0 & 0 & 0 & 1 \\ 0 & 0 & 1 & 0 \end{bmatrix} \tag{1.44}$$

which only applies the σ_x operator to the second qubit if the first qubit is in the state $|1\rangle$. Finally, as a simple example of a quantum circuit, we can combine the Hadamard gate and the CNOT gate to produce the Bell state

$$|\Phi^+\rangle = \frac{1}{\sqrt{2}}|00\rangle + \frac{1}{\sqrt{2}}|11\rangle \tag{1.45}$$

for 2 qubits, starting from an initial state of $|00\rangle$ on the register. This final state can be achieved by first applying a Hadamard gate to the first qubit, then a CNOT gate, where the first qubit is the control, and the second qubit is the one that has σ_x conditionally applied to it. Specifically this quantum circuit amounts to the following.

$$|\Phi^+\rangle = \left(|0\rangle\langle 0| \otimes 1_2 + |1\rangle\langle 1| \otimes \sigma_x\right)\left(H \otimes 1_2\right)|00\rangle \tag{1.46}$$

Due to the lengthy process of writing down each operation for a quantum circuit, it is instead more easily represented graphically. For Eq. 1.46, we can graphically write the circuit

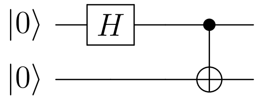

Figure 1.2: Quantum circuit diagram for creating the Bell state from Eq. 1.46 starting with the quantum register in the $|00\rangle$ state.

as shown in Fig. 1.2. The diagram is read from left to right, so the first operation on the initial $|00\rangle$ state is the Hadamard gate on the first (top) qubit. Next is the CNOT gate, where the black dot labels the control qubit, and the $\oplus$ symbol labels the target qubit that will be flipped by the NOT gate, σ_x, conditional upon the first qubit's state. The quantum algorithms in Chapter 4 will follow the conventions and notations presented here.

1.2.2 Quantum Simulation of Molecular Hamiltonians

Simulating Hamiltonians on quantum computers is a highly active research field that is rapidly developing, commonly referred to as "quantum simulation," or "Hamiltonian simulation." In this section, the basics of quantum simulation is presented using the Trotter-Suzuki decomposition [15, 16] and quantum phase estimation (QPE) [17]. However a multitude of different methods exist, for both noisy intermediate scale quantum computers, and fault-tolerant hardware that utilize quantum walks, hybrid quantum-classical optimization, higher-order Trotter-Suzuki formulas, and more. [18, 19, 20, 21, 22].

First, one needs to choose a method of mapping a choice of Hamiltonian to qubits. One of the most common methods is the Jordan-Wigner transformation [23], where in the context of molecular Hamiltonians, one spin-orbital is mapped to one qubit. Specifically, we can take the matrix representation of the creation and annihilation operators and decompose them into Pauli gates, denoted as X, Y, Z (which is just a shorthand notation of Eq. 1.39) which are common gates available on quantum hardware. The creation and annihilation operators acting on a single orbital can be defined as

$$a^\dagger = \begin{bmatrix} 0 & 0 \\ 1 & 0 \end{bmatrix} = \frac{X - iY}{2} \tag{1.47}$$

$$a = \begin{bmatrix} 0 & 1 \\ 0 & 0 \end{bmatrix} = \frac{X + iY}{2}. \tag{1.48}$$

In order to preserve the fermionic antisymmetry requirement, we must also keep track of the sign (parity) with respect to the location of which qubit is being operated on. Therefore, the general form of the Jordan-Wigner transformed creation and annihilation operators for an arbitrary number of modes in the quantum system are

$$a_p^\dagger = Z \otimes Z \otimes \cdots \otimes \left(\frac{X - iY}{2}\right)_p \otimes \mathbf{1}_2 \otimes \mathbf{1}_2 \otimes \cdots \otimes \mathbf{1}_2 \tag{1.49}$$

$$a_p = Z \otimes Z \otimes \cdots \otimes \left(\frac{X + iY}{2}\right)_p \otimes \mathbf{1}_2 \otimes \mathbf{1}_2 \otimes \cdots \otimes \mathbf{1}_2. \tag{1.50}$$

Strings of creation/annihilation operators then transform into a linear combination of local Pauli operators acting on k qubits, where k is the total length of creation/annihilation operators in the string (with additional Z operators in between the qubits of interest to preserve parity.) With this decomposition, we then can represent our second quantized Hamiltonian as linear combinations of local operators

$$\hat{H} = \sum_i^m H_i \tag{1.51}$$

where H_i is a local Hamiltonian that can be defined as an arbitrary Pauli string, with m as the total number of terms. $\hat{H}$ is described as k-local if k is the the total number of qubits operated on for each term H_i.

In order to perform quantum simulations on a quantum computer, we need to be able to build and apply the unitary time evolution operator of the Hamiltonian

$$U(t) = e^{-i\hat{H}t}. \tag{1.52}$$

Since we showed above that we can construct the Hamiltonian out of a linear combination of Pauli operators, we can substitute that into the time evolution operator, and get the resulting Trotter decomposition

$$e^{-i\hat{H}t} = e^{-i\sum_i H_i t} = \prod_i^m e^{-iH_i t} + O(m^2t^2) \tag{1.53}$$

using the exponentiation law where a sum in the argument is equivalent to the product of the exponentiation of each term. However, since this is a matrix exponentiation of the local Hamiltonian terms, they are not guaranteed to commute, so there is a finite error term, $O(m^2t^2)$.

Trotter-Suzuki formulas break the decomposition in Eq. 1.53 further, so that for large times t one can still accurately approximate the time evolution operator by slicing into r time steps.

$$e^{-i\sum_i H_i t} = \left(\prod_i^m e^{-iH_i t/r}\right)^r + O(m^2t^2/r) \tag{1.54}$$

Since we have control over the number of time steps r, and the fact that the error term now scales as the inverse of r, this makes controlling the size of the error in the approximation possible.

Using the Jordan-Wigner transform and the Trotter-Suzuki decomposition of the exact unitary time evolution operator, one can then use the quantum phase estimation procedure to compute the fully correlated, (or FCI) ground state energy of the molecular Hamiltonian with a polynomial number of computing resources. A simple overview of the quantum phase estimation procedure can be broken into a few main steps. First, start with a quantum register that contains $|\psi\rangle$ which is an eigenstate of some unitary operator U, and an ancilla register of zeros

$$|\text{reg}\rangle = |00\cdots 0\rangle \otimes |\psi\rangle \tag{1.55}$$

The goal is to extract the eigenvalue of $|\psi\rangle$ as a phase θ where $U|\psi\rangle = e^{2\pi i\theta}|\psi\rangle$. As an aside, one can see that for the case of extracting energy eigenvalues of a molecular Hamiltonian, then U is just our time evolution operator, and $|\psi\rangle$ is the exact ground state wavefunction. Obviously, in the case of molecular electronic structure we are only able to start with an approximation of $|\psi\rangle$, but if the approximate starting wavefunction has a large overlap with the exact wavefunction, then the exact ground state energy still has a high probability of being extracted from the QPE algorithm. For this overview of QPE we will keep the simplistic view that we are able to prepare $|\psi\rangle$ exactly.

The next step in the algorithm is to apply the Hadamard gate to every n qubits in the ancilla register to prepare a superposition of the computational basis states $|0\rangle$ and $|1\rangle$

$$|\text{reg}\rangle = \frac{1}{2^{n/2}} \left(|0\rangle + |1\rangle\right)^{\otimes n} \otimes |\psi\rangle \tag{1.56}$$

Next, the U operator is applied to the system register $|\psi\rangle$ if an ancilla qubit is in the $|1\rangle$ state, known as a controlled operation, similar to the CNOT gate described in the previous section. The controlled-U $(C - U)$ operator is applied 2^{n-1} times for each nth ancilla qubit producing the state

$$|\text{reg}\rangle = \frac{1}{2^{n/2}} \sum_{k=0}^{2^n-1} e^{2\pi i\theta k}|k\rangle \otimes |\psi\rangle \tag{1.57}$$

where k sums over all possible bit string basis vectors in the space of the ancilla register, so k is an integer corresponding to the binary number representation of each computational basis vector. Finally, an inverse quantum Fourier transform, commonly denoted as QFT^{-1} can be applied to the ancilla register to produce the final state

$$|\text{reg}\rangle = \frac{1}{2^n} \sum_{x=0}^{2^n-1} \sum_{k=0}^{2^n-1} e^{\frac{2\pi ik}{2^n}(x-2^n\theta)}|x\rangle \otimes |\psi\rangle \tag{1.58}$$

Simply, this means that at the end of the algorithm the original eigenstate is left untouched, and now the ancilla register contains a superposition of binary numbers whose probabilty amplitude sharply peaks the closer its value is to the desired phase θ. By measuring the ancilla register, we can extract θ in the computational basis, and use it to easily compute the eigenvalue of $|\psi\rangle$. A more extensive overview of QPE can be found in Ref. [14]

Overall, by using the described methods above, one can simulate a fully correlated molecular Hamiltonian with the goal of finding its ground state energy eigenvalue with just a polynomial number of operations, unlike the exponential scaling of a classical algorithm. In short, the second quantized Hamiltonian is decomposed into local Pauli matrix strings that are simple operations on quantum computers. Next, the unitary time evolution operator can decomposed into exponentials of individual local Pauli matrix strings with an error that can be explicitly controlled. Finally, with an approximate starting wavefunction that has a high overlap with the exact wavefunction, we can use quantum phase estimation with the time evolution operator of the Hamiltonian to extract the exact energy eigenvalues. While they are many methods to accomplish this task, the methods presented here are provided as a straightforward minimal introduction to Hamiltonian simulation on quantum computers.

1.3 Overview

While the proceeding chapters cover a variety of topics and methods in molecular electronic structure, there is a common thread tying these works together. That thread is *relativity.* Specifically, how special relativistic effects arise in quantum chemistry, especially for heavy elements, and how our models and algorithms can be improved to simulate chemistry with high accuracy. In chapter 2, the prediction of L-edge X-ray absorption spectroscopy is investigated using a variational relativistic 2-component Hamiltonian and time-dependent density functional theory. In this work, different basis sets and density functionals are compared and contrasted finding which methods perform best. It is found that the relativistic 2-component time-dependent density functional theory is quite effective for modeling the spin-orbit splitting of core and valence energy levels variationally, but certain spectroscopic features, such as "shake-up" states require a higher level of electronic correlation, such as doubly excited electronic configurations to properly model those X-ray absorption peaks in the spectrum.

While electronic correlation is important, the relativistic Hamiltonian can be improved further to include two-electron spin-orbit and spin-spin interactions, known as the 4-component Dirac-Coulomb-Gaunt Hamiltonian. This Hamiltonian captures the relativistic two-electron interactions which are typically not included in 2-component methods. These effects are not only important in X-ray spectroscopy but also energetics and bonding in heavy element compounds. Additionally, correlated methods all relay on first obtaining a set of mean field electronic orbitals, known as the self-consistent field (SCF) procedure. In chapter 3, the SCF algorithm used to compute the mean-field Hartree-Fock orbitals of the 4-component Dirac-Coulomb-Gaunt Hamiltonian is improved. While each step in the SCF algorithm computing the Hartree-Fock orbitals scales as $O(N^4)$, where N is the number of orbitals, there is a large pre-factor in the computational complexity for the number of contractions involved with the two electron integrals. By changing the basis of the Fock and one particle density matrices into a Pauli spin basis, one is able to reduce the number of operations at each step by a factor of ∼3. While this improvement may seem small, it is useful for several reasons. First, because 4-component SCF calculations can take many steps to reach a solution (usually much more than a standard non-relativistic calculation), and the large basis sets needed for 4-component calculations, the total wall-clock time for an SCF calculation is non negligible. Second, because the prefactor for each $O(N^4)$ step is much larger in 4-component SCF calculations than in a non-relativistic SCF, each step takes longer to compute.

Finally, in chapter 4 further improvements to the description of the relativistic molecular Hamiltonian are explored, with the inclusion of quantum electrodynamical (QED) effects that both standard 2 and 4-component methods ignore. QED effects are small compared to the relativistic effects explored in chapter 2 and 3, however in order to greatly improve quantitatively accurate predictions of molecular properties (especially those containing heavy elements) from first principles, both QED effects and electronic correlation are necessary. In this theoretical algorithmic study, the problem of simulating an effective QED Hamiltonian is examined through the lens of quantum computation. As mentioned above, the possibility of using quantum computers to simulate quantum systems like molecules is exciting because the fully correlated wavefunction can be simulated in polynomial time, wheres classical computers would require exponential time which is intractable for all but the smallest systems. In chapter 4, we show that including QED effects in the molecular Hamiltonian (where the electronic and positrionic fields are now allowed to interact) can still be efficiently simulated in polynomial time on a quantum computer. Additionally, we show that additional terms are necessary in the Jordan-Wigner transform, and preform a preliminary analysis on the computational cost of simulating a simple relativistic jellium model using a planewave basis set.

The overarching theme of this thesis is to improve both the accuracy and efficiency of molecular electronic structure prediction with both relativistic Hamiltonians, and the prospect of performing quantum simulations on quantum computers. The contribution here provides small, but important steps towards the major scientific goal of being able to computationally model molecules and materials from first principles, providing theoretical tools in aiding the design of new molecular and material technologies such as catalysts, photovoltaics, medicine, and more.

Chapter 2

MODELING $L_{2,3}$-EDGE X-RAY ABSORPTION SPECTROSCOPY WITH LINEAR RESPONSE EXACT TWO-COMPONENT RELATIVISTIC TIME-DEPENDENT DENSITY FUNCTIONAL THEORY

X-ray absorption spectroscopy (XAS) is a powerful tool that can provide physical insights into element-specific chemical processes and reactivities. Although relativistic time-dependent density functional theory (TDDFT) has been previously applied to model the L-edge region in XAS, there has not been a more comprehensive study of the choices of basis sets and density functional kernels available for variational relativistic excited state methods. In this chapter we introduce the implementation of the generalized preconditioned locally harmonic residual (GPLHR) algorithm to solve the complex-valued relativistic TDDFT for modeling the L-edge X-ray absorption spectra. We investigate the $L_{2,3}$-edge spectra of a series of molecular complexes using relativistic linear response TDDFT with a hybrid iterative diagonalization algorithm. A systematic error analysis was carried out with a focus on the energetics, intensities, and magnitude of L_2-L_3 splitting compared to experiments. Additionally, the results from relativistic TDDFT calculations are compared to those computed using other theoretical methods, and the multi-determinantal effects on the L-edge XAS were investigated. This work was adapted and reproduced from Stetina, T.F., *et al*, “Modeling $L_{2,3}$-edge X-ray Absorption Spectroscopy with Linear Response Exact Two-Component Relativistic Time-Dependent Density Functional Theory.” *J. Chem. Phys.*, **2019**, 150, 234103., with the permission of AIP Publishing.

2.1 Introduction

X-ray absorption spectroscopy (XAS) is an important tool that can give insight into local molecular geometry and electronic structure through the excitation of core electrons in molecular compounds. Advances in synchrotron technology with greatly improved temporal and spectroscopic resolution have made XAS a powerful tool for investigating the electronic and nuclear structure of molecules and condensed matter.[24, 25, 26, 27, 28, 29, 30, 31, 32, 33] X-ray absorption is element specific, meaning that the absorption spectrum for different elements are highly separated energetically. Because of this energetic separation, XAS has the unique ability to isolate selected elements for physical study. For example, XAS has been especially successful in the characterization and study of metal complexes, including but not limited to charge transfer pathways, [34] oxidation states, [35] observation of spin crossover events [36], and understanding solvation effects. [37, 38]

The near edge X-ray absorption fine structure (NEXAFS), also known as X-ray absorption near edge structure (XANES), contains excitations to bound electronic states close to the ionization potential. [39] In the extended X-ray absorption fine structure (EXAFS) region, continuum effects become more prominent due to ionization and Feshbach resonances. [40] The NEXAFS region is difficult to capture without an accurate description of the electronic structure of the absorbing atom and its neighbors. Previous theoretical methods have been well studied in the non-relativistic regime, but newer relativistic methods have not been characterized in great detail. [41, 42, 43, 44, 45] Relativistic effects are important to properly describe X-ray absorption because core electrons move at a significant percentage of the speed of light, causing core orbitals to contract and lower their energy. For K-edge XAS (excitations from the $1s$ core level), not accounting for relativity in *ab initio* calculations uniformly red-shifts the spectra compared to experiment.[46, 47, 48, 49, 50] However, the relative peaks in the spectrum remain similar, so the overall characterization of K-edge spectra is commonly treated by using a non-relativistic Hamiltonian and uniformly shifting the computed spectrum.

This is not the case for L-edge spectra, where the core orbitals that are being excited are in principal quantum number $n = 2$. Like K-edge XAS, L-edge XAS is also element specific, but L-edge spectra have finer line-widths due to longer core-hole lifetimes.[39] The finer line width allows for a higher sensitivity of element specific characterization, making L-edge XAS a unique probe of molecular properties. Transition probabilities for L-edge spectra are electric dipole-allowed, so issues with origin-dependence need not be considered in computations.[47, 51, 52, 53, 54] In L-edge XAS, the $2s$ and $2p$ orbitals are not only contracted by relativistic effects, but the $2p$ orbitals are split in energy by spin-orbit coupling into $2p_{1/2}$ and $2p_{3/2}$ sets, denoted as the L_2 and L_3 edge in XAS respectively.

Theoretically, spin-orbit coupling terms fall out of the relativistic Dirac equation. As a result, relativistic Hamiltonians are a natural choice for the *ab initio* treatment of L-edge spectroscopy. We do note that it is possible to include spin-orbit coupling perturbatively in a non-relativistic or scalar relativistic Hamiltonian, and methods of this type have been implemented and shown to provide a qualitative description for light elements, such as ZORA [55, 56, 57], MCSCF [58], RASPT2 [59], TDDFT [60], and ROCIS. [61, 62] However, perturbative treatment of relativistic effects will break down for heavier elements.

Previously, variational treatments of spin-orbit coupling in the electronic Hamiltonian within the real-time time-dependent electronic structure framework have been used to model X-ray absorption spectra. [63, 64] These approaches, without explicitly solving for the eigenvectors of excited states, have successfully produced XAS spectra in excellent agreement with experiments. Other alternatives to explicit eigensolvers have also been explored, including frequency dependent-response [65, 66, 67, 68, 42, 69, 70, 71] and model order reduction [72, 73]. When eigenvectors of electronic adiabats are needed for interpretation of chemical properties of XAS, the linear response formalism of the time-dependent Hartree-Fock (LR-TDHF) and time-dependent density functional theory (LR-TDDFT) with the restricted [74, 75, 76, 48, 77] or growing excitation window [78, 77, 49] techniques have been particularly successful for predicting K-edge XAS. However, for systems that exhibit a high degeneracy of excited states in the spectral region of interest, *e.g.*, L-edge XAS of a metal complex, solving the relativistic LR-TDDFT equations is often subject to nontrivial convergence problems. To obtain the interior eigenspace of challenging spectroscopic systems, we have recently developed a hybrid method using the generalized preconditioned locally harmonic residual (GPLHR) [79] algorithm for solving real-valued TDDFT equation. [80]

In this work, we introduce the implementation of the GPLHR algorithm to solve the complex-valued relativistic two-component TDDFT. The aim of this work is to investigate and calibrate the ability of linear response formalism of exact two-component transformed (X2C) time-dependent Hartree-Fock (X2C-TDHF) and time-dependent density functional theory (X2C-TDDFT) [81, 82] for modeling the L-edge X-ray absorption spectra with a focus on first and second row transition metal complexes.

2.2 Theory

2.2.1 Exact Two-component Transformation

Relativistic two-component methods begin with the four-component (4c) relativistic Dirac Hamiltonian for the electron: [83, 84, 85]

$$\hat{H}^{4c} = \begin{bmatrix} V \otimes \mathbf{I} & c\boldsymbol{\sigma} \cdot \mathbf{p} \\ c\boldsymbol{\sigma} \cdot \mathbf{p} & (V - 2mc^2) \otimes \mathbf{I} \end{bmatrix} \tag{2.1}$$

V is the scalar potential, $\boldsymbol{\sigma}$ is the vector of Pauli matrices, $\mathbf{p}$ is the linear momentum operator, and $\mathbf{I}$ is the rank-two identity matrix. The speed of light and mass of the system are given by c and m. The eigenstates of this Hamiltonian can be partitioned into large (L) and small (S) components

$$\Psi^{4c} = \begin{bmatrix} \Psi_L \\ \Psi_S \end{bmatrix} \tag{2.2}$$

that can be subsequently partitioned into spin-up and spin-down components. Since there are both positive and negative energy solutions to the Dirac equation, a variety of algorithms have been devised that isolate the electronic (positive energy) solutions via a unitary transformation:

$$\boldsymbol{\mathcal{U}}^{\dagger}\hat{H}^{4c}\boldsymbol{\mathcal{U}} = \begin{bmatrix} \hat{H}^{+} & \mathbf{0}_2 \\ \mathbf{0}_2 & \hat{H}^{-} \end{bmatrix} ; \boldsymbol{\mathcal{U}} \begin{bmatrix} \Psi_L \\ \Psi_S \end{bmatrix} = \begin{bmatrix} \Psi^{2c} \\ \mathbf{0} \end{bmatrix} \tag{2.3}$$

The Hamiltonians $\hat{H}^{+}$ and $\hat{H}^{-}$ have two-component (2c) eigenstates Ψ^{2c} and describe positive and negative energy states respectively. Although there are many different techniques to form the transformation matrix $\boldsymbol{\mathcal{U}}$, in this work we use the exact two-component (X2C) method [86, 87, 88, 89, 90, 91, 92, 93, 94, 81, 95, 96, 82, 97, 98]. In our implementation we restrict the 4c→2c transformation to the one-electron operator. Because of this approximation, an additional scaling factor for the spin-orbit coupling terms is included to account for the two electron terms in an approximate manner. [99] For the following section we assume that the 4c→2c transformation has been carried out so that all matrix quantities are in the transformed two-component framework, as represented by the tilde.

2.2.2 Linear Response TDDFT

The absorption spectrum for molecules can be obtained using TDDFT [100, 101]. One of the most common approaches is to solve the TDDFT equations using the linear response formalism [102, 103, 104]. This amounts to solving an eigenvalue problem of the form

$$\begin{bmatrix} \tilde{\boldsymbol{A}} & \tilde{\boldsymbol{B}} \\ -\tilde{\boldsymbol{B}}^{*} & -\tilde{\boldsymbol{A}}^{*} \end{bmatrix} \begin{bmatrix} \tilde{X} \\ \tilde{Y} \end{bmatrix} = \omega \begin{bmatrix} \tilde{X} \\ \tilde{Y} \end{bmatrix} \tag{2.4}$$

where ω is the resonant energy, and $\tilde{X}$ and $\tilde{Y}$ are the transition amplitudes. The matrices $\tilde{\boldsymbol{A}}$ and $\tilde{\boldsymbol{B}}$ are given by

$$\tilde{A}_{ai,bj} = \delta_{ab}\delta_{ij}(\epsilon_a - \epsilon_i) + \tilde{K}_{ai,bj} \tag{2.5}$$

and

$$\tilde{B}_{ai,jb} = \tilde{K}_{ai,jb} \tag{2.6}$$

where a, b denote virtual MOs and i, j occupied MOs. The coupling matrix $\tilde{\boldsymbol{K}}$ is given in the AO basis as

$$\tilde{K}_{\mu\nu,\kappa\lambda} = (\mu\nu|\kappa\lambda) + \frac{\partial^2 E_{xc}}{\partial P_{\mu\nu}\partial P_{\kappa\lambda}} \tag{2.7}$$

The functional second derivatives in Eq. 2.7 depend on the particular exchange and correlation functionals. In this work, we use a direct atomic-orbital based X2C transformation with the torque-free spin- density approach as described in Refs. [81, 82, 97]. We note that the extension of standard collinear functionals to 2-component non-collinear DFT is non-trivial, and refer readers to Refs. [105, 97] for a recent review on non-collinear DFT methods. The solution of Eq. 2.4 can be performed in the X2C-transformed frame, since the transition energies E and vectors $|X\,Y\rangle$ for do not depend on the transformation matrix $\boldsymbol{\mathcal{U}}$. [81] However, the evaluation of properties must be done in the nontransformed basis, as is required to avoid the so-called "picture change" error. [81, 106]

In general the size of the matrix in Eq. 2.4 is too large to store in memory and so a variety of iterative methods have been used. Although there is extensive discussion in the literature on iterative eigensolvers, two specific aspects of this problem warrant further elaboration. First, for high energy excitations such as those in X-ray spectroscopy, some type of energy windowing is desirable in the iterative diagonalization of Eq. 2.4. Obtaining only a subset of the spectrum greatly reduces the computational cost by removing the need to converge all lower-energy roots. Energy-specific Davidson [78, 50] and restricted excitation window [76, 75, 107, 77] methods have proved to be fairly successful in this regard. However, recently some alternative methods such as GPLHR [108, 79, 80] and IVI [109, 98] have shown great promise in tackling challenging interior eigenproblems in TDDFT.

Second, though no less important, is the need to use complex arithmetic. Typically implementations of TDDFT in real arithmetic make use of the fact that $\boldsymbol{A}$ and $\boldsymbol{B}$ are Hermitian to simplify Eq. 2.4 to an equivalent problem of half the original dimension: [101]

$$(\boldsymbol{A}-\boldsymbol{B})(\boldsymbol{A}+\boldsymbol{B})|\boldsymbol{X}+\boldsymbol{Y}\rangle = \omega^2|\boldsymbol{X}+\boldsymbol{Y}\rangle \tag{2.8}$$

However, in the general complex case $\boldsymbol{A} \neq \boldsymbol{A}^*$ and $\boldsymbol{B} \neq \boldsymbol{B}^*$ and Eq. 2.4 cannot be reduced to the form of Eq. 2.8. Despite this, the problem still possesses a block structure that can be taken advantage of to improve convergence. Most notably, while general non-Hermitian eigenproblems can have complex eigenvalues, solutions to Eq. 2.4 still have real eigenvalues.

To eliminate intermediate complex eigenvalues one can enforce the block structure of Eq. 2.4 on the subspace problem at each iteration. This is accomplished by incorporating matching trial vectors into the space. While in the real case for every positive energy solution $(\omega, |X\,Y\rangle)$ there is a negative energy solution $(-\omega, |Y\,X\rangle)$, for the complex non-Hermitian problem for each $(\omega, |X\,Y\rangle)$ there is a corresponding "paired" solution $(-\omega^*, |Y^*\,X^*\rangle)$. With both trial vectors included, we retain the same structure as Eq. 2.4 for the subspace problem at each iteration.

2.2.3 Generalized Preconditioned Locally Harmonic Residual (GPLHR)

The full technical report and derivations of the GPLHR algorithm is already published [79], so here we only provide an overview of the algorithm. The TDDFT equation in Eq. 2.4 is a generalized eigenvalue problem of the form

$$\boldsymbol{\mathcal{H}}\boldsymbol{\mathcal{V}} = \Omega\boldsymbol{\mathcal{M}}\boldsymbol{\mathcal{V}} \tag{2.9}$$

The GPLHR algorithm attempts to find the n interior eigenvectors with eigenvalues Ω closest to a specified value σ through a harmonic Rayleigh-Ritz procedure. This procedure is general for a complex non-Hermitian eigenvalue problem, which can in principle have complex eigenvalues, but in the case of LR-TDDFT, $\boldsymbol{\mathcal{H}}$ represents the matrix in Eq. 2.4. For physically meaningful solutions, $\boldsymbol{\mathcal{H}}$ will have all eigenvalues real; complex eigenvalues indicate an instability in the reference. However, intermediate complex eigenvalues can arise during the iterative diagonalization, and care must be taken to ensure these are handled properly.

From an orthonormalized initial guess of n (right) vectors $\boldsymbol{\mathcal{V}}$, the set of vectors $\boldsymbol{\mathcal{Q}}$ is formed in the σ-shifted space

$$\boldsymbol{\mathcal{Q}} = (\boldsymbol{\mathcal{H}} - \sigma\boldsymbol{\mathcal{M}})\boldsymbol{\mathcal{V}} \tag{2.10}$$

After orthonormalization of $\boldsymbol{\mathcal{Q}}$, the initial approximations for the eigenvalues $\tilde{\omega}_i$ are found by solving the generalized eigenproblem in the reduced space given by

$$(\boldsymbol{\mathcal{Q}}^\dagger\boldsymbol{\mathcal{H}}\boldsymbol{\mathcal{V}}, \boldsymbol{\mathcal{Q}}^\dagger\boldsymbol{\mathcal{M}}\boldsymbol{\mathcal{V}}) \tag{2.11}$$

This can be solved by generalized Schur decomposition (also known as QZ factorization), and is preferable over diagonalization when the matrices might become low-rank. From the Schur decomposition of Eq. 2.11 we obtain the triangular factors $\boldsymbol{\mathcal{R}}_1$, $\boldsymbol{\mathcal{R}}_2$, as well as Schur bases $\boldsymbol{\mathcal{Y}}_L$, $\boldsymbol{\mathcal{Y}}_R$ such that

$$\boldsymbol{\mathcal{Q}}^\dagger \boldsymbol{\mathcal{H}} \boldsymbol{\mathcal{V}} = \boldsymbol{\mathcal{Y}}_L \boldsymbol{\mathcal{R}}_1 \boldsymbol{\mathcal{Y}}_R \tag{2.12}$$

$$\boldsymbol{\mathcal{Q}}^\dagger \boldsymbol{\mathcal{M}} \boldsymbol{\mathcal{V}} = \boldsymbol{\mathcal{Y}}_L \boldsymbol{\mathcal{R}}_2 \boldsymbol{\mathcal{Y}}_R \tag{2.13}$$

The eigenvalues are given by the ratio of the diagonal elements of the triangular factors:

$$\omega_j = \boldsymbol{\mathcal{R}}_1(j,j)/\boldsymbol{\mathcal{R}}_2(j,j) \tag{2.14}$$

The Schur vectors $\boldsymbol{\mathcal{Y}}_L$ and $\boldsymbol{\mathcal{Y}}_R$ can be used to update $\boldsymbol{\mathcal{V}}$ and $\boldsymbol{\mathcal{Q}}$, with $\boldsymbol{\mathcal{V}} \rightarrow \boldsymbol{\mathcal{V}}\boldsymbol{\mathcal{Y}}_R$ and $\boldsymbol{\mathcal{Q}} \rightarrow \boldsymbol{\mathcal{Q}}\boldsymbol{\mathcal{Y}}_L$.

Next, a subspace is generated. This trial subspace $\boldsymbol{\mathcal{Z}} = [\boldsymbol{\mathcal{V}}, \boldsymbol{\mathcal{W}}, \boldsymbol{\mathcal{S}}_1, ..., \boldsymbol{\mathcal{S}}_m, \boldsymbol{\mathcal{P}}]$ corresponds to the Krylov-Arnoldi sequence generated by the preconditioned residuals. Note that unlike the Davidson method which increases the subspace size at each iteration, the subspace is of fixed size determined by the integer parameter m. $\boldsymbol{\mathcal{P}}$ is an additional block of saved vectors and is not used on the first iteration. As is done in the Davidson algorithm, we approximate the preconditioner $\mathcal{T}$ as the inverse of the difference between the approximate eigenvalue $\tilde{\omega}$ and the diagonal elements of $\boldsymbol{\mathcal{H}}$, which are given by the orbital energy differences. Additionally, GPLHR projects out components against $\boldsymbol{\mathcal{V}}$ and $\boldsymbol{\mathcal{Q}}$. For the trial space $\boldsymbol{\mathcal{Z}}$ the analogous set of vectors in the σ-shifted test space is formed:

$$\boldsymbol{\mathcal{U}} = (\boldsymbol{\mathcal{H}} - \sigma \boldsymbol{\mathcal{M}}) \boldsymbol{\mathcal{Z}} \tag{2.15}$$

The new reduced-dimensional eigenvalue problem ($\boldsymbol{\mathcal{U}}^\dagger \boldsymbol{\mathcal{H}} \boldsymbol{\mathcal{Z}}$,$\boldsymbol{\mathcal{U}}^\dagger \boldsymbol{\mathcal{M}} \boldsymbol{\mathcal{Z}}$) is solved by Schur decomposition as before. Since the dimension of the eigenproblem in Eq. 2.15 is now larger than the number of roots we seek, the eigenvalue-eigenvector pairs are ordered by closeness to the shift value σ, and can then be used to update $\boldsymbol{\mathcal{V}}$, $\boldsymbol{\mathcal{Q}}$, and $\boldsymbol{\mathcal{P}}$. The convergence of eigenvectors and eigenvalues is evaluated to determine if additional iterations are necessary.

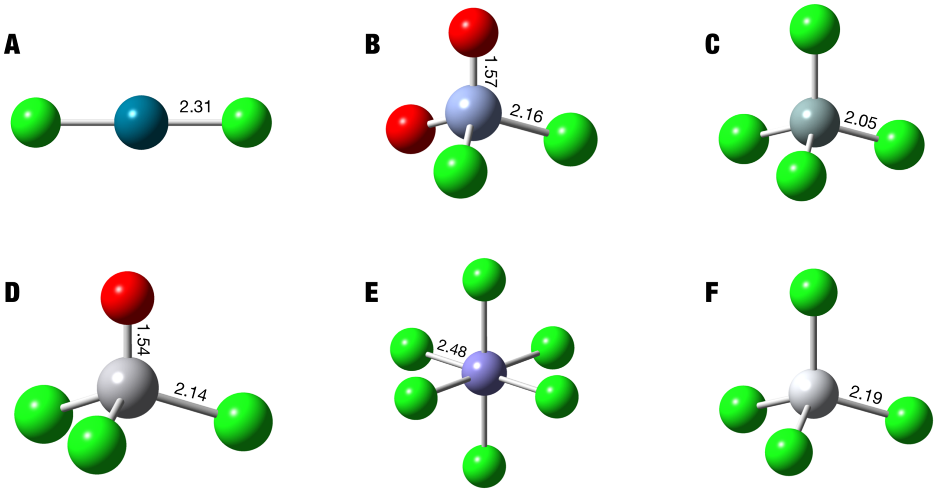

Figure 2.1: Optimized structures of the molecules used in this study: (A) $PdCl_2$, (B) CrO_2Cl_2, (C) $SiCl_4$, (D) $VOCl_3$, (E) $[FeCl_6]^{3-}$, (F) $TiCl_4$. All bond lengths are reported in Angstroms. Full coordinates are given in the Supplementary Information.

2.3 *Benchmark and Discussion*

To better understand how well the DFT-based approach should be expected to perform generally, a variety of different density functional and basis set combinations are used to compute $L_{2,3}$ XAS for a set of transition metal complexes. This set includes metal centers in several rows of the periodic table to test the robustness of the method to capture different symmetry environments as well as varying strengths of bonding and relativistic effects. The basis sets used were the non-relativistic Pople-type 6-311G(d) [110, 111], the relativistically-optimized double-ζ and triple-ζ Sapporo sets [112], and the relativistically-optimized aug-cc-pVTZ-dk. [113, 114, 115, 116] The DFT functionals included B3LYP [117, 118], PBE0 [119, 120], as well as HSE06 [121], CAM-B3LYP [122], and M062X [123]. Results from Hartree-Fock (HF) are also given for comparison. All calculations were run using a locally modified version of the development version of the Gaussian suite of programs. [124] For each complex the geometry was optimized using the LANL2DZ [125, 126, 127] effective core potential and basis set with each density functional. The optimized geometries for the test set of complexes are shown in Fig. 2.1. Convergence of the linear response X2C-TDDFT problem was done using a combination of the energy-specific Davidson method [78, 50] and GPLHR [79, 80] as a hybrid method. It is also important to note that one of the key challenges in solving the linear response X2C-TDDFT problem for L-edge spectra is that there are a large number of roots required to obtain the spectrum. The degeneracies in magnetic microstates (2J+1) lead to a large number excited states, even if they do not contribute oscillator strength to the overall spectrum.

2.3.1 Convergence Behavior of Complex GPHLR for Computing L-edge Eigenstates

The use of GPLHR has been shown to provide improved convergence in TDDFT problems, particularly where there is a dense manifold of states associated with high degeneracy. [80]. For complex two-component TDDFT problems, the proper handling of complex intermediates is essential. We remark large scale systems can introduce a high level of degeneracy of excited states which are spatially distinct in nature. For systems with non-zero total angular momentum, $J > 0$, an additional level of degeneracy arises from magnetic microstates. In this section, we only focus on the convergence behavior of complex GPLHR interior eigensolver for obtaining excited states in the L-edge spectral region using complex X2C-TDDFT. We refer interested readers to Ref. [80] for additional discussion of the computational performance of this type of eigensolver.

In Fig. 2.2 we show the convergence profile and computational cost for computing excited states in the L-edge of $SiCl_4$ using the aug-ccpVTZ-dk basis and the CAM-B3LYP functional. The transitions obtained here are for the first 5 states above 103 eV and correspond belong to the L_3-edge. Since the matrix-vector product (m-vec) is the time consuming step, the total number of m-vecs is used to measure the computational cost. As seen in the convergence profile, the energy-specific Davidson is less smooth and not monotonic. In the energy-specific Davidson algorithm, a fixed number of trial eigenvectors are selected for a given energy window. In cases where there is a high level of degeneracy, there can be a fluctuating

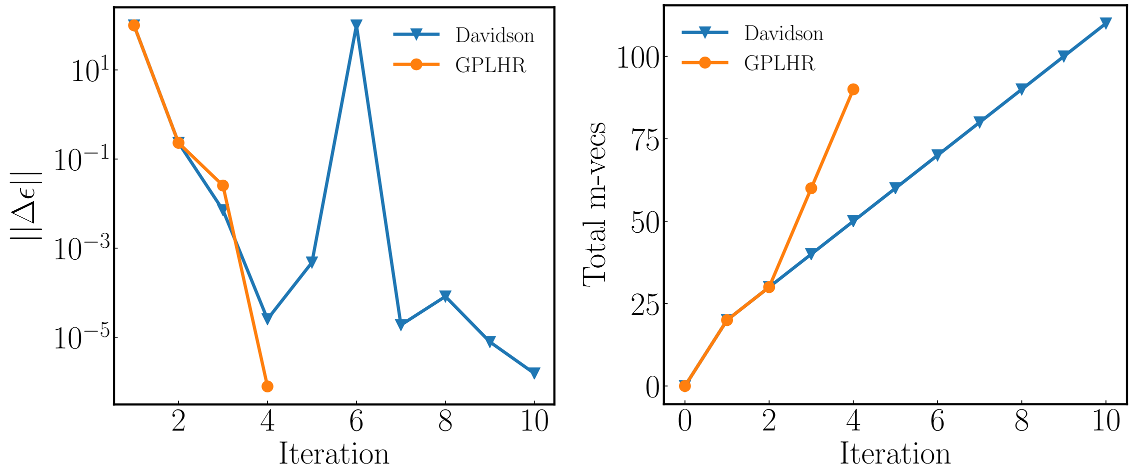

Figure 2.2: The convergence profile and number of matrix vector products to obtain the lowest 5 excited states above 103 eV in the $SiCl_4$ system using both Davidson and the GPLHR hybrid. The excited state shown has an eigenvalue of 103.008 eV.

selection of trial eigenvectors, resulting in an ill-conditioned convergence profile. While this hinders the Davidson algorithm, the problem appears less severe than high levels of spatial degeneracy, presumably because similar sets of orbitals are needed to describe the degeneracies due to different spin states. By contrast, in GPLHR hybrid method there is no hard threshold used to include or exclude certain eigenvalue-eigenvector pairs. As a result, the GPLHR hybrid exhibits a faster and smooth convergence.

2.3.2 Error Analysis and Comparison

For each molecular complex several peaks were identified for comparison to experimental spectra [128, 57, 129, 130, 131], resulting in a total of 40 transitions used in the analysis. However, since the number of states required to cover the X-ray spectrum is quite high and each experimental peak may be composed of multiple roots, instead of analyzing individual eigenvalue-eigenvector solutions, we obtain a Gaussian-broadened spectrum and identify peaks and shoulders using a spline fit and solving for the minima of the second derivative.

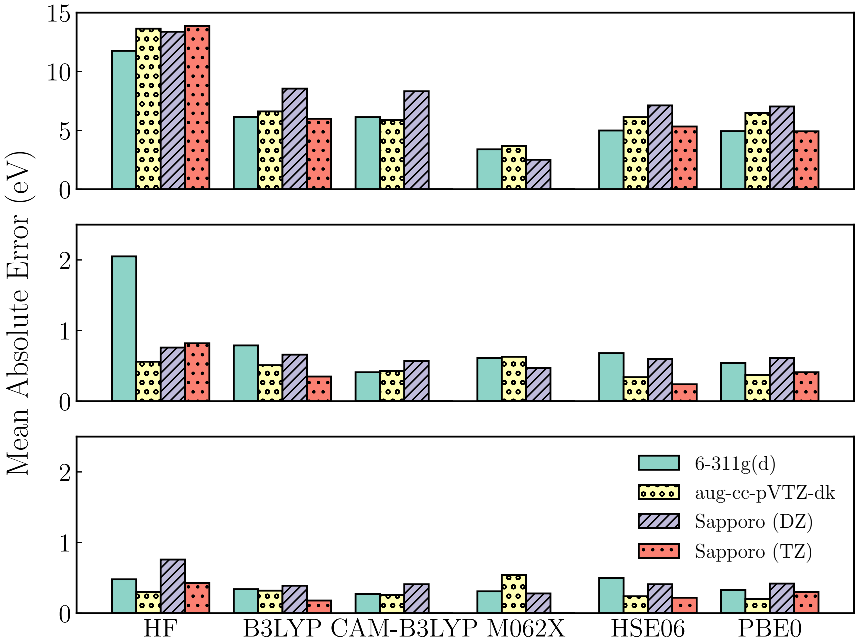

Figure 2.3: The mean absolute errors for basis set and functional combinations across the molecular test set with data from Tab. 2.1. The top panel shows the raw energy values, the middle panel is the uniform shifted energies, and the bottom panel is the uniform shifted energies with the spin-orbit correction.

The broadening parameters were chosen to match qualitatively with the experimental spectra and are given in the Supplementary Information. Note that we were unable to obtain the full spectra for certain combinations of DFT functionals and basis sets due to strong numerical instabilities in the noncollinear formalism. The errors in energy are computed using several methods: unshifted, a single uniform shift for both L_2 and L_3, and using an additional shift for L_2 relative to the shifted L_3. A single uniform shift is used to correct for self-interaction errors in DFT, [132] and the additional L_2-edge shift corrects for the approximate two-electron spin-orbit coupling. [64] Fig. 2.4 plots the shifted spectra of $[FeCl_6]^{3-}$ compared to experimental measurement. [128]

The mean absolute error (MAE) and range of the excitation energies are given in Tab. 2.1. The MAE is also shown in Fig. 2.3 graphically. Since the scale of excitations changes

	Unshifted		Uniform Shift		Uniform and Spin-Orbit Correction	
	MAE	Range	MAE	Range	MAE	Range
HF						
6-311G(d)	11.76	5.75	2.05	5.75	0.48	2.11
aug-cc-pVTZ-dk	13.64	1.40	0.56	1.40	0.30	1.40
Sapporo(TZ)	13.88	1.97	0.82	1.97	0.43	1.40
Sapporo(DZ)	13.38	2.79	0.76	2.79	0.76	2.79
B3LYP						
6-311G(d)	6.14	12.32	0.79	4.58	0.34	1.67
aug-cc-pVTZ-dk	6.61	9.99	0.51	1.55	0.32	1.55
Sapporo(TZ)	5.99	10.02	0.35	1.66	0.18	1.53
Sapporo(DZ)	8.55	5.53	0.66	1.35	0.39	1.35
CAM-B3LYP						
6-311G(d)	6.12	7.95	0.41	1.59	0.27	1.26
aug-cc-pVTZ-dk	5.88	8.43	0.43	1.43	0.26	1.07
Sapporo(TZ)	–	–	–	–	–	–
Sapporo(DZ)	8.32	5.78	0.57	1.39	0.41	1.85
M062X						
6-311G(d)	3.39	9.97	0.61	2.39	0.31	1.52
aug-cc-pVTZ-dk	3.69	9.96	0.63	2.41	0.54	2.42
Sapporo(TZ)	–	–	–	–	–	–
Sapporo(DZ)	2.51	5.87	0.47	1.91	0.28	1.40
HSE06						
6-311G(d)	4.99	10.97	0.68	4.34	0.50	2.85
aug-cc-pVTZ-dk	6.12	9.70	0.34	1.56	0.24	1.11
Sapporo(TZ)	5.33	9.74	0.24	1.53	0.22	1.10
Sapporo(DZ)	7.12	6.08	0.60	1.85	0.41	2.26
PBE0						
6-311G(d)	4.93	10.30	0.54	2.69	0.33	1.65
aug-cc-pVTZ-dk	6.48	9.93	0.37	1.58	0.20	0.97
Sapporo(TZ)	4.92	9.80	0.41	1.69	0.30	1.25
Sapporo(DZ)	7.03	5.72	0.61	1.37	0.42	1.67

Table 2.1: Mean absolute errors (MAE) and the range of errors in eV for several different functional and basis set combinations. Errors for the L_3 and L_2 edges shifted with and without the additional spin-orbit-corrected shift are reported. Values for the shifts can be found in Supplementary Information.

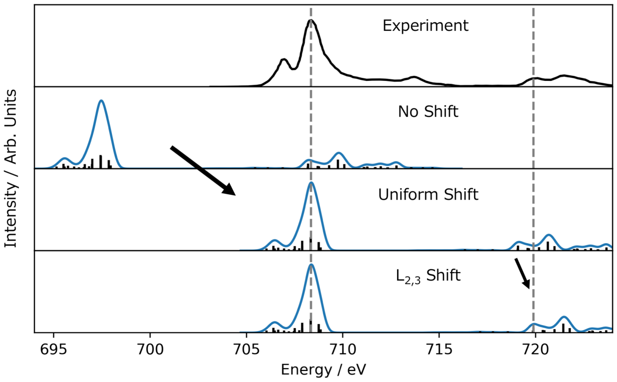

Figure 2.4: Example of different types of energetic shifts for the L-edge X-ray spectra of $[FeCl_6]^{3-}$. The experimental spectra is shown on the top figure from Ref. [128]. The two dashed gray lines mark two reference peaks for the experimental L_2 and L_3 edges, that we want to match with theory. The "No Shift" spectra is the raw calculated spectrum. The "Uniform Shift" applies the same energetic shift to all absorption roots (+10.9 eV), and the "$L_{2,3}$ Shift" moves the L_2 edge in addition to the uniform shift independently to match the experimental reference (+0.8 eV). The calculated spectra above uses the B3LYP functional and the Sapporo(TZ) basis set.

considerably, the data from $PdCl_2$ are not included in Tab. 2.1. When only unshifted errors are considered, self-interaction errors dominate the MAE analysis among the DFT results. There is little difference in MAE between the use of the non-relativistic and the relativistically-optimized basis sets, nor is there a significant difference between different functionals. The large error for HF results is likely due to the lack of electron correlation.

After applying a uniform shift to align the L_3 edge with the experimental value, it is clear that basis sets optimized for relativistic calculations provide a better description of the spectrum. Unsurprisingly using the triple-ζ Sapporo set performs better than the double-ζ. Most noticeably, the HSE06/Sapporo(TZ) and HSE06/aug-cc-pVTZ-dk levels of theory show a remarkably small MAE of 0.24 eV and 0.34 eV, respectively. These two levels of theory also show a small error range (1.53 eV and 1.56 eV, respectively). Table 2.2 shows the relative error in the computed L_2-L_3 splitting compared to experiments. All levels of theory, except for the HF/Sapporo(TZ) and HF/aug-cc-pVTZ-dk, underestimate the magnitude of spin-orbit coupling. It is clear that the description of spin-orbit coupling is greatly improved in aug-cc-pVTZ-dk and Sapporo(TZ) compared to 6-311G(d), most likely due to tight functions near the core. L_2-L_3 splittings from the range-separated HSE06 functional with relativistic-optimized basis sets are in the best agreement with experiments.

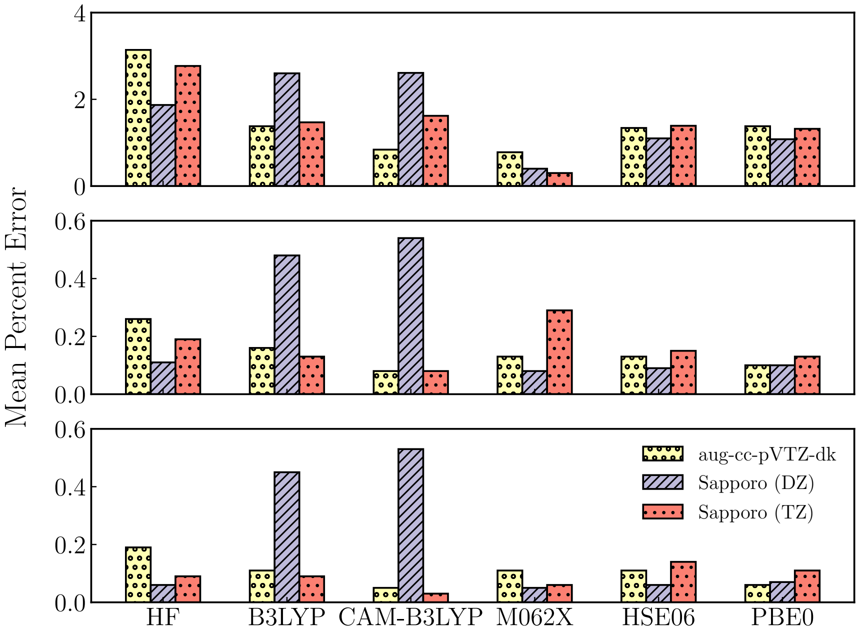

Figure 2.5: The mean percent errors for basis set and functional combinations across the molecular test set from the data in Tab. 2.3. The top panel displays the raw energies, the middle panel is the uniform shifted energies, and the bottom panel is the uniform shifted energies with the spin-orbit correction.

When an additional spin-orbit correction is included by separately aligning the L_2 edge with the experimental value relative to L_3, Tab. 2.1 shows there is not a significant difference in quality between non-relativistic and relativistic basis sets. This is because after all relativistic corrections are applied the overall shape of each edge is dominated by the description of the valence orbitals, which both a relativistic or non-relativistic basis set are able to model with a similar quality. This error analysis also suggests that approximate two-electron spin-orbit treatment, such as the Boettger scaling factor used in this work, [99]

	B3LYP	HSE06	PBE0	HF
6-311G(d)	−1.13	−0.66	−0.58	−3.64
aug-cc-pVTZ-dk	−0.82	−0.40	−0.59	0.65
Sapporo(TZ)	−0.57	−0.29	−0.49	0.78

Table 2.2: Calculated relative errors in the L_2-L_3 splitting (eV).

should be sufficient for calculations of L-edge spectra.

We continue the analysis by including heavier elements ($PdCl_2$) in the benchmark analysis, and no longer include the results with the 6-311G(d) basis. Since this test set contains molecules with metal centers on several periods, the L-edge energies vary from around 100 eV to over 3 keV. In order to appropriately quantify error for transition energies of different orders of magnitude, it is useful to examine the percent error:

$$\frac{|E_{calc} - E_{exp}|}{E_{exp}} \times 100\% \tag{2.16}$$

In Tab. 2.3 the percent errors across the entire test set are shown, and also displayed graphically in Fig. 2.5. Mean percent errors (MPE) and error ranges for unshifted spectra are significant, especially given the large L-edge excitation energy. After the uniform shift, both the mean percent error and error range are drastically improved, with CAM-B3LYP/aug-cc-pVTZ-dk and CAM-B3LYP/Sapporo(TZ) showing a mean percent error of only 0.08%. When an additional spin-orbit correction is applied, these errors are further improved. For the functionals with the PBE correlation (HSE06 and PBE0), the aug-cc-pVTZ-dk basis performs better than Sapporo(TZ). However, the reverse is true for B3LYP and CAM-B3LYP. There does not appear to be any significant difference in overall errors across the different functionals, although CAM-B3LYP had slightly better average error and one of the smallest ranges of error. Surprisingly, the range-corrected HSE06 does not perform better than PBE0 in this study, while CAM-B3LYP performed slightly better than B3LYP, which seems to suggest that range-corrected functionals do not consistently improve L-edge spectra.

	Unshifted		Uniform Shift		Uniform and Spin-Orbit Correction	
	MPE	Range	MPE	Range	MPE	Range
HF						
aug-cc-pVTZ-dk	3.14	3.36	0.26	1.01	0.19	0.78
Sapporo(TZ)	2.77	6.26	0.19	0.63	0.09	0.43
Sapporo(DZ)	1.87	0.36	0.11	0.39	0.06	0.26
B3LYP						
aug-cc-pVTZ-dk	1.38	4.06	0.16	0.65	0.11	0.44
Sapporo(TZ)	1.47	4.11	0.13	0.37	0.09	0.27
Sapporo(DZ)	2.60	4.66	0.48	2.13	0.45	2.13
CAM-B3LYP						
aug-cc-pVTZ-dk	0.84	0.85	0.08	0.28	0.05	0.20
Sapporo(TZ)	1.62	0.10	0.08	0.12	0.03	0.10
Sapporo(DZ)	2.61	4.24	0.54	2.25	0.53	2.21
M062X						
aug-cc-pVTZ-dk	0.78	1.02	0.13	0.44	0.11	0.44
Sapporo(TZ)	0.30	0.72	0.29	0.71	0.06	0.18
Sapporo(DZ)	0.40	0.93	0.08	0.31	0.05	0.23
HSE06						
aug-cc-pVTZ-dk	1.34	4.14	0.13	0.48	0.11	0.48
Sapporo(TZ)	1.39	4.79	0.15	1.08	0.14	0.95
Sapporo(DZ)	1.10	0.70	0.09	0.26	0.06	0.33
PBE0						
aug-cc-pVTZ-dk	1.38	3.78	0.10	0.45	0.06	0.23
Sapporo(TZ)	1.32	4.02	0.13	0.42	0.11	0.30
Sapporo(DZ)	1.08	0.65	0.10	0.19	0.07	0.25

Table 2.3: Mean percent errors (MPE) and its range for several different functional and basis set combinations. Errors for the L_3 and L_2 edges shifted with and without the additional spin-orbit-corrected shift are reported. Values for the shifts can be found in Supplementary Information.

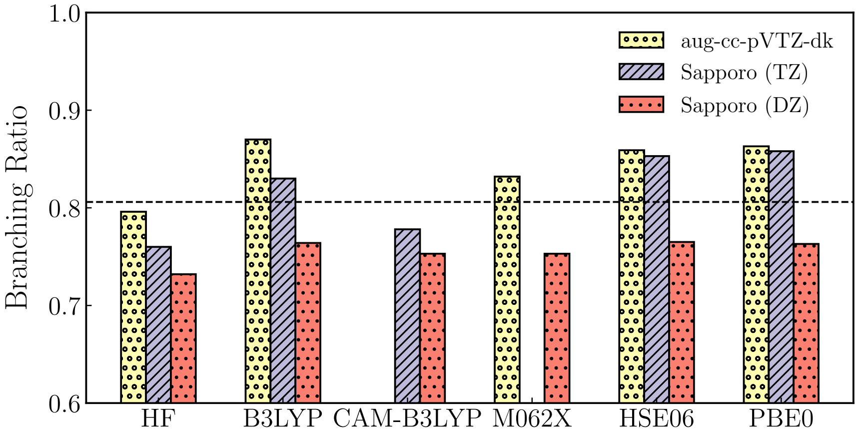

Figure 2.6: Computed branching ratios for $[FeCl_6]^{3-}$. The dashed black line denotes the experimental branching ratio (0.803).

Although obtaining correct excitation energies is important, the computed oscillator strengths must also be correct to match the experimental spectrum. Additionally, relative intensities such as the ratio between the L_2 and L_3 regions are known to contain information about oxidation state and covalency. [133, 134, 135] The branching ratio is defined as

$$\frac{I_{\mathrm{L}_3}}{I_{\mathrm{L}_3} + I_{\mathrm{L}_2}} \tag{2.17}$$

where I_{L_2} and I_{L_3} are the integrated intensities of L_2 and L_3 edges. As plotted in Fig. 2.6 the computed branching ratios of $[FeCl_6]^{3-}$ reflect how accurately the method captures the peak intensities. The double-ζ basis consistently underestimates the experimental branching ratio, most likely due to less variational flexibility. While the triple-ζ basis sets perform more accurately on average, they are also subject to more variation with respect to the DFT functional. We continue our discussion to assess the benefits and drawbacks of using TDDFT to model L-edge spectra. The L-edge X-ray absorption spectrum of $[FeCl_6]^{3-}$ has previously been studied in detail with experimental data and multiple different theoretical techniques, including the restricted active space second order perturbation (RASPT2) method [59], restricted-open-shell configuration interaction with singles (ROCIS) [62], and

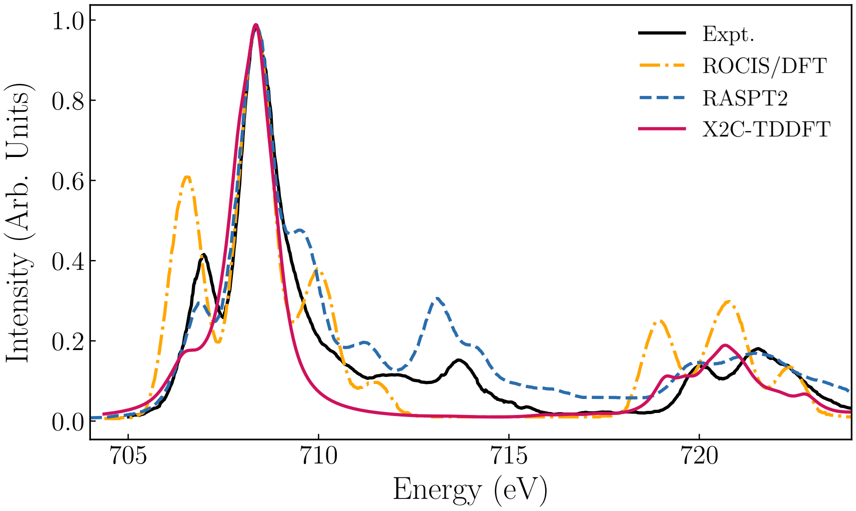

Figure 2.7: Experimental [128] and computed L-edge absorption spectra comparing different computational methods for $[FeCl_6]^{3-}$. The ROCIS/DFT spectrum comes from Ref. [62], RASPT2 comes from Ref. [59], and the X2C-TDDFT spectrum is from this work. Each theoretical spectra was uniform shifted, and normalized to match the experimental peak at 708.5 eV.

the ligand field multiplet (LFM) method [128]. The experimental [128] and computed spectra using RASPT2 [59], ROCIS/DFT,[62] and X2C-TDDFT from this work for $[FeCl_6]^{3-}$ are compared in Fig. 2.7. Each spectrum is normalized and uniformly shifted to match the main experimental L_3 edge peak at 708.5 eV. All three methods are able to qualitatively reproduce the main features in the L-edge spectrum of $[FeCl_6]^{3-}$. Both ROCIS/DFT and RASPT2 results show more peak features than that computed using X2C-TDDFT. However, the additional peak features from ROCIS/DFT seem to arise from overestimated intensities. The RASPT2 result more closely matches the experimental spectrum. Additionally, RASPT2 is the only method able to capture the peak at 713.5 eV, which is due to a “shake up” ligand-to-metal charge transfer excitation.[59] This is possible because RASPT2 includes electronic configurations with more than just single excitation character.

In order to investigate the role of multi-determinantal effects in L-edge spectra further, we

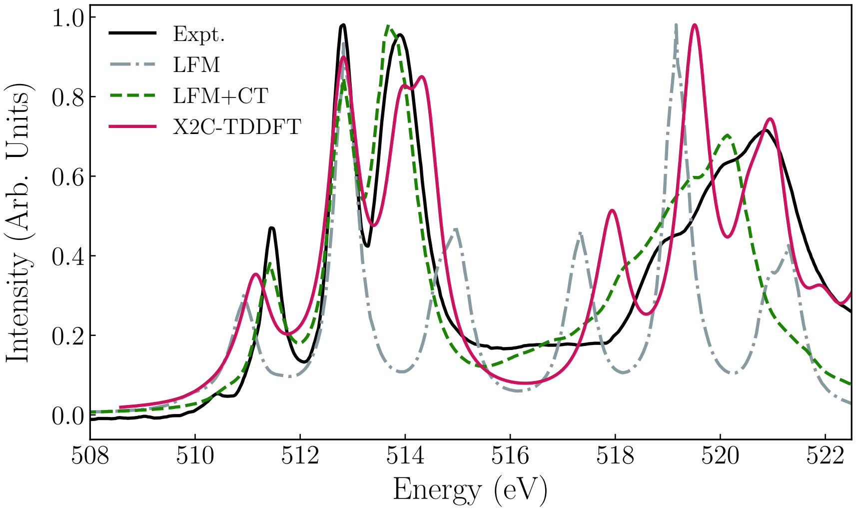

Figure 2.8: Experimental [57] and computed L-edge absorption spectra comparing different computational methods for $VOCl_3$. The LFM and LFM+CT spectra come from Ref. [136], using configuration interaction with a relativistic DFT reference, and each theoretical spectra was uniform shifted, and normalized to match the experimental peak at 513 eV. The X2C-TDDFT spectrum is from this work.

examine electronic structure characteristics of $VOCl_3$. Fig. 2.8 shows the experimental [57] and computed L-edge spectra using LFM [136] and X2C-TDDFT for $VOCl_3$. Each spectrum is normalized and uniformed shifted to the central L_3 edge peak centered at 513 eV. The spectrum denoted as LFM contains the $(2p^5)(3d^1)$ electronic configuration on the metal center. [136] Including additional doubly excited determinants with ligand-to-metal charge transfer character leads to a more accurate spectral prediction, denoted as LFM+CT. [136]

As shown in Fig. 2.8, the X2C-TDDFT result is similar to that computed using LFM+CT for the L_3-edge, with the LFM+CT spectrum agreeing better with the experiment. The LFM approach performs less satisfactorily compared to LFM+CT and X2C-TDDFT. This is likely due to the fact that the X2C-TDDFT result used a hybrid functional, B3LYP, while the spin-orbitals in LFM were computed using the local density approximation. The addition of ligand-to-metal charge transfer from the doubly excited determinants in LFM+CT seems to significantly improve the L-edge prediction. The L_2-edge spectrum computed from LFM+CT shows the best agreement with experiment. This is because the ligand-to-metal charge transfer shake-up states are more important for the electronic transitions in the L_2 region for $VOCl_3$. [136] As a result, the X2C-TDDFT and LFM L_2 spectra are in less satisfactory agreement with experiment.

Generally, the relativistic X2C-TDDFT method exhibits excellent agreement with experiments for main $L_{2,3}$ peaks dominated by single electron transitions. However, within the linear response formalism, X2C-TDDFT is unable to resolve spectral features that need multi-determinantal treatment.

2.4 Conclusion

In this work, we have presented the LR-X2C-TDDFT approach using the hybrid GPLHR-Davidson diagonalization method for the computation of $L_{2,3}$-edge spectra. Several different density functionals and basis sets are used in the benchmarking and comparison. While X2C-TDDFT cannot model satellite “shake-up” peaks due to their doubly excited character, it accurately captures the single excitation features and the energetic splitting of the L_2 and L_3 peaks. The choice of basis set did not have a strong effect on the qualitative character of computed spectra, though a reasonable quantitative improvement is seen from using a triple-ζ rather than double-ζ basis. By contrast, the effect of the choice of exchange-correlation functional has a much stronger effect. Among standard GGAs and hybrid functionals such as B3LYP or PBE0, there was no significant difference, with each performing well in these data. Using range-corrected functionals had only marginal impact on overall quality, with HSE06 slightly less accurate than PBE0, and CAM-B3LYP slightly better than B3LYP. From our test set of metal-centered compounds, the combination of CAM-B3LYP and a relativistically optimized triple-ζ basis set gives us the best result for predicting L-edge spectra.

Chapter 3

EFFICIENT FOUR-COMPONENT DIRAC-COULOMB-GAUNT HARTREE-FOCK IN PAULI SPINOR REPRESENTATION

Four-component Dirac Hartree–Fock is an accurate mean-field method for treating molecular systems where relativistic effects are important. However, the computational cost and complexity of the two-electron interaction makes this method less common, even though we can consider the Dirac Hartree–Fock Hamiltonian the “ground truth” of electronic structure, barring explicit quantum-electrodynamical effects. Being able to calculate these effects is then vital to the design of lower scaling methods for accurate predictions in computational spectroscopy and properties of heavy element complexes that must include relativistic effects for even qualitative accuracy. In this chapter, we present a Pauli quaternion formalism of maximal component- and spin-separation for computing the Dirac-Coulomb-Gaunt Hartree–Fock ground state, with a minimal floating point operation count algorithm. This approach also allows one to explicitly separate different spin physics from the two-body interactions, such as spin-free, spin-orbit, and the spin-spin contributions. Additionally, we use this formalism to examine relativistic trends in the periodic table, and analyze the basis set dependence of atomic gold and gold dimer systems. This work was reproduced with permission from S. Sun, T. F. Stetina, T. Zhang, H. Hu, E. F. Valeev, Q. Sun, and X. Li, “Efficient Four–Component Dirac–Coulomb–Gaunt Hartree–Fock in the Pauli Spinor Representation” *J. Chem. Theory Comput.*, **2021**, 17, 3388-3402. Copyright 2021 American Chemical Society.

3.1 Introduction

Dirac Hartree–Fock (DHF) is a well-established method for molecules and clusters that require accurate treatment of relativistic effects such as core orbital contraction, spin-orbit coupling, and spin-spin interactions. There has been extensive research efforts utilizing four-component DHF based on Gaussian type orbitals. [137, 138, 139, 140, 141, 142, 143, 144, 145, 146] Within the DHF framework, relativistic effects can be introduced through both one-body and two-body interactions. The one-body term includes scalar relativity and one-electron spin-orbit coupling arising from the interaction with the nuclear potential. Including one-body relativistic corrections is computationally inexpensive. There are a number of widely used techniques to account for these effects in existing electronic structure methods, including one-component and two-component frameworks.

On the other hand, the two-electron operator is complicated and computationally expensive. Without going to the full quantum-electrodynamical (QED) regime, the two-electron operator includes the Dirac-Coulomb, Gaunt, and gauge (in the Coulomb gauge) terms with increasing complexity. [147, 83, 148] From the point of view of relativistic particle interactions, these terms lead to two-electron scalar relativity, spin-own-orbit, spin-other-orbit, spin-spin interactions, and also retardation effects from the finite speed of light. Since these important two-electron relativistic effects are computationally expensive, one often has to resort to well-designed algorithms and well-calibrated approximations to strike a balance between theoretical accuracy and computational feasibility.

Various techniques have been explored to lower the computational scaling of four-component calculations, such as the quaternion formalism, [141] resolution of the identity, [146, 149] and quasi-four component approximations. [87, 88] These techniques are all based on the reduction of the dimensionality either in the matrix formalism or in the integral formation. In this work, we introduce a maximally component- and spin-separated formalism that minimizes the floating point operation (FLOP) count in the DHF formation. In the new approach introduced here, the component- and spin-separations are carried out in the restricted kinetic balance (RKB) condition within the Pauli matrix representation. All integrals are retained in the one-component electron repulsion integral (ERI) format instead of in the two-spinor or four-spinor basis. With the Pauli components, the physics of different two-electron spin interactions is easy to recognize and categorize. This work lays the theoretical and computational foundation for practical applications of four-component Dirac Hartree–Fock and correlated relativistic electronic structure methods.

3.2 Dirac-Coulomb-Gaunt Hartree–Fock Formalism in Pauli Matrix Representation

3.2.1 Brief Review of the Dirac Hartree–Fock Equation in the Four-Spinor and Two-Spinor Basis

The one-electron Dirac equation is written in the four-spinor form $\phi = \begin{bmatrix}\psi^L \\ \psi^S\end{bmatrix}$, where ψ^L and ψ^S are two-spinors of the large and small components. The Dirac equation can be written as

$$\begin{bmatrix}\mathbf{I}\otimes V & c\boldsymbol{\sigma}\cdot\mathbf{p} \\ c\boldsymbol{\sigma}\cdot\mathbf{p} & \mathbf{I}\otimes(V-2mc^2)\end{bmatrix}\begin{bmatrix}\psi^L \\ \psi^S\end{bmatrix} = E\begin{bmatrix}\psi^L \\ \psi^S\end{bmatrix} \tag{3.1}$$

where $\mathbf{p} = -i\boldsymbol{\nabla}$ is the momentum operator and $\boldsymbol{\sigma}$ are Pauli matrices.

$$\mathbf{I} = \begin{bmatrix}1 & 0 \\ 0 & 1\end{bmatrix}, \boldsymbol{\sigma}_x = \begin{bmatrix}0 & 1 \\ 1 & 0\end{bmatrix}, \boldsymbol{\sigma}_y = \begin{bmatrix}0 & -i \\ i & 0\end{bmatrix}, \boldsymbol{\sigma}_z = \begin{bmatrix}1 & 0 \\ 0 & -1\end{bmatrix}. \tag{3.2}$$

For the one-electron system, V is the nuclear potential that gives rise to scalar relativistic and spin-orbit effects. For many electron systems, the leading-order two-electron interactions that enter the molecular potential are described by the Coulomb and Gaunt terms:

$$V_{ee} = \sum_{i=1}^{N}\sum_{j>i}(g^C(i,j) - g^G(i,j)) \tag{3.3}$$

$$g^C(i,j) = \frac{1}{r_{ij}} \tag{3.4}$$

$$g^G(i,j) = \frac{\boldsymbol{\alpha}_i\cdot\boldsymbol{\alpha}_j}{r_{ij}} \tag{3.5}$$

where the components of the $\boldsymbol{\alpha}$ matrices are defined as

$$\alpha_{i,J} = \begin{bmatrix}\mathbf{0}_2 & \boldsymbol{\sigma}_J \\ \boldsymbol{\sigma}_J & \mathbf{0}_2\end{bmatrix}, \quad J = \{x,y,z\} \tag{3.6}$$

where i is i-th electron. Note that in this work we do not consider the gauge term which only arises in the non-quantum-electrodynamic treatment of the Coulomb gauge.

To cast the Dirac equation in a finite basis and formulate the Dirac-Coulomb Hartree–Fock (DC-HF) and Dirac-Coulomb-Gaunt Hartree–Fock (DCG-HF) Hamiltonians, the four-spinor molecular orbitals (MO) are expanded in two-spinor basis

$$\psi_p^L = \sum_{\tau} \sum_{\mu=1}^{N} c_{\mu\tau,p}^L \chi_{\mu\tau}^L, \quad \psi_p^S = \sum_{\tau} \sum_{\mu=1}^{N} c_{\mu\tau,p}^S \chi_{\mu\tau}^S \tag{3.7}$$

where $\tau \in \{\alpha, \beta\}$ and N is the number of spatial basis functions. The large component basis is defined as

$$\chi_{\mu\alpha}^L = \begin{bmatrix} \chi_\mu \\ 0 \end{bmatrix}, \qquad \chi_{\mu\beta}^L = \begin{bmatrix} 0 \\ \chi_\mu \end{bmatrix} \tag{3.8}$$

where χ_μ denotes the spatial basis functions. The relationship between the large and small component two-spinor basis can be defined via the restricted kinetic balance (RKB) condition. [150, 151, 152]

$$\chi_\mu^S = \frac{1}{2mc} \boldsymbol{\sigma} \cdot \mathbf{p} \chi_\mu^L \tag{3.9}$$

This relationship ensures the correct symmetry relation (opposite parity) between the small and large components and hence the correct nonrelativistic limit of the positive energy states. [153] For a detailed discussion of different choices of balanced bases, see Ref. [154]. Note that the RKB condition can only be applied to the uncontracted basis functions of all the atoms in a molecule as a whole, although the idea of "from atoms to molecule", [88] where Eq. 3.9 is applied to the uncontracted basis functions of individual atoms, is more efficient. A brief discussion regarding the related issues will be presented in the Conclusion section.

For the Dirac-Coulomb-Gaunt Hamiltonian, the Fock matrix in the four-spinor molecular orbital representation is

$$f_{pq} = h_{pq} + V^{C}_{pq} + V^{G}_{pq} \tag{3.10}$$

$$V^{C}_{pq} = \sum_{i=1}^{N_e}[(pq|ii) - (pi|iq)] \tag{3.11}$$

$$V^{G}_{pq} = -\sum_{i=1}^{N_e}[(p\boldsymbol{\alpha}q| \cdot i\boldsymbol{\alpha}i) - (p\boldsymbol{\alpha}i| \cdot i\boldsymbol{\alpha}q)] \tag{3.12}$$

where N_e is the number of electrons, i is the index for occupied orbitals, and p, q are indices for general four-spinor MOs. Equations 3.10 to 3.12 only sum over positive energy levels. Additionally, we use Mulliken notation for the two-electron integrals. We also introduce "$|\cdot$" notation to indicate that the integral is a dot product of $\boldsymbol{\alpha}$ (or $\boldsymbol{\sigma}$).

The expression of the Dirac-Coulomb-Gaunt Hamiltonian in the four-spinor basis is the simplest, but also the most computationally expensive to construct due to the fact that it is four times the length of the atomic orbital space. Therefore, dimension reduction techniques are usually carried out to lower the computational cost through component and/or spin separation. Unfortunately, dimension reduction procedures inevitably lead to an increased complexity in the underlying mathematical expression.

The four-component Fock matrix can be separated into four blocks (LL, LS, SL, SS) in the two-spinor basis. For example, the four blocks in the Dirac-Coulomb matrix are,

$$V^{C,LL}_{pq} = \sum_{i=1}^{N_e}[(p^L q^L|i^L i^L) + (p^L q^L|i^S i^S) - (p^L i^L|i^L q^L)] \tag{3.13}$$

$$V^{C,SS}_{pq} = \sum_{i=1}^{N_e}[(p^S q^S|i^L i^L) + (p^S q^S|i^S i^S) - (p^S i^S|i^S q^S)] \tag{3.14}$$

$$V^{C,LS}_{pq} = -\sum_{i=1}^{N_e}(p^L i^L|i^S q^S) \tag{3.15}$$

$$V^{C,SL}_{pq} = -\sum_{i=1}^{N_e}(p^S i^S|i^L q^L) \tag{3.16}$$

and the corresponding Gaunt contributions are

$$V_{pq}^{G,LL} = \sum_{i=1}^{N} (p^L \boldsymbol{\sigma} i^S | \cdot i^S \boldsymbol{\sigma} q^L) \tag{3.17}$$

$$V_{pq}^{G,SS} = \sum_{i=1}^{N} (p^S \boldsymbol{\sigma} i^L | \cdot i^L \boldsymbol{\sigma} q^S) \tag{3.18}$$

$$V_{pq}^{G,LS} = -\sum_{i=1}^{N} [(p^L \boldsymbol{\sigma} q^S | \cdot i^L \boldsymbol{\sigma} i^S) + (p^L \boldsymbol{\sigma} q^S | \cdot i^S \boldsymbol{\sigma} i^L) - (p^L \boldsymbol{\sigma} i^S | \cdot i^L \boldsymbol{\sigma} q^S)] \tag{3.19}$$

$$V_{pq}^{G,SL} = -\sum_{i=1}^{N} [(p^S \boldsymbol{\sigma} q^L | \cdot i^L \boldsymbol{\sigma} i^S) + (p^S \boldsymbol{\sigma} q^L | \cdot i^S \boldsymbol{\sigma} i^L) - (p^S \boldsymbol{\sigma} i^L | \cdot i^S \boldsymbol{\sigma} q^L)] \tag{3.20}$$

The DCG Hamiltonian in the two-spinor MO basis can be transformed to the two-spinor atomic orbital basis as

$$V_{\mu\tau_1,\nu\tau_2}^{C,LL} = \sum_{\lambda\tau_4\kappa\tau_3} D_{\lambda\tau_4,\kappa\tau_3}^{LL} [(\mu_{\tau_1}^L \nu_{\tau_2}^L | \kappa_{\tau_3}^L \lambda_{\tau_4}^L) - (\mu_{\tau_1}^L \lambda_{\tau_4}^L | \kappa_{\tau_3}^L \nu_{\tau_2}^L)] + D_{\lambda\tau_4,\kappa\tau_3}^{SS} [(\mu_{\tau_1}^L \nu_{\tau_2}^L | \kappa_{\tau_3}^S \lambda_{\tau_4}^S)] \tag{3.21}$$

$$V_{\mu\tau_1,\nu\tau_2}^{C,SS} = \sum_{\lambda\tau_4\kappa\tau_3} D_{\lambda\tau_4,\kappa\tau_3}^{LL} [(\mu_{\tau_1}^S \nu_{\tau_2}^S | \kappa_{\tau_3}^L \lambda_{\tau_4}^L)] + D_{\lambda\tau_4,\kappa\tau_3}^{SS} [(\mu_{\tau_1}^S \nu_{\tau_2}^S | \kappa_{\tau_3}^S \lambda_{\tau_4}^S) - (\mu_{\tau_1}^S \lambda_{\tau_4}^S | \kappa_{\tau_3}^S \nu_{\tau_2}^S)] \tag{3.22}$$

$$V_{\mu\tau_1\nu\tau_2}^{C,LS} = -\sum_{\lambda\tau_4\kappa\tau_3} D_{\lambda\tau_4,\kappa\tau_3}^{LS} (\mu_{\tau_1}^L \lambda_{\tau_4}^L | \kappa_{\tau_3}^S \nu_{\tau_2}^S) \tag{3.23}$$

$$V_{\mu\tau_1\nu\tau_2}^{C,SL} = -\sum_{\lambda\tau_4\kappa\tau_3} D_{\lambda\tau_4,\kappa\tau_3}^{SL} (\mu_{\tau_1}^S \lambda_{\tau_4}^S | \kappa_{\tau_3}^L \nu_{\tau_2}^L)] \tag{3.24}$$

$$V_{\mu\tau_1,\nu\tau_2}^{G,LL} = \sum_{\lambda\tau_4\kappa\tau_3} D_{\lambda\tau_4,\kappa\tau_3}^{SS} (\mu_{\tau_1}^L \boldsymbol{\sigma} \lambda_{\tau_4}^S | \cdot \kappa_{\tau_3}^S \boldsymbol{\sigma} \nu_{\tau_2}^L) \tag{3.25}$$

$$V_{\mu\tau_1,\nu\tau_2}^{G,SS} = \sum_{\lambda\tau_4\kappa\tau_3} D_{\lambda_{\tau_4},\kappa_{\tau_3}}^{LL} (\mu_{\tau_1}^S \boldsymbol{\sigma} \lambda_{\tau_4}^L | \cdot \kappa_{\tau_3}^L \boldsymbol{\sigma} \nu_{\tau_2}^S) \tag{3.26}$$

$$V_{\mu\tau_1,\nu\tau_2}^{G,LS} = -\sum_{\lambda\tau_4\kappa\tau_3} \{D_{\lambda\tau_4,\kappa\tau_3}^{LS} (\mu_{\tau_1}^L \boldsymbol{\sigma} \nu_{\tau_2}^S | \cdot \kappa_{\tau_3}^S \boldsymbol{\sigma} \lambda_{\tau_4}^L) + D_{\lambda\tau_4,\kappa\tau_3}^{SL} [(\mu_{\tau_1}^L \boldsymbol{\sigma} \nu_{\tau_2}^S | \cdot \kappa_{\tau_3}^L \boldsymbol{\sigma} \lambda_{\tau_4}^S) - (\mu_{\tau_1}^L \boldsymbol{\sigma} \lambda_{\tau_4}^S | \cdot \kappa_{\tau_3}^L \boldsymbol{\sigma} \nu_{\tau_2}^S)]\} \tag{3.27}$$

$$V_{\mu\tau_1,\nu\tau_2}^{G,SL} = -\sum_{\lambda\tau_4\kappa\tau_3} \{D_{\lambda\tau_4,\kappa\tau_3}^{SL} (\mu_{\tau_1}^S \boldsymbol{\sigma} \nu_{\tau_2}^L | \cdot \kappa_{\tau_3}^L \boldsymbol{\sigma} \lambda_{\tau_4}^S) + D_{\lambda\tau_4,\kappa\tau_3}^{LS} [(\mu_{\tau_1}^S \boldsymbol{\sigma} \nu_{\tau_2}^L | \cdot \kappa_{\tau_3}^S \boldsymbol{\sigma} \lambda_{\tau_4}^L) - (\mu_{\tau_1}^S \boldsymbol{\sigma} \lambda_{\tau_4}^L | \cdot \kappa_{\tau_3}^S \boldsymbol{\sigma} \nu_{\tau_2}^L)]\} \tag{3.28}$$

where $\tau_1, \tau_2, \tau_3, \tau_4 \in \{\alpha, \beta\}$, and the density matrix in spin block formation is

$$D^{XY}_{\mu\tau_1,\nu\tau_2} = \sum_{i=1}^{N_e} c^X_{\mu\tau_1,i} c^{Y*}_{\nu\tau_2,i} \quad X, Y = \{L, S\} \tag{3.29}$$

Equations 3.21 to 3.28 show that the Dirac-HF Hamiltonian can be conveniently constructed in the two-spinor atomic orbital basis. Based on these expressions, there are two approaches to construct the DCG-HF Hamiltonian from non-relativistic real-valued atomic basis integrals depending on how the kinetic-balance condition (Eq. 3.9) is incorporated in the two-spinor basis.

In the first approach, small component bases are first generated with an appropriate kinetic-balance condition and the Dirac-HF equation can be completely reformulated in a scalar basis expansion. In this approach, only the electron-repulsion integrals are needed. However, the dimension of the small component basis is usually 2∼3 times larger than that for the large component and the basis can easily become linearly dependent.

The second approach takes advantage of the restricted-kinetic-balance condition (Eq. 3.9) in the two-spinor form. Eq. 3.9 gives rise to a vector form of the small component basis. As a result, the two-spinor atomic basis becomes spin-dependent and the integral-density contraction in Equations 3.21 to 3.28 require a spin-separation step. Although the construction of the Dirac-HF Hamiltonian is more complicated, the dimension of the problem remains $2N$.

Note that these two approaches are well documented and we refer the readers to Ref. [83] for a detailed discussion. We include these expressions herein for the sake of completeness of the theory and benchmark sections. In this work, we introduce a further spin separation step in the Pauli matrix representation. The following method can be considered as a completely component- and spin-separated technique for the Dirac-HF equation.

3.2.2 Dirac-Coulomb-Gaunt in Pauli Matrix Basis

In this section, we will use the two-spinor integral $(\mu^L_{\tau_1} \nu^L_{\tau_2} | \kappa^S_{\tau_3} \lambda^S_{\tau_4})$ as an example to show how component- and spin-separation can be carried out in the Pauli matrix basis. Using the

Dirac identity,[83]

$$(\boldsymbol{\sigma}\cdot\boldsymbol{\mu})(\boldsymbol{\sigma}\cdot\boldsymbol{\nu})=\mathbf{I}\ \ (\boldsymbol{\mu}\cdot\boldsymbol{\nu})+i\boldsymbol{\sigma}\cdot\boldsymbol{\mu}\times\boldsymbol{\nu} \tag{3.30}$$

the integral can be written as

$$\begin{aligned}&(\mu^L_{\tau_1}\nu^L_{\tau_2}|\kappa^S_{\tau_3}\lambda^S_{\tau_4})\\ =&\frac{\delta_{\tau_1\tau_2}}{4m^2c^2}(\mu^L_{\tau_1}\nu^L_{\tau_1}|\boldsymbol{\sigma}(2)\cdot\mathbf{p}(2)\frac{1}{r_{12}}\boldsymbol{\sigma}(2)\cdot\mathbf{p}(2)|\kappa^L_{\tau_3}\lambda^L_{\tau_4})\\ =&\frac{\delta_{\tau_1\tau_2}}{4m^2c^2}[(\xi^\dagger_{\tau_3}\mathbf{I}\xi_{\tau_4})\boldsymbol{\nabla}_\kappa\cdot\boldsymbol{\nabla}_\lambda(\mu\nu|\kappa\lambda)+i\sum_{J=x,y,z}(\xi^\dagger_{\tau_3}\boldsymbol{\sigma}_J\xi_{\tau_4})(\boldsymbol{\nabla}_\kappa\times\boldsymbol{\nabla}_\lambda)_J(\mu\nu|\kappa\lambda)]\end{aligned} \tag{3.31}$$

where $\boldsymbol{\nabla}_\kappa$ is nuclear coordinate derivative of the atomic basis χ_κ. $\mathbf{I}(2)$ and $\boldsymbol{\sigma}(2)$ are the identity and Pauli matrix for electron 2. ξ_τ is spin representation, where

$$\xi_\alpha=\begin{bmatrix}1\\0\end{bmatrix}\qquad \xi_\beta=\begin{bmatrix}0\\1\end{bmatrix}$$

and we have

$$\begin{aligned}&\xi^\dagger_\alpha\boldsymbol{\sigma}_x\xi_\beta=1;\quad \xi^\dagger_\beta\boldsymbol{\sigma}_x\xi_\alpha=1\\ &\xi^\dagger_\alpha\boldsymbol{\sigma}_y\xi_\beta=-i;\quad \xi^\dagger_\beta\boldsymbol{\sigma}_y\xi_\alpha=i\\ &\xi^\dagger_\alpha\boldsymbol{\sigma}_z\xi_\alpha=1;\quad \xi^\dagger_\beta\boldsymbol{\sigma}_z\xi_\beta=-1\\ &\xi^\dagger_\alpha\,\mathbf{I}\,\xi_\alpha=1;\quad \xi^\dagger_\beta\,\mathbf{I}\,\xi_\beta=1\end{aligned}$$

otherwise zero. The two terms in Eq. 3.31 are two-electron spin-free and spin-orbit contributions arising from the Dirac-Coulomb operator (Eq. 3.11).

For the Gaunt term, a similar component- and spin-separation can be achieved. For example,

$$\begin{aligned}&(\mu^L_{\tau_1}\boldsymbol{\sigma}\nu^S_{\tau_2}|\cdot\kappa^S_{\tau_3}\boldsymbol{\sigma}\lambda^L_{\tau_4})\\ =&\frac{1}{(2mc)^2}(\mu^L_{\tau_1}\boldsymbol{\sigma}(1)\boldsymbol{\sigma}(1)\cdot\mathbf{p}(1)\nu^L_{\tau_2}|\cdot\boldsymbol{\sigma}(2)\cdot\mathbf{p}(2)\kappa^L_{\tau_3}\boldsymbol{\sigma}(2)\lambda^L_{\tau_4})\\ =&\ \xi^\dagger_{\tau_1}(1)\xi_{\tau_1}(1)\xi^\dagger_{\tau_3}(2)\xi_{\tau_4}(2)\big[\mathbf{I}(1)\mathbf{I}(2)\boldsymbol{\nabla}_\kappa\cdot\boldsymbol{\nabla}_\nu\\ &+i(\mathbf{I}(1)\boldsymbol{\sigma}(2)+\mathbf{I}(2)\boldsymbol{\sigma}(1))\cdot\boldsymbol{\nabla}_\kappa\times\boldsymbol{\nabla}_\nu\\ &+(\boldsymbol{\sigma}(1)\cdot\boldsymbol{\sigma}(2))(\boldsymbol{\nabla}_\kappa\cdot\boldsymbol{\nabla}_\nu)-(\boldsymbol{\sigma}(1)\cdot\boldsymbol{\nabla}_\kappa)(\boldsymbol{\sigma}(2)\cdot\boldsymbol{\nabla}_\nu)\big](\mu\nu|\kappa\lambda)\end{aligned} \tag{3.32}$$

The detailed derivation can be found in the Appendix A. In the final expression of Eq. 3.32, the first two contributions are the two-electron spin-free and spin-orbit interactions. The final two contributions arise from the spin-spin interaction which only exists in the Gaunt term.

Careful observation of Eq. 3.31 and Eq. 3.32 shows that all two-spinor terms can be organized into the Pauli matrix representation of $(\mathbf{I}, \boldsymbol{\sigma}_x, \boldsymbol{\sigma}_y, \boldsymbol{\sigma}_z)$ in the form of

$$\mathbf{G}^{XY} = \frac{1}{2}\mathbf{G}_s^{XY} \otimes \mathbf{I} + \frac{1}{2}\sum_{J=x,y,z} \mathbf{G}_J^{XY} \otimes \boldsymbol{\sigma}_J \tag{3.33}$$

where $\mathbf{G}_s$ and $\mathbf{G}_J$ are the spin-free and spin-dependent parts of the two-spinor general matrix/tensor, and $\{X, Y\} \in \{L, S\}$.

In fact, both two-spinor Fock $\mathbf{F}^{XY}$ and density $\mathbf{P}^{XY}$ matrices can also be written in the Pauli matrix representation,[97]

$$\mathbf{Q} = \begin{bmatrix} \mathbf{Q}_{\alpha\alpha} & \mathbf{Q}_{\beta\alpha} \\ \mathbf{Q}_{\beta\alpha} & \mathbf{Q}_{\beta\beta} \end{bmatrix} = \frac{1}{2}\begin{bmatrix} \mathbf{Q}_s + \mathbf{Q}_z & \mathbf{Q}_x - i\mathbf{Q}_y \\ \mathbf{Q}_x + i\mathbf{Q}_y & \mathbf{Q}_s - \mathbf{Q}_z \end{bmatrix} = \frac{1}{2}\mathbf{Q}_s \otimes \mathbf{I} + \frac{1}{2}\sum_{J=x,y,z} \mathbf{Q}_J \otimes \boldsymbol{\sigma}_J \tag{3.34}$$

$$\begin{aligned} \mathbf{Q}_s &= \mathbf{Q}_{\alpha\alpha} + \mathbf{Q}_{\beta\beta} \\ \mathbf{Q}_x &= \mathbf{Q}_{\alpha\beta} + \mathbf{Q}_{\beta\alpha} \\ \mathbf{Q}_y &= i(\mathbf{Q}_{\alpha\beta} - \mathbf{Q}_{\beta\alpha}) \\ \mathbf{Q}_z &= \mathbf{Q}_{\alpha\alpha} - \mathbf{Q}_{\beta\beta} \end{aligned}$$

where $\mathbf{Q} \in \{\mathbf{F}^{XY}, \mathbf{P}^{XY}\}$ and $\{X, Y\} \in \{L, S\}$.

These mathematical expressions suggest that the two-spinor form of the Dirac Hamiltonian can be completely cast in the Pauli matrix representation, achieving the maximally component- and spin-separated Dirac Hamiltonian. In the next section, we show that the resulting algebraic expressions turn out to be very complicated. However, upon successful implementation, we are rewarded with an optimally efficient four-component Dirac Hartree–Fock equation, as will be shown in the Results and Discussion Section.

3.2.3 Building Dirac Hartree–Fock Matrix with Pauli Components

A unique advantage of building the DCG-HF matrix in the spin-separated Pauli spinor representation is that terms with the same integral type can be combined. For example, since the spin-free and spin-spin interactions in Eq. 3.32 share a same integral type of $\boldsymbol{\nabla}\cdot\boldsymbol{\nabla}$, they can be combined in the final contraction step, resulting in a computational algorithm of potentially minimal FLOP count. Since the complete derivation is very lengthy and complex, we only present a brief derivation procedure in Appendix A and the final expressions in the main text.

The non-relativistic Coulomb contribution (first and third term in Eq. 3.13) only appears in the LL block of the two-spinor Fock matrix, which can be written in Pauli representation as

$$V^{LL}_{\mu\nu,s} = \sum_{\kappa\lambda} D^{LL}_{\lambda\kappa,s}[2(\mu\nu|\kappa\lambda) - (\mu\lambda|\kappa\nu)] \tag{3.35}$$

$$V^{LL}_{\mu\nu,J} = -\sum_{\kappa\lambda} D^{LL}_{\lambda\kappa,J}(\mu\lambda|\kappa\nu) \tag{3.36}$$

where $J = x, y, z$. Note that the non-relativistic contributions to the Pauli $J = x, y, z$ components of the LL block are all exchange type.

The rest of Dirac–Coulomb contribution involves two-center 2nd-derivatives or four-center 4th-derivatives of electron-repulsion integrals and a prefactor of $\frac{1}{(2mc)^2}$ or $\frac{1}{(2mc)^4}$.

The LL block of the relativistic part (second term in Eq. 3.13) of the two-spinor Dirac–Coulomb matrices in Pauli representation is

$$V^{C,LL}_{\mu\nu,s} = 2\sum_{\kappa\lambda} D^{SS}_{\lambda\kappa,s}\boldsymbol{\nabla}_\kappa\cdot\boldsymbol{\nabla}_\lambda(\mu\nu|\kappa\lambda) + 2i\sum_{J=x,y,z} D^{SS}_{\lambda\kappa J}(\boldsymbol{\nabla}_\kappa\times\boldsymbol{\nabla}_\lambda)_J(\mu\nu|\kappa\lambda) \tag{3.37}$$

where $\boldsymbol{\nabla}_\kappa\cdot\boldsymbol{\nabla}_\lambda(\mu\nu|\kappa\lambda)$ and $(\boldsymbol{\nabla}_\kappa\times\boldsymbol{\nabla}_\lambda)_J(\mu\nu|\kappa\lambda)$ are the dot-product and the J-th component of the cross-product of the κ and λ center gradients.

The Dirac-Coulomb contributions to the SS block (first term in Eq. 3.14) are contracted with the scalar part of the LL density matrix,

$$V^{C,SS}_{\mu\nu,s} = 2\sum_{\kappa\lambda} D^{LL}_{\lambda\kappa,s} \boldsymbol{\nabla}_\mu \ \cdot \boldsymbol{\nabla}_\nu(\mu\nu|\kappa\lambda) \tag{3.38}$$

$$V^{C,SS}_{\mu\nu,J} = 2i\sum_{\kappa\lambda} D^{LL}_{\lambda\kappa,s}(\boldsymbol{\nabla}_\mu \ \times \boldsymbol{\nabla}_\nu)_J(\mu\nu|\kappa\lambda) \tag{3.39}$$

The rest of SS block, known as the $(SS|SS)$ contribution, involves $(p^S q^S|r^S s^S)$ type of four-center ERI 4th-derivatives. The $(SS|SS)$ Dirac-Coulomb term is often ignored in practice due to its large computational cost of ERI 4th-derivatives and its small contribution on the order of $\frac{1}{c^4}$. For the completeness of the derivation and cost analysis, the $(SS|SS)$ contribution to the Dirac-Coulomb SS block is presented in Appendix B.

The Dirac-Coulomb contributions to the LS block are all exchange type integrals:

$$\begin{aligned} V^{C,LS}_{\mu\nu,s} = \big[&- D^{LS}_{\lambda\kappa,s}(\boldsymbol{\nabla}_\kappa \cdot \boldsymbol{\nabla}_\nu) - iD^{LS}_{\lambda\kappa,x}(\boldsymbol{\nabla}_\kappa \times \boldsymbol{\nabla}_\nu)_x \\ &- iD^{LS}_{\lambda\kappa,y}(\boldsymbol{\nabla}_\kappa \times \boldsymbol{\nabla}_\nu)_y - iD^{LS}_{\lambda\kappa,z}(\boldsymbol{\nabla}_\kappa \times \boldsymbol{\nabla}_\nu)_z\big](\mu\lambda|\kappa\nu) \end{aligned} \tag{3.40}$$

$$\begin{aligned} V^{C,LS}_{\mu\nu,z} = \big[&- D^{LS}_{\lambda\kappa,z}(\boldsymbol{\nabla}_\kappa \cdot \boldsymbol{\nabla}_\nu) - D^{LS}_{\lambda\kappa,y}(\boldsymbol{\nabla}_\kappa \times \boldsymbol{\nabla}_\nu)_x \\ &+ D^{LS}_{\lambda\kappa,x}(\boldsymbol{\nabla}_\kappa \times \boldsymbol{\nabla}_\nu)_y - iD^{LS}_{\lambda\kappa,s}(\boldsymbol{\nabla}_\kappa \times \boldsymbol{\nabla}_\nu)_z\big](\mu\lambda|\kappa\nu) \end{aligned} \tag{3.41}$$

$$\begin{aligned} V^{C,LS}_{\mu\nu,x} = \big[&- D^{LS}_{\lambda\kappa,x}(\boldsymbol{\nabla}_\kappa \cdot \boldsymbol{\nabla}_\nu) - iD^{LS}_{\lambda\kappa,s}(\boldsymbol{\nabla}_\kappa \times \boldsymbol{\nabla}_\nu)_x \\ &- D^{LS}_{\lambda\kappa,z}(\boldsymbol{\nabla}_\kappa \times \boldsymbol{\nabla}_\nu)_y + D^{LS}_{\lambda\kappa,y}(\boldsymbol{\nabla}_\kappa \times \boldsymbol{\nabla}_\nu)_z\big](\mu\lambda|\kappa\nu) \end{aligned} \tag{3.42}$$

$$\begin{aligned} V^{C,LS}_{\mu\nu,y} = \big[&- D^{LS}_{\lambda\kappa,y}(\boldsymbol{\nabla}_\kappa \cdot \boldsymbol{\nabla}_\nu) + D^{LS}_{\lambda\kappa,z}(\boldsymbol{\nabla}_\kappa \times \boldsymbol{\nabla}_\nu)_x \\ &- iD^{LS}_{\lambda\kappa,s}(\boldsymbol{\nabla}_\kappa \times \boldsymbol{\nabla}_\nu)_y - D^{LS}_{\lambda\kappa,x}(\boldsymbol{\nabla}_\kappa \times \boldsymbol{\nabla}_\nu)_z\big](\mu\lambda|\kappa\nu) \end{aligned} \tag{3.43}$$

Additionally, for the SL block, we can take advantage of the relation

$$V^{C,SL} = V^{\dagger C,LS}$$

and only compute the $V^{C,LS}$ matrix elements directly.

Next, we consider the Gaunt contribution to the Dirac Hartree–Fock matrix. The Gaunt contribution to the LL and SS blocks are all exchange type:

$$\begin{aligned} V^{G,LL}_{\mu\nu,s} = 3\big[&D^{SS}_{\lambda\kappa,s}\boldsymbol{\nabla}_\lambda \cdot \boldsymbol{\nabla}_\kappa - iD^{SS}_{\lambda\kappa,z}(\boldsymbol{\nabla}_\lambda \times \boldsymbol{\nabla}_\kappa)_z \\ &-iD^{SS}_{\lambda\kappa,x}(\boldsymbol{\nabla}_\lambda \times \boldsymbol{\nabla}_\kappa)_x - iD^{SS}_{\lambda\kappa,y}(\boldsymbol{\nabla}_\lambda \times \boldsymbol{\nabla}_\kappa)_y\big](\mu\lambda|\kappa\nu) \end{aligned} \tag{3.44}$$

$$\begin{aligned} V^{G,LL}_{\mu\nu,z} =& \big\{ - D^{SS}_{\lambda\kappa,z}[-(\boldsymbol{\nabla}_\lambda)_x(\boldsymbol{\nabla}_\kappa)_x - (\boldsymbol{\nabla}_\lambda)_y(\boldsymbol{\nabla}_\kappa)_y + (\boldsymbol{\nabla}_\lambda)_z(\boldsymbol{\nabla}_\kappa)_z] \\ & - iD^{SS}_{\lambda\kappa,s}(\boldsymbol{\nabla}_\lambda \times \boldsymbol{\nabla}_\kappa)_z - D^{SS}_{\lambda\kappa,x}[(\boldsymbol{\nabla}_\lambda)_x(\boldsymbol{\nabla}_\kappa)_z + (\boldsymbol{\nabla}_\lambda)_z(\boldsymbol{\nabla}_\kappa)_x] \\ & - D^{SS}_{\lambda\kappa,y}[(\boldsymbol{\nabla}_\lambda)_y(\boldsymbol{\nabla}_\kappa)_z + (\boldsymbol{\nabla}_\lambda)_z(\boldsymbol{\nabla}_\kappa)_y]\big\}(\mu\lambda|\kappa\nu) \end{aligned} \tag{3.45}$$

$$\begin{aligned} V^{G,LL}_{\mu\nu,x} =& \big\{ - D^{SS}_{\lambda\kappa,x}[(\boldsymbol{\nabla}_\lambda)_x(\boldsymbol{\nabla}_\kappa)_x - (\boldsymbol{\nabla}_\lambda)_y(\boldsymbol{\nabla}_\kappa)_y - (\boldsymbol{\nabla}_\lambda)_z(\boldsymbol{\nabla}_\kappa)_z] \\ & - iD^{SS}_{\lambda\kappa,s}(\boldsymbol{\nabla}_\lambda \times \boldsymbol{\nabla}_\kappa)_x - D^{SS}_{\lambda\kappa,y}[(\boldsymbol{\nabla}_\lambda)_x(\boldsymbol{\nabla}_\kappa)_y + (\boldsymbol{\nabla}_\lambda)_y(\boldsymbol{\nabla}_\kappa)_x] \\ & - D^{SS}_{\lambda\kappa,z}[(\boldsymbol{\nabla}_\lambda)_x(\boldsymbol{\nabla}_\kappa)_z + (\boldsymbol{\nabla}_\lambda)_z(\boldsymbol{\nabla}_\kappa)_x]\big\}(\mu\lambda|\kappa\nu) \end{aligned} \tag{3.46}$$

$$\begin{aligned} V^{G,LL}_{\mu\nu,y} =& \big\{ - D^{SS}_{\lambda\kappa,y}[-(\boldsymbol{\nabla}_\lambda)_x(\boldsymbol{\nabla}_\kappa)_x + (\boldsymbol{\nabla}_\lambda)_y(\boldsymbol{\nabla}_\kappa)_y - (\boldsymbol{\nabla}_\lambda)_z(\boldsymbol{\nabla}_\kappa)_z] \\ & - iD^{SS}_{\lambda\kappa,s}(\boldsymbol{\nabla}_\lambda \times \boldsymbol{\nabla}_\kappa)_y - D^{SS}_{\lambda\kappa,x}[(\boldsymbol{\nabla}_\lambda)_x(\boldsymbol{\nabla}_\kappa)_y + (\boldsymbol{\nabla}_\lambda)_y(\boldsymbol{\nabla}_\kappa)_x] \\ & - D^{SS}_{\lambda\kappa,z}[(\boldsymbol{\nabla}_\lambda)_y(\boldsymbol{\nabla}_\kappa)_z + (\boldsymbol{\nabla}_\lambda)_z(\boldsymbol{\nabla}_\kappa)_y]\big\}(\mu\lambda|\kappa\nu) \end{aligned} \tag{3.47}$$

$$V^{G,SS}_{\mu\nu,s} = \big[3D^{LL}_{\lambda\kappa,s}\boldsymbol{\nabla}_\mu \cdot \boldsymbol{\nabla}_\nu + iD^{LL}_{\lambda\kappa,z}(\boldsymbol{\nabla}_\mu \times \boldsymbol{\nabla}_\nu)_z + iD^{LL}_{\lambda\kappa,x}(\boldsymbol{\nabla}_\mu \times \boldsymbol{\nabla}_\nu)_x + iD^{LL}_{\lambda\kappa,y}(\boldsymbol{\nabla}_\mu \times \boldsymbol{\nabla}_\nu)_y\big](\mu\lambda|\kappa\nu) \tag{3.48}$$

$$\begin{aligned} V^{G,SS}_{\mu\nu,z} = & \big\{ - D^{LL}_{\lambda\kappa,z}[-(\boldsymbol{\nabla}_\mu)_x(\boldsymbol{\nabla}_\nu)_x - (\boldsymbol{\nabla}_\mu)_y(\boldsymbol{\nabla}_\nu)_y + (\boldsymbol{\nabla}_\mu)_z(\boldsymbol{\nabla}_\nu)_z] + 3iD^{LL}_{\lambda\kappa,s}(\boldsymbol{\nabla}_\mu \times \boldsymbol{\nabla}_\nu)_z \\ & -D^{LL}_{\lambda\kappa,x}[(\boldsymbol{\nabla}_\mu)_x(\boldsymbol{\nabla}_\nu)_z + (\boldsymbol{\nabla}_\mu)_z(\boldsymbol{\nabla}_\nu)_x] - D^{LL}_{\lambda\kappa,y}[(\boldsymbol{\nabla}_\mu)_z(\boldsymbol{\nabla}_\nu)_y + (\boldsymbol{\nabla}_\mu)_y(\boldsymbol{\nabla}_\nu)_z]\big\}(\mu\lambda|\kappa\nu) \end{aligned} \tag{3.49}$$

$$\begin{aligned} V^{G,SS}_{\mu\nu,x} = & \big\{ - D^{LL}_{\lambda\kappa,x}[(\boldsymbol{\nabla}_\mu)_x(\boldsymbol{\nabla}_\nu)_x - (\boldsymbol{\nabla}_\mu)_y(\boldsymbol{\nabla}_\nu)_y - (\boldsymbol{\nabla}_\mu)_z(\boldsymbol{\nabla}_\nu)_z] + 3iD^{LL}_{\lambda\kappa,s}(\boldsymbol{\nabla}_\mu \times \boldsymbol{\nabla}_\nu)_x \\ & -D^{LL}_{\lambda\kappa,z}[(\boldsymbol{\nabla}_\mu)_x(\boldsymbol{\nabla}_\nu)_z + (\boldsymbol{\nabla}_\mu)_z(\boldsymbol{\nabla}_\nu)_x] - D^{LL}_{\lambda\kappa,y}[(\boldsymbol{\nabla}_\mu)_x(\boldsymbol{\nabla}_\nu)_y + (\boldsymbol{\nabla}_\mu)_y(\boldsymbol{\nabla}_\nu)_x]\big\}(\mu\lambda|\kappa\nu) \end{aligned} \tag{3.50}$$

$$\begin{aligned} V^{G,SS}_{\mu\nu,y} = & \big\{ - D^{LL}_{\lambda\kappa,y}[-(\boldsymbol{\nabla}_\mu)_x(\boldsymbol{\nabla}_\nu)_x + (\boldsymbol{\nabla}_\mu)_y(\boldsymbol{\nabla}_\nu)_y - (\boldsymbol{\nabla}_\mu)_z(\boldsymbol{\nabla}_\nu)_z] + 3iD^{LL}_{\lambda\kappa,s}(\boldsymbol{\nabla}_\mu \times \boldsymbol{\nabla}_\nu)_y \\ & -D^{LL}_{\lambda\kappa,x}[(\boldsymbol{\nabla}_\mu)_x(\boldsymbol{\nabla}_\nu)_y + (\boldsymbol{\nabla}_\mu)_y(\boldsymbol{\nabla}_\nu)_x] - D^{LL}_{\lambda\kappa,z}[(\boldsymbol{\nabla}_\mu)_z(\boldsymbol{\nabla}_\nu)_y + (\boldsymbol{\nabla}_\mu)_y(\boldsymbol{\nabla}_\nu)_z]\big\}(\mu\lambda|\kappa\nu) \end{aligned} \tag{3.51}$$

The Gaunt contribution to the LS and SL blocks includes both Coulomb and exchange integrals:

$$\begin{aligned}
V^{G,LS}_{\mu\nu,s} = -2\sum_{\kappa\lambda} \big[& D^{LS}_{\lambda\kappa,s} \boldsymbol{\nabla}_\kappa \cdot \boldsymbol{\nabla}_\nu - i \sum_{J=x,y,z} D^{LS}_{\lambda\kappa,J} (\boldsymbol{\nabla}_\nu \times \boldsymbol{\nabla}_\kappa)_J \\
& - D^{SL}_{\lambda\kappa,s} \boldsymbol{\nabla}_\nu \cdot \boldsymbol{\nabla}_\lambda - i \sum_{J=x,y,z} D^{SL}_{\lambda\kappa,J} (\boldsymbol{\nabla}_\nu \times \boldsymbol{\nabla}_\lambda)_J \big] (\mu\nu|\kappa\lambda) \\
& + \big[D^{SL}_{\lambda\kappa,s} \boldsymbol{\nabla}_\lambda \cdot \boldsymbol{\nabla}_\nu - i D^{SL}_{\lambda\kappa,z} (\boldsymbol{\nabla}_\lambda \times \boldsymbol{\nabla}_\nu)_z \\
& - i D^{SL}_{\lambda\kappa,y} (\boldsymbol{\nabla}_\lambda \times \boldsymbol{\nabla}_\nu)_y - i D^{SL}_{\lambda\kappa,x} (\boldsymbol{\nabla}_\lambda \times \boldsymbol{\nabla}_\nu)_x \big] (\mu\lambda|\kappa\nu) \qquad (3.52)
\end{aligned}$$

$$\begin{aligned}
V^{G,LS}_{\mu\nu,z} = & -\big\{ 2D^{SL}_{\lambda\kappa,z} \boldsymbol{\nabla}_\lambda \cdot \boldsymbol{\nabla}_\nu + 2D^{SL}_{\lambda\kappa,y} (\boldsymbol{\nabla}_\lambda \times \boldsymbol{\nabla}_\nu)_x - 2D^{SL}_{\lambda\kappa,x} (\boldsymbol{\nabla}_\lambda \times \boldsymbol{\nabla}_\nu)_y - iD^{SL}_{\lambda\kappa,s} (\boldsymbol{\nabla}_\lambda \times \boldsymbol{\nabla}_\nu)_z \\
& + D^{SL}_{\lambda\kappa,z} \big[-(\boldsymbol{\nabla}_\lambda)_x (\boldsymbol{\nabla}_\nu)_x - (\boldsymbol{\nabla}_\lambda)_y (\boldsymbol{\nabla}_\nu)_y + (\boldsymbol{\nabla}_\lambda)_z (\boldsymbol{\nabla}_\nu)_z \big] \\
& + D^{SL}_{\lambda\kappa,x} \big[(\boldsymbol{\nabla}_\nu)_x (\boldsymbol{\nabla}_\lambda)_z + (\boldsymbol{\nabla}_\nu)_z (\boldsymbol{\nabla}_\lambda)_x \big] + D^{SL}_{\lambda\kappa,y} \big[(\boldsymbol{\nabla}_\nu)_y (\boldsymbol{\nabla}_\lambda)_z + (\boldsymbol{\nabla}_\nu)_z (\boldsymbol{\nabla}_\lambda)_y \big] \big\} (\mu\lambda|\kappa\nu) \\
& - 2\sum_{\kappa\lambda} \big[-iD^{LS}_{\lambda\kappa,S} (\boldsymbol{\nabla}_\nu \times \boldsymbol{\nabla}_\kappa)_z + D^{LS}_{\lambda\kappa,z} (\boldsymbol{\nabla}_\kappa \cdot \boldsymbol{\nabla}_\nu) - \sum_{K=x,y,z} D^{LS}_{\lambda\kappa,K} (\boldsymbol{\nabla}_\nu)_K (\boldsymbol{\nabla}_\kappa)_z \\
& + iD^{SL}_{\lambda\kappa,s} (\boldsymbol{\nabla}_\nu \times \boldsymbol{\nabla}_\lambda)_z + D^{SL}_{\lambda\kappa,z} (\boldsymbol{\nabla}_\nu \cdot \boldsymbol{\nabla}_\lambda) - \sum_{K=x,y,z} D^{SL}_{\lambda\kappa,K} (\boldsymbol{\nabla}_\lambda)_z (\boldsymbol{\nabla}_\nu)_K \big] (\mu\nu|\kappa\lambda) \qquad (3.53)
\end{aligned}$$

$$\begin{aligned}
V^{G,LS}_{\mu\nu,x} = & -\big\{ 2D^{SL}_{\lambda\kappa,x} \boldsymbol{\nabla}_\lambda \cdot \boldsymbol{\nabla}_\nu - 2D^{SL}_{\lambda\kappa,y} (\boldsymbol{\nabla}_\lambda \times \boldsymbol{\nabla}_\nu)_z + 2D^{SL}_{\lambda\kappa,z} (\boldsymbol{\nabla}_\lambda \times \boldsymbol{\nabla}_\nu)_y - iD^{SL}_{\lambda\kappa,s} (\boldsymbol{\nabla}_\lambda \times \boldsymbol{\nabla}_\nu)_x \\
& + D^{SL}_{\lambda\kappa,x} \big[(\boldsymbol{\nabla}_\lambda)_x (\boldsymbol{\nabla}_\nu)_x - (\boldsymbol{\nabla}_\lambda)_y (\boldsymbol{\nabla}_\nu)_y - (\boldsymbol{\nabla}_\lambda)_z (\boldsymbol{\nabla}_\nu)_z \big] \\
& + D^{SL}_{\lambda\kappa,y} \big[(\boldsymbol{\nabla}_\nu)_x (\boldsymbol{\nabla}_\lambda)_y + (\boldsymbol{\nabla}_\nu)_y (\boldsymbol{\nabla}_\lambda)_x \big] + D^{SL}_{\lambda\kappa,z} \big[(\boldsymbol{\nabla}_\nu)_x (\boldsymbol{\nabla}_\lambda)_z + (\boldsymbol{\nabla}_\nu)_z (\boldsymbol{\nabla}_\lambda)_x \big] \big\} (\mu\lambda|\kappa\nu) \\
& - 2\sum_{\kappa\lambda} \big[-iD^{LS}_{\lambda\kappa,s} (\boldsymbol{\nabla}_\nu \times \boldsymbol{\nabla}_\kappa)_x + D^{LS}_{\lambda\kappa,x} (\boldsymbol{\nabla}_\kappa \cdot \boldsymbol{\nabla}_\nu) - \sum_{K=x,y,z} D^{LS}_{\lambda\kappa,K} (\boldsymbol{\nabla}_\nu)_K (\boldsymbol{\nabla}_\kappa)_x \\
& + iD^{SL}_{\lambda\kappa,s} (\boldsymbol{\nabla}_\nu \times \boldsymbol{\nabla}_\lambda)_x + D^{SL}_{\lambda\kappa,x} (\boldsymbol{\nabla}_\nu \cdot \boldsymbol{\nabla}_\lambda) - \sum_{K=x,y,z} D^{SL}_{\lambda\kappa,K} (\boldsymbol{\nabla}_\lambda)_J (\boldsymbol{\nabla}_\nu)_K \big] (\mu\nu|\kappa\lambda) \qquad (3.54)
\end{aligned}$$

$$\begin{aligned}V^{G,LS}_{\mu\nu,y} &= -\big\{2D^{SL}_{\lambda\kappa,y}\boldsymbol{\nabla}_\lambda\cdot\boldsymbol{\nabla}_\nu + 2D^{SL}_{\lambda\kappa,x}(\boldsymbol{\nabla}_\lambda\times\boldsymbol{\nabla}_\nu)_z - 2D^{SL}_{\lambda\kappa,z}(\boldsymbol{\nabla}_\lambda\times\boldsymbol{\nabla}_\nu)_x - iD^{SL}_{\lambda\kappa,s}(\boldsymbol{\nabla}_\lambda\times\boldsymbol{\nabla}_\nu)_y \\ &\quad + D^{SL}_{\lambda\kappa,y}\big[-(\boldsymbol{\nabla}_\lambda)_x(\boldsymbol{\nabla}_\nu)_x + (\boldsymbol{\nabla}_\lambda)_y(\boldsymbol{\nabla}_\nu)_y - (\boldsymbol{\nabla}_\lambda)_z(\boldsymbol{\nabla}_\nu)_z\big] \\ &\quad + D^{SL}_{\lambda\kappa,x}\big[(\boldsymbol{\nabla}_\nu)_x(\boldsymbol{\nabla}_\lambda)_y + (\boldsymbol{\nabla}_\nu)_y(\boldsymbol{\nabla}_\lambda)_x\big] + D^{SL}_{\lambda\kappa,z}\big[(\boldsymbol{\nabla}_\nu)_y(\boldsymbol{\nabla}_\lambda)_z + (\boldsymbol{\nabla}_\nu)_z(\boldsymbol{\nabla}_\lambda)_y\big]\big\}(\mu\lambda|\kappa\nu) \\ &\quad - 2\sum_{\kappa\lambda}\big[-iD^{LS}_{\lambda\kappa,s}(\boldsymbol{\nabla}_\nu\times\boldsymbol{\nabla}_\kappa)_y + D^{LS}_{\lambda\kappa,J}(\boldsymbol{\nabla}_\kappa\cdot\boldsymbol{\nabla}_\nu) - \sum_{K=x,y,z} D^{LS}_{\lambda\kappa,K}(\boldsymbol{\nabla}_\nu)_K(\boldsymbol{\nabla}_\kappa)_y \\ &\quad + iD^{SL}_{\lambda\kappa,s}(\boldsymbol{\nabla}_\nu\times\boldsymbol{\nabla}_\lambda)_y + D^{SL}_{\lambda\kappa,y}(\boldsymbol{\nabla}_\nu\cdot\boldsymbol{\nabla}_\lambda) - \sum_{K=x,y,z} D^{SL}_{\lambda\kappa,K}(\boldsymbol{\nabla}_\lambda)_y(\boldsymbol{\nabla}_\nu)_K\big](\mu\nu|\kappa\lambda) \end{aligned} \tag{3.55}$$

Additionally, for the SL block, we have the symmetry

$$V^{G,SL} = V^{\dagger G,LS}$$

Finally, the core Hamiltonian is then defined as

$$h^{LL}_{\mu\nu,s} = 2\langle\mu|V|\nu\rangle, \quad h^{LL}_{\mu\nu,J} = 0 \tag{3.56}$$

$$h^{LS}_{\mu\nu,s} = 2\langle\mu|T|\nu\rangle, \quad h^{LS}_{\mu\nu,J} = 0 \tag{3.57}$$

$$h^{SS}_{\mu\nu,s} = 2\left[\frac{1}{4m^2c^2}\boldsymbol{\nabla}_\mu\cdot\boldsymbol{\nabla}_\nu\langle\mu|V|\nu\rangle - \langle\mu|T|\nu\rangle\right] \tag{3.58}$$

$$h^{SS}_{\mu\nu,J} = \frac{2i}{4m^2c^2}(\boldsymbol{\nabla}_\mu\times\boldsymbol{\nabla}_\nu)_J\langle\mu|V|\nu\rangle \tag{3.59}$$

where $J = x, y, z$. T and V are kinetic energy and electron-nuclear potential energy operators.

3.2.4 Dirac Hartree–Fock Equation

Collecting all Pauli components for core-Hamiltonian, Dirac-Coulomb, and Gaunt terms, the Fock matrix in Pauli representation can be constructed:

$$\mathbf{F}^{XY}_\Gamma = \mathbf{h}^{XY}_\Gamma + \mathbf{V}^{XY}_\Gamma + \frac{1}{(2mc)^2}\mathbf{V}^{C,XY}_\Gamma + \frac{1}{(2mc)^2}\mathbf{V}^{G,XY}_\Gamma + \frac{1}{(2mc)^4}\mathbf{V}^{C(4),XY}_\Gamma \tag{3.60}$$

where $X, Y \in \{L, S\}$ and $\Gamma \in \{s, x, y, z\}$. The corresponding two-spinor Fock matrix and density matrix can be constructed from their Pauli components:

$$\mathbf{F}^{XY} = \frac{1}{2}\begin{bmatrix} \mathbf{F}_s^{XY} + \mathbf{F}_z^{XY} & \mathbf{F}_x^{XY} - i\mathbf{F}_y^{XY} \\ \mathbf{F}_x^{XY} + i\mathbf{F}_y^{XY} & \mathbf{F}_s^{XY} - \mathbf{F}_z^{XY} \end{bmatrix}, \quad \mathbf{P}^{XY} = \frac{1}{2}\begin{bmatrix} \mathbf{P}_s^{XY} + \mathbf{P}_z^{XY} & \mathbf{P}_x^{XY} - i\mathbf{P}_y^{XY} \\ \mathbf{P}_x^{XY} + i\mathbf{P}_y^{XY} & \mathbf{P}_s^{XY} - \mathbf{P}_z^{XY} \end{bmatrix} \tag{3.61}$$

Finally, the four-component Dirac equation in the restricted-kinetic-balanced condition is expressed as

$$\begin{bmatrix} \mathbf{F}^{LL} & \mathbf{F}^{LS} \\ \mathbf{F}^{SL} & \mathbf{F}^{SS} \end{bmatrix} \begin{bmatrix} \mathbf{C}_L^+ & \mathbf{C}_L^- \\ \mathbf{C}_S^+ & \mathbf{C}_S^- \end{bmatrix} = \begin{bmatrix} \mathbf{I} \otimes \mathbf{S} & \mathbf{0} \\ \mathbf{0} & \mathbf{I} \otimes \frac{1}{2mc^2}\mathbf{T} \end{bmatrix} \begin{bmatrix} \mathbf{C}_L^+ & \mathbf{C}_L^- \\ \mathbf{C}_S^+ & \mathbf{C}_S^- \end{bmatrix} \begin{bmatrix} \boldsymbol{\epsilon}^+ & \mathbf{0} \\ \mathbf{0} & \boldsymbol{\epsilon}^- \end{bmatrix} \tag{3.62}$$

where $\mathbf{S}$ and $\mathbf{T}$ are the one-component overlap and kinetic matrices. $\boldsymbol{\epsilon}^+$, $\boldsymbol{\epsilon}^-$ are the eigenvalues with corresponding molecular orbitals $\begin{bmatrix} \mathbf{C}_L^+ \\ \mathbf{C}_S^+ \end{bmatrix}$ and $\begin{bmatrix} \mathbf{C}_L^- \\ \mathbf{C}_S^- \end{bmatrix}$ for positive- and negative-energy solutions, respectively.

Although the resulting integral-density contraction scheme during the four-component Fock-build is complicated, there are many unique advantages that lead to a highly efficient four-component method:

- The algorithm presented here achieves the maximal component- and spin-separation so that all contractions are essentially done in the one-component framework. In such a framework, terms that use the same type of electron-repulsion integrals can be effectively combined, possibly leading to a minimal FLOP-count algorithm.

- The Pauli matrix representation is ideal for including external electromagnetic field perturbations, because the effects of each component of the electromagnetic field are completely decoupled and spin/component-separated. [155, 156, 157, 158, 159]

- We also argue that the spin-separation in Pauli matrix representation allows for a clear understanding of how different types of spin physics, including two-electron spin-free, spin-orbit, and spin-spin interactions are manifested in electronic structure and light-matter coupling.

In the next section, we substantiate these claims with more details of the computational implementation, and an analysis of computational cost.

3.3 Benchmark and Discussion

3.3.1 Analysis of Computational Cost

As for any form of four-component DHF implementation, the assembly of integrals needed for the Pauli matrix formalism presented in this work also involves computations of two-center 2nd-derivatives of electron repulsion integrals (ERIs). If the $(SS|SS)$ Dirac-Coulomb term is requested, additional four-center 4th-derivatives of ERIs are needed. Although there is no need to assemble real-valued ERIs into two-spinor or four-spinor forms, it is necessary to construct unique integrals needed throughout the Dirac-Coulomb-Gaunt Fock build. For example, in addition to the normal ERI terms, $(\mu\nu|\kappa\lambda)$, four integrals, including $\boldsymbol{\nabla} \cdot \boldsymbol{\nabla}$, $(\boldsymbol{\nabla} \times \boldsymbol{\nabla})_x$, $(\boldsymbol{\nabla} \times \boldsymbol{\nabla})_y$, and $(\boldsymbol{\nabla} \times \boldsymbol{\nabla})_z$, are constructed from two-center ERI 2nd-derivatives in order to form the Dirac-Coulomb Fock matrix with an algorithm using an optimal FLOP count. In the current development, a total of 24 unique integrals are constructed from ERI and ERI 2nd-derivatives in order to form the Dirac-Coulomb-Gaunt Fock matrix without the $(SS|SS)$ contributions.

The following discussion and cost analyses are based on the in-core formalism in which all unique integrals are computed and stored in memory. The computational cost for the $(SS|SS)$ contribution is separated from the Dirac-Coulomb term as it is often ignored in practical calculations. The four-spinor form of the Dirac-Fock build is not considered here because it is mathematically more computationally expensive than those in the two-spinor, scalar basis, or Pauli matrix representation. In the case of the scalar basis formalism, we assume the small component basis is generated through the action of the momenta $\mathbf{p}$ or the unrestricted-kinetic-balance (UKB) condition. For the UKB scalar-basis based method, the following analysis assumes an algorithm of optimal FLOP and storage with all integrals in the scalar one-component form. A detailed analysis for the UKB scalar basis is presented in

Table 3.1: Analysis of memory requirement in terms of the equivalent number of unique real-valued one-component 4-index electron-repulsion-integral tensors needed for forming the four-component Dirac-Coulomb-Gaunt Hamiltonian. N number of atomic basis functions are used in this estimate. Restricted-kinetic-balanced (RKB) basis is compared with the unrestricted-kinetic-balanced (UKB) scalar basis. Dense matrices with no integral or matrix symmetry are considered.

Four-Component Scheme	Equivalent # of Real-Valued N^4 ERI Tensors			Total
	Dirac-Coulomb[a]	$(SS\|SS)$	Gaunt	
Pauli Matrix RKB Basis	5	31	19	55
Two-Spinor RKB Basis[b]	64	32	64	160
UKB Scalar Basis[c]	7.25	39	6.25	52.5

[a] Dirac-Coulomb without the $(SS|SS)$ contribution.

[b] Two-spinor integrals are stored as complex-valued quantities, occupying two double-precision storage.

[c] For scalar-basis based approach, we assume there are $\frac{N}{2}$ number of $L > 0$ atomic basis function in this set, resulting in a total of $2.5N$ number of smaller component basis functions. For the memory requirement estimation, see Appendix C.

Appendix C.

Table 3.1 and 3.2 lists the estimated computational costs in terms of memory requirement and FLOP count for forming the Dirac-Fock matrix from assembled integrals, comparing several different four-component formalisms. In this estimate, we used a Kramers-unrestricted condition where all four Pauli components are non-zero. The cost analysis for UKB scalar basis is based on the assumption that 50% of the basis functions have a non-zero angular momentum.

For all methods considered in Tab. 3.1 and Tab. 3.2, the computational cost of real-valued ERI and ERI derivatives are considered equivalent. We also assume the computational cost of assembling the ERI and ERI derivatives into the corresponding two-spinor form is the same as assembling them into unique one-component integrals needed for the Pauli matrix formalism. With these valid assumptions, the difference in computational cost for all four-component implementations comes from the different ways of computing the integral-density

Table 3.2: Analysis of FLOP count in double-precision operations for forming the four-component Dirac-Coulomb-Gaunt Hamiltonian. N number of atomic basis functions are used in this estimate. Restricted-kinetic-balanced (RKB) basis is compared with the unrestricted-kinetic-balanced (UKB) scalar basis. FLOP counts are separated into Coulomb $\mathbf{J}$ and exchange $\mathbf{K}$ contractions. Dense matrices with no integral or matrix symmetry are considered.

Four-Component Scheme	Number of Integral-Density Contractions $(\mathbf{J}, \mathbf{K})$			Total FLOP[b]
	Dirac-Coulomb[a]	$(SS\|SS)$	Gaunt	
Pauli Matrix RKB Basis	$(9, 20)$	$(12, 33)$	$(28, 57)$	$636N^4$
Two-Spinor RKB Basis	$(48, 48)$	$(16, 16)$	$(64, 64)$	$2048N^4$
UKB Scalar Basis[c]	$(54, 54)$	$(156, 156)$	$(25, 100)$	$2180N^4$

[a] Dirac-Coulomb without the $(SS|SS)$ contribution.

[b] Floating point operation (FLOP) is defined as an arithmetic procedure $(+, -, \times, \mathbf{\nabla}\cdot)$ of two double-precision numbers. Because integrals for Pauli matrix RKB basis and UKB scalar basis are stored as real-valued matrices and density matrices are complex-valued, each contraction step requires $4N^4$ FLOPs. For two-spinor RKB basis, because integrals are complex-valued, each contraction step requires $8N^4$ FLOPs.

[c] For scalar-basis based approach, we assume there are $\frac{N}{2}$ number of $L > 0$ atomic basis function in this set, resulting in a total of $2.5N$ number of smaller component basis functions. For the estimation of operation count, see Appendix C.

contractions in order to form the Dirac-Fock matrix.

For the Pauli matrix formalism presented in this work, and the method based on the UKB scalar basis, instead of assembling ERI and ERI derivatives into the two-spinor form, all integrals remain in the one-component form. As a result, for storing integrals in memory, the Pauli matrix and scalar basis formalisms have a smaller memory storage requirement as shown in Tab. 3.1.

As discussed previously, the maximal component- and spin-separation in the Pauli spinor representation allows for combining all integral-density contractions of a same integral type. As a result, the four-component Dirac equation in the Pauli matrix representation is likely to be the method with minimal FLOP count. Table 3.2 shows the FLOP count for each type of

J and **K** contractions with the density. For the Dirac-Coulomb terms we see that the Pauli matrix formalism has the minimum FLOP count for both **J** and **K** matrices compared to the two-spinor basis and the UKB scalar basis by a factor of $\frac{1}{2}$ or smaller. For the $(SS|SS)$ contribution, the **J** FLOP count of the Pauli matrix formalism is the minimum of the three, but the **K** FLOP count is more than the two-spinor formalism. The UKB scalar basis ends up being more than 5-10 times as expensive overall than the Pauli matrix, or two-spinor formalism. The UKB scalar basis method is particularly disadvantageous for the $(SS|SS)$ term simply because the large N_S^4 operation. Finally, for the Gaunt term we see that the UKB scalar basis has the lowest number of FLOPs for the **J** contraction, but the Pauli matrix formalism has the lowest number for the **K** contraction.

While there isn't one single four-component scheme that has the lowest number of FLOPs for every kind of contraction term, the Pauli matrix formalism is optimal in 4 out of 6 types of integral-density contractions considered here. We see that after including all of the contracted terms for the Dirac-Coulomb-Gaunt Hartree–Fock procedure, the Pauli matrix formalism has the best scaling FLOP prefactor by a factor of $\frac{1}{3}$ or smaller, where the two-spinor and UKB scalar form are comparable.

3.3.2 Integral and Contraction Timings

For the following timing benchmarks, we use a lanthanum dimer with a bond distance of 3.0 Å and the uncontracted ANO-RCC basis set. [160, 161, 162] Computations were performed on an Intel® Xeon® W 2.5 GHz CPU. Additionally, Chronus Quantum was compiled using the Clang Compiler version 12.0.0. Additionally, the integrals are computed using the LIBCINT library [163], with a development version of the Chronus Quantum electronic structure software package. [164] Note that the timings serve the purpose to show the relative costs of computationally dominant steps in Dirac Hartree–Fock build. They should not be used as calibrations of the performance of the program as the code optimization is beyond the scope of this article.

While Tab. 3.2 analyzes the computational cost at the theoretical limit in the absence of

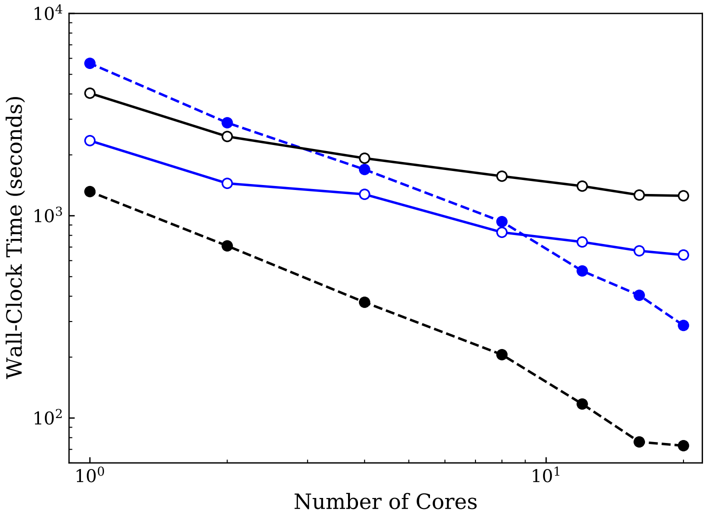

Figure 3.1: Wall-clock timings for the computation of integrals (solid lines with empty circles) and the duration of the AO-direct density-integral contraction (dashed lines with filled circles) for the lanthanum dimer using the uncontracted ANO-RCC basis. The time-reversal symmetry is turned off. The Schwarz integral screening threshold of 10^{-12} is used. The timings for the Dirac-Coulomb and the Gaunt two-body terms, shown in black and blue, respectively, were collected from a single DHF build. Logarithmic wall-clock times are plotted against logarithmic number of CPU cores. The lines are included in this plot are linear interpolations to guide the eye.

all symmetries, benchmark calculations presented here take advantage of integral symmetries and matrix hermiticity. Note that all calculations assume the Kramers' unrestricted case unless otherwise noted. Although both the Dirac-Coulomb (without $(SS|SS)$) and Gaunt integrals are two-center second derivatives, the Gaunt integrals have a 2-fold symmetry whereas the integral symmetry is 4-fold for Dirac-Coulomb integrals (without $(SS|SS)$). The four-center derivatives of the $(SS|SS)$ term has an 8-fold symmetry. Fig. 3.1 shows the wall-clock time for the lanthanum dimer system per number of cores and for each type of two-body integral and density contractions respectively, based on the Pauli spinor representation formalism presented here. For DC-HF, the $(SS|SS)$ term is also included.

The ratio of the contraction times on a single CPU core for the Dirac-Coulomb and the Gaunt term is $\sim 1 : 4.3$. This ratio is close to the theoretical limit of DCG in Pauli representation when integral and matrix symmetries are considered. The lower computational cost for DC contraction is mainly due to the higher symmetry of the underlying integrals. The ratio of the computational cost for calculating the integrals needed for the Dirac-Coulomb and the Gaunt terms is $\sim 1.7 : 1$. In addition to two-center second derivatives, the Dirac-Coulomb term also includes the four-center fourth-derivatives of integrals arising from the $(SS|SS)$ contribution. As a result, the Dirac-Coulomb integrals are more computationally expensive than those for the Gaunt term. The overall ratio of the computational cost, including both integral evaluation and contraction, for the Dirac-Coulomb and the Gaunt terms is $\sim 1 : 1.5$ on a single CPU core.

Fig. 3.1 also shows that on a single CPU core the cost of computing the Dirac-Coulomb term is dominated by the integral evaluations, whereas it is the contraction step that is the more expensive step for the Gaunt term. The timing ratios between the integral evaluation and contraction are $3 : 1$ and $1 : 2.4$ for the Dirac-Coulomb and the Gaunt terms, respectively, on a single CPU core. The times for Dirac-Coulomb and Gaunt contractions decrease roughly $1/n$ for every increase in n CPU cores used. The computational cost of calculating two-electron repulsion integrals and integral derivatives also decreases when increasing the number of CPU cores computing in parallel. The contraction step in AO-direct benefits more from the parallelization, as it is FLOP-bound. At around 8 cores, the cost of the Gaunt contraction decreases below the the cost of integral derivative evaluations.

Next, Fig. 3.2 shows the timing comparison for building the Dirac-Hartree-Fock matrix with the Dirac-Coulomb operator using the RKB spinor and RKB Pauli representations respectively. Computations were performed on an Intel® Xeon® Platinum 8160 CPU. Additionally, Chronus Quantum was compiled using the Intel® C++ Compiler version 19.0.1.144. RKB spinor calculations were performed using PySCF. [165] In order to compare these implementations on the same footing, the calculations in our RKB spinor method for these results were computed utilizing time-reversal symmetry, and the contractions are done using an atomic-orbital direct scheme. The observed ratio of wall-clock times between the two representations for linear Au chains agrees with the time complexity analysis in Tab. 3.2, where the RKB spinor representation is roughly 3 times slower than the RKB Pauli method.

Additionally, we present timings for the Dirac-Fock build in our RKB Pauli representation in Tab. 3.2, split into both the density contraction and integral build times for a 24-core parallel calculation. To showcase this comparison we used bulky Au cluster calculations from Au_{20} to Au_{40}. Since the RKB Pauli representation greatly reduces the density-integral contraction time, it can be seen that the computational cost of the integral build step dominates the overall computational cost. For a Dirac-Coulomb calculation with $\sim$6000 basis functions, the RKB Pauli based density contraction only takes a little more than 2 hours on a 24-core workstation (2.5 GHz Intel Xeon W).

Including relativistic two-electron contributions is by no means computationally cheap, especially including the Gaunt term which dominates the cost by being an order of magnitude greater than both the Dirac-Coulomb and Bare-Coulomb integrals. However, the method presented here is possibly the optimal algorithm for DHF. Integral and contraction acceleration techniques, such as the fast-multipole-method and density-fitting, can be applied to reduce the computational cost further based on the RKB Pauli formalism.

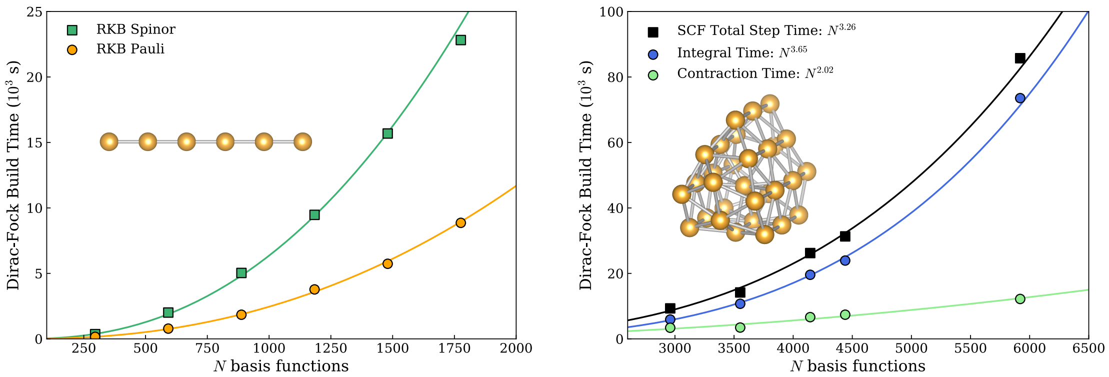

Figure 3.2: (**Left**) Single-core timing comparison for building the Dirac-Hartree-Fock matrix with the Dirac-Coulomb operator without the $(SS|SS)$ term using the RKB spinor and the RKB Pauli representation, respectively. A series of Au linear chains (Au_2 to Au_{12}) were used for this test with the uncontracted Jorge-DZ-DKH basis using an AO direct algorithm. A Schwarz screening threshold of 10^{-12} is used in each calculation. (**Right**) 24-core parallel performance of the RKB Pauli Dirac-Hartree-Fock algorithm with the Dirac-Coulomb operator for building the Dirac-Hartree-Fock matrix. A series of Au clusters (Au_{20} to Au_{40}) were used for this result. The RKB spinor results were computed using PySCF [165] and the RKB Pauli results were computed in ChronusQ. [164]

3.3.3 Atomic Periodic Trend

In the data presented in this section, the integrals and the derivatives of integrals with respect to nuclear coordinates are computed with the LIBINT and LIBCINT libraries. [166, 163] Additionally, the four-component Dirac Hartree–Fock formalism is implemented in a development version of the Chronus Quantum software package. [164] The speed of light constant used in the following calculations is 137.03599967994 a.u.

The main purpose of this work is to introduce the methodological foundation and formalism of the four-component Dirac Hartree–Fock equation in the Pauli spinor representation. The four-component framework is validated by comparing the computed energies using the analytical results of the Dirac equation for hydrogenic atoms, shown in Appendix D, and basis set limit tests, shown in Appendix E. When a large uncontracted basis set is used, the calculations show a percent error on the order of 10^{-3}%. For benchmarking, we focus on analyzing and comparing the ground state DHF energies with different levels of relativistic two-electron interactions. In order to analyze the importance of relativistic two-electron corrections in Dirac Hartree–Fock, we introduce a Bare-Coulomb approximation in matrix form, *i.e.* only the first term in Eq. 3.13 is included.

Several atomic series are selected from the periodic table, including the halogens, the coinage metals, and the lanthanides. In this way we can compare each relativistic two-body interaction contribution as a function of element charge, Z, although this separation of terms is not unique to the RKB Pauli formalism. In this section we report the ground state energies of these atoms using the uncontracted ANO-RCC basis set [160, 161, 162]. The SCF energies for each atom with different levels of relativistic two-electron interaction are shown in Tab. 3.4 for each selected atom.

From the computed data, we see that with each successive correction to the bare non-relativistic Coulomb interaction, the ground state energy increases. This is expected as they all arise from the $\frac{1}{r_{12}}$ two-electron repulsion interaction. The relativistic two-electron interaction increases much faster as Z increases in the same element group down the periodic table than the trend across a same row (such as the lanthanides). By comparing Dirac-Coulomb calculations using the uncontracted ANO-RCC basis with the previously published numerically exact values, [167, 168] the observed errors are on the order of $10^{-7}\%$ to $10^{-5}\%$, showing excellent agreement.

The periodic trends of the relativistic two-electron interactions are plotted in Fig. 3.3. For each data set, a least squares power law fit was applied and displayed as the dashed lines for each subplot in Fig. 3.3. Fig. 3.3A shows that the Dirac-Coulomb and Gaunt contributions to the two-body interaction increase polynomially as Z increases. The Dirac-Coulomb term exhibits a near quartic growth with respect to Z, while the Gaunt term has a $Z^{3.49}$ dependence. It is more meaningful to analyze the energetic contributions in terms of the percentage of the total energy. In Fig. 3.3B, the percent contribution is evaluated with respect to the Bare-Coulomb DHF energy. This plot compares the growth behaviors of relativistic two-electron interactions relative to that exhibited by the Bare-Coulomb ground state energy. It is quite surprising to see that the Gaunt contribution in terms of the percent

Table 3.3: Ground state energies (Hartrees) for selected atoms with the energetic contributions of Dirac-Coulomb and Gaunt terms, computed as $\Delta E^{DC} = E^{DC} - E^{BC}$ and $\Delta E^{G} = E^{DCG} - E^{DC}$ where E^{DCG}, E^{DC}, and E^{BC} are the SCF energies of Dirac-Coulomb-Gaunt, Dirac-Coulomb, and Bare-Coulomb calculations respectively. The uncontracted Jorge-DZP-DKH basis with finite width nuclei was used for this dataset.

Atom	Bare-Coulomb	Dirac-Coulomb^{a}	ΔE^{DC}	Dirac-Coulomb-Gaunt^{a}	ΔE^{G}
Halogen Series					
F	−99.528	−99.492	0.036	−99.480	0.012
Cl	−461.390	−460.931	0.459	−460.814	0.117
Br	−2612.740	−2604.942	7.798	−2603.512	1.430
I	−7155.237	−7115.864	39.374	−7109.836	6.028
Lanthanide Series					
La	−8545.797	−8493.654	52.143	−8485.888	7.766
Ce	−8916.760	−8860.851	55.908	−8852.602	8.250
Pr	−9297.599	−9237.732	59.866	−9229.020	8.713
Nd	−9689.322	−9625.204	64.118	−9616.079	9.125
Pm	−10090.308	−10022.111	68.196	−10012.300	9.811
Sm	−10502.118	−10429.220	72.897	−10418.844	10.376
Eu	−10924.007	−10846.502	77.505	−10835.538	10.963
Gd	−11357.439	−11274.727	82.712	−11263.145	11.582
Tb	−11800.963	−11712.893	88.070	−11700.678	12.214
Dy	−12254.985	−12161.432	93.553	−12148.561	12.871
Ho	−12720.932	−12621.463	99.469	−12607.898	13.565
Er	−13197.900	−13092.311	105.589	−13078.031	14.281
Tm	−13686.192	−13574.174	112.018	−13559.171	15.003
Yb	−14185.430	−14066.771	118.658	−14050.981	15.790
Lu	−14696.968	−14571.361	125.607	−14554.768	16.593
Coinage Metal Series					
Cu	−1657.086	−1653.357	3.729	−1652.612	0.745
Ag	−5339.277	−5314.617	24.660	−5310.646	3.971
Au	−19229.025	−19035.495	193.530	−19011.304	24.191

Table 3.4: Ground state energies (Hartrees) for selected atoms with the energetic contributions of Dirac-Coulomb and Gaunt terms, computed as $\Delta E^{DC} = E^{DC} - E^{BC}$ and $\Delta E^{G} = E^{DCG} - E^{DC}$ where E^{DCG}, E^{DC}, and E^{BC} are the SCF energies of Dirac-Coulomb-Gaunt, Dirac-Coulomb, and Bare-Coulomb calculations respectively. The uncontracted ANO-RCC basis with finite width nuclei was used for this dataset.

Atom	Bare-Coulomb	Dirac-Coulomb	ΔE^{DC}	Dirac-Coulomb-Gaunt	ΔE^{G}
Halogen Series					
F	−99.540917	−99.504738	0.036179	−99.492763	0.011975
Cl	−461.406677	−460.947164	0.459512	−460.830018	0.117146
Br	−2612.852939	−2605.033836	7.819103	−2603.603969	1.429867
I	−7155.395184	−7115.798492	39.596692	−7109.770036	6.028456
Lanthanide Series					
La	−8546.215923	−8493.657945	52.557978	−8485.891031	7.766914
Ce	−8917.383681	−8861.043868	56.339814	−8852.800219	8.243649
Pr	−9298.457621	−9238.164865	60.292756	−9229.419749	8.745116
Nd	−9689.682825	−9625.317052	64.365773	−9616.050622	9.266430
Pm	−10091.178921	−10022.330954	68.847967	−10012.520248	9.810706
Sm	−10502.861365	−10429.356216	73.505149	−10418.975555	10.380661
Eu	−10925.261820	−10846.946858	78.314963	−10835.981295	10.965563
Gd	−11358.014014	−11274.744433	83.269580	−11263.160904	11.583529
Tb	−11801.625306	−11712.825124	88.800182	−11700.608150	12.216974
Dy	−12256.214858	−12161.776442	94.438417	−12148.896505	12.879937
Ho	−12721.922596	−12621.573979	100.348617	−12608.005042	13.568938
Er	−13198.887030	−13092.441227	106.445803	−13078.151685	14.289542
Tm	−13687.098882	−13574.398156	112.700726	−13559.365996	15.032160
Yb	−14187.311321	−14067.663235	119.648086	−14051.865403	15.797831
Lu	−14699.426395	−14572.526419	126.899976	−14555.924058	16.602362
Coinage Metal Series					
Cu	−1657.190117	−1653.453398	3.736719	−1652.708252	0.745146
Ag	−5339.393098	−5314.625699	24.767399	−5310.654463	3.971236
Au	−19231.541954	−19035.579049	195.962905	−19011.375550	24.203499

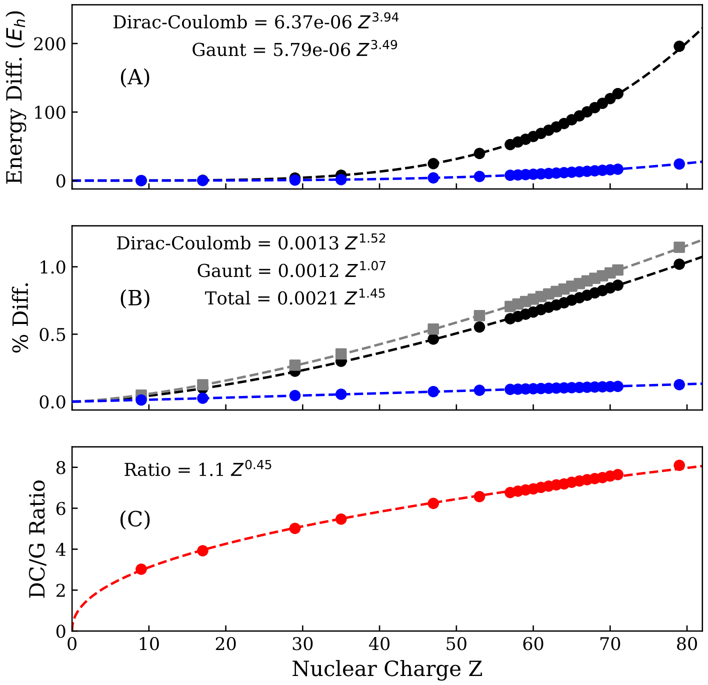

Figure 3.3: (A) Energetic contributions of Dirac-Coulomb (black) and Gaunt (blue) terms, computed as $\Delta E^{DC} = E^{DC} - E^{BC}$ and $\Delta E^{G} = E^{DCG} - E^{DC}$ where E^{DCG}, E^{DC}, and E^{BC} are the SCF energies of Dirac-Coulomb-Gaunt, Dirac-Coulomb, and Bare-Coulomb calculations. (B) Percentage of energy contribution of each two-electron term compared to the Bare-Coulomb ground state DHF energy, presented as $\frac{\Delta E^{DC}}{E^{BC}} \times 100\%$ and $\frac{\Delta E^{G}}{E^{BC}} \times 100\%$. The gray squares correspond to the total relativistic contribution which is $\frac{\Delta E^{DC}+\Delta E^{G}}{E^{BC}} \times 100\%$ (C) The ratio of the energy contribution of the Dirac-Coulomb term vs. the Gaunt term $\frac{\Delta E^{DC}}{E^{G}}$ as a function of increasing nuclear charge for the neutral atom series. The power law fit is displayed as the dashed line, corresponding to the equation in the top left corner of each panel.

of the total energy is almost linear with respect to Z, suggesting that the relativistic Gaunt interaction behaves almost like the Bare-Coulomb term. Fig. 3.3B also shows that the Dirac-Coulomb contribution exhibits a much faster growth behavior than both the Gaunt and the Bare-Coulomb interaction. As a result, Fig. 3.3C shows that the the Dirac-Coulomb interaction is a factor of $3-5$ times larger than the Gaunt contribution for light elements ($Z < 40$), and increases towards a ratio of ~ 9 near the end of the periodic table. As Z increases, this ratio increases as $\sqrt{Z}$ approximately.

3.3.4 Coinage Metal Dimers

In this section, the equilibrium bond lengths and dissociation energies for the coinage metal dimer series including Cu_2, Ag_2, Au_2, are computed. The uncontracted ANO-RCC basis set [161] is used for all calculations throughout this section. For these results we would like to emphasize that agreement with experimental data should not be expected due to the lack of electronic correlation. [169] Analyses presented here aim to provide a qualitative understanding of how the Dirac-Coulomb and Gaunt two-electron relativistic effects change molecular properties compared to the non-relativistic results.

Potential energy scans are carried out using the non-relativistic Hartree-Fock (NR-HF), Dirac-Coulomb, and Dirac-Coulomb-Gaunt Hamiltonians to find the equilibrium bond length for each dimer and level of theory, reported in Tab. 3.5. Additionally, the bond dissociation energy (D_e) is computed as $D_e = 2E_{\text{atom}} - E_{\text{dimer}}$, where E_{atom} is the atomic energy and E_{dimer} is the energy of the dimer at the equilibrium bond length. The theoretical and experimental results for the dissociation energies are presented in Tab. 3.6.

Table 3.5 shows that the Dirac-Coulomb computed bond length contracts for all dimers studied here relative to the non-relativistic result. This is mainly due to the core-electron contraction arising from the scalar relativistic effects. [175] The main takeaway from the equilibrium bond length calculations in Tab. 3.5 is that the Gaunt correction to the Dirac-Coulomb two-electron interaction introduces an additional electron-electron repulsion that elongates the bond length by 0.001–0.004Å. In Tab. 3.6 the Gaunt correction shows a

Table 3.5: The equilibrium bond lengths for each dimer system are reported in Å. The experimental bond lengths are reported under "Exp." The uncontracted ANO-RCC basis is used for all calculations.

Dimer	NR-HF	Dirac-Coulomb	Dirac-Coulomb-Gaunt	Exp.
Cu_2	2.409	2.402	2.403	2.22 [Ref. [170]]
Ag_2	2.770	2.701	2.703	2.53 [Ref. [171]]
Au_2	2.830	2.586	2.590	2.47 [Ref. [172]]

Table 3.6: Equilibrium bond dissociation energies (D_e) for each dimer system are reported in eV. The experimental dissociation energies are reported under "Exp." The uncontracted ANO-RCC basis is used for all calculations.

Dimer	NR-HF	Dirac-Coulomb	Dirac-Coulomb-Gaunt	Exp.
Cu_2	0.600	0.549	0.547	2.01±0.08 [Ref. [170]]
Ag_2	0.486	0.480	0.477	1.65±0.03 [Ref. [173]]
Au_2	0.659	0.865	0.855	2.29±0.02 [Ref. [174]]

systematic trend that lowers the bond dissociation energy on the order of $\sim$10 meV. This observation suggests that the Gaunt term gives rise to a small yet increasingly important repulsive correction to the bond dissociation energy as the atomic number increases.

3.4 Conclusion and Perspective

In this work, we introduced a computationally efficient four-component Dirac Hartree–Fock (DHF) formalism within the maximally component- and spin-separated Pauli spinor representation in the restricted-kinetic-balance condition (denoted "RKB Pauli"). A minimal FLOP count algorithm is developed for the density contraction with the relativistic electron repulsion integrals. All of the required ingredients for this implementation can utilize the non-relativistic atomic orbital electron repulsion integrals and their gradients stored in the one-component form without going through the two-spinor basis construction. Additionally, a detailed cost analysis was presented and compared to other four-component algorithms.

Numerical tests shows that the RKB Pauli representation is physically equivalent to the RKB spinor representation, but computationally much cheaper.

Additionally, the contribution of relativistic two-electron interactions across the periodic table were analyzed. As expected, both Dirac-Coulomb and Gaunt terms increase the total energy, with the Dirac-Coulomb contribution exhibiting a faster growth as Z increases. The importance of the Gaunt interaction to the total atomic energy increases linearly with respect to the non-relativistic Coulomb contribution while the Dirac-Coulomb term becomes more important relative to the Gaunt term as Z increases.

The RKB Pauli formalism of the four-component DHF Hamiltonian presented in this work provides a computationally efficient way to develop relativistic electronic structure theories. Although the final mathematical working expressions are more complicated than those in two-spinor or scalar basis, we are rewarded with an optimal algorithm with a minimal memory requirement and total FLOP count. This work lays the computational foundation for practical applications of four-component DHF, and future developments of correlated wave function methods in the four-component domain.

When it comes to computing bond lengths and dissociation energies for metal dimers, our results show that the Gaunt correction introduces an additional electron-electron repulsion that slightly elongates the bond length and increases the bond dissociation energy. Additionally, as expected, electron correlation is vital for making quantitative comparisons with experimental values.

For this study, we primarily focused on comparing the computational performance of DHF methods utilizing fully uncontracted basis sets. While introducing contracted basis sets can reduce the resulting DHF matrix size, using *standard* contracted basis sets in 4-component DHF is not recommended. [176, 177] Naively fixing the contraction coefficients for both the large and small components of the wave function can lead to variational collapse. [177, 153] One approach to mitigate this problem is to use the atomic balance basis, proposed and pioneered by Visscher and Liu, [177, 153] which allows the small and large component bases to have their own contraction coefficients derived from an atomic calculation with the uncontracted basis. However, the best way to extend the present method to this case is currently under investigation.

Chapter 4

SIMULATING EFFECTIVE QUANTUM ELECTRODYNAMICS ON QUANTUM COMPUTERS

In recent years simulations of chemistry and condensed materials has emerged as one of the preeminent applications of quantum computing offering an exponential speedup for the solution of the electronic structure for certain strongly correlated electronic systems. To date, most treatments have ignored the question of whether relativistic effects, which are described most generally by quantum electrodynamics (QED), can also be simulated on a quantum computer in polynomial time. Here we show that effective QED, which is equivalent to QED to second order in perturbation theory, can be simulated in polynomial time under reasonable assumptions while properly treating all four components of the wavefunction of the fermionic field. In this chapter, a detailed analysis of such simulations in position and momentum basis using Trotter-Suzuki formulas is provided. Further, concrete gate counts for simulating a relativistic version of the uniform electron gas that shows challenging problems can be simulated using fewer than 10^{13} non-Clifford operations is provided. Additionally a detailed discussion of how to prepare MRCISD states in effective QED is included. Finally, the planewave cutoffs needed to accurately simulate heavy elements such as gold is estimated in the final section. This chapter is adapted from T. F. Stetina, A. Ciavarella, X. Li, and N. Wiebe, "Simulating Effective QED on Quantum Computers," *arXiv preprint*, arXiv:2101.00111, with permission from the authors. At the time of writing this thesis, this work is currently submitted for peer review.

4.1 Introduction

Since its inception in the early 1980's [5], quantum computers have been a highly anticipated technology for simulating the laws of physics. Richard Feynman, known mainly for his work contributing to the development of quantum electrodynamics (QED), the quantum field theory of electromagnetism, was also a pioneer of the idea to use real quantum systems for computation [6]. Bringing these two major scientific ideas together, we take a look at how an effective version of QED can be simulated on a universal quantum computer with applications to many body material and molecular systems.

A great body of literature exists that shows that quantum computers can provide exponential advantages for certain *ab initio* electronic structure calculations [178, 13, 19, 179, 180, 181]. The utility of quantum based devices stems from their ability to directly simulate the dynamics of the Coulomb Hamiltonian without making the approximations that are usually required to make their classical counterparts efficiently tractable. However, despite these existing approaches to quantum chemistry, often times they still fall short of being theoretically correct, since the Hamiltonian is still approximate. For example, most approaches to solving the electronic structure problem utilize the Born-Oppenheimer approximation, which assumes that the nuclear wavefunction is uncoupled from the electronic wave function. While this approximation has received substantial attention in recent quantum simulation work [182, 183], comparably less progress has been made to properly treat relativistic effects in electronic structure simulations [184, 185], which give rise to orbital contractions/expansions, spin-orbit coupling, modification of electron-electron repulsion and more [186, 187].

Much work has been done on the quantum simulation of relativistic field theories [188, 189, 190, 191, 192, 193, 194, 195, 196, 197, 198, 199, 200, 201, 202, 203, 204, 205, 206, 207, 208], including a recent paper highlighting lattice gauge theory QED simulations [209], however the absence of relativity from the majority of existing quantum chemistry simulation algorithms raises both practical and a theoretical questions. First, relativistic effects are significant for the ground states of some molecules. For example, atomic gold and uranium dimers both have significant relativistic effects that need need to be considered to accurately model their ground state. Without the ability to simulate these effects, quantum computers face a fundamental precision limit that prevents the proper physics from being simulated within arbitrary accuracy, thereby limiting the primary advantage of quantum computers. While previous work has addressed relativistic Hamiltonian simulation using the Dirac Hartree-Fock method [210], this relies on the no-pair approximation where only electronic orbitals are used from the mean field, ultimately leading to the same form of the Coulomb Hamiltonian, but with different coefficients during quantum simulation. While this no-pair relativistic Hamiltonian will obviously capture a portion of relativistic effects being ignored by the non-relativistic Coulomb Hamiltonian, the positronic manifold, and subsequently quantum electrodynamical (QED) effects are ignored. Some common consequences of QED effects include the Lamb shift, change in ionization energies, energy shifts in absorption spectra, and more. A review on relativistic and QED effects in atoms and molecules can be found in [211]. The leading order source of these QED effects in atomic and molecular material systems are typically known as vacuum polarization, and electron self-energy. These effects arise from the realization that the groundstate of the molecule is a joint groundstate of both the fermionic as well as bosonic fields and is perhaps most striking with the vacuum polarization term which describes the energy contributions from virtual electron/positron productions interacting with the boson field. Going beyond the no-pair approximation for molecular and material systems in general is sparse in the current literature, due to its high computational cost classically and its theoretical complexity. Due to this complexity of including both fermionic and photonic fields for QED corrections in molecular systems, a convenient approximation can be used to neglect the use of photonic modes in exchange for an effective field theory known as effective QED or eQED [212, 213]. By integrating out photonic degrees of freedom, the electronic and positrionic interaction contributions are kept without the added complication of tracking photonic modes present in the vacuum.

The second aspect of why we need to consider including relativity stems from the Quantum Complexity-Theoretic Church-Turing Thesis. This belief, widely held in the quantum information community, is that any physically realistic model of computing can be efficiently simulated by a quantum Turing machine. Viewing physics as providing an analog computational model, and if this statement is correct, then quantum computers must be able to simulate all physical processes in polynomial time. Thus, understanding whether quantum computers can solve the electronic structure problem in polynomial time in the presence of relativistic effects is important since it sheds light on the validity of the Quantum Complexity-Theoretic Church-Turing Thesis.

In this work, we focus on a many-body Hamiltonian perspective and show that quantum computers can efficiently sample from the energy eigenvalues for an approximation to quantum electrodynamics known as eQED. This formulation of quantum electrodynamics is found from expanding the Feynman path integrals that describe quantum electrodynamics to second order from which a Hamiltonian can be derived for only the electronic and positronic degrees of freedom. We specifically provide algorithms for simulating these dynamics in both position and momentum basis both with and without an external vector potential. We then analyze the cost of performing such a simulation using Trotter-Suzuki simulation methods both theoretically and numerically for a relativistic version of the free-electron gas (which we denote rellium). While the rellium model by itself may be considered to be a toy model from an *ab initio* physics simulation perspective, we examine this model for its novel Hamiltonian terms that arise in the context of quantum simulation algorithms, that will be present in more sophisticated relativistic many-body systems. In addition, we discuss how to prepare multi-reference configuration singles and doubles (MRCISD) approximations to the ground state for eQED which is necessary because the strong correlations present in systems where eQED is needed will often make elementary approximations such as Hartree-Fock inaccurate. Finally, we present a simple cost estimate for simulating a gold atom using planewaves in eQED, and context for future work involving QED and relativistic effects in quantum simulation.

4.2 Review of eQED

Quantum electrodynamics (QED) is the quantum field theory that describes the electromagnetic interactions of electrons and positrons. QED is formulated in terms of a four component fermionic spinor field, $\psi_a(x)$ that creates electrons and annihilates positrons and a 4-potential, $A_\mu(x)$, that creates and annihilates photons. It should be noted that the interpretation of $\psi_a(x)$ is not the same as the interpretation of the electron field in non-relativistic field theory. In non-relativistic field theory, applying the electron field operator to a state simply removes a single electron, but in the relativistic case, applying $\psi_a(x)$ to a state will create a superposition of a state with one less electron and a state with one more positron. For this reason, $\psi_a(x)$ can be interpreted as an operator that increases the electric charge of the state by 1. For relativistic chemical physics, the primary goal is to simulate the motion of electrons and positrons, therefore it would be convenient to have a formulation of QED without the photon degrees of freedom. In other words, the goal of effective QED is to derive a Hamiltonian H_{eQED}, such that

$$\langle\phi_f| e^{-iH_{QED}t} |\phi_i\rangle = \left\langle\tilde{\phi}_f\middle| e^{-iH_{eQED}t} \middle|\tilde{\phi}_i\right\rangle \tag{4.1}$$

where $|\phi_i\rangle$ and $|\phi_f\rangle$ are states without free photons propagating, $\left|\tilde{\phi}_i\right\rangle$ and $\left|\tilde{\phi}_f\right\rangle$ are the corresponding states with the photon field integrated out, H_{QED} is the full QED Hamiltonian, and H_{eQED} has the photon field integrated out. The effective Hamiltonian can be derived in the path integral formulation of QED with the Feynman gauge fixing procedure [214], giving

$$\langle\phi_f| e^{-iH_{QED}t} |\phi_i\rangle = \int DA_\mu(x)D\bar{\psi}(x)D\psi(x)\phi_f^*(A_\mu(x),\bar{\psi}(x),\psi(x))\phi_i(A_\mu(x),\bar{\psi}(x),\psi(x))$$
$$\exp\Bigg(i\int d^4x\, i\bar{\psi}(x)\gamma^\mu\partial_\mu\psi(x) - m\bar{\psi}(x)\psi(x) - e\bar{\psi}(x)\gamma^\mu\psi(x)A_\mu(x) - \frac{1}{2}A^\mu(x)\Box A_\mu(x)\Bigg) \tag{4.2}$$

where e is the elementary charge, $\Box = \partial_t^2 - \sum_{i=1}^3 \partial_{x_i}^2$, and $DA_\mu(x)D\bar{\psi}(x)D\psi(x)$ is the functional measure for the fields being integrated over. The repeated upper and lower indices corresponds to Einstein summation convention with a spacetime metric using the mostly negative convention ($g_{\mu\nu} = \text{diag}(1, -1, -1, -1)$), i.e.

$$a^\mu b_\mu = a^0 b^0 - \sum_{i=1}^{3} a^i b^i \quad . \tag{4.3}$$

The γ matrices act on the Fock space that mixes the components of the particles. From this perspective, they are akin to operations such as fermionic swaps which are widely used in the quantum chemistry literature [215, 216]. The γ matrices, when seen as operators acting on the spinor of fermionic operators $[a^\dagger_{\vec{x},0}, a^\dagger_{\vec{x},1}, a^\dagger_{\vec{x},1}, a^\dagger_{\vec{x},2}, a^\dagger_{\vec{x},3}]$, can be represented in the Dirac representation as

$$\begin{aligned} \gamma^0 &= \hat{1} \otimes \hat{\sigma}_3 \\ \gamma^i &= i\hat{\sigma}_2 \otimes \hat{\sigma}_i \end{aligned} \tag{4.4}$$

where $\hat{\sigma}_i$ are the standard Pauli matrices. In Eq. 4.2, $\bar{\psi}(x) = \psi^\dagger(x)\gamma^0$, where the summation over the spinor indices of $\psi^\dagger(x)$ and γ^0 has been suppressed. For states where the electromagnetic field is close to satisfying the classical equations of motion, an action for eQED can be obtained by performing the integral over $A_\mu(x)$ in the stationary phase approximation yielding

$$\begin{aligned} \langle\phi_f|\, e^{-iH_{eQED}t}\,|\phi_i\rangle &= \int DA_\mu(x) D\bar{\psi}(x) D\psi(x) \tilde{\phi}^*_f(\bar{\psi}(x), \psi(x)) \tilde{\phi}_i(\bar{\psi}(x), \psi(x)) \\ \exp\left(i \int d^4x i\bar{\psi}(x)\gamma^\mu \partial_\mu \psi(x) - m\bar{\psi}(x)\psi(x) - \frac{1}{2} e^2 \bar{\psi}(x)\gamma^\mu\psi(x)\Box^{-1}(x,y) \int d^4y \bar{\psi}(y)\gamma_\mu\psi(y) \right) \; . \end{aligned} \tag{4.5}$$

Therefore the action for eQED is given by

$$S_{eQED} = \int d^4x i\bar{\psi}(x)\gamma^\mu\partial_\mu\psi(x) - m\bar{\psi}(x)\psi(x) - \frac{1}{2}e^2\bar{\psi}(x)\gamma^\mu\psi(x)\Box^{-1}(x,y)\int d^4y\bar{\psi}(y)\gamma_\mu\psi(y) \tag{4.6}$$

where $\Box^{-1}(x, y)$ is the Green's function for $\Box$.

$$\Box^{-1}(\vec{x}, t', \vec{y}, t) = \frac{1}{4\pi|\vec{y} - \vec{x}|}\delta(t' - t - |\vec{y} - \vec{x}|) \tag{4.7}$$

so this action is not local in time, which makes it unsuitable for deriving a Hamiltonian for the canonical quantization formulation of quantum mechanics. If the radiation effects are neglected, then

$$\Box^{-1}(\vec{x}', t', \vec{x}, t) \approx \frac{1}{4\pi|\vec{x}' - \vec{x}|}\delta(t' - t) \tag{4.8}$$

In this approximation,

$$S_{eQED} = \int d^4x \, i\bar{\psi}(x)\gamma^\mu\partial_\mu\psi(x) - m\bar{\psi}(x)\psi(x) - \frac{1}{2}e^2\bar{\psi}(x)\gamma^\mu\psi(x)\int d^3y \frac{1}{4\pi|\vec{x} - \vec{y}|}\bar{\psi}(y)\gamma_\mu\psi(y) \tag{4.9}$$

At this point, a Legendre transform can be performed to obtain a Hamiltonian for eQED given by

$$H_{eQED} = \int d^3x \, -i\sum_{j=1}^{3}\bar{\psi}(x)\gamma^j\nabla_j\psi(x) + m\bar{\psi}(x)\psi(x) + \frac{1}{2}e^2\bar{\psi}(x)\gamma^\mu\psi(x)\int d^3y \frac{1}{4\pi|\vec{x} - \vec{y}|}\bar{\psi}(y)\gamma_\mu\psi(y) \quad . \tag{4.10}$$

where ∇_j is the typical 3-space gradient operator. Note that when working in momentum space instead of position space, this issue of time nonlocality can be addressed without resorting to Eq. 4.8.

4.2.1 eQED for Free Electrons

The first case that we will present is the Hamiltonian for eQED for the uniform electron gas. The non-relativistic version of this model is known as jellium, which not only is useful for the foundations of density functional theory but also has become a standard benchmark problem for quantum chemistry simulation [215]. Here we will present a formulation that is appropriate for eQED which we call “rellium” in analogy to the non-relativistic jellium. There are two representations that we will consider for the Hamiltonian: position space and momentum space. Both approaches have different advantages and disadvantages and without further knowledge, it is unclear which will prove to be superior for a given problem without knowing the number of lattice sites in the real-space or reciprocal-space lattice are needed for the simulation.

The Hamiltonian from the previous section can be placed on a discrete cubic lattice with n_s sites and side-length L. In this discrete representation we make the identification that $\psi = a\sqrt{n_s/L^3}$ and $\bar{\psi} = a^\dagger\gamma^0\sqrt{n_s/L^3}$ where a is the standard dimensionless fermionic annihilation operator, and n_s is the total number of lattice sites. The discretized Hamiltonian on the lattice can then be expressed as

$$H_{eQED} = H_K + H_m + V$$

$$H_m = \frac{L^3}{n_s}\sum_{\vec{x}} m\bar{\psi}_{\vec{x}}\psi_{\vec{x}} = \sum_{\vec{x}} m a^\dagger_{\vec{x}}\gamma^0 a_{\vec{x}}$$

$$V = \frac{L^6}{n_s^2}\sum_{\vec{x}\neq\vec{y}}\sum_{\mu=0}^{3} g_{\mu\mu}\frac{e^2 n_s^{1/3}}{8\pi L|\vec{x}-\vec{y}|}(\bar{\psi}_x\gamma^\mu\psi_x)(\bar{\psi}_y\gamma^\mu\psi_y) = \sum_{\vec{x}\neq\vec{y}}\sum_{\mu=0}^{3} g_{\mu\mu}\frac{e^2 n_s^{1/3}}{8\pi L|\vec{x}-\vec{y}|}(a^\dagger_x\gamma^0\gamma^\mu a_x)(a^\dagger_y\gamma^0\gamma^\mu a_y) \tag{4.11}$$

Here we use the convention that $\vec{x}$, $\vec{y}$ and $\vec{p}$ are vectors of integers that index a particular fermionic mode. The state of the system can be represented by using a qubit to represent each $a^\dagger_x a_x$. This will require $4n_s$ qubits total.

A technicality emerges in choosing the correct quantization of the kinetic operator on the lattice, H_K. In particular, if a finite difference on the lattice is used as in

$$H_{\text{naïve}} = \frac{L^{2/3}}{n_s^{2/3}}\sum_{\vec{x}} -i\bar{\psi}_x\sum_{j=1}^{3}\gamma^j\frac{\psi_{x+\hat{j}}-\psi_{x-\hat{j}}}{2} \quad , \tag{4.12}$$

where $\hat{j}$ is a unit vector pointing in the j-th direction, a continuum limit will not be recovered [217, 218]. Consider a free electron with momentum p in one-dimension, the electron's momentum then lies in the range $[-\frac{n_s^{1/3}\pi}{L}, \frac{n_s^{1/3}\pi}{L}]$ where the energy is given by $E = \sqrt{m^2 + \frac{n_s^{2/3}}{L^2}\sin^2(2\pi p/n_s^{1/3})}$. Therefore with this kinetic Hamiltonian, both an electron with momentum $\frac{n_s^{1/3}\pi}{L}$ and an electron with zero momentum have energy m. Likewise, by periodicity, at every energy there will be twice as many states as there are in the continuum limit. This doubling of states prevents this naïve choice of Hamiltonian from correctly reproducing the physics of continuum eQED. Several solutions to this fermion doubling problem have been developed in the study of lattice gauge theories [219, 220, 221, 222]. One solution, known as SLAC fermions, solves this problem by choosing the kinetic term, H_K such that the dispersion relation agrees with the continuum limit [221, 222].

$$H_K \to H_{SLAC} := \frac{2\pi L^2}{n_s^{1/3}} \sum_{\vec{x},\vec{y},\vec{p}} \frac{e^{i2\pi n_s^{-\frac{1}{3}} \vec{p}\cdot(\vec{x}-\vec{y})}}{n_s} \bar{\psi}_{\vec{y}} \gamma^j p_j \psi_{\vec{x}} = \frac{2\pi}{n_s^{1/3} L} \sum_{\vec{x},\vec{y},\vec{p}} e^{i2\pi n_s^{-\frac{1}{3}} \vec{p}\cdot(\vec{x}-\vec{y})} a^\dagger_{\vec{y}} \gamma^0 \gamma^j p_j a_{\vec{x}} \tag{4.13}$$

This choice of kinetic term solves the fermion doubling at the expense of locality. Other solutions exist, such as Wilson's kinetic operator, but for simplicity we focus on the SLAC case.

The momentum space formulation of a relativistic eQED Hamiltonian without an external potential can be viewed as a variant of a well known interacting electron model: jellium. We will follow similar notation to Ref. [215] where the cell volume $\Omega = L^3$ for a cubic simulation cell with side length L. The standard non-relativistic 3 dimensional jellium Hamiltonian is defined as the following in second quantization

$$H_{jel} = \sum_{p,\sigma_1} \frac{k_p^2}{2} a^\dagger_{p,\sigma_1} a_{p,\sigma_1} + \frac{1}{2\Omega} \sum_{\substack{(p,\sigma_1)\neq(q,\sigma_2) \\ \nu\neq 0}} \frac{4\pi}{k_\nu^2} a^\dagger_{p,\sigma_1} a^\dagger_{q,\sigma_2} a_{q+\nu,\sigma_2} a_{p-\nu,\sigma_1} \tag{4.14}$$

where the p, q indexes are momentum space electronic planewave orbitals, L is the length of one dimension of the simulation box, $\sigma_1, \sigma_2 \in [\uparrow, \downarrow]$ are the fermion spin indices, and k is the momentum. In non-relativistic jellium, the planewave basis is only defined for electronic and spin degrees of freedom

$$\varphi_\nu(r) = \sqrt{\frac{1}{\Omega}} e^{ik_\nu \cdot r}, \qquad k_\nu = \frac{2\pi\nu}{L} \tag{4.15}$$

where $\varphi_\nu(r)$ is a single plane wave as a function of the momentum grid point $\nu \in [-N^{(1/3)}, N^{(1/3)}]^3$ and distance is denoted by r. The momentum grid is the same size for both spin-up and spin-down planewaves. In order to extend the 3D jellium Hamiltonian to a relativistic framework, we use the 4-spinor solution to the Dirac equation to build a planewave basis, and use the second order tree Feynman diagrams for eQED to compute the two particle interactions.

As mentioned above, we will refer to this relativistic jellium model as ‘rellium’. In general, the planewave basis has the same form as above, but the total number of planewaves will be doubled, now that positronic degrees of freedom must now be considered. The general form of the rellium Hamiltonian takes into account relativistic particle energies, and also eQED interaction amplitudes that have pair creation ($e^- \rightarrow e^-e^-e^+$) interactions in addition to the typical two body interactions ($e^-e^- \rightarrow e^-e^-$). In this form charge is conserved, but not particle number. The rellium Hamiltonian can be described in second quantization as

$$
\begin{aligned}
H_{rel} =& \sum_{p,\sigma_1} E_p a^{\dagger}_{p,\sigma_1} a_{p,\sigma_1} + \sum_{p,\sigma_1} E_p b^{\dagger}_{p,\sigma_1} b_{p,\sigma_1} \\
&+ \frac{1}{2\Omega} \sum_{\substack{p,q,r \\ \sigma_1,\sigma_2,\sigma_3,\sigma_4}} \frac{\mathcal{M}^{e^-_{r,\sigma_3} e^-_{p+q-r,\sigma_4}}_{e^-_{p,\sigma_1} e^-_{p,\sigma_2}}}{\sqrt{E_p E_q E_r E_{p+q-r}}} a^{\dagger}_{p+q-r,\sigma_4} a^{\dagger}_{r,\sigma_3} a_{q,\sigma_2} a_{p,\sigma_4} \\
&+ \frac{1}{2\Omega} \sum_{\substack{p,q,r \\ \sigma_1,\sigma_2,\sigma_3,\sigma_4}} \frac{\mathcal{M}^{e^+_{r,\sigma_3} e^+_{p+q-r,\sigma_4}}_{e^+_{p,\sigma_1} e^+_{q,\sigma_2}}}{\sqrt{E_p E_q E_r E_{p+q-r}}} b^{\dagger}_{p+q-r,\sigma_4} b^{\dagger}_{r,\sigma_3} b_{q,\sigma_2} b_{p,\sigma_1} \\
&+ \frac{1}{2\Omega} \sum_{\substack{p,q,r \\ \sigma_1,\sigma_2,\sigma_3,\sigma_4}} \frac{\mathcal{M}^{e^-_{r,\sigma_3} e^+_{p+q-r,\sigma_4}}_{e^-_{p,\sigma_1} e^+_{q,\sigma_2}}}{\sqrt{E_p E_q E_r E_{p+q-r}}} b^{\dagger}_{p+q-r,\sigma_4} a^{\dagger}_{r,\sigma_3} b_{q,\sigma_2} a_{p,\sigma_1} \\
&+ \frac{1}{2\Omega} \sum_{\substack{p,q,p_1 \\ \sigma_1,\sigma_2,\sigma_3,\sigma_4}} \frac{\mathcal{M}^{e^+_{q,\sigma_2} e^-_{p_1,\sigma_3} e^-_{p-q-p_1,\sigma_4}}_{e^-_{p,\sigma_1}}}{\sqrt{E_p E_q E_{p_1} E_{p-q-p_1}}} a^{\dagger}_{p-q-p_1,\sigma_4} a^{\dagger}_{p_1,\sigma_3} b^{\dagger}_{q,\sigma_2} a_{p,\sigma_1} + h.c. \\
&+ \frac{1}{2\Omega} \sum_{\substack{p,q,p_1 \\ \sigma_1,\sigma_2,\sigma_3,\sigma_4}} \frac{\mathcal{M}^{e^-_{q,\sigma_2} e^+_{p_1,\sigma_3} e^+_{p-q-p_1,\sigma_4}}_{e^+_{p,\sigma_1}}}{\sqrt{E_p E_q E_{p_1} E_{p-q-p_1}}} b^{\dagger}_{p-q-p_1,\sigma_4} b^{\dagger}_{p_1,\sigma_3} a^{\dagger}_{q,\sigma_2} b_{p,\sigma_1} + h.c. \\
&+ \frac{1}{2\Omega} \sum_{\substack{p,q,r \\ \sigma_1,\sigma_2,\sigma_3,\sigma_4}} \frac{\mathcal{M}_0^{e^-_{p,\sigma_1} e^+_{q,\sigma_2} e^-_{r,\sigma_3} e^+_{-p-q-r,\sigma_4}}}{\sqrt{E_p E_q E_r E_{-p-q-r}}} a^{\dagger}_{p,\sigma_1} b^{\dagger}_{q,\sigma_2} a^{\dagger}_{r,\sigma_3} b^{\dagger}_{-p-q-r,\sigma_4} + h.c. \\
&+ \delta m \sum_{p,\sigma_1,\sigma_2} \frac{1}{2E_p n_s} \Bigg(\bar{u}_{\sigma_1}(p) u_{\sigma_2}(p) a^{\dagger}_{p,\sigma_1} a_{p,\sigma_2} - \bar{v}_{\sigma_1}(p) v_{\sigma_2}(p) b^{\dagger}_{p,\sigma_1} b_{p,\sigma_2} \\
&+ \bar{v}_{\sigma_1}(-p) u_{\sigma_2}(p) b^{\dagger}_{-p,\sigma_1} a_{p,\sigma_2} + \bar{u}_{\sigma_1}(-p) v_{\sigma_2}(p) a^{\dagger}_{-p,\sigma_1} b_{p,\sigma_2} \Bigg) + \Lambda n_s
\end{aligned}
\tag{4.16}
$$

where the relativistic energy E_k is defined as $E_k = \sqrt{k_x^2 + k_y^2 + k_z^2 + m^2}$ where m is the electron mass, a, b are the annihilation operators corresponding to electronic and positronic degrees of freedom respectively, $\mathcal{M}$ represents the computed eQED amplitudes for the interaction, and $\sigma_1, \sigma_2, \sigma_3, \sigma_4 \in [\uparrow, \downarrow]$ are all independent spin indices. δm is the difference between the bare mass and the physical electron mass and Λ is a constant added to guarantee that the vacuum has zero energy. It is necessary to include these terms in the Hamiltonian to guarantee that the particles in this discretized theory have a mass equal to the electron mass and that the correct physics is reproduced in the continuum limit. The helicity spinors are defined by

$$u_1(p) = \sqrt{E_p + m}\begin{bmatrix} 1 \\ 0 \\ \frac{p_z}{E_p+m} \\ \frac{p_x+ip_y}{E_p+m} \end{bmatrix} \quad u_2(p) = \sqrt{E_p + m}\begin{bmatrix} 0 \\ 1 \\ \frac{p_x-ip_y}{E_p+m} \\ \frac{-p_z}{E_p+m} \end{bmatrix}$$

$$v_1(p) = \sqrt{E_p + m}\begin{bmatrix} \frac{p_x-ip_y}{E_p+m} \\ \frac{-p_z}{E_p+m} \\ 0 \\ 1 \end{bmatrix} \quad v_2(p) = \sqrt{E_p + m}\begin{bmatrix} \frac{p_z}{E_p+m} \\ \frac{p_x+ip_y}{E_p+m} \\ 1 \\ 0 \end{bmatrix} \tag{4.17}$$

and are used in the construction of $\mathcal{M}$. The details of the amplitudes $\mathcal{M}$ are discussed in detail in Appendix F. The state of the system can be represented on a quantum computer by using a qubit to represent the value of each $a^\dagger_{p,\sigma}a_{p,\sigma}$ and each $b^\dagger_{p,\sigma}b_{p,\sigma}$. Thus the total number of qubits required to encode the state of the fermionic field here is $4n_s$, in exact agreement with the number required in position space (despite the fact that in momentum basis we explicitly divide the field into a fermionic and anti-fermionic subsystem).

4.2.2 eQED with an External Potential

In the continuum, when eQED is done in the presence of an external vector potential $A^{ex}(x)$, an additional term

$$H_{ext} = -e\int d^3x\bar{\psi}(x)\gamma^\mu\psi(x)A^{ex}_\mu(x) \tag{4.18}$$

must be added to the Hamiltonian. This vector potential term is more general than the Coulomb term commonly used for external potentials in chemistry applications. In part, this is because it applies to general external electric potentials but also because this term includes the vector potential terms needed to describe interactions with external magnetic fields as well.

Since quantum computer simulations necessarily require discretized wave functions, it is necessary to consider discretizations of Eq. 4.18. The two natural approaches to discretize the system in a lattice are in position and momentum representations. In the position representation, the integral of the external potential can be discretized as a finite sum via

$$H_{L,ext} = -ea^3 \sum_x \bar{\psi}_x \gamma^\mu \psi_x A^{ex}_{\mu,x} \quad . \tag{4.19}$$

The momentum space representation can be found from the position space representation by applying the Fourier transform to the field operators. This approach is analogous to the fermionic Fourier transform used in quantum chemistry simulations [223, 215]; however, here the transform needs to be performed over all four components of the field. The transform of the vector potential operator is given by

$$A^{ex}_\mu(x) = \int \frac{d^3x}{(2\pi)^3} e^{-ipx} \tilde{A}^{ex}_\mu(p), \tag{4.20}$$

This term takes the form

$$\begin{aligned} H_{ext} = &- e \sum_{\sigma_1,\sigma_2} \int \frac{d^3p d^3q}{2\sqrt{E_p E_q}} \Bigg(\bar{u}_{\sigma_2}(q)\gamma^\mu u_{\sigma_1}(p) a^\dagger_{q,\sigma_2} a_{p,\sigma_1} \tilde{A}^{ex}_\mu(p-q) \\ &+ \bar{u}_{\sigma_2}(q)\gamma^\mu v_{\sigma_1}(p) a^\dagger_{q,\sigma_2} b^\dagger_{p,\sigma_1} \tilde{A}^{ex}_\mu(-p-q) \\ &+ \bar{v}_{\sigma_2}(q)\gamma^\mu u_{\sigma_1}(p) b_{q,\sigma_2} a_{p,\sigma_1} \tilde{A}^{ex}_\mu(p+q) \\ &+ \bar{v}_{\sigma_2}(q)\gamma^\mu v_{\sigma_1}(p) b_{q,\sigma_2} b^\dagger_{p,\sigma_1} \tilde{A}^{ex}_\mu(q-p) \Bigg) \end{aligned} \tag{4.21}$$

in momentum space.

In the discretized momentum space simulation, the external potential term takes the form of

$$\begin{aligned} H_{p,ext} = &- e \sum_{\sigma_1,\sigma_2} \sum_{p,q} \frac{1}{2\sqrt{E_p E_q} L^3} \Bigg(\bar{u}_{\sigma_2}(q)\gamma^\mu u_{\sigma_1}(p) a^\dagger_{q,\sigma_2} a_{p,\sigma_1} \tilde{A}^{ex}_\mu(p-q) \\ &+ \bar{u}_{\sigma_2}(q)\gamma^\mu v_{\sigma_1}(p) a^\dagger_{q,\sigma_2} b^\dagger_{p,\sigma_1} \tilde{A}^{ex}_\mu(-p-q) \\ &+ \bar{v}_{\sigma_2}(q)\gamma^\mu u_{\sigma_1}(p) b_{q,\sigma_2} a_{p,\sigma_1} \tilde{A}^{ex}_\mu(p+q) \\ &+ \bar{v}_{\sigma_2}(q)\gamma^\mu v_{\sigma_1}(p) b_{q,\sigma_2} b^\dagger_{p,\sigma_1} \tilde{A}^{ex}_\mu(q-p) \Bigg). \end{aligned} \tag{4.22}$$

With these additional definitions, we now have a general form of the eQED Hamiltonian that we can use for cost analysis.

4.3 Trotter-Suzuki Simulations of eQED

There are many techniques that have been proposed thus far for simulating quantum dynamics. The first approach proposed for quantum simulation involves the use of Trotter-Suzuki formulas to compile quantum dynamics into a discrete sequence of gate operations [11, 224, 22, 225, 226]. These approaches are space optimal and can take advantage of properties such as locality and commutation relations that qubitization cannot. For simulations of the free electron gas, known as jellium, recent work has shown that the scaling of the time complexity of Trotter-Suzuki simulation methods and qubitization are nearly equal. For this reason, we focus on Trotter-Suzuki simulations.

Trotter-Suzuki simulations can be viewed as a method for compiling the unitary matrix e^{-iHt} as a sequence of unitary gates, U, such that $\|e^{-iHt} - U\| \leq \delta$. If $H = \sum_j H_j$ for a set of H_j such that $e^{-iH_j\theta}$ can be efficiently compiled as a quantum circuit via

$$U_2(t) := \left(\prod_{j=1}^{m} e^{-iH_jt/2}\right)\left(\prod_{j=m}^{1} e^{-iH_jt/2}\right) = e^{-iHt} + O\left(\max_{j,k,\ell} \|[H_j, [H_k, H_\ell]]\| t^3\right) \tag{4.23}$$

Since each H_j is assumed to be implementable using a polynomial-sized circuit, this approximation effectively compiles e^{-iHt} into a sequence of unitary operations. Higher-order variants of the Trotter-Suzuki approximation can be constructed from the symmetric Trotter formula U_2 via [227, 228]

$$\begin{aligned} U_{2k+2}(t) &:= U_{2k}^2(s_{2k}t)U_{2k}((1-4s_{2k})t)U_{2k}^2(s_{2k}t) \\ &= e^{-iHt} + O\left(\max_{j_1,\dots,j_{2k+3}} (\|[H_{j_1}, [\cdots [H_{2k+2}, H_{2k+3}] \cdots]]\|) t^{2k+3}\right), \end{aligned} \tag{4.24}$$

where $s_{2k} = (4 - 4^{1/(2k+1)})^{-1}$. Such high-order Trotter-Suzuki formulas are not always superior to their lower-order brethren. This is because the number of exponentials in $U_{2k}(t)$ is in $\Theta(5^k m)$ and hence tradeoffs between the exponential improvements to accuracy yielded increasing k and the exponentially increasing costs of doing so must be made. Further, as the error in the Trotter-Suzuki approximation depends on the commutators between the Hamiltonian terms, the cost of such simulations can be better than these upper bounds suggest [229, 230, 228].

Thus in order to construct the operation $U_{2k}(t)$, for some integer value of k, we need to develop circuits for implementing each of the terms in the decomposition separately. That is to say for we need to take each Hamiltonian term present in the Hamiltonian and convert them to easily simulatable Hamiltonians before using the Trotter-Suzuki approximation to compile it to a sequence of operations that can be run on a quantum computer.

The individual H_j in our representation will, similar to chemistry, be expressable as Pauli operators through the use of a Jordan-Wigner transformation. Such a transformation yields the following transformation for the fermionic creation operator $a_x^\dagger$ via

$$a_x^\dagger \mapsto \frac{(X - iY)_x(\bigotimes_{y<x} Z)}{2}, \tag{4.25}$$

for some arbitrary canonical ordering of the site labels. Note that it may be tempting to make this assignment to the field operators $\psi^\dagger$ and ψ but we cannot do so directly since the field operators are dimensionful. For this reason, we discuss in the following the dimensionless fermionic operators a_x and will use these operators interchangeably with their anti-particle counterparts, b_y. Other fermionic representations are possible, such as the Bravyi-Kitaev encoding [231], but here we use Jordan-Wigner for its simplicity.

One technicality that needs to be considered with the Jordan-Wigner encoding is that the pattern of Pauli-Z operations depends on the lexigraphical ordering of the site labels. In one-dimension, such orderings are straight forward, but in higher dimensions there are a multitude of natural lexigraphical orderings of the sites (orbitals) that can be chosen.

Here we focus on a simplified cost model for the simulation wherein non-Clifford operations constitute the majority of the cost. Specifically, we assume our quantum computer has all-to-all couplings between the qubits and can perform CNOT between such pairs as well as all single qubit Clifford operations (which can be formed from products of the Hadamard gate H and the phase gate $S = \sqrt{Z}$). We also assume that the $T = \sqrt{S}$ gate can be applied to each quantum bit. Further we assume that all Clifford operations are free and only T-gates are costly. This further motivates why we choose Jordan-Wigner representation for our problem because the additional gates needed to enforce the correct signs from the lexigraphical ordering are all Clifford operations, which we take to be free. Thus, within our cost model, the choice of the ordering of the labels of the sites will prove to be irrelevant.

With the Jordan-Wigner transformation in place we have all we need to compile the circuit from the Trotter-Suzuki simulation $U_{2k}(t)$ into a sequence of gates that can be executed on a quantum computer. Below, we discuss ways that exponentials of the one- and two-body terms in the Hamiltonian can be compiled into a gateset involving Clifford gates and single qubit rotations. We will discuss later what translations need to be done to convert the single qubit rotations into circuits involving H and T.

4.3.1 Quantum Circuit for the one-body operators

The free piece of the eQED Hamiltonian consists of a sum over terms of the form $\psi_p^\dagger \psi_q$, however the representation of these terms can vary depending on whether we are interested in the position or momentum basis. In the momentum basis formulation, all terms take the form $a_{\sigma,p}^\dagger a_{\sigma,p}$ and $b_{\sigma,p}^\dagger b_{s,p}$, which acts only on a single qubit register and is trivial to simulate. Therefore, evolving according to the free Hamiltonian in the momentum basis require $4n_s$ single qubit gates. In the position space lattice formulation, the free Hamiltonian terms can take one of two more additional forms: $a_x^\dagger a_y + a_y^\dagger a_x$ and $i(a_x^\dagger a_y - a_y^\dagger a_x)$. These operators can then be converted into Pauli operators using the Jordan-Wigner transformation. Assuming without loss of generality that in the canonical ordering we choose $x < y$, the Jordan-Wigner representation of these terms takes the form

1. $a_x^\dagger a_y + a_y^\dagger a_x \xrightarrow{JW} X(\bigotimes_{x<n<y} Z)X + Y(\bigotimes_{x<n<y} Z)Y$

2. $i(a_x^\dagger a_y - a_y^\dagger a_x) \xrightarrow{JW} X(\bigotimes_{x<n<y} Z)Y - Y(\bigotimes_{x<n<y} Z)X$

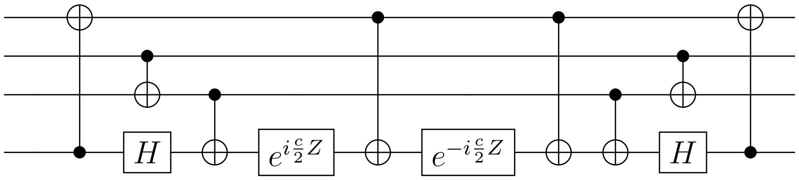

Figure 4.1: Circuit used to implement $e^{ic(X(\bigotimes_{x<n<y} Z)\otimes X+Y(\bigotimes_{x<n<y} Z)\otimes Y)}$ for $y = x + 2$.

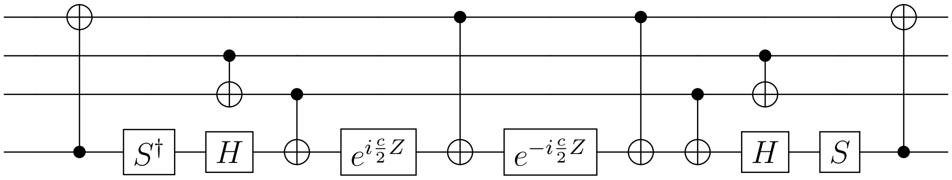

Figure 4.2: Circuit used to implement $e^{ic(X(\bigotimes_{x<n<y} Z)\otimes Y-Y(\bigotimes_{x<n<y} Z)\otimes X)}$ for $y = x + 2$.

While Case 1 appears in standard constructions for quantum circuits for simulating chemistry [13], Case 2 does not typically arise in existing quantum circuit constructions and so we provide optimized networks for implementing it above in Figure 4.2. An optimized circuit for the one-body operations in Case 1 is given in Figure 4.1

There are $2n_s(4n_s - 1)$ couplings of this form in the Hamiltonian. Therefore, Trotter simulation of the free Hamiltonian requires $20n_s(4n_s-1)$ single qubit gates per step. Ignoring the Jordan-Wigner strings, $8n_s(4n_s - 1)$ CNOT's are needed per step. The Jordan Wigner strings require

$$4\sum_{n=0}^{4n_s-1}\sum_{k=0}^{n-1}k = 2\sum_{n=0}^{4n_s-1}n(n-1) = \frac{16}{3}n_s(2n_s-1)(4n_s-1) \tag{4.26}$$

CNOT gates. Therefore a single Trotter step requires $\frac{8}{3}n_s(16n_s^2 - 1)$ CNOT gates for the free Hamiltonian. Importantly, the number of single-qubit Z-rotations needed to perform the simulation is given by

$$N_{rot} = 20n_s(4n_s - 1). \tag{4.27}$$

The focus of the present work is on fault-tolerant quantum simulation and so the cost of simulation is dominated by the number of non-Clifford operations needed to implement the rotations. However, the number of CNOT operations can be reduced to $\widetilde{O}(n_s^2)$ using fermionic swap networks [215, 232, 216].

4.3.2 Interaction Circuits

As shown in the previous section, the eQED Hamiltonian potential is a sum of a 2 → 2 term that takes the same form as the non-relativistic case, and a new 1 → 3 term. New circuits will be required to simulate this 1 → 3 term which takes the form $\sum_{j>k>l,m} V_{j,k,l,m} a_j^\dagger a_k^\dagger a_l^\dagger a_m + h.c.$. Using the Jordan-Wigner encoding, $a_j^\dagger a_k^\dagger a_l^\dagger a_m$ can take 4 different forms depending on value of m.

Case 1. $m < l$

$$a_j^\dagger a_k^\dagger a_l^\dagger a_m = -\frac{(X-iY)_j}{2} \otimes Z^{j-k-1} \otimes \frac{(X-iY)_k}{2} \otimes 1^{k-l-1} \otimes \frac{(X-iY)_l}{2} \otimes Z^{l-m-1} \otimes \frac{(X+iY)_m}{2} \otimes 1^{m-1} \tag{4.28}$$

Case 2. $m \in [l+1, k-1]$

$$a_j^\dagger a_k^\dagger a_l^\dagger a_m = \frac{(X-iY)_j}{2} \otimes Z^{j-k-1} \otimes \frac{(X-iY)_k}{2} \otimes 1^{k-m-1} \otimes \frac{(X+iY)_m}{2} \otimes Z^{m-l-1} \otimes \frac{(X-iY)_l}{2} \otimes 1^{l-1} \tag{4.29}$$

Case 3. $m \in [k+1, j-1]$

$$a_j^\dagger a_k^\dagger a_l^\dagger a_m = -\frac{(X-iY)_j}{2} \otimes Z^{j-m-1} \otimes \frac{(X+iY)_m}{2} \otimes 1^{m-k-1} \otimes \frac{(X-iY)_k}{2} \otimes Z^{k-l-1} \otimes \frac{(X-iY)_l}{2} \otimes 1^{l-1} \tag{4.30}$$

Case 4. $m > j$

$$a_j^\dagger a_k^\dagger a_l^\dagger a_m = \frac{(X+iY)_m}{2} \otimes Z^{m-j-1} \otimes \frac{-(X-iY)_j}{2} \otimes 1^{j-k-1} \otimes \frac{-(X-iY)_k}{2} \otimes Z^{k-l-1} \otimes \frac{-(X-iY)_l}{2} \otimes 1^{l-1} \tag{4.31}$$

Suppressing the chains of Z's and identities, the contribution to the Hamiltonian takes the following forms

Case 1.

$$\begin{aligned} H = &-\frac{V+V^*}{16}(XXXX+XXYY+XYXY-XYYX+YXXY-YXYX-YYXX-YYYY) \\ &-i\frac{V-V^*}{16}(XXXY-XXYX-XYXX-YXXX-XYYY-YXYY-YYXY+YYYX) \end{aligned} \tag{4.32}$$

Case 2.

$$\begin{aligned} H = &\frac{V+V^*}{16}(XXXX+XXYY-XYXY-YXXY+YXYX-YYXX+XYYX-YYYY) \\ &+i\frac{V-V^*}{16}(-XYYY-YXYY+YYXY-YYYX-YXXX-XYXX+XXYX-XXXY) \end{aligned} \tag{4.33}$$

Case 3.

$$\begin{aligned} H = &-\frac{V+V^*}{16}(XXXX-XXYY+XYXY-YXXY-YXYX+YYXX+XYYX-YYYY) \\ &-i\frac{V-V^*}{16}(-XXXY-XXYX+XYXX-YXXX-XYYY+YXYY-YYXY-YYYX) \end{aligned} \tag{4.34}$$

Case 4.

$$H = \frac{V+V^*}{16}(XXXX - XXYY - XYXY + YXXY - XYYX + YXYX + YYXX - YYYY)$$

$$+i\frac{V-V^*}{16}(XYYY - YXYY - YYXY - YYYX - XXXY - XXYX - XYXX + YXXX). \tag{4.35}$$

Additionally, the eQED Hamiltonian also contains 4 creation/annhilation terms when expressed in the planewave basis. The Jordan Wigner representation of these terms is

$$a_j^\dagger a_k^\dagger a_l^\dagger a_m^\dagger = \frac{(X-iY)_j}{2} \otimes Z^{j-k-1} \otimes \frac{(X-iY)_k}{2} \otimes 1^{k-l-1} \otimes \frac{(X-iY)_l}{2} \otimes Z^{l-m-1} \otimes \frac{(X-iY)_m}{2} \otimes 1^{m-1} \tag{4.36}$$

$$H = \frac{V+V^*}{16}(XXXX - XXYY - XYXY - YXXY - XYYX - YXYX - YYXX + YYYY)$$

$$+i\frac{V-V^*}{16}(XYYY + YXYY + YYXY + YYYX - XXXY - XXYX - XYXX - YXXX). \tag{4.37}$$

From these equations, it can be seen that each term contains every possible tensor product of 4 X's and Y's. In a naïve Trotterization simulation, each term would be treated separately. However, this is suboptimal because all terms with an even number of X's and Y's commute and all terms with an odd number of X's and Y's commute. Previous work has introduced a circuit to simulate all terms with an even number of X's and Y's. It will be shown here that the same techniques can be adapted for the odd case as well. A Hamiltonian that contains all terms with odd numbers of X's and Y's can be efficiently simulated by using a circuit that will simultaneously diagonalize all terms.

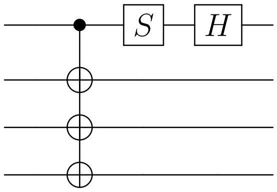

Figure 4.3: Circuit G used to diagonalize all tensor products of an odd number of X's and Y's.

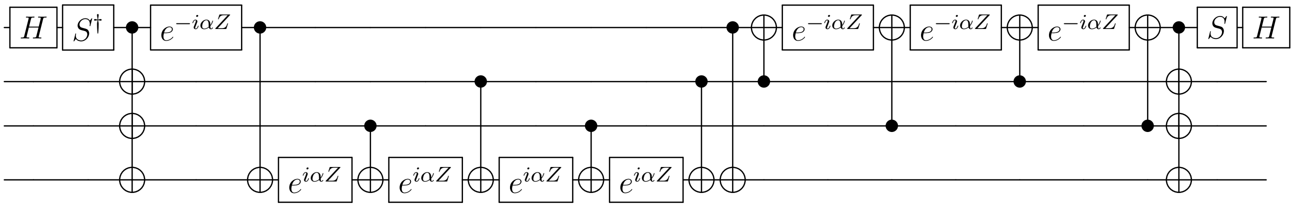

Figure 4.4: Implementation of $e^{i\alpha(XXXY-XXYX-XYXX-YXXX-XYYY-YXYY-YYXY+YYYX)}$

The circuit G can be used to implement time evolution according to a Hamiltonian made out of a sum over the odd tensor products. For example, take

$$H = XXXY-XXYX-XYXX-YXXX-XYYY-YXYY-YYXY+YYYX. \quad (4.38)$$

Then using the results in Appendix G we see that

$$H = G(ZZZZ - ZZZ1 - ZZ11 - Z111 + ZZ1Z + Z11Z + Z1ZZ - Z1Z1)G^\dagger. \quad (4.39)$$

and the circuit in Fig. 4.4 can be used to implement $e^{i\alpha H}$. From Fig. 4.4, it can be seen that single term in the interaction Hamiltonian requires 12 single qubit gates to implement, and 16 CNOT gates in addition to however many CNOT gates are needed to implement the Jordan-Wigner strings. In the position space formulation, there are at most $256n_s^2$ terms and in the momentum space formulation there are at most $8192n_s^3$ terms.

4.4 Cost Estimates for eQED Simulation

The aim of this section is to provide preliminary cost estimates for simulating effective quantum electrodynamics on quantum computers using Trotter-Suzuki approximations and also provide a comparison to the asymptotic scaling expected from a naïve application of qubitization. All such cost estimates are performed within a computational model wherein Clifford gates are free but non-Clifford gates (specifically the T-gate) are not free. We will consider the cost of simulations both for lattice eQED (position space) or momentum space eQED.

4.4.1 Cost Estimates for Lattice eQED

Estimating the trotterization error for eQED requires the computation of nested commutators of terms in the Hamiltonian [233, 228]. The Hamiltonian for eQED in position space is given by

$$H = H_{SLAC} + H_m + H_{int} + H_{L,ext} \tag{4.40}$$

where

$$H_m = \frac{L^3}{n_s} \sum_{\vec{x}} m\bar{\psi}_x \psi_x = \sum_{\vec{x}} m a_{\vec{x}}^\dagger \gamma^0 a_{\vec{x}}$$

$$H_{L,ext} = -e\frac{L^3}{n_s} \sum_{x} \bar{\psi}(x)\gamma^\mu \psi(x) A_\mu^{ex}(x) = -\sum_{\vec{x}} e a_{\vec{x}}^\dagger \gamma^0 \gamma^\mu A_\mu^{ex}(x) a_{\vec{x}}$$

$$H_{SLAC} = \frac{2\pi}{n_s^{1/3} L} \sum_{\vec{x},\vec{y},\vec{p}} e^{i2\pi n_s^{-\frac{1}{3}} \vec{p}\cdot(\vec{x}-\vec{y})} a_{\vec{y}}^\dagger \gamma^0 \gamma^j p_j a_{\vec{x}} =: \sum_{\vec{x},\vec{y}} \sum_{\mu,\mu'} T_{\vec{x},\vec{y}}^{(\mu,\mu')} a_{\vec{x},\mu}^\dagger a_{\vec{y},\mu'}$$

$$H_{int} = \sum_{\vec{x}\neq\vec{y}} \sum_{\mu=0}^{3} g_{\mu\mu} \frac{n_s^{1/3} e^2}{8\pi L|\vec{x}-\vec{y}|} (a_{\vec{x}}^\dagger \gamma^0 \gamma^\mu a_{\vec{x}})(a_{\vec{y}}^\dagger \gamma^0 \gamma^\mu a_{\vec{y}}) =: \sum_{\vec{x}\neq\vec{y}} \sum_{\mu,\mu'} V_{\vec{x},\vec{y}}^{(\mu,\mu',\nu,\nu')} a_{\vec{x},\mu}^\dagger a_{\vec{x},\mu'} a_{\vec{y},\nu}^\dagger a_{\vec{y},\nu'}, \tag{4.41}$$

here we have taken the convention that $\vec{x}$ and $\vec{y}$ are 4-vectors of integers and that the indices μ, ν specify one of the components of the 4-vector.

Theorem 1. *Let H be the Hamiltonian of Eq. 4.40 with $n_s \geq 8$ sites in the cubic lattice with side-length L and external vector potential operator $A^{ex}(x)$ and let* $\Lambda := \max\left(m + e\max_x \|A^{ex}(x)\|, \frac{e^2 n_s}{L}, \frac{n_s^{4/3}}{L}\right)$. *Finally let $|\psi\rangle$ be an eigenstate of H such that $H|\psi\rangle = E|\psi\rangle$. The number of T-gates, N_T, needed to estimate E within error ϵ and constant failure probability less than $1/3$ obeys*

$$N_T \in \left(\frac{\Lambda n_s^2}{\epsilon}\right)^{1+o(1)}.$$

Proof. In order to estimate the error in the Trotter-Suzuki approximation, we need to evaluate the commutators between all these terms. A first step towards this is to estimate the commutators between the individual terms involved.

In order to evaluate the commutator terms involving H_{SLAC} we need to estimate the magnitude of these terms. As seen above, this involves estimating an oscillating sum. This expression is symmetric with respect to exchange of x, y, z axis labels and so we will proceed by bounding the coefficient for $k = 1$ (i.e. the x component of the momentum. Further, let $\vec{\Delta} = \vec{x} - \vec{y}$, and p_k be the kth component of vector $\vec{p}$.

$$\begin{aligned} T^{(1,1)}_{\vec{x},\vec{y}} &= \frac{2\pi}{n_s^{\frac{1}{3}} L} \sum_{\vec{p}} p_1 \left(e^{i2\pi n_s^{-\frac{1}{3}} \vec{p}\cdot\vec{\Delta}} \right) \\ &= \frac{2\pi}{n_s^{\frac{1}{3}} L} \left(\sum_{p_1 = -n_s^{1/3}/2+1}^{n_s^{1/3}/2} p_1 e^{i2\pi n_s^{-1/3} p_1 \Delta_1} \left(\sum_{p_2, p_3 = -n_s^{1/3}/2+1}^{n_s^{1/3}/2} e^{i2\pi n_s^{-1/3}(p_2\Delta_2 + p_3\Delta_3)} \right) \right) \end{aligned} \tag{4.42}$$

Next let us assume $\Delta_2 > 0$ and $\Delta_3 > 0$. In this case we have from the formula for the sum of a geometric series that under these circumstances

$$\left| \sum_{p_2 = -n_s^{1/3}/2+1}^{n_s^{1/3}/2} e^{i2\pi n_s^{-1/3}(p_2\Delta_2)} \right| = 1 + O(n_s^{-1/3}). \tag{4.43}$$

Similarly, if $\Delta_2 = 0$ then

$$\left| \sum_{p_2 = -n_s^{1/3}/2+1}^{n_s^{1/3}/2} e^{i2\pi n_s^{-1/3}(p_2\Delta_2)} \right| = n_s^{1/3}. \tag{4.44}$$

We then have that, for $n_s^{1/3} \geq 2$

$$\begin{aligned}
|T_{\vec{x},\vec{y}}^{(1,1)}| &\leq \frac{2\pi}{n_s^{\frac{1}{3}} L} \left| \sum_{p_1=-n_s^{1/3}/2+1}^{n_s^{1/3}/2} p_1 e^{i2\pi n_s^{-1/3} p_1 \Delta_1} \left(\sum_{p_2,p_3=-n_s^{1/3}/2+1}^{n_s^{1/3}/2} e^{i2\pi n_s^{-1/3}(p_2\Delta_2+p_3\Delta_3)} \right) \right| \\
&\leq \frac{2\pi}{n_s^{\frac{1}{3}} L} \left(\sum_{p_1=-n_s^{1/3}/2+1}^{n_s^{1/3}/2} |p_1| \left| \sum_{p_2,p_3=-n_s^{1/3}/2+1}^{n_s^{1/3}/2} e^{i2\pi n_s^{-1/3}(p_2\Delta_2+p_3\Delta_3)} \right| \right) \\
&\in O\left(\frac{1}{n_s^{\frac{1}{3}} L} \left(\sum_{p_1=-n_s^{1/3}/2}^{n_s^{1/3}/2} |p_1| (1+\delta_{\Delta_2,0} n_s^{1/3})(1+\delta_{\Delta_3,0} n_s^{1/3}) \right) \right) \\
&\subseteq O\left(\frac{1}{n_s^{\frac{1}{3}} L} \left(\frac{n_s^{1/3}}{2} \left(\frac{n_s^{1/3}}{2} + 1 \right) (1+\delta_{\Delta_2,0} n_s^{1/3})(1+\delta_{\Delta_3,0} n_s^{1/3}) \right) \right) \\
&\subseteq O\left(\frac{n_s^{1/3}}{L} (1+\delta_{\Delta_2,0} n_s^{1/3})(1+\delta_{\Delta_3,0} n_s^{1/3}) \right) \qquad (4.45)
\end{aligned}$$

By symmetry, the exact same bound holds by permuting the labels of the indices,

$$|T_{\vec{x},\vec{y}}^{(\chi,\chi)}| \in O\left(\frac{n_s^{1/3}}{L} (1+\delta_{\Delta_{\chi+1 \bmod 3+1},0} n_s^{1/3})(1+\delta_{\Delta_{\chi+2 \bmod 3+1},0} n_s^{1/3}) \right) \qquad (4.46)$$

The exact same argument can be applied to find a similar expression for $|T_{\vec{x},\vec{y}}^{(\chi,\xi)}|$ for $\xi \neq \chi$. Specifically, it can be shown that for each χ, ξ there exist $f, g \in \{1,2,3\}$ such that

$$|T_{\vec{x},\vec{y}}^{(\chi,\xi)}| \in O\left(\frac{n_s^{1/3}}{L} (1+\delta_{\Delta_f,0} n_s^{1/3})(1+\delta_{\Delta_g,0} n_s^{1/3}) \right) \qquad (4.47)$$

Next it is straight forward to see that for each of the n_s terms in H_m, their coefficients are at most m. The situation for H_{int} is a little more complicated since the coefficients for a given term vary with the distance between $\vec{x}, \vec{y}$. It is useful for us to envision a probability distribution over the possible coefficients that emerge in the expansion. Let V be a random variable drawn from a uniform distribution over upper bounds on the coefficients of T. It follows from the above discussion that there exist constants κ_1 and κ_2 such that the distribution on the upper bounds on the coefficients for the creation operators in the potential term obeys

$$P(V \leq (\kappa_1 e^2/L) \in O(1), \qquad P(V \geq (\kappa_2 e^2 n_s^{1/3}/L)) \in O(1/n_s). \tag{4.48}$$

Thus we have that the expectation value of V satisfies

$$\mathbb{E}(V) \in O\left(\frac{e^2}{L}\right) \tag{4.49}$$

Similarly, from the previous discussion it follows that if we define W to be a random variable found by sampling $T_{\vec{x},\vec{y}}^{(\chi,\xi)}$ we find that there exist constants K_1, K_2, K_3, K_4 such that the sampled upper bound on the coefficients reads

$$P\left(W \leq \left(\frac{K_1 n_s^{\frac{1}{3}}}{L}\right)\right) \in O(1), \qquad P\left(W \in \left[\frac{K_2 n_s^{2/3}}{L}, \frac{K_3 n_s^{2/3}}{L}\right]\right) \in O(1/n_s^{1/3}),$$
$$P\left(W \geq \left(\frac{K_4 n_s}{L}\right)\right) \in O(1/n_s^{2/3}) \tag{4.50}$$

Hence the expectation value of W satisfies

$$\mathbb{E}(W) \in O\left(\frac{n_s^{1/3}}{L}\right). \tag{4.51}$$

Thus since $W > 0$ we have from Chebyshev's inequality that for any constant $\delta > 0$, $P(W \geq \delta\mathbb{E}(W)) \in O(1/\delta)$. Thus from the union bound for independent and identically distributed variables $W_1, \ldots, W_N$, $P(W_1 \cdots W_N \geq \delta\mathbb{E}(W)^N) \in O(N/\delta)$. Therefore taking $\delta \in \Theta(n_s^{\lambda N})$ for some constant $\lambda > 0$ yields $P(W_1 \cdots W_N \geq (n_s^{\lambda}\mathbb{E}(W))^N) \in O(N n_s^{-\lambda N})$. Thus because $W \in O(n_s/L)$ for all inputs,

$$W^N \in N\mathbb{E}(W)^{N+O(1)}. \tag{4.52}$$

The exact same reasoning implies that V^N is similarly bounded.

Now let us consider all commutators consisting of N_m mass terms, N_{ext} external potential terms, N_T kinetic terms and N_V two-body interaction terms. Each such commutator is a Lie-product between even monomials of creation and annihilation operators of degree at most 4. Each commutator at most doubles the number of terms in the polynomial and increases the degree of each monomial by at most 4. For example, we have that if $\phi_{s_1}\phi_{s_2}\phi_{s_3}\phi_{s_4}$

is a monomial taken from the set $\phi \in \{a_1^\dagger, a_1, \ldots, a_{n_s}^\dagger, a_{n_s}, 1\}$ that for any polynomial in the creation and annihilation operators of degree d, P, which can be expressed as $P = \sum_j c_j \phi_{\sigma_{j,1}} \cdots \phi_{\sigma_{j,d}}$ we have that

$$\begin{aligned}
[\phi_{s_1}\phi_{s_2}\phi_{s_3}\phi_{s_4}, P] &= \sum_j c_j [\phi_{s_1}\phi_{s_2}\phi_{s_3}\phi_{s_4}, \phi_{\sigma_{j,1}} \cdots \phi_{\sigma_{j,d}}] \\
&= \sum_{j:\{\phi_s\}\bigcap\{\phi_{\sigma_{j,1}}\cdots\phi_{\sigma_{j,d}}\}\not\subseteq\{\emptyset,1\}} c_j [\phi_{s_1}\phi_{s_2}\phi_{s_3}\phi_{s_4}, \phi_{\sigma_{j,1}} \cdots \phi_{\sigma_{j,d}}] \qquad (4.53)
\end{aligned}$$

Therefore there exists a polynomial Q of degree at most $d+4$ in the elements of ϕ and a sequence $\Sigma_{\ell,j}$ such that

$$Q = \sum_\ell \gamma_\ell \phi_{\Sigma(\ell,1)} \cdots \phi_{\Sigma(\ell,d+4)} = [\phi_{s_1}\phi_{s_2}\phi_{s_3}\phi_{s_4}, P], \qquad (4.54)$$

where $\max(|\gamma_\ell|) = \max(|c_j|)$ and $|\{\gamma_\ell\}| \le 2|\{c_j : \{\phi_s\}\bigcap\{\phi_{\sigma_{j,1}} \cdots \phi_{\sigma_{j,d}}\} \not\subseteq \{\emptyset, 1\}\}| \le 2|\{c_j\}|$ If we consider an initial term P_0 to be of the form $\phi_{t_1}\phi_{t_2}\phi_{t_3}\phi_{t_4}$ then it is easy to validate that follows that for any $\phi_{s_1}\phi_{s_2}\phi_{s_3}\phi_{s_4}$, $[\phi_{t_1}\phi_{t_2}\phi_{t_3}\phi_{t_4}, c\phi_{s_1}\phi_{s_2}\phi_{s_3}\phi_{s_4}]$ is at most an eighth-order polynomial with coefficients at most c. Therefore we have by induction that for any sequence χ

$$\|[\phi_{\chi_{1,\ell}}\phi_{\chi_{2,\ell}}\phi_{\chi_{3,\ell}}\phi_{\chi_{4,\ell}}, [\cdots, [\phi_{\chi_{1,2}}\phi_{\chi_{2,2}}\phi_{\chi_{3,2}}\phi_{\chi_{4,2}}, \phi_{\chi_{1,1}}\phi_{\chi_{2,1}}\phi_{\chi_{3,1}}\phi_{\chi_{4,1}}]\cdots]]\| \le 2^\ell \max_j \|\phi_j\|^{4\ell} = 2^\ell \qquad (4.55)$$

Setting $\ell = N_m + N_{\text{ext}} + N_T + N_V$ we find that It therefore follows that the expectation value over indices $\vec{x}, \vec{y}$ norm of the commutators of such terms is with constant probability greater than 2/3, from the triangle inequality, Eq. 4.52 and the sub-multiplicative property of the operator norm, in

$$\begin{aligned}
&O(2^\ell \|H_m + H_{L,ext}\|^{N_m+N_{ext}} (N_T N_V)(\mathbb{E}(V))^{N_T} \mathbb{E}(W)^{N_V}) \\
&\subseteq 2^{N_m+N_{ext}+N_T+N_V} N_T N_V (m + e \max_{\vec{x}} \|A^{ex}(x)\|)^{N_m+N_{ext}} (\max(\kappa_1, \kappa_2) e^2/L)^{N_T+O(1)} \\
&\qquad \times (\max(K_1, K_2, K_3, K_4)/(n_s^{1/3} L))^{N_V+O(1)}) \\
&\subseteq 3^{N_m+N_{ext}+N_T+N_V} (m + e \max_{\vec{x}} \|A^{ex}(x)\|)^{N_m+N_{ext}} (\max(\kappa_1, \kappa_2) e^2/L)^{N_T+O(1)} \\
&\qquad \times (\max(K_1, K_2, K_3, K_4)/(n_s^{1/3} L))^{N_V+O(1)}) \qquad (4.56)
\end{aligned}$$

The maximum number of non-zero commutators that can arise in the commutator series can be bounded using the following argument. Let us consider the simplest non-trivial commutator which is of the form $[a_x^\dagger a_y, a_u^\dagger a_v]$. There are clearly $O(n_s^4)$ possible combinations. However, unless the sets $\{x, y\}$ and $\{u, v\}$ have a non-empty intersection the commutator is zero. Therefore there are actually $O(n_s^3)$ rather than $O(n_s^4)$ possible non-zero commutators of this form. Iterating this, it is clear that there are $O(n_s^4)$ non-zero commutators of the form $[a_s^\dagger a_u, [a_x^\dagger a_y, a_u^\dagger a_v]]$. In general it follows by induction that for the k-fold nested commutator (if $k \in O(1)$) that there are at most n_s^{1+k} such terms.

The situation is even more constrained with terms that arise from the external potential as well as the mass. Such terms consist of creation and annihilation operators that only act on one fermion site (and 4 potential components). Therefore for each such term introduced the site must match one of the other terms in the commutator product otherwise the commutator will be zero. Thus the number of non-zero commutators in a k-fold nested commutator series, where $k \in O(1)$, is also in $O(1)$.

Thus combining these two observations we see that the total number of non-zero commutators that can be formed from a general product is in

$$O(n_s^{1+N_V+N_T}) \tag{4.57}$$

Thus the sum over all terms formed by these commutators is simply the number of commutators multiplied by the expectation value of the coefficients. We can use the expression in Eq. 4.56 to estimate the sum over all commutators by simply multiplying the mean by the number of commutator terms in Eq. 4.57 this yields

$$O\left(n_s 3^{N_m+N_{ext}+N_T+N_v}\left(m + e\max_x \|A^{ex}(x)\|\right)^{N_m+N_{ext}}\left(\frac{e^2 n_s}{L}\right)^{N_T+O(1)}\left(\frac{n_s^{4/3}}{L}\right)^{N_V+O(1)}\right) \tag{4.58}$$

Next let $\Lambda := \max\left(m + e\max_x \|A^{ex}(x)\|, \frac{e^2 n_s}{L}, \frac{n_s^{4/3}}{L}\right)$. The sum of over all commutators with $N_m + N_{ext} + N_T + N_v = \ell$ is then in

$$n_s \Lambda^{\ell+O(1)} e^{O(\ell)} \tag{4.59}$$

Therefore the size of any commutator that arises from the expansion of the error in the Trotter-Suzuki formula, using time-step t, is in

$$n_s(\Lambda t)^\ell e^{O(\ell)} \tag{4.60}$$

It then follows from Theorem 11 of [234] that the Trotter-Suzuki error for a p^{th} order formula is therefore in

$$\Delta_{TS}(p) \in n_s(\Lambda t)^{p+1} e^{O(p)}. \tag{4.61}$$

Thus we can choose t such that the error, Δ_{TS} is at most ϵ_{TS} for

$$t \in O\left(\frac{1}{\Lambda}\left(\frac{\epsilon_{TS}}{n_s \Lambda^{O(1)}}\right)^{1/(p+1)}\right) \tag{4.62}$$

Next note that each product formula of order p consists of a product of $5^{p/2-1}$ second-order Trotter formulas. Each such product formula is composed of $O(n_s^2)$ exponentials. Therefore we have that the number of exponentials in the product formula is [22]

$$N_{\text{exp}} = O\left(n_s^2 5^{p/2-1}\right) \tag{4.63}$$

Next let $U_{\text{TS}}(t)$ be the Trotter-Suzuki formula for e^{-iHt}. If we apply phase estimation to $U_{\text{TS}}(t)$ the eigenvalues returned are, with high probability, those of Ht. Therefore if we wish to estimate the eigenvalues of H within error $O(\epsilon_{\text{TS}})$ the phase estimation protocol requires $O(1/(\epsilon_{\text{TS}} t)$ repetitions.

The cost of performing phase estimation and estimating the energy within error $\epsilon = \Theta(\epsilon_{TS} t)$ and probability of failure $\delta < 1/3$ is in

$$O\left(\frac{N_{\text{exp}}}{\epsilon_{\text{TS}} t}\right) \subseteq O\left(\frac{n_s^{2+1/(p+1)} \Lambda^{1+o(1)} 5^{p/2}}{\epsilon_{\text{TS}}^{1+1/(p+1)}}\right) \tag{4.64}$$

In practice, however, we only guarantee that $\|e^{-iHt} - U_{\text{TS}}(t)\| \le \epsilon_{\text{TS}}$ and need to ensure that the errors in the eigenvalues of the unitaries are comparable. The necessary result follows from Theorem 6.3.2 of [235] and using this result and the fact that unitary matrices are unitarily diagonalizable that if $\lambda_x(\cdot)$ is the x^{th} eigenvalue of a matrix then for any x there exists a y such that

$$\epsilon := |\lambda_x(e^{-iHt}) - \lambda_y(U_{\mathrm{TS}}(t))| \leq \|e^{-iHt} - U_{\mathrm{TS}}(t)\| \leq \epsilon_{TS}. \tag{4.65}$$

We then have ,that after optimizing over the value of p as per [22] the number of exponentials needed for the simulation is in

$$O\left(\frac{N_{\mathrm{exp}}}{\epsilon_{\mathrm{TS}}t}\right) \subseteq \left(\frac{\Lambda^{1+o(1)}n_s^{2+o(1)}}{\epsilon_{TS}^{1+o(1)}}\right). \tag{4.66}$$

Gate complexity estimates then easily follow from Eq. 4.66. The exponential that requires the most T-gates to simulate is given in Fig. 4.4. It consists of 8 Pauli operations. From Box 4.1 of Nielsen and Chuang [14], it suffices to synthesize each rotation within error $\epsilon_{\mathrm{TS}}/N_{\mathrm{exp}}$. Using an optimal synthesis method, such as [236, 237] this can be achieved using $O(\log(N_{\mathrm{exp}}/\epsilon_{\mathrm{TS}}))$ T-gates. Therefore the number of T-gates needed for the simulation is in

$$N_T \in \left(\frac{\Lambda n_s^2}{\epsilon_{TS}}\right)^{1+o(1)}. \tag{4.67}$$

□

A key assumption in eQED is that the mass energy of the electrons dominates the momentum contributions. This is necessary because the derivation of eQED truncates the path integral expansion of the propagator at second order. The case that most closely resembles the canonical case in the electronic structure literature is where $n_s^{1/3}/L \ll m \ll n_s^{4/3}/L$ [215, 238, 181]. In this case, the Trotter error is dominated by the momentum of the terms in the Hamiltonian and the number of T gates needed for the simulation scales as $N_T \in (n_s^{10/3}/L\epsilon)^{1+o(1)}$. If we consider the thermodynamic limit where $L \in \Theta(n_s^{1/3})$, we then have that $N_T \in (n_s^3/\epsilon)^{1+o(1)}$. This result is comparable to some of the earlier results for simulations of electronic structure in local-bases [215], but does not precisely match these bounds because of the use of the SLAC kinetic operator, which is much less local than the corresponding kinetic operator used in planewave-dual simulations [215, 234].

4.4.2 Cost Estimates for Momentum Basis Simulations using Trotter

The calculation of the norm of the nested commutators for the momentum space Hamiltonian are needed to estimate the Trotterization error for the momentum space simulation. Fortunately, these nested commutators are much easier to evaluate than their position space brethren because of the lack of summation over auxiliary indices in the definition of the interaction and constraint terms in the Hamiltonian.

Theorem 2. *Let H_p be the momentum space effective QED Hamiltonian of Eq. 4.16 and Eq. 4.22 in three spatial dimensions in a cavity of volume L^3 with electrons with mass m and charge $e \in O(1)$ and external vector potential A^{ex} such that for any momentum mode within $|p\rangle$ within the reciprocal lattice $|E_p - m| \in o(1)$. There exists a quantum algorithm that when provided a state $|\psi\rangle$ such that $H_p|\psi\rangle = E|\psi\rangle$ can estimate E within error ϵ for any $\epsilon > 0$ and failure probability at most $1/3$ using a number of T-gates that is in*

$$\left(\frac{n_s^3 \Lambda_p}{\epsilon}\right)^{1+o(1)},$$

where $\Lambda_p = O\left(n_s\left(\frac{m}{n_s} + \frac{e^2 n_s}{L} + e|A^{ex}|\right)\right)$.

Proof. The Hamiltonian is the sum of three terms, the kinetic energy term, the electron-electron interaction term and the external potential term. First let us consider the kinetic term, which is trivial in a momentum basis

$$H = \sum_{\sigma,\nu} C_{\sigma,\nu}(a^\dagger_{\sigma,\nu} a_{\sigma,\nu} + b^\dagger_{\sigma,\nu} b_{\sigma,\nu}) \tag{4.68}$$

where

$$C_{\sigma,\nu} := E_\nu = \sqrt{m^2 + \frac{4\pi^2}{L^2}|\vec{\nu}|^2} \in \Theta(m) \tag{4.69}$$

The two-body interactions are much more complicated in momentum representation. For example, the fermion-fermion interaction can be written as

$$\sum_{p,q,r,\sigma_1,\sigma_2,\sigma_3,\sigma_4} e^2 D_{p,q,r,\sigma_1,\sigma_2,\sigma_3,\sigma_4} a^\dagger_{(p+q-r),\sigma_4} a^\dagger_{r,\sigma_3} a_{q,\sigma_2} a_{p,\sigma_1}, \tag{4.70}$$

where

$$|D_{p,q,r,\sigma_1,\sigma_2,\sigma_3,\sigma_4}| \leq \frac{\mathcal{M}}{4L^3\sqrt{E_{p+q-r}E_rE_pE_q}} \in \Theta\left(\frac{\mathcal{M}}{L^3m^2}\right). \tag{4.71}$$

Here for convenience we take $\mathcal{M}$ an upper bound on the values of the coefficients in Eq. F.1, Eq. F.2, Eq. F.3, Eq. F.4 and Eq. F.5. By doing, so we make the result of Eq. 4.71 hold for all the two body interactions in the problem. First, we see that (in units where $e = 1$)

$$\begin{aligned}\mathcal{M} &\in O\left(\max_{p,q}\left(\frac{\max_j\{\|u_j(p)\|^4, \|v_j(p)\|^4\}}{|(E_p - E_q)^2 - \frac{4\pi^2}{L^2}|\vec{p} - \vec{q}|^2|}\right)\right)\\ &\subseteq O\left(\max_p\left(\frac{(E_p + m)^2}{\min_q|(E_p - E_q)^2 - |\vec{p} - \vec{q}|^2/L^2|}\right)\right) \subseteq O\left(m^2L^2\right)\end{aligned} \tag{4.72}$$

Therefore

$$|D_{p,q,r,\sigma_1,\sigma_2,\sigma_3,\sigma_4}| \in O\left(\frac{1}{L}\right). \tag{4.73}$$

The exact same scaling holds by inspection for every two body term in the momentum space Hamiltonian.

The external potential (in momentum space) is given by Eq. 4.22. The Hamiltonian in this case can be chosen (in units where $e = 1$) to be

$$H_{p,ext} = \sum_{\sigma_1,\sigma_2,p,q} E_{\sigma_1,\sigma_2,p,q}a_p^\dagger a_q \tag{4.74}$$

where

$$|E_{\sigma_1,\sigma_2,p,q}| \in O\left(\frac{\max_p|u_p|^2e\max|A^{ex}|}{m}\right) \subseteq O\left(\frac{\max_p(E_p + m)e\max|A^{ex}|}{m}\right) \subseteq O(e|A^{ex}|). \tag{4.75}$$

Next let us consider a Lie-Polynomial of kinetic, mass, interaction and external potential terms consisting of $N_m, N_{\text{ext}}, N_T, N_V$ mass, external potential, kinetic and two-body interaction terms. As noted above, the indices for each mass term must match the indices of existing terms in the polynomial; whereas all other terms must match at least one term. Therefore the total number of valid commutators that can be present is in

$$O(n_s^{1+N_{\text{ext}}+2N_V}). \tag{4.76}$$

Next, let us assume that $N_{\text{ext}} + N_T + N_V = \ell$. We can then see that the sum of all nested commutators of order ℓ is in

$$
\begin{aligned}
&O\left(2^\ell(\max_{\sigma,\nu}|C_{\sigma,\nu}|^{N_T}\max_{p,q,r,\sigma_1,\sigma_2,\sigma_3,\sigma_4}|D_{p,q,r,\sigma_1,\sigma_2,\sigma_3,\sigma_4}|^{N_v}+\max_{p,q,\sigma_1,\sigma_2}|E_{p,q,\sigma_1,\sigma_2}|^{N_{ext}}n_s^{1+N_{ext}+2N_V})\right)\\
&\subseteq O\left((2n_s)^\ell\left(\frac{(\max_{\sigma,\nu}|C_{\sigma,\nu}/n_s|}{n_s}\right)^{N_T}\max_{p,q,r,\sigma_1,\sigma_2,\sigma_3,\sigma_4}(e^2|D_{p,q,r,\sigma_1,\sigma_2,\sigma_3,\sigma_4}|)^{N_v}\left(n_s\max_{p,q,\sigma_1,\sigma_2}|E_{p,q,\sigma_1,\sigma_2}|\right)^{N_{ext}}\right)
\end{aligned}
\tag{4.77}
$$

Next if we let

$$
\begin{aligned}
\Lambda_p &:= \max\left\{\frac{\max_{\sigma,\nu}|C_{\sigma,\nu}/n_s|}{n_s}, \max_{p,q,r,\sigma_1,\sigma_2,\sigma_3,\sigma_4}e^2|D_{p,q,r,\sigma_1,\sigma_2,\sigma_3,\sigma_4}|, n_s\max_{p,q,\sigma_1,\sigma_2}|E_{p,q,\sigma_1,\sigma_2}|\right\}\\
&\in O\left(n_s\left(\frac{m}{n_s}+\frac{e^2n_s}{L}+e\max|A^{ex}|\right)\right)
\end{aligned}
\tag{4.78}
$$

We then have from Theorem 11 of [234] that the error in the p^{th}-order Trotter-Suzuki formula is

$$
\Delta_{TS}(p) \in n_s(\Lambda_p t)^{p+1}e^{O(p)}. \tag{4.79}
$$

Thus if we wish to have $\Delta_{TS}(p) \le \epsilon_{TS}$ then it suffices to choose

$$
t \in \Theta\left(\frac{1}{\Lambda_p}\left(\frac{\epsilon_{TS}}{n_s}\right)^{1/(p+1)}\right) \tag{4.80}
$$

We can then invoke Eq. 4.65 to show that this corresponds to a systematic error of at most ϵ_{TS} in the eigenvalues of e^{-iHt} that arises from the Trotter-Suzuki approximation. Let us define the correct eigenphase that we would see from phase estimation to be Et and the approximate phase $\widetilde{E}_{TS}t$. This means we can use phase estimation on the Trotter-Suzuki approximation to learn the eigenphase $\widetilde{E}_{TS}t$ within error $\epsilon_{TS}t$ and probability of failure less than 1/3 using $O(1/\epsilon_{TS}t)$ applications of the Trotter-Suzuki formula [239]. Thus the total number of operator exponentials that need to be invoked in the simulation in order to learn the $\widetilde{E}t$ within error $O(\epsilon_{TS}t)$ is in

$$
O\left(\frac{N_{\text{exp}}}{\epsilon_{\text{TS}}t}\right) \subseteq O\left(\frac{n_s^{3+1/(p+1)}\Lambda_p 5^{p/2}}{\epsilon_{\text{TS}}^{1+1/(p+1)}}\right), \tag{4.81}
$$

Provided that $t(\|H\| + \epsilon_{TS}) \leq \pi$, we can unambiguously infer E from this result by taking

$$E = \frac{\widetilde{E}t}{t} + O(\epsilon_{TS}), \tag{4.82}$$

which implies that this estimate also suffices to provide E within error $O(\epsilon_{TS})$ with probability at least $2/3$.

The final step involves following the reasoning laid out in [22, 234] to choose p to minimize the number of operator exponentials needed to achieve error $\epsilon \geq \epsilon_{\mathrm{TS}}$. This corresponds to taking $p \in O(\sqrt{\log(n_s t/\epsilon)})$, which when substituted into Eq. 4.81 leads to a number of operator exponentials that scales as $(\frac{n_s^3 \Lambda_p}{\epsilon})^{1+o(1)}$, where $(\cdot)^{o(1)}$ is used to refer to factors that are at most sub-polynomial (but not necessarily poly-logarithmic).

We then see from our circuit constructions that each operator exponential requires a number of T gates that scales as $O(\log(n_s \Lambda t/\epsilon))$ thus the number of T-gates required by the simulation obeys

$$N_T \in \left(\frac{n_s^3 \Lambda_p}{\epsilon}\right)^{1+o(1)}. \tag{4.83}$$

□

The asymptotics of the simulation complexity in momentum space are interesting for a number of reasons. First, let us consider the case where the two-body interaction term dominates the Trotter-Suzuki error. This occurs when $\frac{n_s^{1/3}}{L} \ll m \ll \frac{n_s^2}{L}$. Note that we require that the lower bound hold in order to justify the assumptions in Theorem 2 as well as to ensure that we remain in the situation where effective QED, rather than full QED, is appropriate. In the thermodynamic limit, we take $L \propto n_s^{1/3}$ and therefore have that

$$N_T^{therm} \in \left(\frac{n_s^{4+2/3}}{\epsilon}\right)^{1+o(1)} \tag{4.84}$$

The continuum limit, unfortunately, is not naturally defined without making further promises on the system. This is because in the continuum limit we need to take $L \in o(n_s^{1/3})$, which leads to momentum modes where the kinetic contribution to the energy dominates the mass energy. Such modes invalidate our assumptions and so effective QED cannot be considered valid in the continuum limit for finite mass electrons without imposing restrictions on the input state. Taking the continuum limit is also complicated by the issue of renormalization. To ensure the electron mass takes the correct value and the potential between two electrons has the correct $1/r$ dependence, the electron mass and charge in the Hamiltonian must be varied as a function of the lattice spacing. For the continuum limit of QED, this leads to the electron charge being forced to zero as the lattice spacing goes to zero. This is known as triviality and is due to QED likely not being a valid interacting field theory when defined without a cutoff [240, 241, 242, 243].

4.4.3 Cost Estimates for Qubitization

In recent years, qubitization has emerged as an alternative to Trotter-Suzuki simulations on fault tolerant hardware [244, 18, 245, 246, 180, 181]. Unlike Trotter-Suzuki methods, qubitization is known to saturate lower bounds on the query complexity for quantum simulation. Further, it is much simpler to provide tight bounds for the complexity of simulation using qubitization [229]. However, qubitization is not space optimal and further cannot directly exploit locality of the Hamiltonian to reduce the costs of simulation unlike Trotter-Suzuki methods. For these reasons, qubitization does not supplant Trotter-Suzuki methods but rather provide us with a new set of tools that can perform favorably to Trotter-Suzuki methods under certain circumstances.

The central idea of qubitization is that a walk operator, $W \in \mathbb{C}^{(N+M)\times(N+M)}$, can be constructed for any Hamiltonian such that if $H = \sum_j \lambda_j H_j \in \mathbb{C}^{N\times N}$ for unitary H_j then for every eigenvector $|\psi\rangle$ of H and any integer q, $W^q |\psi\rangle |0\rangle^M$ is a vector within a two dimensional subspace spanned by the non-orthogonal vectors $|\psi\rangle |0\rangle^M$ and $W |\psi\rangle |0\rangle^M$. Further let $\lambda = \sum_{j=1}^m |\lambda_j|$. With these assumptions in place, if we define $|\psi\rangle^\perp$ to be the orthogonal component of $W |\psi\rangle |0\rangle^M$ within this two dimensional subspace then within the basis $|\psi\rangle |0\rangle^M$ and $\left|\psi^\perp\right\rangle$

the walk operator restricted to this two-dimensional subspace then takes the form

$$(|\psi\rangle\langle\psi| \otimes |0\rangle\langle 0| + |\psi^\perp\rangle\langle\psi^\perp|)W(|\psi\rangle\langle\psi| \otimes |0\rangle\langle 0| + |\psi^\perp\rangle\langle\psi^\perp|) = \begin{bmatrix} \frac{\langle\psi|H|\psi\rangle}{\lambda} & -\sqrt{1-\frac{\langle\psi|H|\psi\rangle^2}{\lambda^2}} \\ \sqrt{1-\frac{\langle\psi|H|\psi\rangle^2}{\lambda^2}} & \frac{\langle\psi|H|\psi\rangle}{\lambda} \end{bmatrix} \tag{4.85}$$

which is isospectral (within this two-dimensional space) to the rotation $e^{-iY\cos^{-1}(\langle\psi|H|\psi\rangle/\lambda)}$.

This shows that we can estimate the eigenvalues of H, given knowledge of λ, we can then construct an estimator $\hat{E}$ for the energy from an estimator for the phase $\hat{\phi}$ using [246, 247]

$$\hat{E} = \lambda\cos\left(\hat{\phi}\right). \tag{4.86}$$

Thus the energy can be estimated within error ϵ using $O(\lambda/\epsilon)$ applications of W [246]. The position space normalization can be found by examining the Jordan-Wigner representation of each of the terms individually. Specifically, we have that for each $\vec{x}$ $a^\dagger_{\vec{x}}$ is expressed as a sum of 2 Pauli-operators in the Jordan-Wigner representations. Since Pauli operators are unitary we can compute the asymptotic scaling of any term in the Hamiltonian by treating the fermionic operators as if they were unitary because only constant factors are introduced by expanding the Jordan-Wigner representaiton. We further have that $\lambda = \lambda_m + \lambda_{ext} + \lambda_{int} + \lambda_{SLAC}$, which are the contributions to the normalization terms from the mass, external vector potential and the kinetic operator. These expressions are straight forward to compute

$$\begin{aligned} H_m &= \sum_{\vec{x}} m a^\dagger_{\vec{x}}\gamma^0 a_{\vec{x}} \Rightarrow \lambda_m \in O(mn_s) \\ H_{L,ext} &= \sum_{\vec{x}} e a^\dagger_{\vec{x}}\gamma^0\gamma^\mu A^{ex}_\mu(\vec{x}) a_{\vec{x}} \Rightarrow \lambda_{ext} \in O\left(n_s e \max_{\vec{x}} |A^{ex}(\vec{x})|\right) \\ H_{SLAC} &= \frac{2\pi}{n_s^{1/3}L}\sum_{\vec{x},\vec{y},\vec{p}} e^{-i2\pi n_s^{-1/3}\vec{p}\cdot(\vec{x}-\vec{y})} a^\dagger_{\vec{x}}\gamma^0\gamma^j p_j a_{\vec{x}} \Rightarrow \lambda_{SLAC} \in O\left(\frac{n_s^{5/3}}{L}\right) \\ H_{int} &= \sum_{\vec{x}\neq\vec{y}}\sum_{\mu,\nu} g_{\mu\mu}\frac{n_s^{1/3}e^2}{8\pi L|\vec{x}-\vec{y}|}(a^\dagger_{\vec{x}}\gamma^0\gamma^\mu a_{\vec{x}})(a^\dagger_{\vec{y}}\gamma^0\gamma^\nu a_{\vec{y}}) \Rightarrow \lambda_{int} \in O\left(\frac{n_s^2 e^2}{L}\right), \end{aligned} \tag{4.87}$$

where the last expression in Eq. 4.87 follows from the average over position of $1/|\vec{x}-\vec{y}|$ given in Eq. 4.49. We therefore have that the normalization constant in position space eQED is

$$\lambda_{pos} \in O\left(mn_s + n_s e \max_{\vec{x}} |A^{ex}(\vec{x})| + (n_s^{-1/3} + e^2)\frac{n_s^2}{L})\right) \tag{4.88}$$

It is straight forward to compute the values of λ for the momentum space formalism for eQED under worst-case assumptions about the functional form of the external vector potential $A^{ex}(x)$:

$$\lambda_{mom} \in O\left(mn_s + \frac{n_s^3}{L} + n_s^2 e \max_{\vec{x}} |A^{ex}(\vec{x})|\right) \tag{4.89}$$

More specifically, the walk operator is constructed from a pair of unitary operations `SELECT` and `PREPARE`. For simplicity let us assume without loss of generality that $\lambda_j \geq 0$ (any signs or phases can be absorbed into the H_j). The operator `PREPARE` is defined to prepare an initial state

$$\texttt{PREPARE}\left|0\right\rangle = \frac{1}{\sqrt{m}}\sum_j \sqrt{\frac{\lambda_j}{\lambda}}\left|j\right\rangle . \tag{4.90}$$

Note the operation of `PREPARE` on states other than $|0\rangle$ is not specified here because any unitary matrix that satisfies Eq. 4.90 can be used to construct the walk operator W.

The action of select is similarly defined via

$$\texttt{SELECT}\left|j\right\rangle\left|\psi\right\rangle = \left|j\right\rangle H_j \left|\psi\right\rangle . \tag{4.91}$$

The walk operator W is then defined to be

$$W := (1 - 2\texttt{PREPARE}\left|0\right\rangle\!\left\langle 0\right| \texttt{PREPARE}^\dagger)\texttt{SELECT}. \tag{4.92}$$

It is then clear from this exposition that the cost of performing the quantum simulation depends directly on two quantities: the normalization constant λ and the costs of performing `SELECT` and `PREPARE`. The costs, however, depend sensitively on the construction used for these two operations and the circuit constructions for the two operations are complicated relative to those used in Trotter-Suzuki simulations.

For simplicity, we will adapt the construction of [238, 246] which was derived for simulations of non-relativistic chemistry in an arbitrary basis to the relativistic case considered here. The prepare circuit is implemented using a memory access model known as a QROM, which can be thought of as an oracle replacement that uses a lookup table to store each of the unique amplitudes in the state `PREPARE` $|0\rangle$. If there are K such amplitudes then the cost of preparing the state within error ϵ is in $O(K + \log(1/\epsilon))$ using the approach outlined in Section 3.D of [246].

The number of unique coefficients in the position space Hamiltonian, K_{pos}, is substantially lower than the number of of terms in the Hamiltonian. While the number of terms in the postion space Hamiltonian is in $O(n_s^2)$ only $O(n_s)$ of these can take unique values. This can easily be seen from Eq. 4.87 wherein H_m only takes $O(1)$ values, $H_{L,ext}$ takes at most $O(n_s)$ values (assuming each $A^{ex}(\vec{x})$ is unique). H_{SLAC} contains $O(n_s^{2/3})$ unique exponentials of the form $e^{-i2\pi n_s^{-1/3}\vec{p}\cdot(\vec{x}-\vec{y})}$ and $O(n_s^{1/3})$ values of p_j. Thus the total number of distinct amplitudes for H_{SLAC} is at most in $O(n_s)$ as well. Finally the fermion-fermion interaction consists of only $O(n_s^{1/3})$ distinct values and hence

$$K_{pos} \in O(n_s). \tag{4.93}$$

The number of unique coefficients in the momentum space Hamiltonian is much more challenging to analyze and such simple patterns in the magnitudes of the coefficients do not naturally reveal themselves. As such, we use the trivial bound of

$$K_{mom} \in O(n_s^3). \tag{4.94}$$

It is likely, however, that by refactoring the momentum space Hamiltonian using techniques analogous to [248] that a substantial reduction in K_{mom} may be attainable.

The last piece that needs to be considered is the implementation of `SELECT`. The approach that we use again mirrors the presentation in Fig. 9 of [246]. The strategy we take is to decompose the fermionic operators into Majorana operators of the form $X \otimes Z \otimes \cdots \otimes Z$ and $Y \otimes Z \otimes \cdots Z$. At most four Majorana operators are needed in both position and momentum space and thus the cost of implementing the select operator is $O(1)$ times the cost of applying the selected Majorana operator. The construction in [249] allows such

Majorana operators to be selected in time $O(n_s)$ and therefore the cost of the select circuit is in $O(n_s)$ in both the position and momentum bases. Therefore, with this construction the cost of state preparation dominates the cost of the select circuit.

The number of T-gates needed in the qubitized simulation is therefore the product of the number of applications of W needed by phase estimation and the sum of the number of T-gates needed by the prepare and select circuits. This means that the complexity for the position space simulation under the assumption that $e^2 \gg n_s^{-1/3}$ is

$$N_{T,pos} \in \widetilde{O}\left(\frac{\lambda_{pos}(K_{pos} + n_s)}{\epsilon}\right) \subseteq \widetilde{O}\left(\frac{n_s^2(m + e\max_{\vec{x}}|A^{ex}(\vec{x})| + e^2\frac{n_s}{L})}{\epsilon}\right). \tag{4.95}$$

Similarly, the number of gates needed to perform the momentum space simulation at most scales as

$$N_{T,mom} \in \widetilde{O}\left(\frac{\lambda_{mom}(K_{mom} + n_s)}{\epsilon}\right) \subseteq \widetilde{O}\left(\frac{n_s^4(m + \frac{n_s^2}{L} + n_s e\max_{\vec{x}}|A^{ex}(\vec{x})|)}{\epsilon}\right). \tag{4.96}$$

If we assume the thermodynamic limit, then we have that the scaling of qubitization is upper bounded by $\widetilde{O}(\frac{n_s^{2+2/3}}{\epsilon})$ in position space and $\widetilde{O}(\frac{n_s^{5+2/3}}{\epsilon})$ in momentum space. The scaling of qubitization in position basis is slightly superior to the upper bound on Trotterization's scaling of $(\frac{n_s^3}{\epsilon})^{1+o(1)}$. In momentum basis, the use of a brute force prepare circuit switches this behavior and leads to worse scaling than the $(n_s^{4+2/3}/\epsilon)^{1+o(1)}$ scaling provided by Trotter formulas. This bound, however, is likely pessimistic and by taking advantage of symmetries in the Hamiltonian terms it is likely that the number of unique coefficients can be further compressed.

A final point of interest is that the performance of Trotter-Suzuki methods in the non-relativistic limit may be superior to qubitization. Specifically, if we define the non-relativistic limit to be the case where $m \gg n_s^2/L$, then the scaling of position space simulation using Trotter-Suzuki methods becomes $(n_s^2 m/\epsilon)^{1+o(1)}$. On the other hand, qubitization's cost scales as $\widetilde{O}(n_s^2 m/\epsilon)$ in this limit. Thus for cases where relativistic effects are small, but highly accurate simulations are required then the bounds for Trotterization coincide (up to sub-polynomial factors) with those of qubitization. Further, since the empirical performance of

Trotter-Suzuki methods is often much better than the upper bounds [179, 229] it is natural to suspect that Trotter's performance may be even better than this bound as also noted in the following section.

4.5 Rellium Model Analysis

4.5.1 Numerical Evaluation of Momentum Space Commutators

In this section, we present a numerical study of the momentum space rellium Hamiltonian commutators. We focus on the momentum space Hamiltonian because the rellium Hamiltonian in momentum basis can be constructed utilizing the SymPy software package [250], which allows us to simply construct the spinor interaction terms in the planewave integral calculations. For the following simulations, the cell box size was kept constant at $L = 1$. Each successive model system with different numbers of planewaves n_s, were created by modifying the planewave energy cutoff, E_{cut} within this constant box size. Additionally, renormalization terms in the rellium Hamiltonian, Eq. 4.16, were ignored for simplicity.

In the following result, the expectation value over i, j, k of the nested commutator, also called the second order commutator, $\|[H_i, [H_j, H_k]]\|$ (where $\| \cdot \|$ is the spectral norm) was computed by randomly sampling Hamiltonian terms using Monte Carlo. The indices i, j, k in this case represent any possible term in the Hamiltonian. A total of 8 different rellium systems were used by defining the planewave energy cutoff values at $E_{cut} = 8, 9, 11, 14, 15, 17, 20, 23, 26$ eV which correspond to the number of planewaves being $N = 24, 72, 104, 128, 224, 320, 584, 808, 1216$ respectively. Each average commutator value was computed by running a Monte Carlo simulation with increasing sample numbers in order to evaluate the limit of the average commutator, and then taking the average of the corresponding Monte Carlo runs. Specifically, 13 simulations were performed for each rellium system equally spaced on the logarithmic scale between a minimum of 10^6 and a maximum of 10^{10} samples inclusively. The results of the Monte Carlo simulations are presented in Fig. 4.5, where each data point is the average of all runs for each system, including the

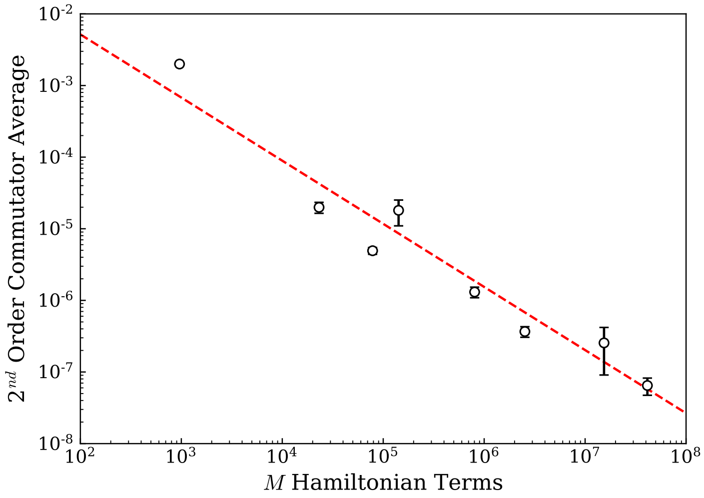

Figure 4.5: The Monte Carlo sampled 2^{nd} order commutator average for different E_{cut} values defining different rellium systems with constant box length $L = 1$. Plotted points are the average value across all Monte Carlo runs, and the error bars denote the standard deviation. The dashed red line corresponds to the least-squares power law fit where $f(M) = 0.3M^{-0.9}$

standard deviation in the error bars. By using a least squares power law fit, we can compare how the number of terms in the Hamiltonian, M, affect the average second order commutator. The power law fit function from the commutator average data in Fig. 4.5, results in $f(M) = 0.3M^{-0.9}$. Using the fact that the number of terms in the Hamiltonian M scales as $O(n_s^3)$ with the number of planewaves, we can naïvely state that the complexity of the second order commutator would scale $O(n_s^9)$. However, since there needs to be at least one index in common between each Hamiltonian term, the upper bound is actually $O(n_s^7)$. We can then see that from our numerical result, the relationship of this complexity is observed to be $\sim O(n_s^4)$, performing better than the upper bound.

4.5.2 Cost Estimate for QPE

The most common goal of Hamiltonian simulation in general is to find ground state energies. By using the above rellium model for analysis, we can gain an understanding of the error scaling throughout the Trotter-Suzuki decomposition, quantum phase estimation (QPE), and T-gate synthesis. First, in the standard surface code model of fault-tolerant quantum computation, all Clifford gates are trivial in cost, where non-Clifford gates such as the T-gate end up dominating the computational cost of an arbitrary circuit. Therefore, we can simply understand the cost of our simulation with the number of R_z gates required, which are typically implemented as a circuit of multiple T-gates.

Second, it is important to note that the problem of finding groundstates is generically hard. Specifically, if we could find a groundstate energy in polynomial time then the complexity class BQP would contain QMA, which is the quantum analog of $\mathsf{P} = \mathsf{NP}$. For this reason, we strongly suspect that the groundstate preparation problem is intractable on quantum computers unless a sufficiently good guess of the groundstate can be provided to the phase estimation algorithm. Although we discuss in the following section strategies that can ammeliorate this problem, it is important to note that we do not necessarily know how well these methods will work with a particular instance of a rellium simulation and hence the only thing we can say with confidence is that the estimates contained here will give the cost of sampling from the spectrum of rellium.

In order to eventually compute the ground state energy tolerance within some precision ϵ, we first need to find out the error scaling in the Trotter-Suzuki (TS) decomposition, ϵ_{TS}. Specifically we will focus on the second order decomposition of our unitary time propagator the error in which is given by [228] to be at most

$$\begin{aligned}\epsilon_{TS} &\leq \frac{t^3}{12}\sum_{\gamma}\left|\left|\left[\sum_{\alpha} H_\alpha, \left[\sum_{\beta} H_\beta, H_\gamma\right]\right]\right|\right| + \frac{t^3}{24}\sum_{\gamma}\left|\left|\left[H_\gamma, \left[\sum_{\beta} H_\gamma, H_\beta\right]\right]\right|\right| \\ &\leq \frac{t^3}{8}\sum_{\gamma,\alpha,\beta} ||[H_\alpha, [H_\beta, H_\gamma]]|| \end{aligned} \tag{4.97}$$

Using Ref. [251], the root-mean-square error in the measured phase during phase estimation can be denoted as the following

$$\Delta\phi \approx \sqrt{\left(\frac{\pi}{2^{n+1}}\right)^2 + \left(\epsilon_{\mathrm{TS}} + \epsilon_{\mathrm{syn}} + \pi\epsilon_{\mathrm{QFT}}\right)^2} \tag{4.98}$$

where n is the number of ancilla qubits used. We will now neglect the cost of the quantum Fourier transform as it needs to be done only once and so ϵ_{QFT} can be taken to be an incredibly small value without altering the time-complexity of the simulation.

$$\Delta\phi \approx \sqrt{\left(\frac{\pi}{2^{n+1}}\right)^2 + (\epsilon_{\mathrm{TS}} + \epsilon_{\mathrm{syn}})^2} \tag{4.99}$$

We can now set the phase error target to be equivalent to the total RMS error in the energy multiplied by the total time propagation t

$$\epsilon = \frac{\Delta\phi}{t} \approx \frac{1}{t}\sqrt{\left(\frac{\pi}{2^{n+1}}\right)^2 + (\epsilon_{\mathrm{TS}} + \epsilon_{\mathrm{syn}})^2} \tag{4.100}$$

For simplicity, we choose $\epsilon_{TS} = \epsilon_{syn} = \pi\sqrt{3}/2^{n+2}$. With this choice we find

$$\epsilon \approx \frac{1}{t}\sqrt{\frac{1}{4}\left(\frac{\pi}{2^n}\right)^2 + \frac{3}{4}\left(\frac{\pi}{2^n}\right)^2} = \frac{\pi}{t2^n}, \tag{4.101}$$

where n is the number of qubits used in the phase estimation routine.

Next, using the fitted function from the Monte Carlo simulation given in Figure 4.5, we can take

$$\sum_{\gamma,\alpha,\beta} |||[H_\alpha, [H_\beta, H_\gamma]]||| \approx \frac{0.3n_s^7}{M^{0.9}} = 0.3n_s^{4.3} \tag{4.102}$$

which we can define as

$$\chi_H = An_s^b \tag{4.103}$$

where $A = 0.3$ and $b = 4.3$. Note that if we assumed the worst case commutator scaling that would be predicted from the commutators would be $b = 7$ for momentum basis simulations. This shows that substantial gaps likely exist between the worst case scalings and the actual scaling for eQED, similar to observations that have already been made for quantum simulations of non-relativistic chemistry.

Therefore, we can substitute the estimate in Eq. 4.102 into ϵ_{TS} to find

$$\frac{\pi\sqrt{3}}{2^{n+2}} \le \frac{t^3\chi_H}{8} \tag{4.104}$$

Now we find that the correct choice of t, relative to these bounds, will satisfy

$$\sqrt[3]{\frac{\pi\sqrt{3}}{\chi_H 2^{n-1}}} \leq t \tag{4.105}$$

Picking t to saturate the lower bound (which corresponds to the worst-case scenario) we find that $t = \sqrt[3]{\frac{\pi\sqrt{3}}{\chi_H 2^{n-1}}}$, we can solve for the number of qubits required in the QPE procedure.

$$n = \left\lceil \frac{\log\left(\frac{\pi^2 \chi_H}{2\sqrt{3}\epsilon^3}\right)}{2\log(2)} \right\rceil \tag{4.106}$$

For a single trotter step, the number of rotations required is based on the total number of terms in the Hamiltonian.

$$N_{terms} = 2n_s + 9n_s^3 \tag{4.107}$$

Using the above formula, the max number of rotations required for a single term being equal to 8, and the fact that the number of exponentials required for the second order TS formula is $N_{exp} = 2N_{terms}$. The total number of rotations per trotter step is

$$N_{Rot} = 8 \times 2N_{terms} \leq 32n_s + 144n_s^3 \tag{4.108}$$

The number of rotations needed in QPE is 2^n, therefore the overall number of rotations needed for the simulation is

$$N_{Rot}^{Sim} = 2^n \left(32n_s + 144n_s^3\right) \tag{4.109}$$

Using chemical accuracy, $\epsilon = 1.6\text{mHa}$ for our error target, we can then estimate the number of qubits needed for QPE, and ultimately the number of T-gates required to obtain the ground state energy eigenvalue within the error tolerance of choice. To estimate the number of T-gates per rotation can be computed using the scaling from Ref. [252], and our chosen error for the T-gate synthesis, ϵ_{syn}, where

$$N_T = 1.15\log_2(1/\epsilon_{syn}) \times N_{Rot}^{Sim} \tag{4.110}$$

Since the error in the eigenvalue scales at most linearly with the error in the unitary matrix [235] and since the error in the unitary scales at most linearly with the number of gates

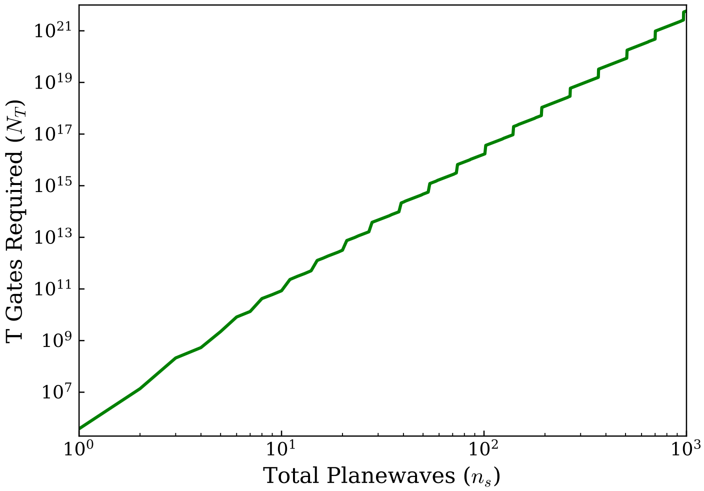

Figure 4.6: The estimated total number of T-gates required to sample from the spectrum of the rellium Hamiltonian for a box of length $L = 1$ within an error tolerance of $\epsilon = 1.6$mHa corresponding to chemical accuracy as a function of the number of planewaves in the system, n_s.

comprising the unitary from Box 4.1 of [14] we have that it suffices to take $\epsilon_{syn} = \epsilon N_{Rot}$. With this assignment N_T becomes

$$N_T = 1.15 \log_2(N_{Rot}/\epsilon) \times N_{Rot}^{Sim} \tag{4.111}$$

Using the empirical values for A and b defined above, chemical accuracy ϵ, the number of qubits necessary for QPE in Eq. 4.106, the relation for T-gate count in Eq. 4.111, we can finally estimate the T-gate count for the full QPE routine given some number of planewaves for the system, n_s. The log-log plot of this relationship is given in Fig. 4.6. The full equation for this relationship is

$$N_T = \left\lceil 1.15 \times 2^n \left(32n_s + 144n_s^3\right) \log_2\left(\frac{(32n_s + 144n_s^3)}{\pi\sqrt{3}/2^{n+2}}\right)\right\rceil \in \widetilde{O}\left(\frac{n_s^3\sqrt{\chi_H}}{\epsilon^{3/2}}\right) = \widetilde{O}\left(\frac{n_s^{5.2}}{\epsilon^{3/2}}\right) \tag{4.112}$$

for an error of $\epsilon = 1.6$mHa, and n is determined from Eq. 4.106.

In contrast to Eq. 4.112, the costs for such a planewave simulation in the constant L and ϵ

limit are given by Theorem 2 to be in $n_s^{5+o(1)}$ for adaptively chosen high-order Trotter-Suzuki formulas. In contrast, we find empirically that for the second-order Trotter-Suzuki formula the number of gates needed to reach 1.6mHa is in $\widetilde{O}(n_s^{5.2})$. This suggests that, the empirical performance of this simulation is comparable to what we expect from our prior theoretical analysis; however, it is worth considering that this analysis still does rely on crude triangle-inequality based estimates that disregard cancellation between terms in the expansion of the error operator and that further studies may be needed to determine the impact of neglecting such cancellations.

Finally, the number of non-Clifford operations needed to perform a classically challenging simulation using 20 plane waves (comprising 80 logical qubits) is projected by our results to be on the order of 10^{13} non-Clifford operations. In contrast, the best known results for simulating jellium using Trotter methods are on the order of 10^9 non-Clifford operations for systems of 27 spin orbitals (54 qubits). The gulfs between these two estimates suggest that further optimization may be needed to allow eQED to reach the same levels of performance that we can reach for non-relativistic electronic structure calculations, however, the gulfs between the two are not so large as to suspect that such simulations will be infeasible once subjected to the same optimizations that lowered the costs of simulation for challenge problems in chemistry from 10^{14} non-Clifford gates [186] to on the order of 10^9 non-Clifford gates. [181, 180]

4.6 State Preparation

In order to efficiently simulate any Hamiltonian on a quantum register, it is necessary to start with a high quality wavefunction ansatz that has a large overlap with the true wavefunction. For the jellium or rellium Hamiltonian, the degeneracy of the ground state is a non-trivial problem. Typically this is referred to as "strong correlation" where many different electronic configurations are entangled and contribute to the ground state wavefunction. This is in contrast to the familiar Hartee-Fock ground state, where a single electronic configuration *is* the wavefunction. Ground state electronic systems where the Hartree-Fock configuration is not dominant are sometimes called multi-reference (MR) ground states, where using the Hartree-Fock reference has a small overlap with the true ground state wavefunction due to other configurations being just as important. The multi-reference nature of electronic systems is also present in many chemical systems, typically large conjugated carbon systems, and multi-metal centered molecules due to the abundance of low lying spin states.

A commonly known classical method for computing multi-reference wavefunctions for quantum chemistry is known as multi-reference configuration interaction (MRCI). [253, 254] In short, this method captures static correlation by first expanding the Hartree-Fock reference into a complete active space (CAS) of all configurations included within a truncated orbital and particle space, typically centered around the occupied and unoccupied valence orbitals. Next, a number of additional configurations are added for capturing correlation effects beyond the CAS space, sometimes referred to as "dynamic correlation." A common version of MRCI, is MRCI singles and doubles (MRCISD), where additional determinants are added to the CAS wavefunction, including single and double particle excitations. Additionally, the singly and doubly excited particle and hole space spans a larger space then just the initial CAS determinants, and are commonly referred as restricted active space 1 (RAS1) for the additional occupied orbitals, and subsequently RAS3 for the virtual orbitals. The single and double excitations span across all three spaces. As an aside, RAS2 sometimes refers to the original CAS space in the literature.

The number of determinants required to build an MRCI ansatz can be defined by the chosen active spaces, RAS1, CAS, and RAS3. Following the notation in Ref. [255] where we only consider singly occupied spin-orbitals that follow the Jordan-Wigner mapping.

$$N_{\text{det}}^{MRCI} = \sum_{i_h=0}^{m_h} \sum_{i_e=0}^{m_e} \binom{N_{RAS1}}{i_h} \binom{N_{CAS}}{n_e - N_{RAS1} + i_h - i_e} \binom{N_{RAS3}}{i_e} \tag{4.113}$$

where N_{RAS1}, N_{CAS}, and N_{RAS3} are the number of orbitals in each active space respectively, n_e is the total number of electrons in all of the correlated spaces, i_h is the hole index, i_e is the particle index, m_h and m_e are the number of holes in RAS1 and the particles in RAS3 respectively. For the MRCISD ansatz the number of determinants then scales exponentially with N_{CAS}, but quadratically in both N_{RAS1} and N_{RAS3}. Additionally for MRCISD, $m_h = m_e = 2$.

For the purpose of state-preparation on a quantum computer, we can pre-compute the MRCISD wave function classically, and then use the coefficients for the determinants to initialize a better wavefunction that hopefully has a much higher overlap with the true ground state. A convenient method to prepare the initial MRCISD state is to use a Givens rotation on the creation and annihilation operators, defined by a general slater determinant generated by the classical MRCISD wavefunction. [256, 215] The general Slater determinant can be defined as

$$|\Phi\rangle = \hat{d}_1^\dagger \cdots \hat{d}_{N_f}^\dagger |0\rangle, \qquad \hat{d}_i^\dagger = \sum_j^{n_s} Q_{ij} \hat{c}_j^\dagger \tag{4.114}$$

where $\hat{c}^\dagger$ is the arbitrary particle type creation operator in the computational basis, $\hat{d}^\dagger$ is the rotated creation operator for the new basis based off of fractional particle occupation, N_f is the number of fermions, and n_s is the number of orbitals in the chosen basis. The $N_f \times n_s$ matrix Q rotates the original creation/annihilation operators into the rotated basis based off the choice of initial wavefunction. Therefore the rows of Q correspond to single particle wavefunctions that are linear combinations of the original orbital basis. In general, the rotated slater determinant can be generated by a unitary rotation of a simple computational basis state generated by the original creation operators

$$|\Phi\rangle = U \hat{c}_1^\dagger \cdots \hat{c}_{N_f}^\dagger |0\rangle, \qquad \hat{d}_i^\dagger = U \hat{c}_i^\dagger U^\dagger \tag{4.115}$$

Following Ref. [256] we see that this unitary transformation can be represented by sequences of 2-qubit rotations, also known as Givens rotations where

$$U = G_{N_G} \cdots G_2 G_1 \tag{4.116}$$

where N_G is the total number of Givens rotations, and the Givens rotation matrix between spin-orbitals p, q is defined as

$$G(\theta, \varphi) = \begin{pmatrix} \cos\theta & -e^{i\varphi} \sin\theta \\ \sin\theta & e^{i\varphi} \cos\theta \end{pmatrix} \tag{4.117}$$

where the angles θ and φ can be solved classically by diagonalizing the Q matrix. The number of Givens rotations required to perform the basis transform is

$$N_G = (n_s - N_f)\, N_f \in O(n_s^2). \tag{4.118}$$

Each Givens rotation, $G(\theta, \varphi)$, can be implemented using a rotation of the form $e^{-i(e^{-i\varphi}a_p^\dagger a_q + e^{i\varphi}a_q^\dagger a_p)\theta}$. As discussed, each exponential can be simulated using $O(\log(1/\epsilon))$ T-gates. The complexity of performing this state preparation is therefore in $O(n_s^2 \log(n_s^2/\epsilon))$, which is sub-dominant to the cost of simulation in momentum basis which is in $\widetilde{O}(n_s^{4+2/3}/\epsilon)$ in the thermodynamic limit. For this reason, we neglect the cost of the state preparation in all of our previous analysis.

Additionally, for typical electronic systems of interest, we only care about linear combinations of electronic single particle functions and the positronic block is trivially occupied. This means that for a system of N_{elec} number of electrons our matrix Q will be already be diagonalized in the positronic space, meaning simply that $N_f = N_{elec}$.

4.7 Planewave Cutoff Estimates for Heavy Atoms

In this section we will provide heuristic arguments that estimate the number of planewaves needed to solve a realistic relativistic problem in momentum basis. This is important because the cost of both the MRCISD ansatz as well as the simulation of the dynamics. As a target problem, we focus on the simulation of atomic gold. This is chosen because relativistic effects are needed in order to even qualitatively understand the spectrum of gold and thus such a simulation is arguably the first logical benchmark problem to consider after simulation of the relativistic free electron gas (rellium).

For the momentum space planewave Hamiltonian, we estimate that a single all-electron gold atom will require at least 31 million planewaves, which is obviously beyond the reach of quantum computers in the foreseeable future. The number of planewaves N_{PW} needed for an arbitrary system is defined by the cell volume L^3 and energy cutoff.

$$N_{PW} = \frac{L^3}{2\pi^2} E_{cut}^{3/2} \tag{4.119}$$

To find the lowest possible cutoff energy, we can calculate the highest possible kinetic energy of an electron in an atomic potential with nuclear charge Z, which will be in the $1s$ orbital, so the principle quantum number $n = 1$. The kinetic energy of the $1s$ electron can be estimated to be the following, using the hydrogenic Dirac equation

$$E = c^2 \left[\frac{1}{\sqrt{1 + \frac{Z^2\alpha^2}{\left(n-(j+1/2)+\sqrt{(j+1/2)^2 - Z^2\alpha^2}\right)^2}}} - 1 \right] \tag{4.120}$$

where α is the fine structure constant, $n = 1$ is the principle quantum number and for the ground state s orbital, $j = \frac{1}{2}$. By plugging in $Z = 79$ and $L = 2r_A$ where r_A is the atomic radius, using $3.14a_0$ for gold , and finally setting $E_{cut} = E_{kin}$ we estimate that the all electron gold atom to require at least 3.08×10^7 planewaves and in turn roughly 1.23×10^8 logical qubits. This suggests further suggests based on the number of sites in the reciprocal lattice that the cost of simulation within chemical accuracy (1.6 mHa) will be roughly on the order of 10^{38} non-Clifford operations for a momentum space simulation. Our analysis therefore suggests that such simulations will likely be out of reach for simulations and since the number of planewaves for a single atom all electron system is expected to increase as $O(L^3Z^3)$, we expect similar conclusions to hold for other heavy atomic systems.

This is not too surprising since planewave simulations in general need a large number of basis functions to properly describe atomic core orbitals. The most obvious remedy to this issue is to switch to a different basis set. In particular, Gaussian orbitals model the nuclear cusp condition much better than planewaves and so the number of Gaussians needed to describe the system to within chemical accuracy can be substantially lower. This makes them often a more natural choice.

The opposite approach would be to instead of investigating eQED in second quantization to look at it instead in first quantization using an appropriately anti-symmetrized wave function. Within such a framework, the number of qubits needed to store the atomic configuration can be exponentially smaller. The prefactors, however, make such applications outside of the reach of existing or near-future quantum computers.

4.8 Conclusion

In this work we have presented how to simulate the eQED Hamiltonian on a quantum computer. Specifically, we presented an analysis of both the position basis using a cubic lattice, and the momentum basis planewave formulations of the Hamiltonians. From this analysis we find that for the position basis, the number of T-gates required for simulating the Hamiltonian scales as $\left(\frac{\Lambda n_s^2}{\epsilon}\right)^{1+o(1)}$ where $\Lambda = \max\left(m + e\max_x \|A^{ex}(x)\|, \frac{e^2 n_s}{L}, \frac{n_s^{4/3}}{L}\right)$. For the momentum basis, the number of T-gates required scales as $\left(\frac{\Lambda_p n_s^3}{\epsilon}\right)^{1+o(1)}$ where $\Lambda_p \in O\left(n_s\left(\frac{m}{n_s} + \frac{n_s}{L} + e|A_\mu^{ex}|\right)\right)$. This shows that the the ground state energy can be computed in polynomial time provided that a copy of the groundstate is provided to a quantum computer, which suggests that the problem of deciding whether there exists an eigenstate with energy less than a threshold can be is contained within the complexity class QMA within effective QED. This is relevant because it provides further vindication that relativistic effects do not invalidate the Quantum Complexity-Theoretic Church-Turing Thesis.

Further, we investigated the cost of using quantum phase estimation to estimate the ground state energy of the relativistic jellium (rellium) model as the simplest momentum based eQED Hamiltonian. Specifically we computed the number of T-gates needed empirically for quantum phase estimation using the second order Trotter-Suzuki decomposition, and using Monte Carlo sampling of different rellium Hamiltonians by increasing the cutoff energy for the system. For this routine, we find that for a constant box size, $L = 1$, the number of T-gates needed to estimate the ground state energy eigenvalue within an error of chemical accuracy $\epsilon = 1.6$mHa is on the order of 10^{16} T-gates for a classically intractable problem involving 100 planewaves (400 qubits) or 10^{13} T-gates for a classically challenging problem with 20 plane waves (80) qubits. These costs, while substantial, suggest that by further optimizing our simulation algorithm that the costs of quantum simulation may be reduced to reasonable levels.

While this work has explored how eQED can been simulated in general, the momentum space and lattice formulations of the Hamiltonian are not necessarily the most pertinent for all applications to physics and chemistry. Specifically, the focus of including QED corrections to relativistic effects in molecular systems is most prominent for heavy elements at the bottom of the periodic table which have large potential wells from the nuclear charge. However, QED corrections to the energies and properties of light elements can be important in certain situations as well. Future work will focus on adapting this method for simulating eQED on quantum computers to other more convenient basis sets for chemistry, such as the well known Gaussian basis sets that can more compactly model the electronic wavefunction at the nuclear cusp.

BIBLIOGRAPHY

[1] John Neumann, Eugene Paul Wigner, and Robert Hofstadter. *Mathematical foundations of quantum mechanics.* Princeton university press, 1955.

[2] Max Born and Robert Oppenheimer. Zur quantentheorie der molekeln. *Annalen der Physik*, 389(20):457–484, 1927.

[3] Attila Szabo and Neil S Ostlund. *Modern quantum chemistry: introduction to advanced electronic structure theory.* Courier Corporation, 2012.

[4] Trygve Helgaker, Poul Jørgensen, and Jeppe Olsen. *Molecular electronic-structure theory.* John Wiley & Sons, 2014.

[5] Yuri Manin. Computable and uncomputable. *Sovetskoye Radio, Moscow*, 128, 1980.

[6] Richard P Feynman. Simulating physics with computers. *Int. J. Theor. Phys*, 21(6/7), 1982.

[7] Peter W Shor. Algorithms for quantum computation: discrete logarithms and factoring. In *Proceedings 35th annual symposium on foundations of computer science*, pages 124–134. Ieee, 1994.

[8] Ethan Bernstein and Umesh Vazirani. Quantum complexity theory. *SIAM Journal on computing*, 26(5):1411–1473, 1997.

[9] Andrew M Childs, Richard Cleve, Enrico Deotto, Edward Farhi, Sam Gutmann, and Daniel A Spielman. Exponential algorithmic speedup by a quantum walk. In *Proceedings of the thirty-fifth annual ACM symposium on Theory of computing*, pages 59–68, 2003.

[10] Aram W Harrow, Avinatan Hassidim, and Seth Lloyd. Quantum algorithm for linear systems of equations. *Physical review letters*, 103(15):150502, 2009.

[11] Seth Lloyd. Universal quantum simulators. *Science*, pages 1073–1078, 1996.

[12] Alán Aspuru-Guzik, Anthony D Dutoi, Peter J Love, and Martin Head-Gordon. Simulated quantum computation of molecular energies. *Science*, 309(5741):1704–1707, 2005.

[13] James D Whitfield, Jacob Biamonte, and Alán Aspuru-Guzik. Simulation of electronic structure hamiltonians using quantum computers. *Molecular Physics*, 109(5):735–750, 2011.

[14] Michael A Nielsen and Isaac Chuang. Quantum computation and quantum information, 2002.

[15] Hale F Trotter. On the product of semi-groups of operators. *Proceedings of the American Mathematical Society*, 10(4):545–551, 1959.

[16] Masuo Suzuki. Generalized trotter's formula and systematic approximants of exponential operators and inner derivations with applications to many-body problems. *Communications in Mathematical Physics*, 51(2):183–190, 1976.

[17] A Yu Kitaev. Quantum measurements and the abelian stabilizer problem. *arXiv preprint quant-ph/9511026*, 1995.

[18] Guang Hao Low and Isaac L Chuang. Hamiltonian simulation by qubitization. *Quantum*, 3:163, 2019.

[19] Alberto Peruzzo, Jarrod McClean, Peter Shadbolt, Man-Hong Yung, Xiao-Qi Zhou, Peter J Love, Alán Aspuru-Guzik, and Jeremy L O'brien. A variational eigenvalue solver on a photonic quantum processor. *Nature communications*, 5(1):1–7, 2014.

[20] Earl Campbell. Random compiler for fast hamiltonian simulation. *Physical review letters*, 123(7):070503, 2019.

[21] Guang Hao Low and Nathan Wiebe. Hamiltonian simulation in the interaction picture. *arXiv preprint arXiv:1805.00675*, 2018.

[22] Dominic W Berry, Graeme Ahokas, Richard Cleve, and Barry C Sanders. Efficient quantum algorithms for simulating sparse hamiltonians. *Communications in Mathematical Physics*, 270(2):359–371, 2007.

[23] E Wigner and Pascual Jordan. Über das paulische äquivalenzverbot. *Z. Phys*, 47:631, 1928.

[24] Christoph Rose-Petruck, Ralph Jimenez, Ting Guo, Andrea Cavalleri, Craig W Siders, Ferenc Rksi, Jeff A Squier, Barry C Walker, Kent R Wilson, and Christopher PJ Barty. Picosecond–milliångström Lattice Dynamics Measured by Ultrafast X-ray Diffraction. *Nature*, 398(6725):310–312, 1999.

[25] Christian Rischel, Antoine Rousse, Ingo Uschmann, Pierre-Antoine Albouy, Jean-Paul Geindre, Patrick Audebert, Jean-Claude Gauthier, Eckhart Fröster, Jean-Louis Martin, and André Antonetti. Femtosecond Time-resolved X-ray Diffraction from Laser-heated Organic Films. *Nature*, 390(6659):490–492, 1997.

[26] Ivan V Tomov, Dmitri A Oulianov, Peilin Chen, and Peter M Rentzepis. Ultrafast Time-Resolved Transient Structures of Solids and Liquids Studied by Means of X-ray Diffraction and EXAFS. *J. Phys. Chem. B*, 103(34):7081–7091, 1999.

[27] RW Schoenlein, S Chattopadhyay, HH Chong, TE Glover, PA Heimann, CV Shank, AA Zholents, and MS Zolotorev. Generation of Femtosecond Pulses of Synchrotron Radiation. *Science*, 287(5461):2237–2240, 2000.

[28] Evgeny Kleymenov, Jeroen A van Bokhoven, Christian David, Pieter Glatzel, Markus Janousch, Roberto Alonso-Mori, Marco Studer, Markus Willimann, Anna Bergamaschi, Beat Henrich, and Maarten Nachtegaal. Five-element johann-type x-ray emission spectrometer with a single-photon-counting pixel detector. *Rev. Sci. Instrum.*, 82(6):065107, 2011.

[29] Isabelle Llorens, Eric Lahera, William Delnet, Olivier Proux, Aurélien Braillard, Jean-Louis Hazemann, Alain Prat, Denis Testemale, Quentin Dermigny, Frédéric Gélébart, Marc Morand, Abhay Shukla, Nathalie Bardou, Olivier Ulrich, Stéphan Arnaud, Jean-François Berar, Nathalie Boudet, Bernard Caillot, Perrine Chaurand, Jérôme Rose, Emmanuel Doelsch, Philippe Martin, and Pier Lorenzo Solari. High energy resolution five-crystal spectrometer for high quality fluorescence and absorption measurements on an x-ray absorption spectroscopy beamline. *Rev. Sci. Instrum.*, 83(6):063104, 2012.

[30] M Kavčič, M Budnar, A Mühleisen, F Gasser, M Žitnik, K Bučar, and R Bohinc. Design and performance of a versatile curved-crystal spectrometer for high-resolution spectroscopy in the tender x-ray range. *Rev. Sci. Instrum.*, 83(3):033113, 2012.

[31] GT Seidler, DR Mortensen, AJ Remesnik, JI Pacold, NA Ball, N Barry, M Styczinski, and OR Hoidn. A laboratory-based hard x-ray monochromator for high-resolution x-ray emission spectroscopy and x-ray absorption near edge structure measurements. *Rev. Sci. Instrum.*, 85(11):113906, 2014.

[32] Devon R Mortensen, Gerald T Seidler, Alexander S Ditter, and Pieter Glatzel. Benchtop nonresonant x-ray emission spectroscopy: Coming soon to laboratories and xas beamlines near you. In *J. Phys. Conf. Ser.*, volume 712, page 012036, 2016.

[33] Ryan Beck, Alessio Petrone, Joseph M. Kasper, Matthew J. Crane, Peter J. Pauzauskie, and Xiaosong Li. Effect of surface passivation on nanodiamond crystallinity. *J. Phys. Chem. C*, 122(15):8573–8580, 2018.

[34] James J Yan, Margarita A Gonzales, Pradip K Mascharak, Britt Hedman, Keith O Hodgson, and Edward I Solomon. L-edge x-ray absorption spectroscopic investigation of {FeNO} 6: Delocalization vs antiferromagnetic coupling. *J. Am. Chem. Soc.*, 139(3):1215–1225, 2017.

[35] Fan Zheng, Selim Alayoglu, Jinghua Guo, Vladimir Pushkarev, Yimin Li, Per-Anders Glans, Jeng-lung Chen, and Gabor Somorjai. In-situ x-ray absorption study of evolution of oxidation states and structure of cobalt in co and copt bimetallic nanoparticles (4 nm) under reducing (h2) and oxidizing (o2) environments. *Nano Lett.*, 11(2):847–853, 2011.

[36] Ben Warner, Jenny C Oberg, Tobias G Gill, Fadi El Hallak, Cyrus F Hirjibehedin, Michele Serri, Sandrine Heutz, Marie-Anne Arrio, Philippe Sainctavit, Matteo Mannini, Giordano Poneti, Roberta Sessoli, and Patrick Rosa. Temperature- and light-induced spin crossover observed by x-ray spectroscopy on isolated fe (ii) complexes on gold. *J. Phys. Chem. Lett.*, 4(9):1546–1552, 2013.

[37] A. Wildman, E. Martinez-Baez, J. Fulton, G. Schenter, C. Pearce, A. Clark, and X. Li. Anticorrelated contributions to pre-edge features of aluminate near-edge x-ray absorption spectroscopy in concentrated electrolytes. *J. Phys. Chem. Lett.*, 9(10):2444–2449, 2018.

[38] T. Stetina, A. Clark, and X. Li. X-ray absorption signatures of hydrogen-bond structure in water-alcohol solutions. *Int. J. Quant. Chem.*, 119:e25802, 2019.

[39] J. Stöhr. *NEXAFS Spectroscopy.* Springer-Verlag, 2003.

[40] Thomas-C Jagau, Ksenia B Bravaya, and Anna I Krylov. Extending quantum chemistry of bound states to electronic resonances. *Annu. Rev. Phys. Chem.*, 68:525–553, 2017.

[41] L Triguero, L.G.M Pettersson, and H Ågren. Calculations of near-edge x-ray absorption spectra of gas-phase and chemisorbed molecules by means of density-functional and transition-potential theory. *Phys. Rev. B*, 58(12):8097, 1998.

[42] Sonia Coriani, Ove Christiansen, Thomas Fransson, and Patrick Norman. Coupled-cluster response theory for near-edge x-ray-absorption fine structure of atoms and molecules. *Phys. Rev. A*, 85(2):022507, 2012.

[43] Ranelka G Fernando, Mary C Balhoff, and Kenneth Lopata. X-ray Absorption in Insulators with Non-Hermitian Real-Time Time-Dependent Density Functional Theory. *J. Chem. Theory Comput.*, 11(2):646–654, 2015.

[44] Jan Wenzel, Michael Wormit, and Andreas Dreuw. Calculating core-level excitations and x-ray absorption spectra of medium-sized closed-shell molecules with the algebraic-diagrammatic construction scheme for the polarization propagator. *J. Comput. Chem.*, 35(26):1900–1915, 2014.

[45] Jan Wenzel, Michael Wormit, and Andreas Dreuw. Calculating x-ray absorption spectra of open-shell molecules with the unrestricted algebraic-diagrammatic construction scheme for the polarization propagator. *J. Chem. Theory Comput.*, 10(10):4583–4598, 2014.

[46] G Fronzoni, R De Francesco, and M Stener. Time Dependent Density Functional Theory of X-ray Absorption Spectroscopy of Alkaline-Earth Oxides. *J. Phys. Chem. B*, 109(20):10332–10340, 2005.

[47] Serena DeBeer George, Taras Petrenko, and Frank Neese. Time-dependent density functional calculations of ligand k-edge x-ray absorption spectra. *Inorg. Chim. Acta*, 361(4):965–972, 2008.

[48] Nicholas A Besley and Frans A Asmuruf. Time-dependent density functional theory calculations of the spectroscopy of core electrons. *Phys. Chem. Chem. Phys.*, 12(38):12024–12039, 2010.

[49] Patrick J. Lestrange, Phu D. Nguyen, and Xiaosong Li. Calibration of energy-specific tddft for modeling k-edge xas spectra of light elements. *J. Chem. Theory Comput.*, 11:2994–2999, 2015.

[50] Bo Peng, Patrick J Lestrange, Joshua J Goings, Marco Caricato, and Xiaosong Li. Energy-specific equation-of-motion coupled-cluster methods for high-energy excited states: Application to k-edge x-ray absorption spectroscopy. *J. Chem. Theory Comput.*, 11(9):4146–4153, 2015.

[51] Stephan Bernadotte, Andrew J Atkins, and Christoph R Jacob. Origin-independent Calculation of Quadrupole Intensities in X-ray Spectroscopy. *J. Chem. Phys.*, 137(20):204106, 2012.

[52] Nanna Holmgaard List, Joanna Kauczor, Trond Saue, Hans Jørgen Aagaard Jensen, and Patrick Norman. Beyond the Electric-dipole Approximation: A Formulation and Implementation of Molecular Response Theory for the Description of Absorption of Electromagnetic Field Radiation. *J. Chem. Phys.*, 142(24):244111, 2015.

[53] Patrick J. Lestrange, Franco Egidi, and Xiaosong Li. The consequences of improperly describing oscillator strengths beyond the electric dipole approximation. *J. Chem. Phys.*, 143:234103, 2015.

[54] Lasse Kragh Sørensen, Meiyuan Guo, Roland Lindh, and Marcus Lundberg. Applications to metal k pre-edges of transition metal dimers illustrate the approximate origin independence for the intensities in the length representation. *Mol. Phys.*, pages 1–16, 2016.

[55] G Fronzoni, M Stener, P Decleva, F Wang, T Ziegler, E Van Lenthe, and EJ Baerends. Spin–orbit relativistic time dependent density functional theory calculations for the description of core electron excitations: Ticl4 case study. *Chem. Phys. Lett.*, 416(1-3):56–63, 2005.

[56] Maurizio Casarin, Paola Finetti, Andrea Vittadini, Fan Wang, and Tom Ziegler. Spin-orbit relativistic time-dependent density functional calculations of the metal and ligand pre-edge xas intensities of organotitanium complexes: Ticl$_4$, ti(η^5-c$_5$h$_5$)cl$_3$, and ti(η^5-c$_5$h$_5$)$_2$cl$_2$. *J. Chem. Phys.*, 111:5270, 2007.

[57] G Fronzoni, M Stener, P Decleva, M de Simone, M Coreno, P Franceschi, C Furlani, and KC Prince. X-ray absorption spectroscopy of vocl3, cro2cl2, and mno3cl: An experimental and theoretical study. *J. Phys. Chem. A*, 113(12):2914–2925, 2009.

[58] Ida Josefsson, Kristjan Kunnus, Simon Schreck, Alexander Föhlisch, Frank de Groot, Philippe Wernet, and Michael Odelius. Ab initio calculations of x-ray spectra: Atomic multiplet and molecular orbital effects in a multiconfigurational scf approach to the l-edge spectra of transition metal complexes. *J. Phys. Chem. Lett.*, 3(23):3565–3570, 2012.

[59] Rahul V Pinjari, Mickaël G Delcey, Meiyuan Guo, Michael Odelius, and Marcus Lundberg. Restricted active space calculations of l-edge x-ray absorption spectra: From molecular orbitals to multiplet states. *J. Chem. Phys.*, 141(12):124116, 2014.

[60] Benjamin E Van Kuiken, Marat Valiev, Stephanie L Daifuku, Caitlin Bannan, Matthew L Strader, Hana Cho, Nils Huse, Robert W Schoenlein, Niranjan Govind, and Munira Khalil. Simulating ru l3-edge x-ray absorption spectroscopy with time-dependent density functional theory: Model complexes and electron localization in mixed-valence metal dimers. *J. Phys. Chem. A*, 117(21):4444–4454, 2013.

[61] Michael Roemelt and Frank Neese. Excited States of Large Open-Shell Molecules: An Efficient, General, and Spin-Adapted Approach Based on a Restricted Open-Shell Ground State Wave function. *J. Phys. Chem. A*, 117(14):3069–3083, 2013.

[62] Michael Roemelt, Dimitrios Maganas, Serena DeBeer, and Frank Neese. A combined dft and restricted open-shell configuration interaction method including spin-orbit coupling: Application to transition metal l-edge x-ray absorption spectroscopy. *J. Chem. Phys.*, 138(20):204101, 2013.

[63] Marius Kadek, Lukas Konecny, Bin Gao, Michal Repisky, and Kenneth Ruud. X-ray Absorption Resonances near $L_{2,3}$-edges from Real-time Propagation of the Dirac-Kohn-Sham Density Matrix. *Phys. Chem. Chem. Phys.*, 17(35):22566–22570, 2015.

[64] Joseph M. Kasper, Patrick J. Lestrange, Torin F. Stetina, and Xiaosong Li. Modeling $l_{2,3}$-edge x-ray absorption spectroscopy with real-time exact two-component relativistic time-dependent density functional theory. *J. Chem. Theory Comput.*, 14(4):1998–2006, 2018.

[65] Sonia Coriani, Thomas Fransson, Ove Christiansen, and Patrick Norman. Asymmetric-lanczos-chain-driven implementation of electronic resonance convergent coupled-cluster linear response theory. *J. Chem. Theory Comput.*, 8(5):1616–1628, 2012.

[66] Thomas Fransson, Sonia Coriani, Ove Christiansen, and Patrick Norman. Carbon x-ray absorption spectra of fluoroethenes and acetone: A study at the coupled cluster, density functional, and static-exchange levels of theory. *J. Chem. Phys.*, 138(12):124311, 2013.

[67] Joanna Kauczor, Patrick Norman, Ove Christiansen, and Sonia Coriani. Communication: A reduced-space algorithm for the solution of the complex linear response equations used in coupled cluster damped response theory, 2013.

[68] Tobias Fahleson, Hans Ågren, and Patrick Norman. A polarization propagator for nonlinear x-ray spectroscopies. *J. Phys. Chem. Lett.*, 7(11):1991–1995, 2016.

[69] Mathieu Linares, Sven Stafström, Zilvinas Rinkevicius, Hans Ågren, and Patrick Norman. Complex polarization propagator approach in the restricted open-shell, self-consistent field approximation: The near k-edge x-ray absorption fine structure spectra of allyl and copper phthalocyanine. *J. Phys. Chem. B*, 115(18):5096–5102, 2010.

[70] Ulf Ekström, Patrick Norman, Vincenzo Carravetta, and Hans Ågren. Polarization propagator for x-ray spectra. *Phys. Rev. Lett.*, 97(14):143001, 2006.

[71] Thomas Fransson, Daria Burdakova, and Patrick Norman. K-and l-edge x-ray absorption spectrum calculations of closed-shell carbon, silicon, germanium, and sulfur compounds using damped four-component density functional response theory. *Phys. Chem. Chem. Phys.*, 18(19):13591–13603, 2016.

[72] Jiri Brabec, Lin Lin, Meiyue Shao, Niranjan Govind, Chao Yang, Yousef Saad, and Esmond G Ng. Efficient algorithms for estimating the absorption spectrum within linear response tddft. *J. Chem. Theory Comput.*, 11(11):5197–5208, 2015.

[73] Roel Van Beeumen, David B. Williams-Young, Joseph M. Kasper, Chao Yang, Esmond G. Ng, and Xiaosong Li. Model order reduction algorithm for estimating the absorption spectrum. *J. Chem. Theory Comput.*, 13(10):4950–4961, 2017.

[74] M Stener, G Fronzoni, and M de Simone. Time Dependent Density Functional Theory of Core Electrons Excitations. *Chem. Phys. Lett.*, 373(1-2):115–123, 2003.

[75] Kallol Ray, Serena DeBeer George, Edward I Solomon, Karl Wieghardt, and Frank Neese. Description of the ground-state covalencies of the bis (dithiolato) transition-metal complexes from x-ray absorption spectroscopy and time-dependent density-functional calculations. *Chem. Eur. J.*, 13(10):2783–2797, 2007.

[76] Frans A Asmuruf and Nicholas A Besley. Time Dependent Density Functional Theory Study of the Near-edge X-ray Absorption Fine Structure of Benzene in Gas Phase and on Metal Surfaces. *J. Chem. Phys.*, 129(6):064705, 2008.

[77] K Lopata, Benjamin E Van Kuiken, Munira Khalil, and Niranjan Govind. Linear-response and real-time time-dependent density functional theory studies of core-level near-edge x-ray absorption. *J. Chem. Theory Comput.*, 8(9):3284–3292, 2012.

[78] Wenkel Liang, Sean A. Fischer, Michael J. Frisch, and Xiaosong Li. Energy-specific linear response tdhf/tddft for calculating high-energy excited states. *J. Chem. Theory Comput.*, 7(11):3540–3547, 2011.

[79] Eugene Vecharynski, Chao Yang, and Fei Xue. Generalized preconditioned locally harmonic residual method for non-hermitian eigenproblems. *SIAM J. Sci. Comp.*, 38(1):A500–A527, 2016.

[80] Joseph M. Kasper, David B. Williams-Young, Eugene Vecharynski, Chao Yang, and Xiaosong Li. A well-tempered hybrid method for solving challenging time-dependent density functional theory (tddft) systems. *J. Chem. Theory Comput.*, 14(4):2034–2041, 2018.

[81] Franco Egidi, Joshua J. Goings, Michael J. Frisch, and Xiaosong Li. Direct atomic-orbital-based relativistic two-component linear response method for calculating excited-state fine structures. *J. Chem. Theory Comput.*, 12(8):3711–3718, 2016.

[82] Franco Egidi, Shichao Sun, Joshua J. Goings, Giovanni Scalmani, Michael J. Frisch, and Xiaosong Li. Two-component non-collinear time-dependent spin density functional theory for excited state calculations. *J. Chem. Theory Comput.*, 13(6):2591–2603, 2017.

[83] Kenneth G. Dyall and Knut Fægri, Jr. *Introduction to Relativistic Quantum Chemistry.* Oxford University Press, 2007.

[84] Markus Reiher and Alexander Wolf. *Relativistic Quantum Chemistry.* Wiley-VCH, second edition, 2015.

[85] Wenjian Liu. *Handbook of Relativistic Quantum Chemistry.* Springer, 2017.

[86] Werner Kutzelnigg and Wenjian Liu. Quasirelativistic theory equivalent to fully relativistic theory. *J. Chem. Phys.*, 123:241102, 2005.

[87] Wenjian Liu and Daoling Peng. Infinite-order quasirelativistic density functional method based on the exact matrix quasirelativistic theory. *J. Chem. Phys.*, 125:044102, 2006.

[88] Daoling Peng, Wenjian Liu, Yunlong Xiao, and Lan Cheng. Making four- and two-component relativistic density functional methods fully equivalent based on the idea of from atoms to molecule. *J. Chem. Phys.*, 127:104106, 2007.

[89] Wenhua Xu, Jianyi Ma, Daoling Pen, Wenli Zou, Wenjian Liu, and Volker Staemmler. Excited states of reo_4^-: A comprehensive time-dependent relativistic density functional theory study. *Chem. Phys.*, 356:219–228, 2009.

[90] Wenhua Xu, Yong Zhang, and Wenjian Liu. Time-dependent relativistic density functional study of yb and ybo. *Sci. China Ser. B Chem.*, 52:1945–1953, 2009.

[91] W. Liu and D. Peng. Exact two-component hamiltonians revisited. *J. Chem. Phys.*, 131(3):031104, 2009.

[92] Yong Zhang, Wenhua Xu, Qiming Sun, Wenli Zou, and Wenjian Liu. Excited states of oso_4: A comprehensive time-dependent relativistic density functional theory study. *J. Comput. Chem.*, 31:532–551, 2010.

[93] Miroslav̂ Ilias and Trond Saue. An infinite-order relativistic hamiltonian by a simple one-step transformation. *J. Chem. Phys.*, 126:064102, 2007.

[94] Daoling Peng, Nils Middendorf, Florian Weigend, and Markus Reiher. An efficient implementation of two-component relativistic exact-decoupling methods for large molecules. *J. Chem. Phys.*, 138:184105, 2013.

[95] Joshua J. Goings, Joseph M. Kasper, Franco Egidi, Shichao Sun, and Xiaosong Li. Real time propagation of the exact two component time-dependent density functional theory. *J. Chem. Phys.*, 145(10):104107, 2016.

[96] David Williams-Young, Franco Egidi, and Xiaosong Li. Relativistic two-component particle-particle tamm-dancoff approximation. *J. Chem. Theory Comput.*, 12(11):5379–5384, 2016.

[97] Alessio Petrone, David B. Williams-Young, Shichao Sun, Torin F. Stetina, and Xiaosong Li. An efficient implementation of two-component relativistic density functional theory with torque-free auxiliary variables. *Euro. Phys. J. B*, 91(7):169, 2018.

[98] Wenjian Liu and Yunlong Xiao. Relativistic time-dependent density functional theories. *Chem. Soc. Rev.*, 47:4481–4509, 2018.

[99] J. C. Boettger. Approximate two-electron spin-orbit coupling term for density-functional-theory DFT calculations using the Douglas-Kroll-Hess transformation. *Phys. Rev. B*, 62:7809–7815, 2000.

[100] A. Dreuw and M. Head-Gordon. Single-reference ab initio methods for the calculation of excited states of large molecules. *Chem. Rev.*, 105:4009–4037, 2005.

[101] R Eric Stratmann, Gustavo E Scuseria, and Michael J Frisch. An efficient implementation of time-dependent density-functional theory for the calculation of excitation energies of large molecules. *J. Chem. Phys.*, 109(19):8218–8224, 1998.

[102] E. Runge and E. K. U. Gross. Density-functional theory for time-dependent systems. *Phys. Rev. Lett.*, 52(12):9971–1000, 1984.

[103] Mark E. Casida. Time-dependent density functional response theory for molecules. In Delano P. Chong, editor, *Recent Advances in Density Functional Methods Part I*, pages 155–192. World Scientific, Singapore, 1995.

[104] M. Petersilka, U. J. Gossmann, and E. K. U. Gross. Excitation energies from time-dependent density-functional theory. *Phys. Rev. Lett.*, 76:1212–1215, 1996.

[105] J. J. Goings, F. Egidi, and X Li. Current development of non-collinear electronic structure theory. *Int. J. Quant. Chem.*, 118:e25398, 2018.

[106] Alexander Wolf and Markus Reiher. Exact decoupling of the Dirac hamiltonian. III. molecular properties. *J. Chem. Phys.*, 121:064102, 2004.

[107] Yu Zhang, Jason D Biggs, Daniel Healion, Niranjan Govind, and Shaul Mukamel. Core and valence excitations in resonant x-ray spectroscopy using restricted excitation window time-dependent density functional theory. *J. Chem. Phys.*, 137(19):194306, 2012.

[108] Dmitry Zuev, Eugene Vecharynski, Chao Yang, Natalie Orms, and Anna I Krylov. New algorithms for iterative matrix-free eigensolvers in quantum chemistry. *J. Comput. Chem.*, 36(5):273–284, 2015.

[109] Chao Huang, Wenjian Liu, Yunlong Xiao, and Mark R Hoffmann. ivi: An iterative vector interaction method for large eigenvalue problems. *J. Comput. Chem.*, 38(29):2481–2499, 2017.

[110] RBJS Krishnan, J Stephen Binkley, Rolf Seeger, and John A Pople. Self-consistent molecular orbital methods. xx. a basis set for correlated wave functions. *J. Chem. Phys.*, 72(1):650–654, 1980.

[111] Timothy Clark, Jayaraman Chandrasekhar, Günther W Spitznagel, and Paul Von Ragué Schleyer. Efficient diffuse function-augmented basis sets for anion calculations. iii. the 3-21+ g basis set for first-row elements, li–f. *J. Comput. Chem.*, 4(3):294–301, 1983.

[112] Takeshi Noro, Masahiro Sekiya, and Toshikatsu Koga. Segmented contracted basis sets for atoms H through Xe: Sapporo-(DK)-nZP sets (n = D, T, Q). *Theor. Chem. Acc.*, 131:1124, 2012.

[113] Thom H Dunning Jr. Gaussian basis sets for use in correlated molecular calculations. I. the atoms boron through neon and hydrogen. *J. Chem. Phys.*, 90(2):1007–1023, 1989.

[114] David E Woon and Thom H Dunning, Jr. Gaussian basis sets for use in correlated molecular calculations. III. The atoms aluminum through argon. *J. Chem. Phys.*, 98(2):1358–1371, 1993.

[115] Nikolai B. Balabanov and Kirk A. Peterson. Systematically convergent basis sets for transition metals. I. All-electron correlation consistent basis sets for the 3d elements Sc-Zn. *J. Chem. Phys.*, 123:064107, 2005.

[116] Nikolai B Balabanov and Kirk A Peterson. Basis Set Limit Electronic Excitation Energies, Ionization Potentials, and Electron Affinities for the 3d Transition Metal Atoms: Coupled Cluster and Multireference Methods. *J. Chem. Phys.*, 125(7):074110, 2006.

[117] Axel D Becke. A New Mixing of Hartree–Fock and Local Density functional Theories. *J. Chem. Phys.*, 98(2):1372–1377, 1993.

[118] P. J. Stephens, F. J. Devlin, C. F. Chabalowski, and M. J. Frisch. Ab initio calculation of vibrational absorption and circular dichroism spectra using density functional force fields. *J. Phys. Chem.*, 98(45):11623–11627, 1994.

[119] Carlo Adamo and Vincenzo Barone. Toward Reliable Density Functional Methods Without Adjustable Parameters: The PBE0 Model. *J. Chem. Phys.*, 110(13):6158–6170, 1999.

[120] J. P. Perdew, K. Burke, and M. Ernzerhof. Generalized gradient approximation made simple. *Phys. Rev. Lett.*, 77:3865–3868, 1996.

[121] Jochen Heyd, Gustavo E Scuseria, and Matthias Ernzerhof. Hybrid functionals based on a screened coulomb potential. *J. Chem. Phys.*, 118(18):8207–8215, 2003.

[122] Takeshi Yanai, David P Tew, and Nicholas C Handy. A new hybrid exchange–correlation functional using the coulomb-attenuating method (cam-b3lyp). *Chem. Phys. Lett.*, 393(1-3):51–57, 2004.

[123] Yan Zhao, Nathan E Schultz, and Donald G Truhlar. Design of density functionals by combining the method of constraint satisfaction with parametrization for thermochemistry, thermochemical kinetics, and noncovalent interactions. *J. Chem. Theory Comput.*, 2(2):364–382, 2006.

[124] M. J. Frisch, G. W. Trucks, H. B. Schlegel, G. E. Scuseria, M. A. Robb, J. R. Cheeseman, G. Scalmani, V. Barone, B. Mennucci, G. A. Petersson, H. Nakatsuji, M. Caricato, X. Li, H. P. Hratchian, A. F. Izmaylov, J. Bloino, G. Zheng, J. L. Sonnenberg, W. Liang, M. Hada, M. Ehara, K. Toyota, R. Fukuda, J. Hasegawa, M. Ishida, T. Nakajima, Y. Honda, O. Kitao, H. Nakai, T. Vreven, Jr. J. A. Montgomery, J. E. Peralta, F. Ogliaro, M. Bearpark, J. J. Heyd, E. Brothers, K. N. Kudin, V. N. Staroverov, T. Keith, R. Kobayashi, J. Normand, K. Raghavachari, A. Rendell, J. C. Burant, S. S. Iyengar, J. Tomasi, M. Cossi, N. Rega, J. M. Millam, M. Klene, J. E. Knox, J. B. Cross, V. Bakken, C. Adamo, J. Jaramillo, R. Gomperts, R. E. Stratmann, O. Yazyev, A. J. Austin, R. Cammi, C. Pomelli, J. W. Ochterski, R. L. Martin, K. Morokuma, V. G. Zakrzewski, G. A. Voth, P. Salvador, J. J. Dannenberg, S. Dapprich, P. V. Parandekar, N. J. Mayhall, A. D. Daniels, Ö. Farkas, J. B. Foresman, J. V. Ortiz, J. Cioslowski, and D. J. Fox. Gaussian Development Version Revision I.11p.

[125] P Jeffrey Hay and Willard R Wadt. Ab initio effective core potentials for molecular calculations. potentials for the transition metal atoms sc to hg. *J. Chem. Phys.*, 82(1):270–283, 1985.

[126] P Jeffrey Hay and Willard R Wadt. Ab initio effective core potentials for molecular calculations. potentials or k to au including the outermost core orbitals. *J. Chem. Phys.*, 82(1):299–310, 1985.

[127] Thom Dunning Jr and P. J. Hay. chapter 1, pages 1–28. Plenum, New York, 1977.

[128] Erik C Wasinger, Frank MF De Groot, Britt Hedman, Keith O Hodgson, and Edward I Solomon. L-edge x-ray absorption spectroscopy of non-heme iron sites: Experimental determination of differential orbital covalency. *J. Am. Chem. Soc.*, 125(42):12894–12906, 2003.

[129] JD Bozek, KH Tan, GM Bancroft, and JS Tse. High resolution gas phase photoabsorption spectra of sicl4 and si(ch3)$_4$ at the silicon l edges: Characterization and assignment of resonances. *Chem. Phys. Lett.*, 138(1):33–42, 1987.

[130] TK Sham. L-edge x-ray absorption spectra of pdal$_3$ and pdcl$_2$: A study of charge redistribution in compounds of an element with a nearly full 4d shell. *Phys. Rev. B*, 31(4):1903, 1985.

[131] E Hudson, DA Shirley, M Domke, G Remmers, A Puschmann, T Mandel, C Xue, and G Kaindl. High-resolution measurements of near-edge resonances in the core-level photoionization spectra of sf$_6$. *Phys. Rev. A*, 47(1):361, 1993.

[132] Serena DeBeer George, Taras Petrenko, and Frank Neese. Prediction of iron k-edge absorption spectra using time-dependent density functional theory. *J. Phys. Chem. A*, 112(50):12936–12943, 2008.

[133] RD Leapman and LA Grunes. Anomalous l$_3$/l$_2$ white-line ratios in the $3d$ transition metals. *Phys. Rev. Lett.*, 45(5):397, 1980.

[134] BT Thole and G van der Laan. Branching ratio in x-ray absorption spectroscopy. *Phys. Rev. B*, 38(5):3158, 1988.

[135] MR Pederson, AY Liu, Tunna Baruah, EZ Kurmaev, A Moewes, S Chiuzbăian, M Neumann, CR Kmety, KL Stevenson, and D Ederer. Electronic structure of the molecule-based magnet mn[n(cn)$_2$]$_2$ from theory and experiment. *Phys. Rev. B*, 66(1):014446, 2002.

[136] Hidekazu Ikeno, Frank M F de Groot, and Isao Tanaka. *Ab-initio* CI Calculations for $3d$ Transition Metal L$_{2,3}$ X-ray Absorption Spectra of TiCl$_4$ and VOCl$_3$. *J. Phys. Conf. Ser.*, 190:012005, 2009.

[137] A. Mohanty and E. Clementi. Dirac-fock self-consistent field method for closed-shell molecules with kinetic balance and finite nuclear size. *Int. J. Quant. Chem.*, 39(3):487–517, 1991.

[138] L. Visscher, O. Visser, P.J.C. Aerts, H. Merenga, and W.C. Nieuwpoort. Relativistic quantum chemistry: the molfdir program package. *Comp. Phys. Comm.*, 81(1):120 – 144, 1994.

[139] Lucas Visscher. Approximate molecular relativistic dirac-coulomb calculations using a simple coulombic correction. *Theor. Chem. Acc.*, 98(2-3):68–70, 1997.

[140] Trond Saue, Knut Fægri, Trygve Helgaker, and Odd Gropen. Principles of direct 4-component relativistic scf: Application to caesium auride. *Mol. Phys.*, 91(5):937–950, 1997.

[141] T. Saue and H. J. Aa Jensen. Quaternion symmetry in relativistic molecular calculations: The dirachartreefock method. *J. Chem. Phys.*, 111(14):6211–6222, 1999.

[142] H.M. Quiney, H. Skaane, and I.P. Grant. Ab initio relativistic quantum chemistry: Four-components good, two-components bad! volume 32 of *Adv. Quantum Chem.*, pages 1 – 49. Academic Press, 1998.

[143] Ian P. Grant and Harry M. Quiney. Application of relativistic theories and quantum electrodynamics to chemical problems. *Int. J. Quant. Chem.*, 80(3):283–297, 2000.

[144] Takeshi Yanai, Takahito Nakajima, Yasuyuki Ishikawa, and Kimihiko Hirao. A new computational scheme for the dirachartreefock method employing an efficient integral algorithm. *J. Chem. Phys.*, 114(15):6526–6538, 2001.

[145] Takeshi Yanai, Takahito Nakajima, Yasuyuki Ishikawa, and Kimihiko Hirao. A highly efficient algorithm for electron repulsion integrals over relativistic four-component gaussian-type spinors. *J. Chem. Phys.*, 116(23):10122–10128, 2002.

[146] Matthew S. Kelley and Toru Shiozaki. Large-scale diracfockbreit method using density fitting and 2-spinor basis functions. *J. Chem. Phys.*, 138(20):204113, 2013.

[147] Kenneth G. Dyall. An exact separation of the spinfree and spindependent terms of the diraccoulombbreit hamiltonian. *J. Chem. Phys.*, 100(3):2118–2127, 1994.

[148] Markus Reiher and Alexander Wolf. *Relativistic Quantum Chemistry.* Wiley-VCH, second edition, 2015.

[149] Michal Repisky, Stanislav Komorovsky, Marius Kadek, Lukas Konecny, Ulf Ekstrm, Elena Malkin, Martin Kaupp, Kenneth Ruud, Olga L. Malkina, and Vladimir G. Malkin. Respect: Relativistic spectroscopy dft program package. *J. Chem. Phys.*, 152(18):184101, 2020.

[150] Richard E. Stanton and Stephen Havriliak. Kinetic balance: A partial solution to the problem of variational safety in dirac calculations. *J. Chem. Phys.*, 81(4):1910–1918, 1984.

[151] Yasuyuki Ishikawa, R.C. Binning, and K.M. Sando. Dirac-fock discrete-basis calculations on the beryllium atom. *Chem. Phys. Lett.*, 101(1):111 – 114, 1983.

[152] Kenneth G. Dyall and Knut Fgri. Kinetic balance and variational bounds failure in the solution of the dirac equation in a finite gaussian basis set. *Chem. Phys. Lett.*, 174(1):25 – 32, 1990.

[153] Wenjian Liu. Ideas of relativistic quantum chemistry. *Mol. Phys.*, 108:1679–1706, 2010.

[154] Qiming Sun, Wenjian Liu, and Werner Kutzelnigg. Comparison of restricted, unrestricted, inverse, and dual kinetic balances for four-component relativistic calculations. *Theor. Chem. Acc.*, 129:423–436, 2011.

[155] Shichao Sun and Xiaosong Li. Relativistic effects in magnetic circular dichroism: Restricted magnetic balance and temperature dependence. *J. Chem. Theory Comput.*, 16(7):4533–4542, 2020.

[156] S. Sun, R. Beck, D. B. Williams-Young, and X. Li. Simulating magnetic circular dichroism spectra with real-time time-dependent density functional theory in gauge including atomic orbitals. *J. Chem. Theory Comput.*, 15:6824–6831, 2019.

[157] Torin Stetina, Shichao Sun, David B Williams-Yong, and Xiaosong Li. Modeling magneto-photoabsorption using time-dependent complex generalized hartree-fock. *ChemPhotoChem*, 3:739–746, 2019.

[158] Shichao Sun, David Williams-Young, and Xiaosong Li. An ab initio linear response method for computing magnetic circular dichroism spectra with nonperturbative treatment of magnetic field. *J. Chem. Theory Comput.*, 15:3162–3169, 2019. PMID: 30933558.

[159] Shichao Sun, David Williams-Young, Torin F. Stetina, and Xiaosong Li. Generalized hartree-fock with non-perturbative treatment of strong magnetic field: Application to molecular spin phase transition. *J. Chem. Theory Comput.*, 15:348–356, 2019.

[160] Björn O Roos, Roland Lindh, Per-Åke Malmqvist, Valera Veryazov, and Per-Olof Widmark. Main group atoms and dimers studied with a new relativistic ano basis set. *J. Phys. Chem. A*, 108(15):2851–2858, 2004.

[161] Björn O Roos, Roland Lindh, Per-Åke Malmqvist, Valera Veryazov, and Per-Olof Widmark. New relativistic ano basis sets for transition metal atoms. *J. Phys. Chem. A*, 109(29):6575–6579, 2005.

[162] Bjorn O Roos, Roland Lindh, Per-Åke Malmqvist, Valera Veryazov, Per-Olof Widmark, and Antonio Carlos Borin. New relativistic atomic natural orbital basis sets for lanthanide atoms with applications to the ce diatom and luf$_3$. *J. Phys. Chem. A*, 112(45):11431–11435, 2008.

[163] Qiming Sun. Libcint: An efficient general integral library for gaussian basis functions. *J. Comput. Chem.*, 36:1664–1671, 2015.

[164] David B Williams-Young, Alessio Petrone, Shichao Sun, Torin F Stetina, Patrick Lestrange, Chad E Hoyer, Daniel R Nascimento, Lauren Koulias, Andrew Wildman, Joseph Kasper, Joshua J. Goings, Feizhi Ding, A. Eugene DePrince III, Edward F. Valeev, and Xiaosong Li. The chronus quantum (chronusq) software package. *WIREs Comput. Mol. Sci.*, 10:e1436, 2020.

[165] Qiming Sun, Timothy C. Berkelbach, Nick S. Blunt, George H. Booth, Sheng Guo, Zhendong Li, Junzi Liu, James D. McClain, Elvira R. Sayfutyarova, Sandeep Sharma, Sebastian Wouters, and Garnet Kin-Lic Chan. Pyscf: the python-based simulations of chemistry framework. *WIREs Comput. Mol. Sci.*, 8(1):e1340, 2018.

[166] E. F. Valeev. Libint: A library for the evaluation of molecular integrals of many-body operators over gaussian functions. http://libint.valeyev.net/, 2020. version 2.7.0-beta.6.

[167] A. K. Mohanty and E. Clementi. Kinetically balanced geometric gaussian basis sets for relativistic atoms. *J. Chem. Phys.*, 93(3):1829–1833, 1990.

[168] L. Visschera and K. G. Dyall. Dirac-fock atomic electronic structure calculations using different nuclear charge distributions. 67:207–224, 1997.

[169] Ralf Wesendrup, Jon K. Laerdahl, and Peter Schwerdtfeger. Relativistic effects in gold chemistry. vi. coupled cluster calculations for the isoelectronic series aupt$^-$, au$_2$, and auhg$^+$. *J. Chem. Phys.*, 110(19):9457–9462, 1999.

[170] Michael D Morse. Clusters of transition-metal atoms. *Chem. Rev.*, 86(6):1049–1109, 1986.

[171] Benoit Simard, Peter A Hackett, Andrew M James, and Patrick RR Langridge-Smith. The bond length of silver dimer. *Chem. Phys. Lett.*, 186(4-5):415–422, 1991.

[172] LL Ames and RF Barrow. Rotational analysis of bands of the gaseous au$_2$ molecule. *Transactions of the Faraday Society*, 63:39–44, 1967.

[173] K Hilpert and KA Gingerich. Atomization enthalpies of the molecules cu_3, ag_3, and au_3. *Berichte der Bunsengesellschaft für physikalische Chemie*, 84(8):739–745, 1980.

[174] J Kordis, KA Gingerich, and RJ Seyse. Atomization energies and heats of formation of gaseous au_2, tb_2, tbau, hoau, $tbau_2$, and $hoau_2$. *J. Chem. Phys.*, 61(12):5114–5121, 1974.

[175] J. Autschbach, S. Siekierski, M. Seth, P. Schwerdtfeger, and W. H. E. Schwarz. Dependence of relativistic effects on electronic configuration in the neutral atoms of d- and f-block elements. *J. Comput. Chem.*, 23(8):804–813, 2002.

[176] Knut Fægri Jr. Relativistic gaussian basis sets for the elements k–uuo. *Theor. Chem. Acc.*, 105(3):252–258, 2001.

[177] L. Visscher, P. J. C. Aerts, O. Visser, and W. C. Nieuwpoort. Kinetic balance in contracted basis sets for relativistic calculations. *Int. J. Quant. Chem.*, 40(S25):131–139, 1991.

[178] Benjamin P Lanyon, James D Whitfield, Geoff G Gillett, Michael E Goggin, Marcelo P Almeida, Ivan Kassal, Jacob D Biamonte, Masoud Mohseni, Ben J Powell, Marco Barbieri, et al. Towards quantum chemistry on a quantum computer. *Nature chemistry*, 2(2):106–111, 2010.

[179] Markus Reiher, Nathan Wiebe, Krysta M Svore, Dave Wecker, and Matthias Troyer. Elucidating reaction mechanisms on quantum computers. *Proceedings of the National Academy of Sciences*, 114(29):7555–7560, 2017.

[180] Vera von Burg, Guang Hao Low, Thomas Häner, Damian S Steiger, Markus Reiher, Martin Roetteler, and Matthias Troyer. Quantum computing enhanced computational catalysis. *arXiv preprint arXiv:2007.14460*, 2020.

[181] Joonho Lee, Dominic Berry, Craig Gidney, William J Huggins, Jarrod R McClean, Nathan Wiebe, and Ryan Babbush. Even more efficient quantum computations of chemistry through tensor hypercontraction. *arXiv preprint arXiv:2011.03494*, 2020.

[182] Ian D Kivlichan, Nathan Wiebe, Ryan Babbush, and Alán Aspuru-Guzik. Bounding the costs of quantum simulation of many-body physics in real space. *Journal of Physics A: Mathematical and Theoretical*, 50(30):305301, 2017.

[183] Ryan Babbush, Dominic W Berry, Jarrod R McClean, and Hartmut Neven. Quantum simulation of chemistry with sublinear scaling in basis size. *npj Quantum Information*, 5(1):1–7, 2019.

[184] Rene Gerritsma, Gerhard Kirchmair, Florian Zähringer, E Solano, R Blatt, and CF Roos. Quantum simulation of the dirac equation. *Nature*, 463(7277):68–71, 2010.

[185] François Fillion-Gourdeau, Steve MacLean, and Raymond Laflamme. Algorithm for the solution of the dirac equation on digital quantum computers. *Physical Review A*, 95(4):042343, 2017.

[186] Markus Reiher and Alexander Wolf. *Relativistic Quantum Chemistry: The Fundamental Theory of Molecular Science*. John Wiley & Sons, 2014.

[187] Kenneth G Dyall and Knut Fægri Jr. *Introduction to Relativistic Quantum Chemistry*. Oxford University Press, 2007.

[188] N. Klco, E. F. Dumitrescu, A. J. McCaskey, T. D. Morris, R. C. Pooser, M. Sanz, E. Solano, P. Lougovski, and M. J. Savage. Quantum-classical computation of Schwinger model dynamics using quantum computers. *Phys. Rev.*, A98(3):032331, 2018.

[189] C. Kokail, C. Maier, R. van Bijnen, T. Brydges, M. K. Joshi, P. Jurcevic, C. A. Muschik, P. Silvi, R. Blatt, C. F. Roos, and et al. Self-verifying variational quantum simulation of lattice models. *Nature*, 569(7756):355360, May 2019.

[190] Dmitri E. Kharzeev and Yuta Kikuchi. Real-time chiral dynamics from a digital quantum simulation, 2020.

[191] Hsuan-Hao Lu, Natalie Klco, Joseph M. Lukens, Titus D. Morris, Aaina Bansal, Andreas Ekstrm, Gaute Hagen, Thomas Papenbrock, Andrew M. Weiner, Martin J. Savage, and et al. Simulations of subatomic many-body physics on a quantum frequency processor. *Physical Review A*, 100(1), Jul 2019.

[192] C. Kokail, C. Maier, R. van Bijnen, T. Brydges, M. K. Joshi, P. Jurcevic, C. A. Muschik, P. Silvi, R. Blatt, C. F. Roos, and et al. Self-verifying variational quantum simulation of lattice models. *Nature*, 569(7756):355360, May 2019.

[193] Bipasha Chakraborty, Masazumi Honda, Taku Izubuchi, Yuta Kikuchi, and Akio Tomiya. Digital quantum simulation of the schwinger model with topological term via adiabatic state preparation, 2020.

[194] Alexander F. Shaw, Pavel Lougovski, Jesse R. Stryker, and Nathan Wiebe. Quantum algorithms for simulating the lattice schwinger model, 2020.

[195] Julian Bender, Erez Zohar, Alessandro Farace, and J Ignacio Cirac. Digital quantum simulation of lattice gauge theories in three spatial dimensions. *New Journal of Physics*, 20(9):093001, Sep 2018.

[196] Erez Zohar and Michele Burrello. Formulation of lattice gauge theories for quantum simulations. *Physical Review D*, 91(5), Mar 2015.

[197] Natalie Klco, Jesse R. Stryker, and Martin J. Savage. Su(2) non-abelian gauge field theory in one dimension on digital quantum computers, 2019.

[198] Erez Zohar, J. Ignacio Cirac, and Benni Reznik. Quantum simulations of gauge theories with ultracold atoms: Local gauge invariance from angular-momentum conservation. *Physical Review A*, 88(2), Aug 2013.

[199] Erez Zohar, J Ignacio Cirac, and Benni Reznik. Quantum simulations of lattice gauge theories using ultracold atoms in optical lattices. *Reports on Progress in Physics*, 79(1):014401, Dec 2015.

[200] Henry Lamm, Scott Lawrence, and Yukari Yamauchi. General methods for digital quantum simulation of gauge theories. *Physical Review D*, 100(3), Aug 2019.

[201] Andrei Alexandru, Paulo F. Bedaque, Siddhartha Harmalkar, Henry Lamm, Scott Lawrence, and Neill C. Warrington. Gluon field digitization for quantum computers. *Physical Review D*, 100(11), Dec 2019.

[202] Andrei Alexandru, Paulo F. Bedaque, Henry Lamm, and Scott Lawrence. Sigma models on quantum computers. *Physical Review Letters*, 123(9), Aug 2019.

[203] Henry Lamm, Scott Lawrence, and Yukari Yamauchi. Parton physics on a quantum computer. *Physical Review Research*, 2(1), Mar 2020.

[204] Mari Carmen Bauls, Rainer Blatt, Jacopo Catani, Alessio Celi, Juan Ignacio Cirac, Marcello Dalmonte, Leonardo Fallani, Karl Jansen, Maciej Lewenstein, Simone Montangero, and et al. Simulating lattice gauge theories within quantum technologies. *The European Physical Journal D*, 74(8), Aug 2020.

[205] L. Tagliacozzo, A. Celi, P. Orland, M. W. Mitchell, and M. Lewenstein. Simulation of non-abelian gauge theories with optical lattices. *Nature Communications*, 4(1), Oct 2013.

[206] L. Tagliacozzo, A. Celi, A. Zamora, and M. Lewenstein. Optical abelian lattice gauge theories. *Annals of Physics*, 330:160191, Mar 2013.

[207] Leonardo Mazza, Alejandro Bermudez, Nathan Goldman, Matteo Rizzi, Miguel Angel Martin-Delgado, and Maciej Lewenstein. An optical-lattice-based quantum simulator for relativistic field theories and topological insulators. *New Journal of Physics*, 14(1):015007, jan 2012.

[208] A. Bermudez, L. Mazza, M. Rizzi, N. Goldman, M. Lewenstein, and M. A. Martin-Delgado. Wilson fermions and axion electrodynamics in optical lattices. *Phys. Rev. Lett.*, 105:190404, Nov 2010.

[209] Simon V Mathis, Guglielmo Mazzola, and Ivano Tavernelli. Toward scalable simulations of lattice gauge theories on quantum computers. *Physical Review D*, 102(9):094501, 2020.

[210] Libor Veis, Jakub Višňák, Timo Fleig, Stefan Knecht, Trond Saue, Lucas Visscher, and Jiří Pittner. Relativistic quantum chemistry on quantum computers. *Physical Review A*, 85(3):030304, 2012.

[211] Pekka Pyykkö. The physics behind chemistry and the periodic table. *Chemical reviews*, 112(1):371–384, 2012.

[212] Wenjian Liu. Effective quantum electrodynamics hamiltonians: A tutorial review. *International Journal of Quantum Chemistry*, 115(10):631–640, 2015.

[213] Wenjian Liu and Ingvar Lindgren. Going beyond no-pair relativistic quantum chemistry. *The Journal of Chemical Physics*, 139(1):014108, 2013.

[214] Matthew D. Schwartz. *Quantum Field Theory and the Standard Model*. Cambridge University Press, 2014.

[215] Ryan Babbush, Nathan Wiebe, Jarrod McClean, James McClain, Hartmut Neven, and Garnet Kin-Lic Chan. Low-depth quantum simulation of materials. *Physical Review X*, 8(1):011044, 2018.

[216] Tobias Hagge. Optimal fermionic swap networks for hubbard models. *arXiv preprint arXiv:2001.08324*, 2020.

[217] Holger Bech Nielsen and M. Ninomiya. No Go Theorem for Regularizing Chiral Fermions. *Phys. Lett. B*, 105:219–223, 1981.

[218] Holger Bech Nielsen and M. Ninomiya. Absence of Neutrinos on a Lattice. 2. Intuitive Topological Proof. *Nucl. Phys. B*, 193:173–194, 1981.

[219] Kenneth G Wilson. New phenomena in subnuclear physics, 1977.

[220] John Kogut and Leonard Susskind. Hamiltonian formulation of wilson's lattice gauge theories. *Phys. Rev. D*, 11:395–408, Jan 1975.

[221] Sidney D. Drell, Marvin Weinstein, and Shimon Yankielowicz. Strong-coupling field theories. ii. fermions and gauge fields on a lattice. *Phys. Rev. D*, 14:1627–1647, Sep 1976.

[222] Paolo Nason. The lattice schwinger model with slac fermions. *Nuclear Physics B*, 260(2):269 – 284, 1985.

[223] Frank Verstraete, J Ignacio Cirac, and José I Latorre. Quantum circuits for strongly correlated quantum systems. *Physical Review A*, 79(3):032316, 2009.

[224] Christof Zalka. Simulating quantum systems on a quantum computer. *Proceedings of the Royal Society of London. Series A: Mathematical, Physical and Engineering Sciences*, 454(1969):313–322, 1998.

[225] Nathan Wiebe, Dominic W Berry, Peter Høyer, and Barry C Sanders. Simulating quantum dynamics on a quantum computer. *Journal of Physics A: Mathematical and Theoretical*, 44(44):445308, 2011.

[226] Yuan Su, Hsin-Yuan Huang, and Earl T Campbell. Nearly tight trotterization of interacting electrons. *arXiv preprint arXiv:2012.09194*, 2020.

[227] Masuo Suzuki. Fractal decomposition of exponential operators with applications to many-body theories and monte carlo simulations. *Physics Letters A*, 146(6):319–323, 1990.

[228] Andrew M Childs, Yuan Su, Minh C Tran, Nathan Wiebe, and Shuchen Zhu. A theory of trotter error. *arXiv preprint arXiv:1912.08854*, 2019.

[229] Andrew M Childs, Dmitri Maslov, Yunseong Nam, Neil J Ross, and Yuan Su. Toward the first quantum simulation with quantum speedup. *Proceedings of the National Academy of Sciences*, 115(38):9456–9461, 2018.

[230] Matthew B Hastings, Dave Wecker, Bela Bauer, and Matthias Troyer. Improving quantum algorithms for quantum chemistry. *Quantum Information & Computation*, 15(1-2):1–21, 2015.

[231] Jacob T Seeley, Martin J Richard, and Peter J Love. The bravyi-kitaev transformation for quantum computation of electronic structure. *The Journal of chemical physics*, 137(22):224109, 2012.

[232] Bryan O'Gorman, William J Huggins, Eleanor G Rieffel, and K Birgitta Whaley. Generalized swap networks for near-term quantum computing. *arXiv preprint arXiv:1905.05118*, 2019.

[233] Ryan Babbush, Jarrod McClean, Dave Wecker, Alán Aspuru-Guzik, and Nathan Wiebe. Chemical basis of trotter-suzuki errors in quantum chemistry simulation. *Physical Review A*, 91(2):022311, 2015.

[234] Andrew M Childs, Yuan Su, Minh C Tran, Nathan Wiebe, and Shuchen Zhu. A theory of trotter error. *arXiv preprint arXiv:1912.08854*, 2019.

[235] Roger A Horn and Charles R Johnson. *Matrix Analysis*. Cambridge university press, 2012.

[236] Vadym Kliuchnikov, Dmitri Maslov, and Michele Mosca. Fast and efficient exact synthesis of single qubit unitaries generated by clifford and t gates. *arXiv preprint arXiv:1206.5236*, 2012.

[237] Neil J Ross and Peter Selinger. Optimal ancilla-free clifford+ t approximation of z-rotations. *arXiv preprint arXiv:1403.2975*, 2014.

[238] Dominic W Berry, Craig Gidney, Mario Motta, Jarrod McClean, and Ryan Babbush. Qubitization of arbitrary basis quantum chemistry by low rank factorization. *arXiv preprint arXiv:1902.02134*, 2019.

[239] Brendon L Higgins, Dominic W Berry, Stephen D Bartlett, Howard M Wiseman, and Geoff J Pryde. Entanglement-free heisenberg-limited phase estimation. *Nature*, 450(7168):393–396, 2007.

[240] AA Abrikosov, LD Landau, and IM Khalatnikov. On the elimination of infinities in quantum electrodynamics'. In *Dokl. Akad. Nauk SSSR*, volume 95, page 497, 1954.

[241] David J.E. Callaway. Triviality pursuit: Can elementary scalar particles exist? *Physics Reports*, 167(5):241 – 320, 1988.

[242] M. Gockeler, R. Horsley, E. Laermann, P. Rakow, G. Schierholz, R. Sommer, and U.J. Wiese. The continuum limit of qed. renormalization group analysis and the question of triviality. *Physics Letters B*, 251(4):567 – 574, 1990.

[243] D. Djukanovic, J. Gegelia, and Ulf-G. Meiner. Triviality of quantum electrodynamics revisited. *Communications in Theoretical Physics*, 69(3):263, Mar 2018.

[244] Andrew M Childs. On the relationship between continuous-and discrete-time quantum walk. *Communications in Mathematical Physics*, 294(2):581–603, 2010.

[245] András Gilyén, Yuan Su, Guang Hao Low, and Nathan Wiebe. Quantum singular value transformation and beyond: exponential improvements for quantum matrix arithmetics. In *Proceedings of the 51st Annual ACM SIGACT Symposium on Theory of Computing*, pages 193–204, 2019.

[246] Ryan Babbush, Craig Gidney, Dominic W Berry, Nathan Wiebe, Jarrod McClean, Alexandru Paler, Austin Fowler, and Hartmut Neven. Encoding electronic spectra in quantum circuits with linear t complexity. *Physical Review X*, 8(4):041015, 2018.

[247] David Poulin, Alexei Kitaev, Damian S Steiger, Matthew B Hastings, and Matthias Troyer. Quantum algorithm for spectral measurement with a lower gate count. *Physical review letters*, 121(1):010501, 2018.

[248] Mario Motta, Erika Ye, Jarrod R McClean, Zhendong Li, Austin J Minnich, Ryan Babbush, and Garnet Kin Chan. Low rank representations for quantum simulation of electronic structure. *arXiv preprint arXiv:1808.02625*, 2018.

[249] Ian D Kivlichan, Jarrod McClean, Nathan Wiebe, Craig Gidney, Alán Aspuru-Guzik, Garnet Kin-Lic Chan, and Ryan Babbush. Quantum simulation of electronic structure with linear depth and connectivity. *Physical review letters*, 120(11):110501, 2018.

[250] Aaron Meurer, Christopher P. Smith, Mateusz Paprocki, Ondřej Čertík, Sergey B. Kirpichev, Matthew Rocklin, AMiT Kumar, Sergiu Ivanov, Jason K. Moore, Sartaj Singh, Thilina Rathnayake, Sean Vig, Brian E. Granger, Richard P. Muller, Francesco Bonazzi, Harsh Gupta, Shivam Vats, Fredrik Johansson, Fabian Pedregosa, Matthew J. Curry, Andy R. Terrel, Štěpán Roučka, Ashutosh Saboo, Isuru Fernando, Sumith Kulal, Robert Cimrman, and Anthony Scopatz. Sympy: symbolic computing in python. *PeerJ Computer Science*, 3:e103, January 2017.

[251] Ryan Babbush, Craig Gidney, Dominic W Berry, Nathan Wiebe, Jarrod McClean, Alexandru Paler, Austin Fowler, and Hartmut Neven. Encoding electronic spectra in quantum circuits with linear t complexity. *Physical Review X*, 8(4):041015, 2018.

[252] Alex Bocharov, Martin Roetteler, and Krysta M Svore. Efficient synthesis of universal repeat-until-success quantum circuits. *Physical Review Letters*, 114(8):080502, 2015.

[253] Peter G Szalay, Thomas Muller, Gergely Gidofalvi, Hans Lischka, and Ron Shepard. Multiconfiguration self-consistent field and multireference configuration interaction methods and applications. *Chemical reviews*, 112(1):108–181, 2012.

[254] Hans Lischka, Ron Shepard, Franklin B Brown, and Isaiah Shavitt. New implementation of the graphical unitary group approach for multireference direct configuration interaction calculations. *International Journal of Quantum Chemistry*, 20(S15):91–100, 1981.

[255] Hang Hu, Andrew J. Jenkins, Hongbin Liu, Joseph M. Kasper, Michael J. Frisch, and Xiaosong Li. Relativistic two-component multireference configuration interaction method with tunable correlation space. *J. Chem. Theory Comput.*, 16(5):2975–2984, 2020.

[256] Zhang Jiang, Kevin J Sung, Kostyantyn Kechedzhi, Vadim N Smelyanskiy, and Sergio Boixo. Quantum algorithms to simulate many-body physics of correlated fermions. *Physical Review Applied*, 9(4):044036, 2018.

[257] Rulin Feng and Kirk A. Peterson. Correlation consistent basis sets for actinides. ii. the atoms ac and nplr. *J. Chem. Phys.*, 147(8):084108, 2017.

[258] Stanislav Komorovský, Michal Repiský, Olga L. Malkina, Vladimir G. Malkin, Irina Malkin Ondík, and Martin Kaupp. A fully relativistic method for calculation of nuclear magnetic shielding tensors with a restricted magnetically balanced basis in the framework of the matrix dirac-kohn-sham equation. *J. Chem. Phys.*, 128(10):104101, 2008.

[259] Lan Cheng, Yunlong Xiao, and Wenjian Liu. Four-component relativistic theory for nuclear magnetic shielding: Magnetically balanced gauge-including atomic orbitals. *J. Chem. Phys.*, 131(24):244113, 2009.

[260] Praphull Chandra and Bernd Artur Heß. A finite-nucleus model for relativistic electronic structure calculations using a douglas-kroll-transformed hamiltonian. *Theor. Chem. Acc.*, 88(3):183–199, 1994.

[261] DIRAC, a Relativistic Ab Initio Electronic Structure Program, Release DIRAC19 (2019), written by A. S. P. Gomes, T. Saue, L. Visscher, H. J. Aa. Jensen, and R. Bast, with contributions from I. A. Aucar, V. Bakken, K. G. Dyall, S. Dubillard, U. Ekström, E. Eliav, T. Enevoldsen, E. Faßhauer, T. Fleig, O. Fossgaard, L. Halbert, E. D. Hedegård, B. Heimlich–Paris, T. Helgaker, J. Henriksson, M. Iliaš, Ch. R. Jacob, S. Knecht, S. Komorovský, O. Kullie, J. K. Lærdahl, C. V. Larsen, Y. S. Lee, H. S. Nataraj, M. K. Nayak, P. Norman, G. Olejniczak, J. Olsen, J. M. H. Olsen,

Y. C. Park, J. K. Pedersen, M. Pernpointner, R. di Remigio, K. Ruud, P. Sałek, B. Schimmelpfennig, B. Senjean, A. Shee, J. Sikkema, A. J. Thorvaldsen, J. Thyssen, J. van Stralen, M. L. Vidal, S. Villaume, O. Visser, T. Winther, and S. Yamamoto.

[262] Trond Saue, Radovan Bast, Andr Severo Pereira Gomes, Hans Jrgen Aa. Jensen, Lucas Visscher, Ignacio Agustn Aucar, Roberto Di Remigio, Kenneth G. Dyall, Ephraim Eliav, Elke Fasshauer, Timo Fleig, Loc Halbert, Erik Donovan Hedegrd, Benjamin Helmich-Paris, Miroslav Ilia, Christoph R. Jacob, Stefan Knecht, Jon K. Laerdahl, Marta L. Vidal, Malaya K. Nayak, Magorzata Olejniczak, Jgvan Magnus Haugaard Olsen, Markus Pernpointner, Bruno Senjean, Avijit Shee, Ayaki Sunaga, and Joost N. P. van Stralen. The dirac code for relativistic molecular calculations. *J. Chem. Phys.*, 152(20):204104, 2020.

Appendix A

SPIN-SEPARATION FOR GAUNT INTERACTION

The Gaunt term integrals can be separate into spin-free, spin-own-orbit, and spin-other-orbit interactions in the Pauli spinor representation. In this section, detailed derivations will be shown for the $(\mu^L\boldsymbol{\sigma}\nu^S|\cdot\kappa^S\boldsymbol{\sigma}\lambda^L)$ type of integral which contributes to the exchange term in $V^{G,LL}$ and Coulomb term in $V^{G,LS}$.

The $(\mu^L\boldsymbol{\sigma}\nu^S|\cdot\kappa^S\boldsymbol{\sigma}\lambda^L)$ integral can be written as (prefactor $\frac{1}{(2mc)^2}$ is ignored for brevity),

$$\begin{aligned}(\mu^L_{\tau_1}\boldsymbol{\sigma}\nu^S_{\tau_2}|\cdot\kappa^S_{\tau_3}\boldsymbol{\sigma}\lambda^L_{\tau_4}) =&(\mu^L_{\tau_1}\boldsymbol{\sigma}(1)\boldsymbol{\sigma}(1)\cdot\mathbf{p}(1)\nu^L_{\tau_2}|\cdot\boldsymbol{\sigma}(2)\cdot\mathbf{p}(2)\kappa^L_{\tau_3}\boldsymbol{\sigma}(2)\lambda^L_{\tau_4})\\ =&-(\mu^L_{\tau_1}\boldsymbol{\sigma}(1)\boldsymbol{\sigma}(1)\cdot\boldsymbol{\nabla}(1)\nu^L_{\tau_2}|\cdot\boldsymbol{\sigma}(2)\cdot\boldsymbol{\nabla}(2)\kappa^L_{\tau_3}\boldsymbol{\sigma}(2)\lambda^L_{\tau_4})\end{aligned}$$

where we used the restricted-kinetic-balance condition $\mu^S=\frac{1}{2mc}\boldsymbol{\sigma}\cdot\mathbf{p}\mu^L$. $\boldsymbol{\nabla}_\kappa$ and $\boldsymbol{\nabla}_\nu$ are gradients with respect to basis centers of κ^L and ν^L, respectively.

We now switch from Mulliken notation to Dirac notation to carry out the spin-separation

$$\begin{aligned}&-(\mu^L_{\tau_1}\boldsymbol{\sigma}(1)\boldsymbol{\sigma}(1)\cdot\boldsymbol{\nabla}(1)\nu^L_{\tau_2}|\cdot\boldsymbol{\sigma}(2)\cdot\boldsymbol{\nabla}(2)\kappa^L_{\tau_3}\boldsymbol{\sigma}(2)\lambda^L_{\tau_4})\\ =&-\left\langle\mu^L_{\tau_1}\boldsymbol{\sigma}(2)\cdot\boldsymbol{\nabla}_\kappa\kappa^L_{\tau_3}\right|\frac{\boldsymbol{\sigma}(1)\cdot\boldsymbol{\sigma}(2)}{r_{12}}\boldsymbol{\sigma}(1)\cdot\boldsymbol{\nabla}_\nu\left|\nu^L_{\tau_2}\lambda^L_{\tau_4}\right\rangle\\ =&\left\langle\mu^L_{\tau_1}\kappa^L_{\tau_3}\right|\boldsymbol{\sigma}(2)\cdot\boldsymbol{\nabla}_\kappa\frac{\boldsymbol{\sigma}(1)\cdot\boldsymbol{\sigma}(2)}{r_{12}}\boldsymbol{\sigma}(1)\cdot\boldsymbol{\nabla}_\nu\left|\nu^L_{\tau_2}\lambda^L_{\tau_4}\right\rangle \qquad \text{(A.1)}\end{aligned}$$

where we used the relationship $\boldsymbol{\nabla}(2)=-\boldsymbol{\nabla}_\kappa$ between basis function derivative with respect to the electronic coordinate $\boldsymbol{\nabla}(2)$ and with respect to basis function center $\boldsymbol{\nabla}_\kappa$.

By using the Dirac identity, $(\boldsymbol{\sigma}(1)\cdot\boldsymbol{\sigma}(2))(\boldsymbol{\sigma}(1)\cdot\boldsymbol{\nabla}_\nu)=\mathbf{I}(1)\,\boldsymbol{\sigma}(2)\cdot\boldsymbol{\nabla}_\nu+i\boldsymbol{\sigma}(1)\cdot\boldsymbol{\sigma}(2)\times\boldsymbol{\nabla}_\nu$, Eq. A.1 can be written as,

$$\begin{aligned}&\left\langle\mu^L_{\tau_1}\kappa^L_{\tau_3}\right|\boldsymbol{\sigma}(2)\cdot\boldsymbol{\nabla}_\kappa\frac{\boldsymbol{\sigma}(1)\cdot\boldsymbol{\sigma}(2)}{r_{12}}\boldsymbol{\sigma}(1)\cdot\boldsymbol{\nabla}_\nu\left|\nu^L_{\tau_2}\lambda^L_{\tau_4}\right\rangle\\ =&\left\langle\mu^L_{\tau_1}\kappa^L_{\tau_3}\right|\boldsymbol{\sigma}(2)\cdot\boldsymbol{\nabla}_\kappa\frac{1}{r_{12}}[\mathbf{I}(1)\boldsymbol{\sigma}(2)\cdot\boldsymbol{\nabla}_\nu+i\boldsymbol{\sigma}(1)\cdot\boldsymbol{\sigma}(2)\times\boldsymbol{\nabla}_\nu]\left|\nu^L_{\tau_2}\lambda^L_{\tau_4}\right\rangle. \qquad \text{(A.2)}\end{aligned}$$

Additional applications of the Dirac identity are carried out to further spin-separate the two terms in Eq. A.2:

$$\begin{aligned}&\left\langle\mu^L_{\tau_1}\kappa^L_{\tau_3}\right|\boldsymbol{\sigma}(2)\cdot\boldsymbol{\nabla}_\kappa\frac{1}{r_{12}}\mathbf{I}(1)\boldsymbol{\sigma}(2)\cdot\boldsymbol{\nabla}_\nu\left|\nu^L_{\tau_2}\lambda^L_{\tau_4}\right\rangle\\&=\left\langle\mu^L_{\tau_1}\kappa^L_{\tau_3}\right|\mathbf{I}(1)\frac{1}{r_{12}}[\mathbf{I}(2)\boldsymbol{\nabla}_\kappa\cdot\boldsymbol{\nabla}_\nu+i\boldsymbol{\sigma}(2)\cdot\boldsymbol{\nabla}_\kappa\times\boldsymbol{\nabla}_\nu]\left|\nu^L_{\tau_2}\lambda^L_{\tau_4}\right\rangle\end{aligned}\tag{A.3}$$

and

$$\begin{aligned}&\left\langle\mu^L_{\tau_1}\kappa^L_{\tau_3}\right|\boldsymbol{\sigma}(2)\cdot\boldsymbol{\nabla}_\kappa\frac{1}{r_{12}}i\boldsymbol{\sigma}(1)\cdot\boldsymbol{\sigma}(2)\times\boldsymbol{\nabla}_\nu\left|\nu^L_{\tau_2}\lambda^L_{\tau_4}\right\rangle\\&=\left\langle\mu^L_{\tau_1}\kappa^L_{\tau_3}\right|i\frac{1}{r_{12}}[\mathbf{I}(2)\boldsymbol{\nabla}_\kappa\cdot(\boldsymbol{\nabla}_\nu\times\boldsymbol{\sigma}(1))+i\boldsymbol{\sigma}(2)\cdot\boldsymbol{\nabla}_\kappa\times(\boldsymbol{\nabla}_\nu\times\boldsymbol{\sigma}(1))]\left|\nu^L_{\tau_2}\lambda^L_{\tau_4}\right\rangle\\&=\left\langle\mu^L_{\tau_1}\kappa^L_{\tau_3}\right|\frac{1}{r_{12}}[i\mathbf{I}(2)\boldsymbol{\sigma}(1)\cdot(\boldsymbol{\nabla}_\kappa\times\boldsymbol{\nabla}_\nu)+(\boldsymbol{\sigma}(2)\times\boldsymbol{\nabla}_\kappa)\cdot(\boldsymbol{\sigma}(1)\times\boldsymbol{\nabla}_\nu)]\left|\nu^L_{\tau_2}\lambda^L_{\tau_4}\right\rangle\end{aligned}\tag{A.4}$$

Combining Eq. A.3 and Eq. A.4 into Eq. A.2, and write the integrals in Mulliken notation, we arrive at the following expression:

$$\begin{aligned}(\mu^L_{\tau_1}\boldsymbol{\sigma}\nu^S_{\tau_2}|\cdot\kappa^S_{\tau_3}\boldsymbol{\sigma}\lambda^L_{\tau_4})=\xi^\dagger_{\tau_1}(1)\xi_{\tau_2}(1)\xi^\dagger_{\tau_3}(2)\xi_{\tau_4}(2)\big[&\mathbf{I}(1)\mathbf{I}(2)\boldsymbol{\nabla}_\kappa\cdot\boldsymbol{\nabla}_\nu\\&+i(\mathbf{I}(1)\boldsymbol{\sigma}(2)+\mathbf{I}(2)\boldsymbol{\sigma}(1))\cdot\boldsymbol{\nabla}_\kappa\times\boldsymbol{\nabla}_\nu\\&+(\boldsymbol{\sigma}(2)\times\boldsymbol{\nabla}_\kappa)\cdot(\boldsymbol{\sigma}(1)\times\boldsymbol{\nabla}_\nu)\big](\mu\nu|\kappa\lambda)\end{aligned}\tag{A.5}$$

In Eq. A.5, the integral type of $\mathbf{I}(1)\mathbf{I}(2)\boldsymbol{\nabla}_\kappa\cdot\boldsymbol{\nabla}_\nu$ gives rise to the spin-free term. The contribution from the integral type of $\mathbf{I}(1)\boldsymbol{\sigma}(2)\cdot\boldsymbol{\nabla}(2)\frac{1}{r_{12}}\times\boldsymbol{\nabla}(1)$ is the spin-other-orbit term, while $\mathbf{I}(2)\boldsymbol{\sigma}(1)\cdot\boldsymbol{\nabla}(2)\frac{1}{r_{12}}\times\boldsymbol{\nabla}(1)$ is the spin-own-orbit term.

The last term $(\boldsymbol{\sigma}(2)\times\boldsymbol{\nabla}_\kappa)\cdot(\boldsymbol{\sigma}(1)\times\boldsymbol{\nabla}_\nu)$ is the spin-spin interaction which can be further separated using the scalar quadruple product rule,

$$(\boldsymbol{\sigma}(2)\times\boldsymbol{\nabla}_\kappa)\cdot(\boldsymbol{\sigma}(1)\times\boldsymbol{\nabla}_\nu)=(\boldsymbol{\sigma}(1)\cdot\boldsymbol{\sigma}(2))(\boldsymbol{\nabla}_\kappa\cdot\boldsymbol{\nabla}_\nu)-(\boldsymbol{\sigma}(1)\cdot\boldsymbol{\nabla}_\kappa)(\boldsymbol{\sigma}(2)\cdot\boldsymbol{\nabla}_\nu).$$

The final, completely spin-separated expression for the $(\mu^L_{\tau_1}\boldsymbol{\sigma}\nu^S_{\tau_2}|\cdot\kappa^S_{\tau_3}\boldsymbol{\sigma}\lambda^L_{\tau_4})$ integral is

$$\begin{aligned}(\mu^L_{\tau_1}\boldsymbol{\sigma}\nu^S_{\tau_2}|\cdot\kappa^S_{\tau_3}\boldsymbol{\sigma}\lambda^L_{\tau_4})=\xi^\dagger_{\tau_1}(1)\xi_{\tau_1}(1)\xi^\dagger_{\tau_3}(2)\xi_{\tau_4}(2)\big[&\mathbf{I}(1)\mathbf{I}(2)\boldsymbol{\nabla}_\kappa\cdot\boldsymbol{\nabla}_\nu\\&+i(\mathbf{I}(1)\boldsymbol{\sigma}(2)+\mathbf{I}(2)\boldsymbol{\sigma}(1))\cdot\boldsymbol{\nabla}_\kappa\times\boldsymbol{\nabla}_\nu\\&+(\boldsymbol{\sigma}(1)\cdot\boldsymbol{\sigma}(2))(\boldsymbol{\nabla}_\kappa\cdot\boldsymbol{\nabla}_\nu)-(\boldsymbol{\sigma}(1)\cdot\boldsymbol{\nabla}_\kappa)(\boldsymbol{\sigma}(2)\cdot\boldsymbol{\nabla}_\nu)\big](\mu\nu|\kappa\lambda)\end{aligned}\tag{A.6}$$

Appendix B

CONTRIBUTIONS FROM THE $(SS|SS)$ TERM

The SS block of the Dirac-Coulomb matrix has contributions from $(p^S q^S|r^S s^S)$ types of integral with a prefactor of $\frac{1}{(2mc)^4}$, denoted as $V^{C(4)}$.

$$V^{C(4),SS}_{\mu\tau_1,\nu\tau_2} = \sum_{\lambda\tau_4\kappa\tau_3} D^{SS}_{\lambda\tau_4\kappa\tau_3}[(\mu^S_{\tau_1}\nu^S_{\tau_2}|\kappa^S_{\tau_3}\lambda^S_{\tau_4}) - (\mu^S_{\tau_1}\lambda^S_{\tau_4}|\kappa^S_{\tau_3}\nu^S_{\tau_2})] \tag{B.1}$$

These contributions are collectively known as the $(SS|SS)$ term, which is often ignored due to its large computational cost and small energetic contribution. The $(SS|SS)$ contribution in the Pauli spinor representation is:

$$\begin{aligned}
V^{C(4),SS}_{\mu\nu,s} = {} & 2\sum_{\lambda\kappa}\left[D^{SS}_{\lambda\kappa,s}(\boldsymbol{\nabla}_\mu\cdot\boldsymbol{\nabla}_\nu)(\boldsymbol{\nabla}_\kappa\cdot\boldsymbol{\nabla}_\lambda) + i\sum_{J=x,y,z} D^{SS}_{\lambda\kappa,J}(\boldsymbol{\nabla}_\mu\cdot\boldsymbol{\nabla}_\nu)(\boldsymbol{\nabla}_\kappa\times\boldsymbol{\nabla}_\lambda)_J\right](\mu\nu|\kappa\lambda) \\
& - \sum_{\lambda\kappa} D^{SS}_{\lambda\kappa,s}\left[(\boldsymbol{\nabla}_\mu\cdot\boldsymbol{\nabla}_\lambda)(\boldsymbol{\nabla}_\kappa\cdot\boldsymbol{\nabla}_\nu) - \sum_{J=x,y,z}(\boldsymbol{\nabla}_\mu\times\boldsymbol{\nabla}_\lambda)_J(\boldsymbol{\nabla}_\kappa\times\boldsymbol{\nabla}_\nu)_J\right](\mu\lambda|\kappa\nu) \\
& - i\sum_{\lambda\kappa}\sum_{J=x,y,z} D^{SS}_{\lambda\kappa,J}\left[(\boldsymbol{\nabla}_\mu\times\boldsymbol{\nabla}_\lambda)_J(\boldsymbol{\nabla}_\kappa\cdot\boldsymbol{\nabla}_\nu) + (\boldsymbol{\nabla}_\mu\cdot\boldsymbol{\nabla}_\lambda)(\boldsymbol{\nabla}_\kappa\times\boldsymbol{\nabla}_\nu)_J\right](\mu\lambda|\kappa\nu) \\
& - i\sum_{\lambda\kappa} D^{SS}_{\lambda\kappa,z}\left[(\boldsymbol{\nabla}_\mu\times\boldsymbol{\nabla}_\lambda)_x(\boldsymbol{\nabla}_\kappa\times\boldsymbol{\nabla}_\nu)_y - (\boldsymbol{\nabla}_\mu\times\boldsymbol{\nabla}_\lambda)_y(\boldsymbol{\nabla}_\kappa\times\boldsymbol{\nabla}_\nu)_x\right](\mu\lambda|\kappa\nu) \\
& - i\sum_{\lambda\kappa} D^{SS}_{\lambda\kappa,y}\left[(\boldsymbol{\nabla}_\mu\times\boldsymbol{\nabla}_\lambda)_z(\boldsymbol{\nabla}_\kappa\times\boldsymbol{\nabla}_\nu)_x - (\boldsymbol{\nabla}_\mu\times\boldsymbol{\nabla}_\lambda)_x(\boldsymbol{\nabla}_\kappa\times\boldsymbol{\nabla}_\nu)_z\right](\mu\lambda|\kappa\nu) \\
& - i\sum_{\lambda\kappa} D^{SS}_{\lambda\kappa,x}\left[(\boldsymbol{\nabla}_\mu\times\boldsymbol{\nabla}_\lambda)_y(\boldsymbol{\nabla}_\kappa\times\boldsymbol{\nabla}_\nu)_z - (\boldsymbol{\nabla}_\mu\times\boldsymbol{\nabla}_\lambda)_z(\boldsymbol{\nabla}_\kappa\times\boldsymbol{\nabla}_\nu)_y\right](\mu\lambda|\kappa\nu)
\end{aligned} \tag{B.2}$$

$$
\begin{aligned}
V^{C(4),SS}_{\mu\nu,z} = {} & 2\sum_{\lambda\kappa}\Bigg[iD^{SS}_{\lambda\kappa,s}(\boldsymbol{\nabla}_\mu \times \boldsymbol{\nabla}_\nu)_z(\boldsymbol{\nabla}_\kappa \cdot \boldsymbol{\nabla}_\lambda) - \sum_{J=x,y,z} D^{SS}_{\lambda\kappa,J}(\boldsymbol{\nabla}_\mu \times \boldsymbol{\nabla}_\nu)_z(\boldsymbol{\nabla}_\kappa \times \boldsymbol{\nabla}_\lambda)_J\Bigg](\mu\nu|\kappa\lambda) \\
& - \sum_{\lambda\kappa} D^{SS}_{\lambda\kappa,z}\Bigg[(\boldsymbol{\nabla}_\mu \cdot \boldsymbol{\nabla}_\lambda)(\boldsymbol{\nabla}_\kappa \cdot \boldsymbol{\nabla}_\nu) - (\boldsymbol{\nabla}_\mu \times \boldsymbol{\nabla}_\lambda)_z(\boldsymbol{\nabla}_\kappa \times \boldsymbol{\nabla}_\nu)_z\Bigg](\mu\lambda|\kappa\nu) \\
& - \sum_{\lambda\kappa} D^{SS}_{\lambda\kappa,z}\Bigg[(\boldsymbol{\nabla}_\mu \times \boldsymbol{\nabla}_\lambda)_x(\boldsymbol{\nabla}_\kappa \times \boldsymbol{\nabla}_\nu)_x + (\boldsymbol{\nabla}_\mu \times \boldsymbol{\nabla}_\lambda)_y(\boldsymbol{\nabla}_\kappa \times \boldsymbol{\nabla}_\nu)_y\Bigg](\mu\lambda|\kappa\nu) \\
& - i\sum_{\lambda\kappa} D^{SS}_{\lambda\kappa,s}\Bigg[(\boldsymbol{\nabla}_\mu \cdot \boldsymbol{\nabla}_\lambda)(\boldsymbol{\nabla}_\kappa \times \boldsymbol{\nabla}_\nu)_z + (\boldsymbol{\nabla}_\mu \times \boldsymbol{\nabla}_\lambda)_z(\boldsymbol{\nabla}_\kappa \cdot \boldsymbol{\nabla}_\nu)\Bigg](\mu\lambda|\kappa\nu) \\
& - \sum_{\lambda\kappa} D^{SS}_{\lambda\kappa,y}\Bigg[(\boldsymbol{\nabla}_\mu \cdot \boldsymbol{\nabla}_\lambda)(\boldsymbol{\nabla}_\kappa \times \boldsymbol{\nabla}_\nu)_x - (\boldsymbol{\nabla}_\mu \times \boldsymbol{\nabla}_\lambda)_x(\boldsymbol{\nabla}_\kappa \cdot \boldsymbol{\nabla}_\nu)\Bigg](\mu\lambda|\kappa\nu) \\
& + \sum_{\lambda\kappa} D^{SS}_{\lambda\kappa,x}\Bigg[(\boldsymbol{\nabla}_\mu \cdot \boldsymbol{\nabla}_\lambda)(\boldsymbol{\nabla}_\kappa \times \boldsymbol{\nabla}_\nu)_y - (\boldsymbol{\nabla}_\mu \times \boldsymbol{\nabla}_\lambda)_y(\boldsymbol{\nabla}_\kappa \cdot \boldsymbol{\nabla}_\nu)\Bigg](\mu\lambda|\kappa\nu) \\
& + i\sum_{\lambda\kappa} D^{SS}_{\lambda\kappa,s}\Bigg[(\boldsymbol{\nabla}_\mu \times \boldsymbol{\nabla}_\lambda)_x(\boldsymbol{\nabla}_\kappa \times \boldsymbol{\nabla}_\nu)_y - (\boldsymbol{\nabla}_\mu \times \boldsymbol{\nabla}_\lambda)_y(\boldsymbol{\nabla}_\kappa \times \boldsymbol{\nabla}_\nu)_x\Bigg](\mu\lambda|\kappa\nu) \\
& + \sum_{\lambda\kappa} D^{SS}_{\lambda\kappa,x}\Bigg[(\boldsymbol{\nabla}_\mu \times \boldsymbol{\nabla}_\lambda)_x(\boldsymbol{\nabla}_\kappa \times \boldsymbol{\nabla}_\nu)_z + (\boldsymbol{\nabla}_\mu \times \boldsymbol{\nabla}_\lambda)_z(\boldsymbol{\nabla}_\kappa \times \boldsymbol{\nabla}_\nu)_x\Bigg](\mu\lambda|\kappa\nu) \\
& + \sum_{\lambda\kappa} D^{SS}_{\lambda\kappa,y}\Bigg[(\boldsymbol{\nabla}_\mu \times \boldsymbol{\nabla}_\lambda)_y(\boldsymbol{\nabla}_\kappa \times \boldsymbol{\nabla}_\nu)_z + (\boldsymbol{\nabla}_\mu \times \boldsymbol{\nabla}_\lambda)_z(\boldsymbol{\nabla}_\kappa \times \boldsymbol{\nabla}_\nu)_y\Bigg](\mu\lambda|\kappa\nu) \qquad \text{(B.3)}
\end{aligned}
$$

$$
\begin{aligned}
V^{C(4),SS}_{\mu\nu,x} = {} & 2\sum_{\lambda\kappa}\left[iD^{SS}_{\lambda\kappa,s}(\boldsymbol{\nabla}_\mu\times\boldsymbol{\nabla}_\nu)_x(\boldsymbol{\nabla}_\kappa\cdot\boldsymbol{\nabla}_\lambda)-\sum_{J=x,y,z}D^{SS}_{\lambda\kappa,J}(\boldsymbol{\nabla}_\mu\times\boldsymbol{\nabla}_\nu)_x(\boldsymbol{\nabla}_\kappa\times\boldsymbol{\nabla}_\lambda)_J\right](\mu\nu|\kappa\lambda)\\
& -\sum_{\lambda\kappa}D^{SS}_{\lambda\kappa,x}\Big[(\boldsymbol{\nabla}_\mu\cdot\boldsymbol{\nabla}_\lambda)(\boldsymbol{\nabla}_\kappa\cdot\boldsymbol{\nabla}_\nu)-(\boldsymbol{\nabla}_\mu\times\boldsymbol{\nabla}_\lambda)_x(\boldsymbol{\nabla}_\kappa\times\boldsymbol{\nabla}_\nu)_x\Big](\mu\lambda|\kappa\nu)\\
& -\sum_{\lambda\kappa}D^{SS}_{\lambda\kappa,x}\Big[(\boldsymbol{\nabla}_\mu\times\boldsymbol{\nabla}_\lambda)_y(\boldsymbol{\nabla}_\kappa\times\boldsymbol{\nabla}_\nu)_y+(\boldsymbol{\nabla}_\mu\times\boldsymbol{\nabla}_\lambda)_z(\boldsymbol{\nabla}_\kappa\times\boldsymbol{\nabla}_\nu)_z\Big](\mu\nu|\kappa\lambda)\\
& -i\sum_{\lambda\kappa}D^{SS}_{\lambda\kappa,s}\Big[(\boldsymbol{\nabla}_\mu\cdot\boldsymbol{\nabla}_\lambda)(\boldsymbol{\nabla}_\kappa\times\boldsymbol{\nabla}_\nu)_x+(\boldsymbol{\nabla}_\mu\times\boldsymbol{\nabla}_\lambda)_x(\boldsymbol{\nabla}_\kappa\cdot\boldsymbol{\nabla}_\nu)\Big](\mu\nu|\kappa\lambda)\\
& +\sum_{\lambda\kappa}D^{SS}_{\lambda\kappa,y}\Big[(\boldsymbol{\nabla}_\mu\cdot\boldsymbol{\nabla}_\lambda)(\boldsymbol{\nabla}_\kappa\times\boldsymbol{\nabla}_\nu)_z-(\boldsymbol{\nabla}_\mu\times\boldsymbol{\nabla}_\lambda)_z(\boldsymbol{\nabla}_\kappa\cdot\boldsymbol{\nabla}_\nu)\Big](\mu\nu|\kappa\lambda)\\
& -\sum_{\lambda\kappa}D^{SS}_{\lambda\kappa,z}\Big[(\boldsymbol{\nabla}_\mu\cdot\boldsymbol{\nabla}_\lambda)(\boldsymbol{\nabla}_\kappa\times\boldsymbol{\nabla}_\nu)_y-(\boldsymbol{\nabla}_\mu\times\boldsymbol{\nabla}_\lambda)_y(\boldsymbol{\nabla}_\kappa\cdot\boldsymbol{\nabla}_\nu)\Big](\mu\lambda|\kappa\nu)\\
& +i\sum_{\lambda\kappa}D^{SS}_{\lambda\kappa,s}\Big[(\boldsymbol{\nabla}_\mu\times\boldsymbol{\nabla}_\lambda)_y(\boldsymbol{\nabla}_\kappa\times\boldsymbol{\nabla}_\nu)_z-(\boldsymbol{\nabla}_\mu\times\boldsymbol{\nabla}_\lambda)_z(\boldsymbol{\nabla}_\kappa\times\boldsymbol{\nabla}_\nu)_y\Big](\mu\lambda|\kappa\nu)\\
& +\sum_{\lambda\kappa}D^{SS}_{\lambda\kappa,y}\Big[(\boldsymbol{\nabla}_\mu\times\boldsymbol{\nabla}_\lambda)_x(\boldsymbol{\nabla}_\kappa\times\boldsymbol{\nabla}_\nu)_y+(\boldsymbol{\nabla}_\mu\times\boldsymbol{\nabla}_\lambda)_y(\boldsymbol{\nabla}_\kappa\times\boldsymbol{\nabla}_\nu)_x\Big](\mu\lambda|\kappa\nu)\\
& +\sum_{\lambda\kappa}D^{SS}_{\lambda\kappa,z}\Big[(\boldsymbol{\nabla}_\mu\times\boldsymbol{\nabla}_\lambda)_x(\boldsymbol{\nabla}_\kappa\times\boldsymbol{\nabla}_\nu)_z+(\boldsymbol{\nabla}_\mu\times\boldsymbol{\nabla}_\lambda)_z(\boldsymbol{\nabla}_\kappa\times\boldsymbol{\nabla}_\nu)_x\Big](\mu\lambda|\kappa\nu)
\end{aligned}
\tag{B.4}
$$

$$
\begin{aligned}
V^{C(4),SS}_{\mu\nu,y} &= 2\sum_{\lambda\kappa}\left[iD^{SS}_{\lambda\kappa,s}(\boldsymbol{\nabla}_\mu\times\boldsymbol{\nabla}_\nu)_y(\boldsymbol{\nabla}_\kappa\cdot\boldsymbol{\nabla}_\lambda) - \sum_{J=x,y,z}D^{SS}_{\lambda\kappa,J}(\boldsymbol{\nabla}_\mu\times\boldsymbol{\nabla}_\nu)_y(\boldsymbol{\nabla}_\kappa\times\boldsymbol{\nabla}_\lambda)_J\right](\mu\nu|\kappa\lambda) \\
&- \sum_{\lambda\kappa}D^{SS}_{\lambda\kappa,y}\left[(\boldsymbol{\nabla}_\mu\cdot\boldsymbol{\nabla}_\lambda)(\boldsymbol{\nabla}_\kappa\cdot\boldsymbol{\nabla}_\nu) - (\boldsymbol{\nabla}_\mu\times\boldsymbol{\nabla}_\lambda)_y(\boldsymbol{\nabla}_\kappa\times\boldsymbol{\nabla}_\nu)_y\right](\mu\lambda|\kappa\nu) \\
&- \sum_{\lambda\kappa}D^{SS}_{\lambda\kappa,y}\left[(\boldsymbol{\nabla}_\mu\times\boldsymbol{\nabla}_\lambda)_x(\boldsymbol{\nabla}_\kappa\times\boldsymbol{\nabla}_\nu)_x + (\boldsymbol{\nabla}_\mu\times\boldsymbol{\nabla}_\lambda)_z(\boldsymbol{\nabla}_\kappa\times\boldsymbol{\nabla}_\nu)_z\right](\mu\lambda|\kappa\nu) \\
&- i\sum_{\lambda\kappa}D^{SS}_{\lambda\kappa,s}\left[(\boldsymbol{\nabla}_\mu\cdot\boldsymbol{\nabla}_\lambda)(\boldsymbol{\nabla}_\kappa\times\boldsymbol{\nabla}_\nu)_y + (\boldsymbol{\nabla}_\mu\times\boldsymbol{\nabla}_\lambda)_y(\boldsymbol{\nabla}_\kappa\cdot\boldsymbol{\nabla}_\nu)\right](\mu\lambda|\kappa\nu) \\
&- \sum_{\lambda\kappa}D^{SS}_{\lambda\kappa,x}\left[(\boldsymbol{\nabla}_\mu\cdot\boldsymbol{\nabla}_\lambda)(\boldsymbol{\nabla}_\kappa\times\boldsymbol{\nabla}_\nu)_z - (\boldsymbol{\nabla}_\mu\times\boldsymbol{\nabla}_\lambda)_z(\boldsymbol{\nabla}_\kappa\cdot\boldsymbol{\nabla}_\nu)\right](\mu\lambda|\kappa\nu) \\
&+ \sum_{\lambda\kappa}D^{SS}_{\lambda\kappa,z}\left[(\boldsymbol{\nabla}_\mu\cdot\boldsymbol{\nabla}_\lambda)(\boldsymbol{\nabla}_\kappa\times\boldsymbol{\nabla}_\nu)_x - (\boldsymbol{\nabla}_\mu\times\boldsymbol{\nabla}_\lambda)_x(\boldsymbol{\nabla}_\kappa\cdot\boldsymbol{\nabla}_\nu)\right](\mu\lambda|\kappa\nu) \\
&- i\sum_{\lambda\kappa}D^{SS}_{\lambda\kappa,s}\left[(\boldsymbol{\nabla}_\mu\times\boldsymbol{\nabla}_\lambda)_x(\boldsymbol{\nabla}_\kappa\times\boldsymbol{\nabla}_\nu)_z - (\boldsymbol{\nabla}_\mu\times\boldsymbol{\nabla}_\lambda)_z(\boldsymbol{\nabla}_\kappa\times\boldsymbol{\nabla}_\nu)_x\right](\mu\lambda|\kappa\nu) \\
&+ \sum_{\lambda\kappa}D^{SS}_{\lambda\kappa,x}\left[(\boldsymbol{\nabla}_\mu\times\boldsymbol{\nabla}_\lambda)_x(\boldsymbol{\nabla}_\kappa\times\boldsymbol{\nabla}_\nu)_y + (\boldsymbol{\nabla}_\mu\times\boldsymbol{\nabla}_\lambda)_y(\boldsymbol{\nabla}_\kappa\times\boldsymbol{\nabla}_\nu)_x\right](\mu\lambda|\kappa\nu) \\
&+ \sum_{\lambda\kappa}D^{SS}_{\lambda\kappa,z}\left[(\boldsymbol{\nabla}_\mu\times\boldsymbol{\nabla}_\lambda)_y(\boldsymbol{\nabla}_\kappa\times\boldsymbol{\nabla}_\nu)_z + (\boldsymbol{\nabla}_\mu\times\boldsymbol{\nabla}_\lambda)_z(\boldsymbol{\nabla}_\kappa\times\boldsymbol{\nabla}_\nu)_y\right](\mu\lambda|\kappa\nu) \qquad \text{(B.5)}
\end{aligned}
$$

Appendix C

COST ANALYSIS OF DIRAC-HARTREE–FOCK IN UNRESTRICTED-KINETIC-BALANCED SCALAR BASIS

The computational cost of the four-component method using the unrestricted-kinetic-balanced (UKB) scalar basis strongly depends on the nature of the implementation. This is because upon the generation of small component basis, the kinetic-balance condition no longer directly appears in the two-spinor basis. This allows an implementation in scalar basis to adapt various techniques developed for non-relativistic methods. This is especially true for the Dirac-Coulomb term where Pauli spinors do not enter the integrals.

In this analysis, we assume that all integrals and integral-density contractions in UKB scalar basis are in the non-relativistic one-component framework, and all integrals are stored as real-valued quantities. In this discussion, N_L and N_S are the numbers of basis functions for the large and small component, respectively, in UKB scalar basis. We also assume that both the Fock and density matrices are in the quaternion representation so that the following expressions represent the optimal algorithm in terms of both memory requirement and FLOP count.

For the Coulomb operator, the contraction pattern can be separated into Coulomb $\mathbf{J}^C$

and exchange $\mathbf{K}^C$ matrices,

$$J^{C,LL}_{\mu\nu} = \sum_{\gamma=0,1,2,3}\sum_{\kappa\lambda}(\mu^L\nu^L|\kappa^L\lambda^L)D^{LL}_{\lambda\kappa,\gamma}\hat{\mathbf{e}}_\gamma + \sum_{\gamma=0,1,2,3}\sum_{\kappa\lambda}(\mu^L\nu^L|\kappa^S\lambda^S)D^{SS}_{\lambda\kappa,\gamma}\hat{\mathbf{e}}_\gamma \tag{C.1}$$

$$J^{C,SS}_{\mu\nu} = \sum_{\gamma=0,1,2,3}\sum_{\kappa\lambda}(\mu^S\nu^S|\kappa^L\lambda^L)D^{LL}_{\lambda\kappa,\gamma}\hat{\mathbf{e}}_\gamma + \sum_{\gamma=0,1,2,3}\sum_{\kappa\lambda}(\mu^S\nu^S|\kappa^S\lambda^S)D^{SS}_{\lambda\kappa,\gamma}\hat{\mathbf{e}}_\gamma \tag{C.2}$$

$$K^{C,LL}_{\mu\nu} = \sum_{\gamma=0,1,2,3}\sum_{\kappa\lambda}(\mu^L\lambda^L|\kappa^L\nu^L)D^{LL}_{\lambda\kappa,\gamma}\hat{\mathbf{e}}_\gamma \tag{C.3}$$

$$K^{C,LS}_{\mu\nu} = \sum_{\gamma=0,1,2,3}\sum_{\kappa\lambda}(\mu^L\lambda^L|\kappa^S\nu^S)D^{LS}_{\lambda\kappa,\gamma}\hat{\mathbf{e}}_\gamma \tag{C.4}$$

$$K^{C,SL}_{\mu\nu} = \sum_{\gamma=0,1,2,3}\sum_{\kappa\lambda}(\mu^S\lambda^S|\kappa^L\nu^L)D^{SL}_{\lambda\kappa,\gamma}\hat{\mathbf{e}}_\gamma \tag{C.5}$$

$$K^{C,SS}_{\mu\nu} = \sum_{\gamma=0,1,2,3}\sum_{\kappa\lambda}(\mu^S\lambda^S|\kappa^S\nu^S)D^{SS}_{\lambda\kappa,\gamma}\hat{\mathbf{e}}_\gamma \tag{C.6}$$

where $(\hat{\mathbf{e}}_0, \hat{\mathbf{e}}_1, \hat{\mathbf{e}}_2, \hat{\mathbf{e}}_3)$ is the quaternion basis of choice. Based on these expressions, constructing the Coulomb $\mathbf{J}^C$ matrix requires $4 \times (N_L^4 + 2N_L^2N_S^2 + N_S^4)$ number of integral-density contraction operations, and the $\mathbf{K}$ matrix requires $4\times(N_L^4+2N_L^2N_S^2+N_S^4)$ operations, where the factor of 4 comes from the contraction with four quaternion components. The memory requirement for building the Dirac-Coulomb matrix is $N_L^4 + N_L^2N_S^2 + N_S^4$. All N_S^4 quantities in the analysis correspond to the contributions from the $(SS|SS)$ term.

In order to build the Gaunt operator in UKB scalar basis with the lowest computational cost, the Pauli spin matrices are also cast in the quaternion representation,

$$\boldsymbol{\sigma} = \begin{pmatrix} \sum_\gamma \sigma_{x,\gamma}\hat{\mathbf{e}}_\gamma \\ \sum_\gamma \sigma_{y,\gamma}\hat{\mathbf{e}}_\gamma \\ \sum_\gamma \sigma_{z,\gamma}\hat{\mathbf{e}}_\gamma \end{pmatrix}.$$

As a result, the Gaunt operator under UKB scalar basis can be evaluated with the real scalar

ERIs,

$$J^{G,LS}_{\mu\nu,\tau} = \sum_{\gamma=0,1,2,3} \hat{\mathbf{e}}_\tau \circ \boldsymbol{\sigma}(1) \cdot \left[\boldsymbol{\sigma}(2) \circ (\mu^L \nu^S|\kappa^L \lambda^S)(D^{LS}_{\kappa\lambda,\gamma}\hat{\mathbf{e}}_\gamma + D^{SL}_{\lambda\kappa,\gamma}\hat{\mathbf{e}}_\gamma)\right] \tag{C.7}$$

$$K^{G,LL}_{\mu\nu,\tau} = \sum_{\gamma=0,1,2,3} \hat{\mathbf{e}}_\tau \circ \boldsymbol{\sigma}(1) \cdot \left[\boldsymbol{\sigma}(2) \circ (\mu^L \lambda^S|\nu^L \kappa^S) D^{SS}_{\lambda\kappa,\gamma}\hat{\mathbf{e}}_\gamma\right] \tag{C.8}$$

$$K^{G,SS}_{\mu\nu,\tau} = \sum_{\gamma=0,1,2,3} \hat{\mathbf{e}}_\tau \circ \boldsymbol{\sigma}(1) \cdot \left[\boldsymbol{\sigma}(2) \circ (\lambda^L \mu^S|\kappa^L \nu^S) D^{LL}_{\lambda\kappa,\gamma}\hat{\mathbf{e}}_\gamma\right] \tag{C.9}$$

$$K^{G,LS}_{\mu\nu,\tau} = \sum_{\gamma=0,1,2,3} \hat{\mathbf{e}}_\tau \circ \boldsymbol{\sigma}(1) \cdot \left[\boldsymbol{\sigma}(2) \circ (\mu^L \lambda^S|\kappa^L \nu^S) D^{SL}_{\lambda\kappa,\gamma}\hat{\mathbf{e}}_\gamma\right] \tag{C.10}$$

$$K^{G,SL}_{\mu\nu,\tau} = \sum_{\gamma=0,1,2,3} \hat{\mathbf{e}}_\tau \circ \boldsymbol{\sigma}(1) \cdot \left[\boldsymbol{\sigma}(2) \circ (\lambda^L \mu^S|\nu^L \kappa^S) D^{LS}_{\lambda\kappa,\gamma}\hat{\mathbf{e}}_\gamma\right] \tag{C.11}$$

where we use '$\circ$' to represent dot-product in the quaternion space and '$\cdot$' for dot-product in the Pauli spinor space. It is clear that building the $\mathbf{J}^G$ and $\mathbf{K}^G$ matrix requires $4N_L^2N_S^2$ and $16N_L^2N_S^2$ numbers of integral-density contraction operations with a memory requirement of only $N_L^2N_S^2$.

Appendix D

CALCULATIONS OF HYDROGENIC CATIONS/ATOM COMPARED WITH ANALYTICAL RESULTS OF DIRAC EQUATION

Energy levels of the relativistic Dirac hydrogen atom and hydrogenic cations can be evaluated analytically using the following relation (in atomic units)

$$E = c^2 \times \left[\frac{1}{\sqrt{1 + (\frac{Z\alpha}{n-(j+1/2)+\sqrt{(j+1/2)^2 - Z^2\alpha^2}})^2}} - 1 \right] \tag{D.1}$$

where Z is the nuclear charge and α is fine structure constant. For one electron systems in their ground states, $n = 1$ and $j = \frac{1}{2}$. In order to validate the four-component Dirac–Hartree–Fock implementation, we compare the computed energies with analytical values in Tab. D.1. For a better description of the steep electronic wave function near the nucleus, seven additional steep s functions are added to the uncontracted basis set, with exponents ranging from 3^1 to 3^7 times the largest exponent in the original basis. [258, 259] From this series, we see that the largest error between the analytical result and the Dirac Hartree-Fock result is 0.00352 % for In^{48+} when a uncontracted basis is used, showing good agreement and validating our implementation.

Table D.1: Calculated Dirac-Hartree-Fock ground state energies (Hartrees) for the hydrogen atom and a series of hydrogenic cations compared with the analytical solution of the Dirac equation. The uncontracted Sapporo-DKH3-QZP-2012-no basis is used for all elements except actinides (Ac^{88+}, Es^{98+}, Md^{100+}). Actinide calculations use uncontracted cc-pwCVDZ-X2C basis [257]. Seven steep *s* functions are added to the uncontracted basis. Point charge nuclear model is used.

element	analytical solution	uncontracted basis	percent error ($\times 10^{-3}\%$)
H	−0.5000067	−0.5000029	0.75
B^{4+}	−12.5041630	−12.5038524	2.48
F^{8+}	−40.5437672	−40.5428584	2.24
Al^{12+}	−84.6909743	−84.6891918	2.10
Cl^{16+}	−145.0602703	−145.0573482	2.01
Mn^{24+}	−315.1443548	−315.1385013	1.86
Rb^{26+}	−697.4517670	−697.4334697	2.62
Mo^{41+}	−903.7467394	−903.7213445	2.81
In^{48+}	−1241.5414919	−1241.4977248	3.52
Cs^{54+}	−1578.8736026	−1578.8504245	1.47
Ta^{72+}	−2886.3133130	−2886.2556854	2.00
Ac^{88+}	−4499.5659601	−4499.5624725	0.08
Es^{98+}	−5794.4853497	−5794.4685369	0.29
Md^{100+}	−6087.0342057	−6087.0107482	0.39

Appendix E

DIRAC–COULOMB BASIS SET LIMIT

In order to compare our results to the "true" basis set limit, we can look at the results from Visscher [168] and Hess [260] that utilized a numerical grid basis for both point nuclei and finite Gaussian nuclei. As shown in Tab. E.1, we can see that using an uncontracted basis set gives the expected variational upper bound to the numerically exact limit. The error in the ground state energy is only ∼0.015 E_h for the Gaussian nuclei model, with all three representations (RKB Pauli, RKB spinor, UKB scalar) behaving similarly. (Additionally the UKB scalar calculation includes the average of configuration method for open shell systems.)

Table E.1: Ground state energies (Hartrees) for Au atom with the Dirac-Coulomb Hamiltonian with a Gaussian nuclear model uncontracted ANO-RCC basis is used. RKB Pauli, RKB spinor, and UKB scalar results were obtained using ChronusQ, [164] PySCF, [165] and DIRAC, [261] respectively. Note that the UKB scalar basis is transformed to the RKB spinor during the orthonomalization step. [262]

Model	Energy
Numerical Grid (Ref. [168])	−19035.59510
RKB Pauli	−19035.57905
RKB Spinor	−19035.57905
UKB Scalar	−19035.57807

Appendix F

EQED MOMENTUM SPACE HAMILTONIAN

The interactions in an effective field theory should be chosen to correctly reproduce some physics of the full model. To correctly reproduce the physics of QED, the effective interaction will be chosen to correctly reproduce the QED scattering amplitudes at lowest order in perturbation theory. This means the potential will consist of 4 fermion terms which describe the scattering processes $e^{\pm}e^{\pm} \rightarrow e^{\pm}e^{\pm}$, $e^{+}e^{-} \rightarrow e^{+}e^{-}$, $e^{\pm} \rightleftharpoons e^{\pm}e^{+}e^{-}$ and $0 \rightleftharpoons e^{+}e^{-}e^{+}e^{-}$. Note that the $1 \rightarrow 3$ and $0 \rightarrow 4$ scattering amplitudes will always be off-shell, so these scattering processes will not be directly observed, but including them in the Hamiltonian is necessary for scattering amplitudes at higher orders to be correctly reproduced. The necessary scattering amplitudes in the following subsections are computed using Feynman diagrams at leading order. Further details of these derivations can be found in [214].

F.0.1 $e^{\pm}e^{\pm} \rightarrow e^{\pm}e^{\pm}$ Amplitudes

The electron scattering amplitude is given by

$$\mathcal{M}^{e^{-}_{r,\sigma_3} e^{-}_{p+q-r,\sigma_4}}_{e^{-}_{p,\sigma_1} e^{-}_{p,\sigma_2}} = e^2 \left(\frac{\bar{u}_{\sigma_3}(p_3)\gamma^{\mu}u_{\sigma_1}(p_1)\bar{u}_{\sigma_4}(p_4)\gamma_{\mu}u_{\sigma_2}(p_2)}{(E_{p_3}-E_{p_1})^2-(\vec{p_3}-\vec{p_1})^2} - \frac{\bar{u}_{\sigma_4}(p_4)\gamma^{\mu}u_{\sigma_1}(p_1)\bar{u}_{\sigma_3}(p_3)\gamma_{\mu}u_{\sigma_2}(p_2)}{(E_{p_4}-E_{p_1})^2-(\vec{p_4}-\vec{p_1})^2} \right) . \tag{F.1}$$

The positron scattering amplitude takes a similar form and it is given by

$$\mathcal{M}^{e^{+}_{r,\sigma_3} e^{+}_{p+q-r,\sigma_4}}_{e^{+}_{p,\sigma_1} e^{+}_{q,\sigma_2}} = e^2 \left(\frac{\bar{v}_{\sigma_1}(p_1)\gamma^{\mu}v_{\sigma_3}(p_3)\bar{v}_{\sigma_2}(p_2)\gamma_{\mu}v_{\sigma_4}(p_4)}{(E_{p_3}-E_{p_1})^2-(\vec{p_3}-\vec{p_1})^2} - \frac{\bar{v}_{\sigma_1}(p_1)\gamma^{\mu}v_{\sigma_4}(p_4)\bar{v}_{\sigma_2}(p_2)\gamma_{\mu}v_{\sigma_3}(p_3)}{(E_{p_4}-E_{p_1})^2-(\vec{p_4}-\vec{p_1})^2} \right). \tag{F.2}$$

F.0.2 $e^+e^- \to e^+e^-$ Amplitude

The electron positron scattering amplitude is given by

$$\mathcal{M}_{e^-_{p,\sigma_1} e^+_{q,\sigma_2}}^{e^-_{r,\sigma_3} e^+_{p+q-r,\sigma_4}} = e^2 \left(\frac{\bar{v}_{\sigma_2}(q_1)\gamma^\mu u_{\sigma_1}(p_1)\bar{u}_{\sigma_3}(p_2)\gamma_\mu v_{\sigma_4}(q_2)}{(E_{p_1} + E_{p_2})^2 - (\vec{p_1} + \vec{p_2})^2} + \frac{\bar{u}_{\sigma_3}(p_2)\gamma^\mu u_{\sigma_1}(p_1)\bar{v}_{\sigma_3}(q_1)\gamma_\mu v_{\sigma_4}(q_2)}{(E_{p_1} - E_{p_2})^2 - (\vec{p_1} - \vec{p_2})^2} \right) \quad . \tag{F.3}$$

F.0.3 $e^\pm \to e^+e^-e^\pm$ Amplitude

The $e^- \to e^-e^+e^-$ scattering amplitude is given by

$$\mathcal{M}_{e^-_{p,\sigma_1}}^{e^+_{q,\sigma_2} e^-_{p_1,\sigma_3} e^-_{p-q-p_1,\sigma_4}} = e^2 \left(\frac{\bar{u}_{\sigma_3}(p_1)\gamma^\mu u_{\sigma_1}(p)\bar{u}_{\sigma_4}(p_2)\gamma_\mu v_{\sigma_2}(q)}{(E_p - E_{p_1})^2 - (\vec{p} - \vec{p_1})^2} - \frac{\bar{u}_{\sigma_4}(p_2)\gamma^\mu u_{\sigma_1}(p)\bar{u}_{\sigma_3}(p_1)\gamma_\mu v_{\sigma_2}(q)}{(E_p - E_{p_2})^2 - (\vec{p} - \vec{p_2})^2} \right) . \tag{F.4}$$

The $e^+ \to e^+e^+e^-$ scattering amplitude is given by

$$\mathcal{M}_{e^+_{p,\sigma_1}}^{e^-_{q,\sigma_2} e^+_{p_1,\sigma_3} e^+_{p-q-p_1,\sigma_4}} = e^2 \left(\frac{\bar{u}_{\sigma_2}(q)\gamma^\mu v_{\sigma_4}(p_2)\bar{v}_{\sigma_1}(p)\gamma_\mu v_{\sigma_3}(p_1)}{(E_p - E_{p_1})^2 - (\vec{p} - \vec{p_1})^2} - \frac{\bar{u}_{\sigma_2}(q)\gamma^\mu v_{\sigma_3}(p_3)\bar{v}_{\sigma_1}(p)\gamma_\mu v_{\sigma_4}(p_2)}{(E_p - E_{p_2})^2 - (\vec{p} - \vec{p_2})^2} \right) . \tag{F.5}$$

F.0.4 Naïve Vacuum Coupling

The amplitude describing the coupling of the naïve vacuum to states with nonzero electron and positron number is given by

$$\mathcal{M}_0^{e^-_{p,\sigma_1} e^+_{q,\sigma_2} e^-_{r,\sigma_3} e^+_{-p-q-r,\sigma_4}} = \frac{\bar{u}_{\sigma_1}(p)\gamma^\mu v_{\sigma_2}(q)\bar{u}_{\sigma_3}(r)\gamma_\mu v_{\sigma_4}(-p-q-r)}{(E_p + E_q)^2 - (\vec{p} + \vec{q})^2} \quad . \tag{F.6}$$

Appendix G

DIAGONALIZATION OF EQED INTERACTION TERMS

In order to derive our simulation circuits for the imaginary terms in the eQED Hamiltonian we need to show explicit simulation circuits for the mutually commuting Pauli operators of the form $YXXX, XYXX, \ldots, XYYY$. There are eight possible combinations of which four cases need to be considered. To see why this is, let us consider the cases $XYYY, YXYY, YYXY, YYYX$. The GHZ preparation circuit, G, has a symmetry in that the circuit is invariant under swaps of qubits $2, 3$ and 4. Thus if we utilize this permutational symmetry, the only cases that need to be considered are $XYYY$ and $YXYY$ as the other two are equivalent to $YXYY$ under exchange of the last three qubits. The exact same argument holds true for $XXXY, \ldots, YXXX$ and so only four cases need to be considered to understand how the modified GHZ preparation circuit G diagonalizes such terms.

Original	Equivalent	Original	Equivalent
$G^\dagger(XYYY)G$	$-ZZZZ$	$G^\dagger(YXXX)G$	$Z111$
$G^\dagger(YYYX)G$	$-ZZZ1$	$G^\dagger(XXXY)G$	$Z11Z$
$G^\dagger(YYXY)G$	$-ZZ1Z$	$G^\dagger(XXYX)G$	$Z1Z1$
$G^\dagger(YXYY)G$	$-Z1ZZ$	$G^\dagger(XYXX)G$	$ZZ11$

Table G.1: Summary of diagonalization of Hamiltonian terms using the GHZ preparation circuit G

The proof that the circuit G introduced in section 4.3.2 diagonalizes all the relevant Pauli operators will make use of the X and Z error propagation identity shown in Fig. G.1.

In the first line of Fig. G.2, the identity $Y = iXZ$ has been used to replace the Y gate

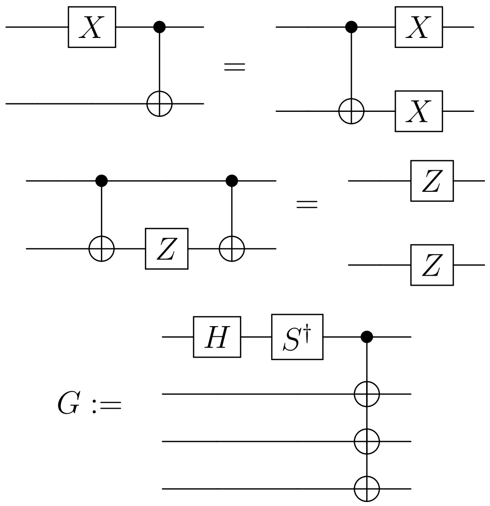

Figure G.1: X and Z Error Propagation Identities and definition of the GHZ transformation circuit G

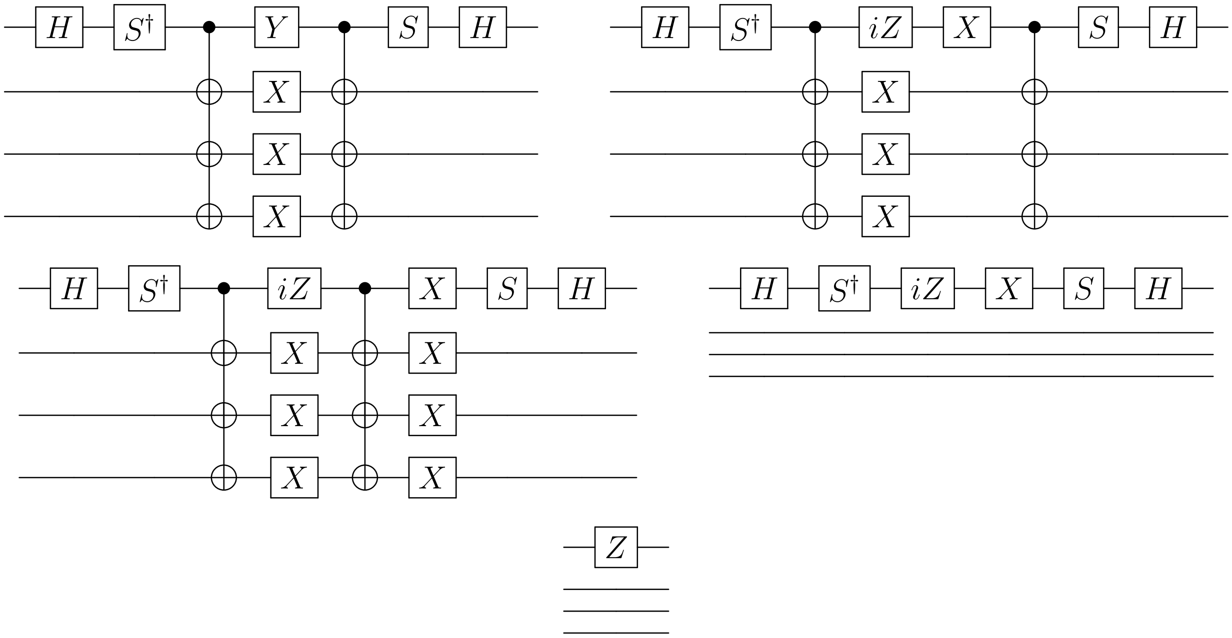

Figure G.2: Diagonalization of $YXXX$

acting on the first qubit. The X error identity was then used to move the X gate acting on the first qubit past the CNOT gate. Since a Z gate acting on the control of a CNOT

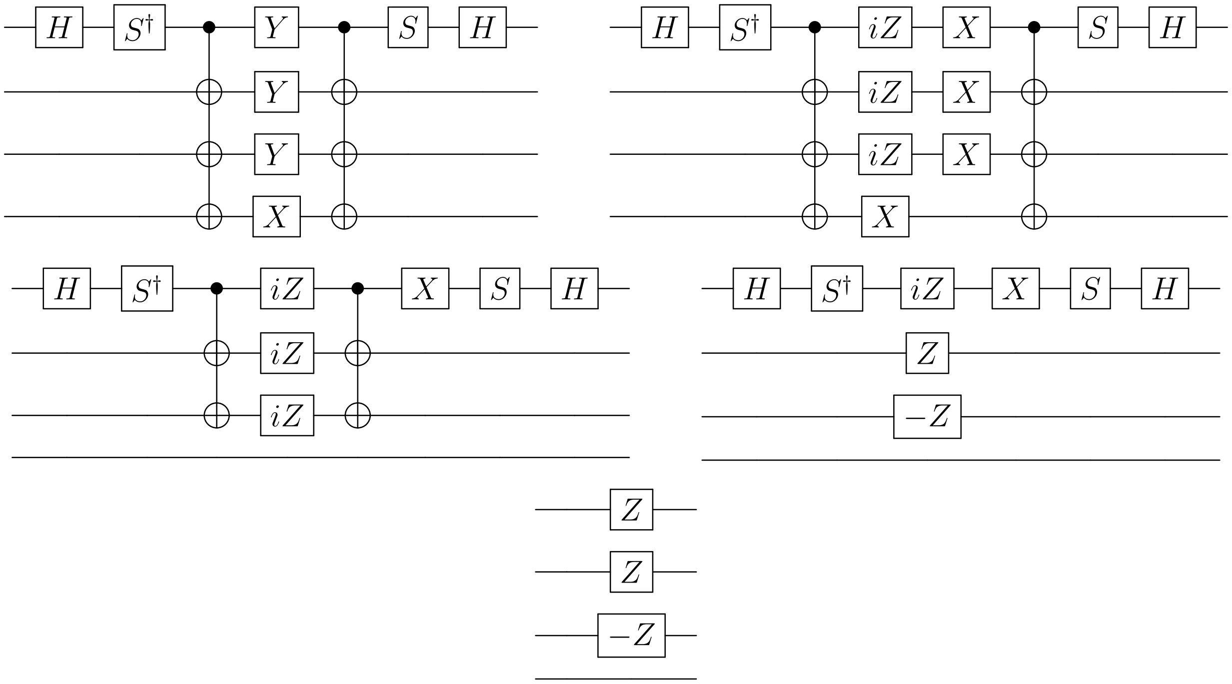

Figure G.3: Steps involved in showing the diagonalization of $YYYX$ using GHZ transformations.

commutes with the CNOT and an X gate acting on the target of a CNOT commutes with the CNOT, the Z gate acting on the first qubit can be moved past the CNOT's and the X gates acting on the lower qubits can be moved past the CNOT's. This results in a cancellation of all of the CNOT's and X's acting on the three lower qubits. Calculating $G^\dagger(YXXX)G$ is reduced to computing the product of the single qubit gates in the second to last diagram of Fig. G.2 which concludes the proof that $G^\dagger(YXXX)G = Z111$. The same techniques are applied in the following diagrams to diagonalize the remaining relevant Pauli operators.

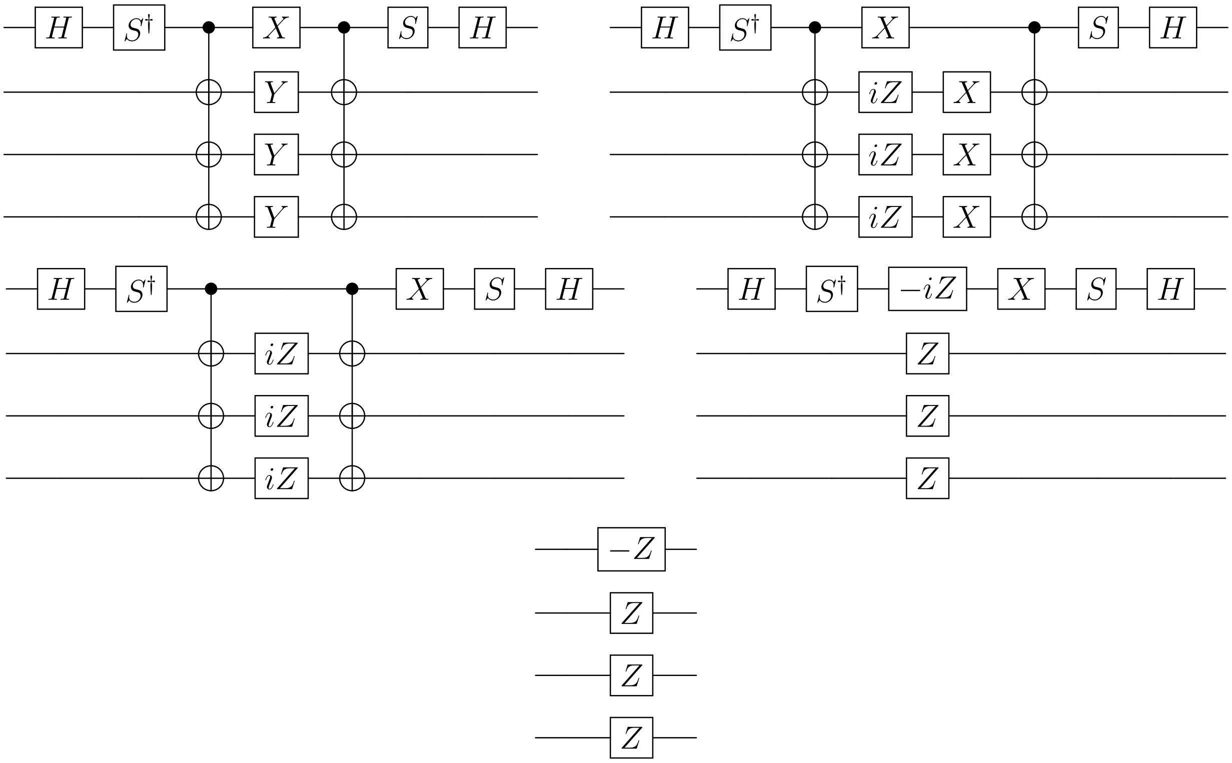

Figure G.4: Diagonalization of $XYYY$

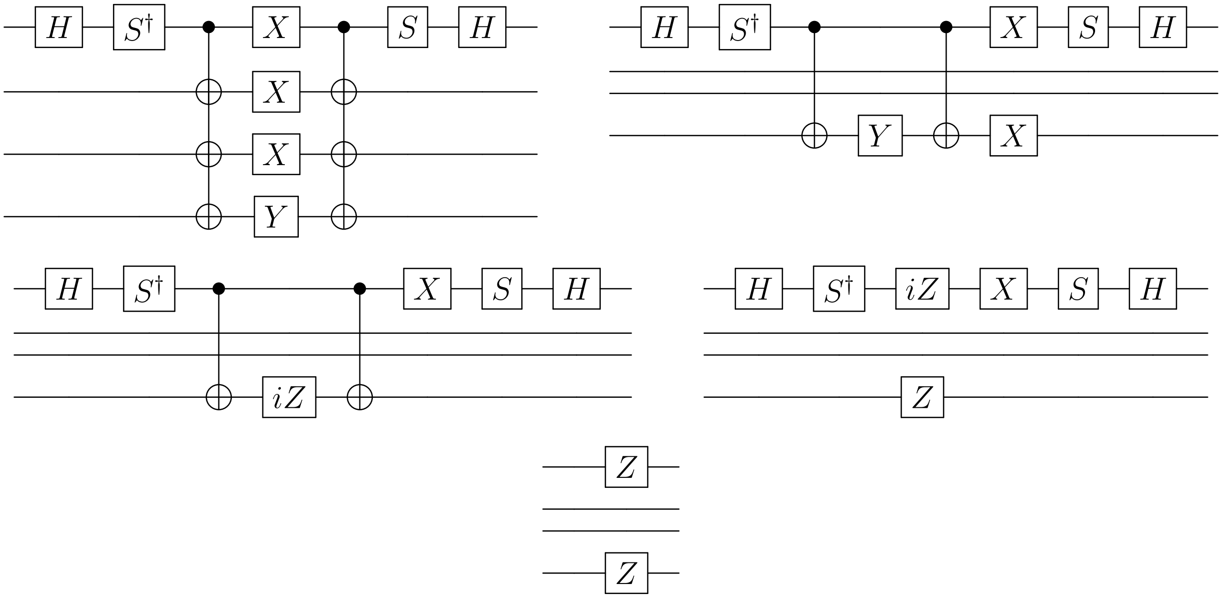

Figure G.5: Diagonalization of $XXXY$